INNOVATIVE ELECTROCONDUCTIVE CERAMIC COMPOSITES BASED ON Si_3N_4

Aljoša Maglica

Doctoral Dissertation
Jožef Stefan International Postgraduate School
Ljubljana, Slovenia, March 2011

Supervisor: *Prof. Dr. Tomaž Kosmač*

Co-supervisor: *Assist. Prof. Dr. Kristoffer Krnel*

Evaluation Board:

Assist. Prof. Dr. Goran Dražić, Jožef Stefan Institute, Jamova 39, 1000 Ljubljana

Prof. Dr. Darko Makovec, Jožef Stefan Institute, Jamova 39, 1000 Ljubljana

Prof. Dr. Mihael Drofenik, Faculty of Chemistry and Chemical Technology, 2000 Maribor

Aljoša Maglica

INNOVATIVE ELECTROCONDUCTIVE CERAMIC COMPOSITES BASED ON Si_3N_4

Doctoral Dissertation

INOVATIVNI ELEKTRIČNO PREVODNI KERAMIČNI KOMPOZITI NA OSNOVI Si_3N_4

Doktorska disertacija

Supervisor: Prof. Dr. Tomaž Kosmač

Co-Supervisor: Assist. Prof. Dr. Kristoffer Krnel

March 2011

MEDNARODNA PODIPLOMSKA ŠOLA JOŽEFA STEFANA
JOŽEF STEFAN INTERNATIONAL POSTGRADUATE SCHOOL
Ljubljana, Slovenia

Table of Contents

Abstract

This thesis describes an investigation of electrically conductive composites based on Si_3N_4 with dispersed TiN or ZrN particles fabricated by an in-situ composite method. The influence of the amount of conductive phase of the Si_3N_4/TiN and Si_3N_4/ZrN composites on the density, the flexural strength and the electrical conductivity were evaluated.

The first part of my work was focused on the formation of TiN and ZrN nanoparticles on the Si_3N_4 powder surface by an in-situ gel-precipitation of Ti- and $Zr(OH)_4$ and a subsequent chemical reaction at an elevated temperature. The results showed that the conversion of TiO_2 to TiN with a narrow particle size distribution, ranging from 4 nm to 10 nm can be completed after a thermal treatment at 900 °C for 6 h in a NH_3 gas flow. The in-situ formation of nano-sized ZrN on the Si_3N_4 particles is more challenging, due to the higher reaction temperature between the ZrO_2 and Si_3N_4 and due to the change in the SiO partial pressure. The complete conversion of ZrO_2 to ZrN with an average particle size of 40 nm can be attained at 1600 °C for 3 h in flowing nitrogen at low pressure.

In the second part of my research, relatively dense and homogeneous Si_3N_4/TiN and Si_3N_4/ZrN composites were fabricated by the pressureless sintering of compacted TiN- or ZrN-coated Si_3N_4 powders with Y_2O_3 and Al_2O_3 sintering additives at 1850 °C for 2 h in N_2. The results of the flexural strength and the electrical resistivity measurements indicate that with an increasing amount of TiN and ZrN in the composites, the electrical conductivity increases, while at the same time the flexural strength decreases, making these ceramics containing 24 vol. % of TiN and 47 vol. % of ZrN suitable for the production of heating elements. The percolation threshold for the electrical conductivity of these composites was two times lower than in the case of the composites prepared with the conventional composite method using mechanically mixed powders. In addition, a simple theoretical percolation-threshold model was developed by considering the various aspect ratios of the insulating ellipsoids as well as the different diameters of the conductive particles. The results revealed that this model provides a good interpretation of the obtained experimental results for the electrical conductivity of both composites.

In the third part an attempt was made to fabricate the Si_3N_4/ZrN composites by the direct sintering of ZrO_2-coated Si_3N_4 powders together with yttria and alumina additives. It was expected that the reaction of ZrO_2 with Si_3N_4 would take place during the heating stage. The results demonstrated that when the composite contained 20 vol. % of ZrO_2 in the starting composition, the reaction leading to the formation of ZrN was not completed. Irrespective of the density gradient from the core to the outer surface of the sample, the composite exhibited a high flexural strength and its surface was electrically conductive, while the internal part remained as an insulator. We found that these results are promising for the production of heating elements. As a result, a one-step manufacturing process for a composite ceramic heater was patented.

Povzetek

Doktorsko delo obravnava raziskavo električno prevodnih kompozitov na osnovi Si_3N_4 z dispergiranimi delci TiN ali ZrN pripravljenih z in-situ kompozitno metodo. Določili smo vpliv količine prevodnih delcev v Si_3N_4/TiN in Si_3N_4/ZrN kompozitih na gostoto, upogibno trdnost in električno prevodnost.

V prvem delu mojega dela sem se osredotočil na tvorbo TiN in ZrN nanodelcev na površini Si_3N_4 prahu, pripravljenih z in-situ gel precipitacijo Ti- in $Zr(OH)_4$ in naknadne kemijske reakcije pri povišani temperaturi. Rezultati so pokazali, da je konverzija TiO_2 v TiN z ozko porazdelitvijo velikostjo delcev v območju od 4 nm do 10 nm zaključena po toplotni obdelavi pri 900 °C, 6 h, v pretoku plinastega amoniaka. In-situ tvorba nanometrskih delcev ZrN na površini Si_3N_4 delcev je tehnološko zahtevnejša, zaradi višje temperature reakcije med ZrO_2 in Si_3N_4 in spremembe parcialnega tlaka SiO. Popolna konverzija ZrO_2 v ZrN s povprečno velikostjo delcev 40 nm je dosežena pri 1600 °C, 3 h, v pretoku dušika pri nizkem tlaku.

V drugem delu raziskav sem pripravil relativno goste in homogene kompozite Si_3N_4/TiN in Si_3N_4/ZrN s sintranjem stisnjenih mešanic prahu Si_3N_4 oblečenega s TiN ali ZrN nanodelci in dodatkov za sintranje (Y_2O_3 in Al_2O_3) pri 1850 °C, 2 h, v pretoku dušika pri tlaku 1 atm. Rezultati meritev upogibne trdnosti in električne prevodnosti kažejo, da električna prevodnost z večanjem deleža TiN in ZrN narašča, medtem ko upogibna trdnost pada. Takšna keramika s 24 vol. % TiN ali 47 vol. % ZrN je primerna za izdelavo grelnih teles. Perkolacijski prag za električno prevodnost takšnih kompozitov je dvakrat nižji v primerjavi s kompoziti, ki so pripravljeni z običajnim postopkom mešanja izhodnih praškov. Poleg tega smo postavili preprost, teoretični model za določitev perkolacijskega praga z upoštevanjem različnega razmerja med dolžino in širino izolativnih elipsoidov in velikosti prevodnih delcev. Rezultati so pokazali, da je omenjeni model dobra interpretacija za dosežene vrednosti električne prevodnosti obeh kompozitov.

V zadnjem delu sem skušal pripraviti kompozite Si_3N_4/ZrN z direktnim sintranjem prahu Si_3N_4 oblečenega z ZrO_2 nanodelci skupaj z dodatki Y_2O_3 in Al_2O_3. V tem primeru smo pričakovali, da bo reakcija med ZrO_2 in Si_3N_4 potekla med segrevanjem vzorca do temperature sintranja. V kompozitu z 20 vol. % ZrO_2 v začetni mešanici tvorba ZrN preko reakcije med ZrO_2 in Si_3N_4 ni potekla do konca. Ne glede na različno gostoto materiala iz sredice do zunanje površine vzorca ima kompozit visoko upogibno trdnost in je električno prevoden na površini, medtem ko je notranji del kompozita izolator. Na podlagi rezultatov smo zaključili, da je takšen postopek obetaven za izdelavo grelnih teles in tako patentirali enostopenjski postopek izdelave kompozitnega keramičnega grelca.

Abbreviations

EDM = Electrical discharge machining

RBSN = Reaction-bonded silicon nitride

HPSN = Hot-pressed silicon nitride

SSN = Sintered silicon nitride

HIPSN = Hot isostatically pressed silicon nitride

XRD = X-ray diffractometry

SEM = Scanning electron microscopy

PVD = Physical vapour deposition

SPS = Spark plasma sintering

BSE = Back-scattered electron

TEM = Transmission electron microscopy

CTRN = Carbothermal-nitridation process

CNT = Carbon nanotube

STEM = Scanning transmission electron microscopy

HRTEM = High resolution transmission microscopy

TMAH = Tetramethylammonium hydroxide

SAED = Selected-area electron diffraction

EDXS = Energy-dispersive x-ray spectroscopy

ΔG = Gibbs free energy change

CS = Cross-section

IP = Internal-part

VR = Volume ratio of conducting and insulating phases

1 Introduction

1.1 Electroconductive ceramic composites

Silicon-nitride-based ceramics are used for high-temperature structural applications because of their excellent combination of properties, such as strength, hardness, and thermal and chemical stability.[1,2,3,4,5] In addition, it is well known that the properties of ceramic materials can be tailored by an addition of secondary particles. In the past two decades much attention has been devoted to the production of particulate-reinforced silicon nitride (Si_3N_4) materials, because of their improved toughness and strength, as well as their mechanical reliability.[6] Another potential advantage of such composite materials is their multifunctionality, in particular their variable electrical conductivity, obtained by the incorporation of electrically conductive particles into the matrix phase.[7] Due to their excellent mechanical properties and good oxidation and corrosion resistance such materials are interesting for the applications where electrically conductive components are needed, for example, in ceramic glow plugs for diesel engines, heaters, igniters, etc.[8,9,10,11] Another benefit of these composites is that they can be formed into complex shapes by electrical discharge machining (EDM)[12,13], which is the method most suitable for the shaping of hard electrically conductive materials. For EDM the required electrical resistivity of the materials, in order to support sparking, is typically less than 100 Ω cm.[14,15]

Electroconductive ceramic composites consist of a strong and tough non-oxide matrix phase and an electrically conductive second phase. The appropriate composite material for the matrix phase has to be made from a nonconductive, non-oxide material, which serves as an insulator. The second phase has to contain a fine electrically conductive material that has good electrical properties. Both components must be chemically compatible and they should have suitable sintering kinetics and an appropriate thermal-expansion coefficient.

The most commonly used materials or systems are $Si_3N_4/MoSi_2$,[16,17,18,19] Si_3N_4/WC[20] and AlN-SiC solid solutions with dispersed $MoSi_2$ particles.[21,22,23,24,25,26] In the past three decades many investigations have focused on the preparation and the properties of Si_3N_4 ceramics with incorporated $MoSi_2$ or WC particles in order to produce highly electoconductive materials for ceramic heaters and ceramic glow plugs. Most of these materials or systems are protected with several patents (US 6309589B1, US 6084212, EP 1477740 and US 5993722). Recently, attempts were made to use a silicon-nitride matrix with titanium nitride as its conductive phase.[27,28,29,30] The research of modern engineering ceramics also aims at using cheaper and more easily available raw materials.

The state-of-the art electoconductive materials are generally prepared from a powder mixture where the grain size of the conductive particles influences the percolation threshold. The composites prepared with such a method sometimes have poor mechanical and electrical properties due to the large second-phase particles and their agglomeration. In order to achieve the desirable electrical conductivity with large, second-phase particles, the percolation threshold is around 25 to 35 vol. % of the conductive phase. Such a large amount of secondary phases can also lead to poor sinterability of the system. In order to attain desirable mechanical and electrical properties, high-quality and expensive materials are needed and techniques of densification under pressure should be applied. An alternative method, developed recently, is an in-situ composite method, where conductive particles are formed in the reaction during the sintering process, which can result in a homogenous distribution of the electrically conductive phase with a small particle size, and this can lead to a decrease in the percolation threshold for electrical conductivity.[31,32,33]

In this work the TiN and ZrN were used as a conductive phase. These materials were selected since the Si_3N_4 powder can be coated by the TiN and ZrN particles from different inorganic precursors using a subsequent thermal treatment where the chemical reaction leading to the formation of TiN and ZrN is taking place. The benefit of these conductive materials is that they can be prepared by using cheaper raw materials and can be densified with Si_3N_4 almost to the theoretical density with a pressureless sintering technique. Moreover, the Si_3N_4/ZrN composites prepared with ZrN-coated Si_3N_4 powders will represent a novel approach to the preparation of electrically conductive ceramic composites.

1.1.1 Potential materials for the matrix phase

Potential materials for the production of ceramic heaters or ceramic glow plugs for diesel engines have to match certain criteria relating to the combination of at least two different monolithic or composite materials, which have to be compatible. During the sintering process the stresses of differential shrinkage or thermal stresses, which develop during cooling, should not occur. Therefore, the materials must exhibit matching thermal expansion coefficients and densification kinetics. They must have good thermal conductivity, and a conductive phase with suitable electrical properties is required. Such composite ceramic materials must have a high chemical (corrosion) and mechanical resistance (high fracture toughness, strength and thermal shock resistance) at elevated temperatures.

A review of the accessible literature and a comparative study of the properties for the nonconductive ceramic matrix component indicates that the most commonly used materials are Si_3N_4 and a glass phase from the polymeric precursor ($Si_xO_yC_zN_w$). The composites based on the AlN-SiC solid solution, the transition-metal-borides-based composites and SiAlONs can also be found. However, the properties of such materials are less suitable and therefore these glow plugs are still not on the market. The reason is that the AlN-SiC solid solution and the transition-metal-borides-based composites have lower mechanical properties than the Si_3N_4 matrix. In contrast to SiAlONs that have good mechanical properties, they exhibit a lower thermal conductivity due to the incorporated oxygen in the crystal lattice. The oxide ceramics like Al_2O_3, ZrO_2 and SiO_2 are not appropriate for such applications due to their low thermal conductivity.

1.1.1.1 Silicon Nitride

Silicon nitride has been studied intensively for more than 40 years, principally in response to the challenge to develop a suitable ceramic for high-temperature structural applications in (gas turbo) engines.[34] The material was first fabricated in the 1950's for the use of thermocouple tubes, crucibles for molten metal and for rocket nozzles.[35] This type of material was produced by a direct nitriding of the silicon-powder parts in the temperature range from 1100 °C to 1450 °C and was later termed reaction-bonded silicon nitride (RBSN).[36] There are two major ceramic forms of silicon nitride ceramics, i.e., the reaction bonded and sintered form, as well as the often overlooked, but extremely important, amorphous form, normally used as a thin film. Each form has its characteristic productions routes, compositions, microstructures, properties, and underlying all the forms there are the fundamental physical and chemical properties of the basic structural unit itself, Si_3N_4, which, at the atomic and unit-cell level, provides the basis for many of the bulk property values. The ceramic parts are usually fabricated by traditional ceramic powder-processing route, which includes powder production, shaping and consolidation. Each of these steps, when determining the microstructural quality, has an important influence on the final bulk properties (notably the mechanical strength) that can completely override the fundamental structural aspects.

The reaction-bonded materials are not completely dense. In order to achieve good properties of Si_3N_4, the starting powders must be homogenously densified into compacts. Unfortunately, this was not possible because suitable densification techniques were lacking. For an intrinsically high-strength, high-hardness material such as Si_3N_4, the high-energy covalent chemical bonds giving rise to these mechanical properties are a disadvantage in the sintering processes. The self-diffusivity in Si_3N_4 is quite low and atomic species only become sufficiently mobile for densification at the temperatures where the decomposition of Si_3N_4 begins (above 1850 °C under 1 atm of N_2 pressure). The production of high-density Si_3N_4 materials only became possible after the techniques of densification had been established. Therefore, alternative approaches were developed and, during the 1960s, increased densities resulted from hot-pressing previously formed Si_3N_4 powder with various sintering additives.[37] With magnesium oxide (MgO) a full density close to the theoretical density of the material was produced by hot-pressing at 1850 °C under 23 MPa and the strength was substantially improved over that of the RBSN. In addition, MgO was also used as the densification additive in the first commercial hot-pressed silicon nitride (HPSN).[38] Though today the densification of Si_3N_4 powders is possible by applying normal sintering without additional pressure, the additives are, in general, still a necessity. Densification without additives is possible only when high pressures and temperatures are applied. As a consequence, the resulting materials do not exhibit pure Si_3N_4 qualities, as they are mixtures or alloys of Si_3N_4 and additional compounds necessary for a complete densification.

Since the 1970s, an investigation into improved materials has led to a better understanding of the role of sintering additives in densification and the microstructural development of silicon-based ceramics, and their influence on final properties.[39] Improvements in powder manufacturing and ceramic-forming techniques, as well as the development of alternative firing processes, have led to a complete "family" of Si_3N_4 materials, including RBSN, HPSN, sintered silicon nitride (SSN), sintered reaction-bonded silicon nitride (SRBSN), hot isostatically pressed silicon nitride (HIPSN) and solid solutions such as SiAlONs, named after their major elemental components.

Crystal structure and transformations

Early discussions concerned the composition of the compound obtained by heating the mixtures of SiO_2 and carbon or by silicon alone in nitrogen: SiN_2, Si_2N_2 and Si_3N_4 were proposed[40] as formulas, with "normal" Si_3N_4 being shown to have the 3:4 stoichiometry. Detailed X-ray diffractometry (XRD) examinations in the mid-1950's proved the existence of two major crystallographic modifications, α and β that are both hexagonal.[41,42] The c-axis dimension of the unit cell of the α phase is approximately twice the size of the β phase, with the phenacite (Be_2SiO_4) structure, in which the oxygen atoms are replaced by nitrogen and the beryllium atoms by silicon. The bonding leads to a framework of SiN_4 tetrahedra (slightly distorted) joined by sharing nitrogen corners so that each nitrogen is common to three tetrahedra. The unit cell of β-Si_3N_4 consists of Si_6N_8, which Hardie and Jack assigned to the space group $P6_3/m$ (Figure 1). The structure of α-Si_3N_4, shown in Figure 2, was determined to be closely related to that of β-Si_3N_4 consisting of alternate basal layers of β-Si_3N_4 and a mirror image of β-Si_3N_4, accounting for the doubled c-axis dimensions, and a unit-cell composition $Si_{12}N_{16}$ (space group $P3_1c$).

The α→β transformation in Si_3N_4 requires a lattice reconstruction. This type of process usually occurs only when the transforming material is in contact with a solvent. The greater solubility of the more unstable α-phase drives it into solution, after which it precipitates as the less-soluble, more-stable β-phase. The predominantly α-Si_3N_4 powder used to produce dense Si_3N_4 ceramics was observed to transform into the β modification during the sintering process at temperatures in excess of 1400 °C, when the original α phase is in contact with a metal-silicon-oxynitride liquid phase.[43,44] Therefore, the transformation was impurity controlled, and later shown to take place readily in the presence of a liquid phase through a reconstructive transformation.[45]

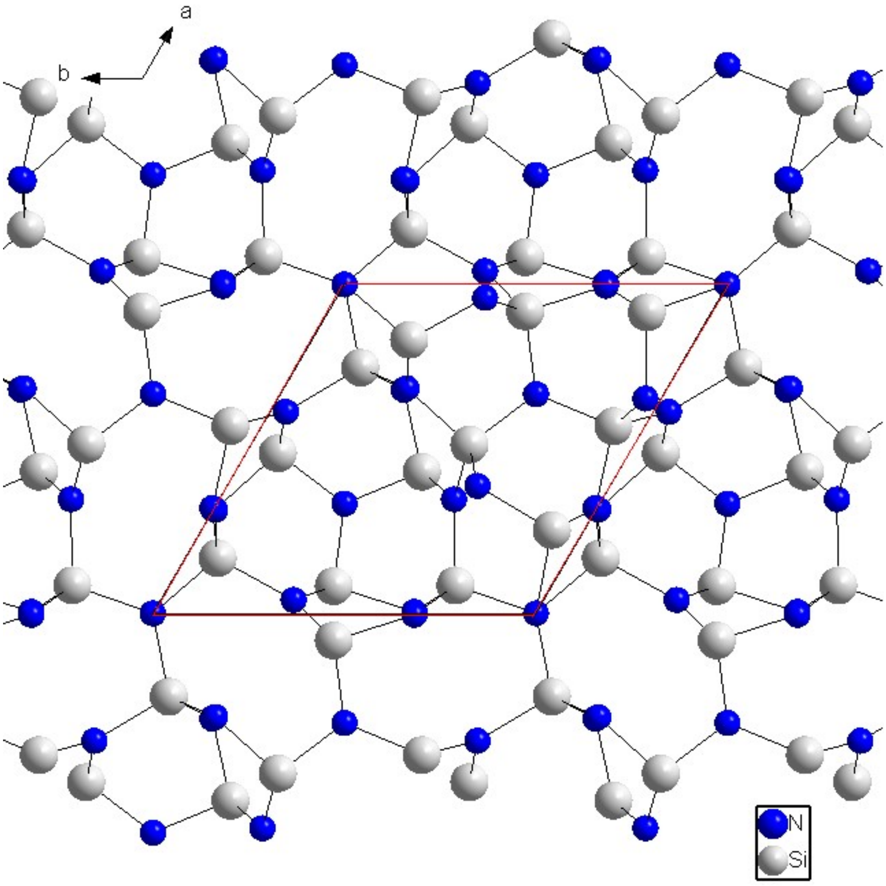

Figure 1: β-Si_3N_4 unit cell linked along [001] directions.

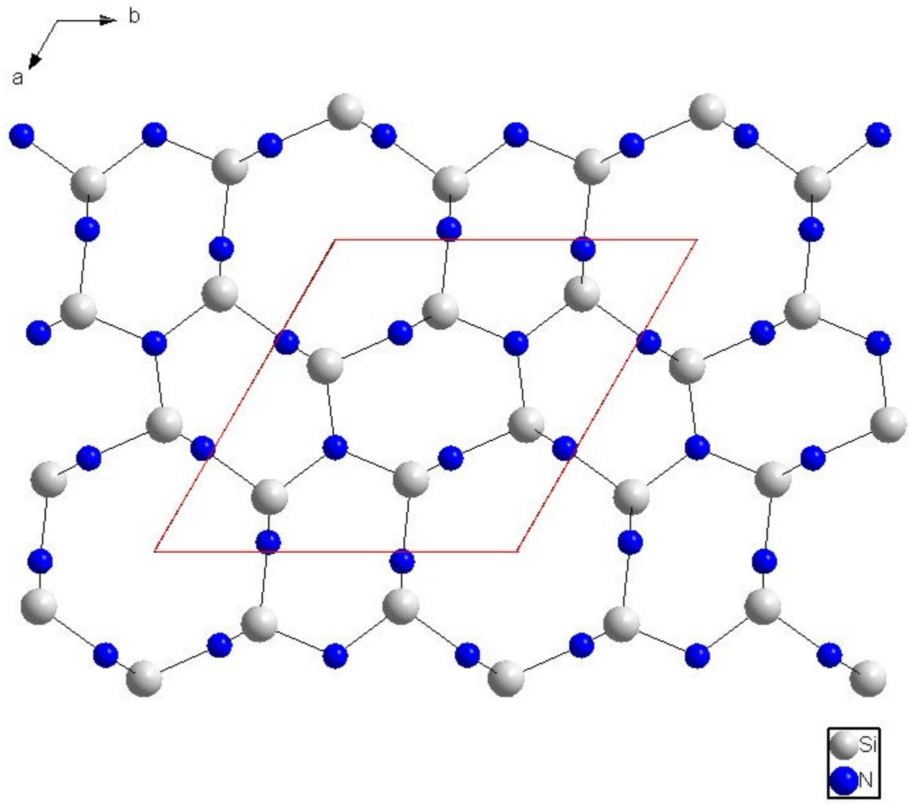

Figure 2: α-Si_3N_4 unit cell linked along [001] directions.

The α→β transformation involves breaking and reforming six Si-N bonds in each unit cell, with a change in the position of one nitrogen and a small displacement of the neighbouring atoms. As the difference in the Gibbs free energy between β-Si_3N_4 and α-Si_3N_4 is small and the activation energy is high, the process can apparently only proceed readily in the presence of liquids (silicon, silicides or silicates), which lowers the transformation activation energy. The reverse β-Si_3N_4 to α-Si_3N_4 transformation has never been observed, but it would be expected to be too slow to be detected at temperatures below 1400 °C.

Liquid-phase sintering and microstructural development in silicon nitride

Every powder particle of Si_3N_4 is surrounded by a surface layer of silica. Oxide additives needed for consolidation of Si_3N_4 react with the silica and some of the nitride itself at the sintering temperatures to form an oxynitide liquid, which promotes densification by solution-precipitation.[46] The α-Si_3N_4 dissolves in the liquid phase and is precipitated as β-Si_3N_4, which grows in the longitudinal direction as prismatic, hexagonal, rod-like crystals that eventually impinge on each other, forming an interlocked microstructure. The liquid cools as an intergranular phase, usually a glass, according to Equation 1:

$$\alpha\text{-}Si_3N_4 + SiO_2 + M_XO_Y \rightarrow \beta\text{-}Si_3N_4 + \text{M-Si-O-N phase} \qquad (1)$$

Initially, additives such as MgO or Y_2O_3 were used to sinter Si_3N_4[47,48] and subsequently, mixed-oxide additives such as Y_2O_3 + Al_2O_3[49,50,51,52] and various rare-earth oxides[53,54] were explored to develop specific microstructures by modifying the nature of the grain-boundary phase. A scanning electron micrograph of a sintered Si_3N_4 with Y_2O_3 + Al_2O_3 additives is presented in Figure 3. As described, elongated rod-like β-Si_3N_4 grains surrounded by a Y-Si-Al-O-N glassy phase are clearly visible.

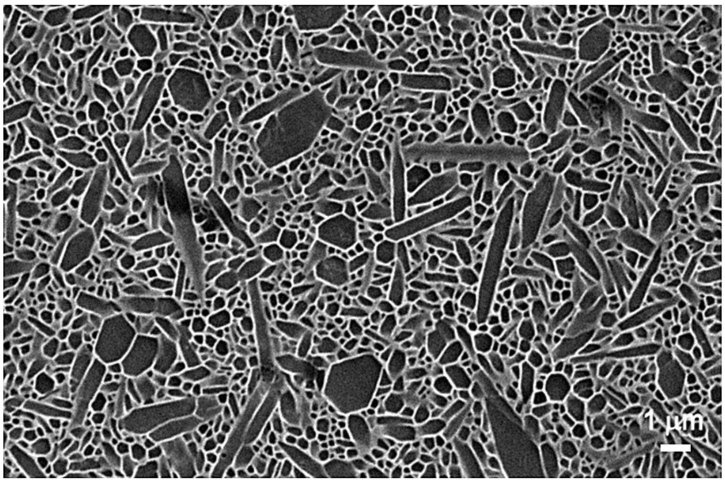

Figure 3: SEM micrograph of Si_3N_4 densified by Y_2O_3 + Al_2O_3.[46]

Sintering of the Si_3N_4 ceramic to almost theoretical density is possible by using sintering additives that form an intergranular liquid phase. During sintering the equilibrium partial pressure of Si above the SiO_2 and the sintering additives has to be reached. If Si_3N_4 is sufficiently soluble in the liquid then the densification of Si_3N_4 can be described with the classical sintering theory proposed by Kingery.

The only systematic study[55,56] of pressureless sintering kinetics applies the Kingery liquid-phase sintering model[57] in which three stages are indentified, as summarized by the log-shrinkage/log-time plot of Figure 4.

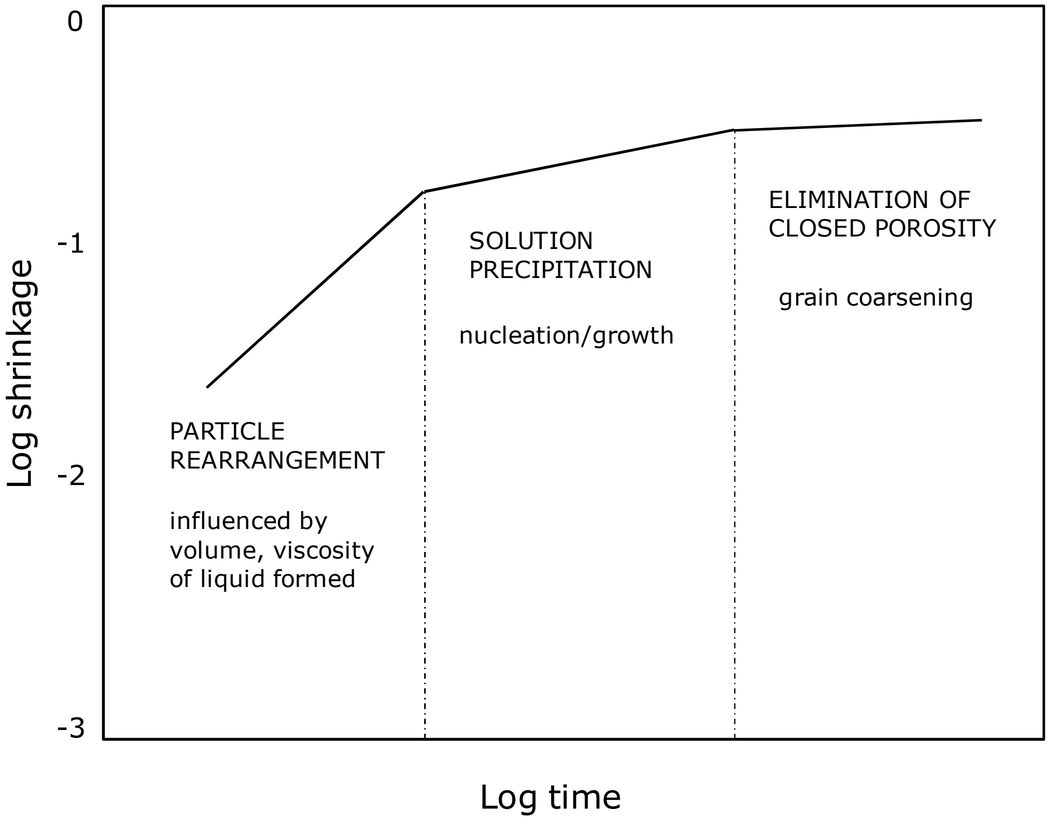

Figure 4: Schematic plot of the three stages of the liquid-phase sintering of Si_3N_4.[55]

These stages are as follows:

1) Particle rearrangement within the initial liquid, where the rate and the extent of shrinkage depend on the volume and viscosity of the liquid. This is the so-called incubation period for the α→β transformation.

2) Solution-diffusion-reprecipitation, where shrinkage can be expressed as:

$$\Delta V/V_o \ \alpha \ t^{1/n} \qquad (2)$$

where t is the time; n = 3 if the solution into, or the precipitation from, the liquid is rate controlling and this was found to be the case for the MgO additive; n = 5 if diffusion through the liquid is rate controlling as in the case for the Y_2O_3 additive, where diffusion through a more viscous oxynitride liquid is much slower. The α-β transformation begins during this stage and is more rapid in the case of Y_2O_3.

3) Final elimination of the closed porosity during which the liquid acts to form a more rounded grain morphology. The final density is higher than 95 % of the theoretical value. The type and amount of the additive used for sintering not only aids densification but also determines the nature and the quantity of the resulting grain-boundary phase, as indicated in Equation 2. The concept of "grain-boundary engineering" sought to control the structure of, and reactions occurring at, the grain boundaries in Si_3N_4-based materials and significant advances in the materials' properties were realized as a result of this approach.

The typical properties of a liquid phase sintered silicon nitride ceramics are shown in Table 1.

Table 1: Properties of Si_3N_4[34]

Properties	Si_3N_4
Crystal structure	
α-modification	hexagonal, a=0.775-0.777 nm c=0.516-0.569 nm
β-modification	hexagonal, a=0.759-0.761 nm c=0.271-0.292 nm
Decomposition temperature [°C]	1900
Theoretical density *[g/cm³]*	
α-modification	3.168-3.188
β-modification	3.19-3.202
Density [% TD]	90-100
Specific energy [J/kgK]	700
Electrical resistivity [Ωm]	10^{11}
Thermal expansion coefficient [1/K] (20-1500°C)	$2.9\text{-}3.6 \times 10^{-6}$
Thermal conductivity [W/mK]	15-50
Microhardness, Vickers, [GPa]	1.6-2.2
Young's modulus [GPa]	300-330
Flexural strength [MPa]	400-950
Fracture toughness [MN/m$^{3/2}$]	3.4-8.2

1.1.2 Potential materials for the conductive phase

To fabricate an electrically conductive ceramic composite the conductive particles have to be added into the matrix phase in order to achieve a suitable electrical conductivity required for the production of ceramic heaters. The most commonly used electoconductive materials in these composites are nitrides,[58,59] carbides[60], carbonitrides,[7,29] silicides[61,62] and borides[63] of the 3rd, 4th, 5th and 6th groups of transition metals having a high melting point. In the literature, WC and $MoSi_2$ can be found as the most generally used electroconductive secondary phases[64] in the production of heating elements. However, there are also reports of using $NbSi_2$, TiB_2, TiN, TiCN, TaN, TiC, ZrN, ZrB_2 and WSi_2.

1.1.2.1 Titanium nitride and zirconium nitride: properties and applications

Titanium nitride (TiN) and zirconium nitride (ZrN) exhibit a number of useful properties, including high hardness, high melting point, good chemical durability, high electrical conductivity, and good wear resistance. They are popular second-phase additives when sintered in nitrogen to improve the fracture toughness of Si_3N_4 due to their good compatibility with Si_3N_4.[65,66,67]

TiN and ZrN are extremely hard ceramic materials and are cements like refractory material. Their properties also make them attractive coating materials (Figure 5), often used as a hard coating for machine tools like drill bits and burs in order to improve the substrate's surface properties. Such coatings are deposited by using processes like physical vapour deposition (PVD). Due to their golden appearance they can also be used for decorative purposes.

It is well known that both materials exhibit a high electrical conductivity, i.e., $\sigma_{20°C}(TiN) = 4.6 \times 10^4\ \Omega^{-1}m^{-1}$ and $\sigma_{20°C}(ZrN) = 7.4 \times 10^4\ \Omega^{-1}m^{-1}$, that can be used to attain the percolation threshold in the preparation of electrically conductive ceramic composites. An addition of the proper amount of TiN or ZrN to the matrix, e.g., Si_3N_4, SiC, Y_2O_3, can also improve the Young's modulus, fracture toughness, hardness, strength, wear and oxidation resistance in the final composite.[64]

Figure 5: TiN coated punches.[64]

The physical properties of both materials are presented in Table 2. As can be seen, the characteristic properties of both materials are very similar. Furthermore, they have a cubic crystal structure of the NaCl-type with a broad range of stoichiometry. TiN_x compounds with x ranging from 0.6 to 1.2 are thermodynamically stable. However, both materials can readily oxidize even at 600 °C in a normal atmosphere and are chemically stable at room temperature.[68]

Table 2: Physical properties of TiN and ZrN[69,70,71]

Physical properties	TiN	ZrN
Density [g/cm^3]	5.44	7.09
Electrical resistivity [Ωm]	3.3×10^{-7}	1.8×10^{-7}
Microhardness [GPa]	20.5	16.7
Thermal expansion coefficient [1/K]	8.0×10^{-6}	7.2×10^{-6}
Young's modulus [GPa]	430-469	561

It is known that the oxidation resistance of the carbides and nitrides of refractory metals is lower than that of Si_3N_4.[72] Therefore, their addition can put limitations on the application of the composites at high temperatures. In addition, there is a marked increase in the oxidative attack with an increasing amount and grain size of TiN and ZrN. On the surface of the samples with 40 or 50 wt. % of these nitrides, the formation of a continuous oxide layer, which has low protective properties, can be found. The growth of such a scale should be related to the diffusion of titanium and zirconium to the surface of the composite and their oxidation according to the reactions 3[30] and 4[73].

$$2TiN + 2O_2 \leftrightarrow 2TiO_2 + N_2 \quad (3)$$

$$2ZrN + 2O_2 \leftrightarrow 2ZrO_2 + N_2 \quad (4)$$

With a decreasing amount of TiN or ZrN, only those groups of grains that exist near the surface can be oxidized because the TiN or ZrN grains are present as isolated inclusions in the Si_3N_4 matrix. Oxide islands protruding from the oxide layer were formed in these areas only. Above 1100-1200 °C the formation of a viscous silicate film on the surface of the composites, due to the oxidation of Si_3N_4 according to reaction 5[9] can protect them from further oxidation even at the relatively high TiN or ZrN contents.

$$Si_3N_4 + 3O_2 \rightarrow 3SiO_2 + 2N_2 \quad (5)$$

In this case the presence of small conductive particles is desirable, because coarse TiN or ZrN grains prevent the formation of a continuous silicate film on the surface and decrease its protective properties.[30]

1.2 Preparation and properties of the Si_3N_4/TiN composites

The Si_3N_4/TiN composites were investigated in order to obtain a combination of high fracture toughness, high hardness and low electrical resistivity. Composites with more than 30 vol. % of TiN have a high electrical conductivity, which is very useful for the final shaping using electrical discharge methods or other applications where the electrical conductivity is involved. The specific resistivity depends on the grain size of the TiN particles and changes drastically with a drop from high values (10^{13} Ωcm) to low ones (10^{-1}-10^{-3} Ωcm) between 25-35 vol. %. This drastic drop shifts with a decreasing particle size to lower volume contents of TiN. Martin et al.[12] reported that the Si_3N_4/TiN composites which contained 33 vol. % of TiN are suitable for machining by EDM. Their electrical resistivity should be less than 5×10^{-3} Ωcm. This criterion of electrical resistivity was also confirmed by Kamijo[74] and Bellosi[27]. Most of the Si_3N_4/TiN composite materials were produced by mixing TiN powders with Si_3N_4.[11,15,87,75] The additions of nanosized TiN particles to Si_3N_4 were also tested successfully.[76] However, the mechanical mixing of the powders introduces an inhomogeneity to the mixture and necessitates additional TiN to achieve a high electrical conductivity. The electrical conductivity of ceramic materials is strongly affected by the distribution of the electrically conductive second phase. Many studies have been initiated to increase the electrical conductivity of ceramic materials. A preferable alternative approach to achieve electrical conductivity is coating the Si_3N_4 matrix particles with chemical metal-organic precursors which promote the in-situ formations of conductive particles such as TiN.[32,77,78,79] On the other hand, the complexity of the chemical methods and the application of additional heat treatment processes make the possible commercial use of these techniques difficult. Furthermore, the occurrence of gaseous reaction products and the grain growth of nano-sized particles at the sintering temperature of the Si_3N_4/SiAlON matrix material affects the densification and electrical conductivity, even when different sintering methods were employed.[80,81]

The preparation of TiN-coated Si_3N_4 particles has been studied by Kawano et al.[78] These authors prepared Si_3N_4/TiN composites by spark-plasma sintering (SPS) of Si_3N_4 particles coated with 20 nm TiN nanoparticles at 1600 °C in N_2. α-Si_3N_4 particles were coated with various amounts of nano-sized TiN by coating the surface of the Si_3N_4 particles with TiO_2, followed by a nitridation. With zeta-potential measurements they showed that the TiO_2 coating on the surface of the Si_3N_4 particles occurs at a pH between 3.7 and 4.3 having an attractive force of opposite charges.

When the TiO_2 on the surface of the Si_3N_4 is nitrided with NH_3 gas at 1000 °C for 180 min, it is completely converted to TiN with a uniform particle size. During the nitridation of TiO_2 to form TiN, the following reaction[82,83] takes place:

$$6TiO_2 + 8NH_3 \rightarrow 6TiN + 12H_2O\uparrow + N_2\uparrow \qquad (\Delta G = -48\ \text{kJ/mol},\ 1000\ °C) \qquad (6)$$

The relationship between the particle size and the nitridation temperature with the same holding time of 5 h was investigated by Li et al.[83] These authors showed that when the nitridation temperature is higher, the particle size of TiN is larger. The TiN powders, with average particle sizes ranging from 20 to 72 nm, were observed at different nitridation temperatures from 800 to 1100 °C, respectively.

The TEM images of TiO_2- and TiN-coated Si_3N_4 powders are displayed in Figure 6.[83] Kawano et al.[78] demonstrated that the TiO_2 and TiN nanoparticles with a particle size of 10 nm and 20 nm uniformly coated the surface of the Si_3N_4 powder. As prepared, the TiN-coated Si_3N_4 powders were sintered at 1600 °C in N_2 under a uniaxial pressure of 39 MPa using a controlled electric current.

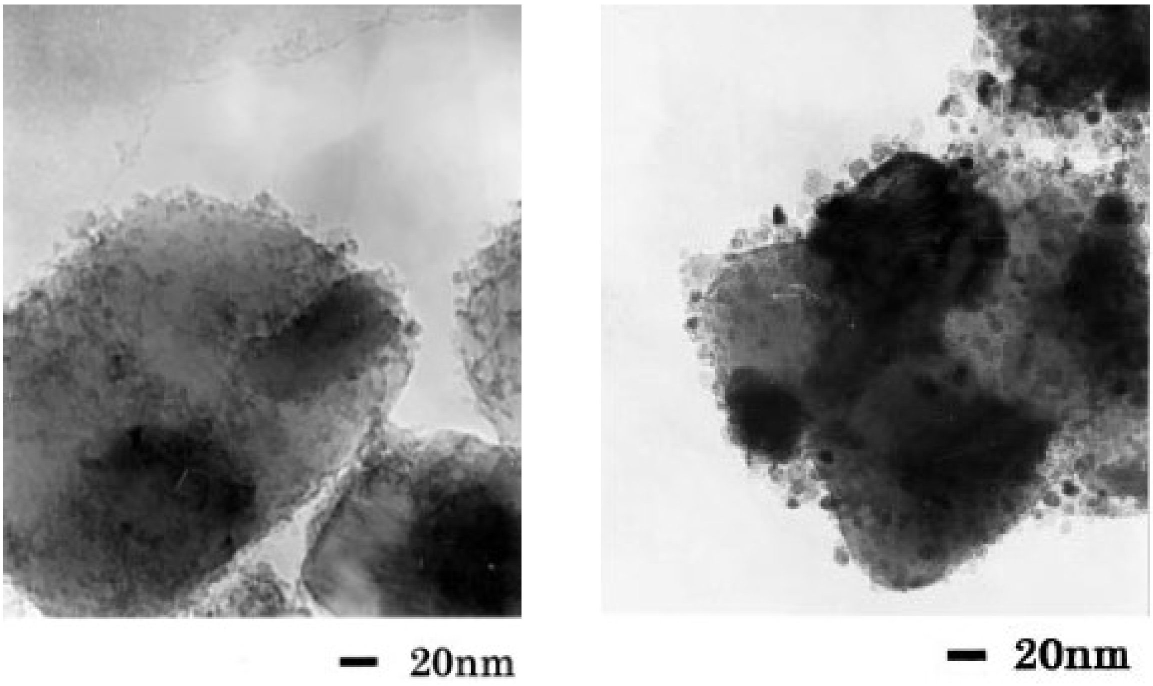

a) b)

Figure 6: TEM image of a) TiO_2-coated Si_3N_4 and b) TiN-coated Si_3N_4 particles.[83]

For comparison, these authors also sintered mechanically mixed powders containing Si_3N_4 and 25 vol. % of TiN at the same sintering conditions.[78] The mixtures in the latter sintering experiment were prepared with two methods. One method involved ball milling of commercial TiN and Si_3N_4 and drying at 60 °C for a one day. The second one was to ball mill nano-sized TiO_2 (prepared with a thermal hydrolysis of $TiCl_4$ and urea[79]), together with Si_3N_4, followed by drying at 60 °C for one day and a nitridation at 1000 °C. Figure 7[78] shows backscattered SEM images of the polished composites' surfaces containing 25 vol. % of TiN prepared from TiN-coated Si_3N_4 particles, a mechanical mixture of commercial TiN and Si_3N_4, and a mechanical mixture of nano-sized TiN and Si_3N_4, all sintered at 1600 °C. The difference in the backscattering properties of the lighter and heavier atoms shows up as the gray and white regions corresponding to Si_3N_4 and TiN, respectively. The composites prepared from TiN-coated Si_3N_4 (Figure 7 a) show aggregated gray Si_3N_4 regions surrounded by successive white TiN layers, even though some aggregated TiN particles are formed. The ceramics derived from the mechanical mixture of the commercial TiN and Si_3N_4 are porous and have about 1–7-μm-sized TiN grains (white particles) (Figure 7 b), which exist separately from the Si_3N_4 grains.

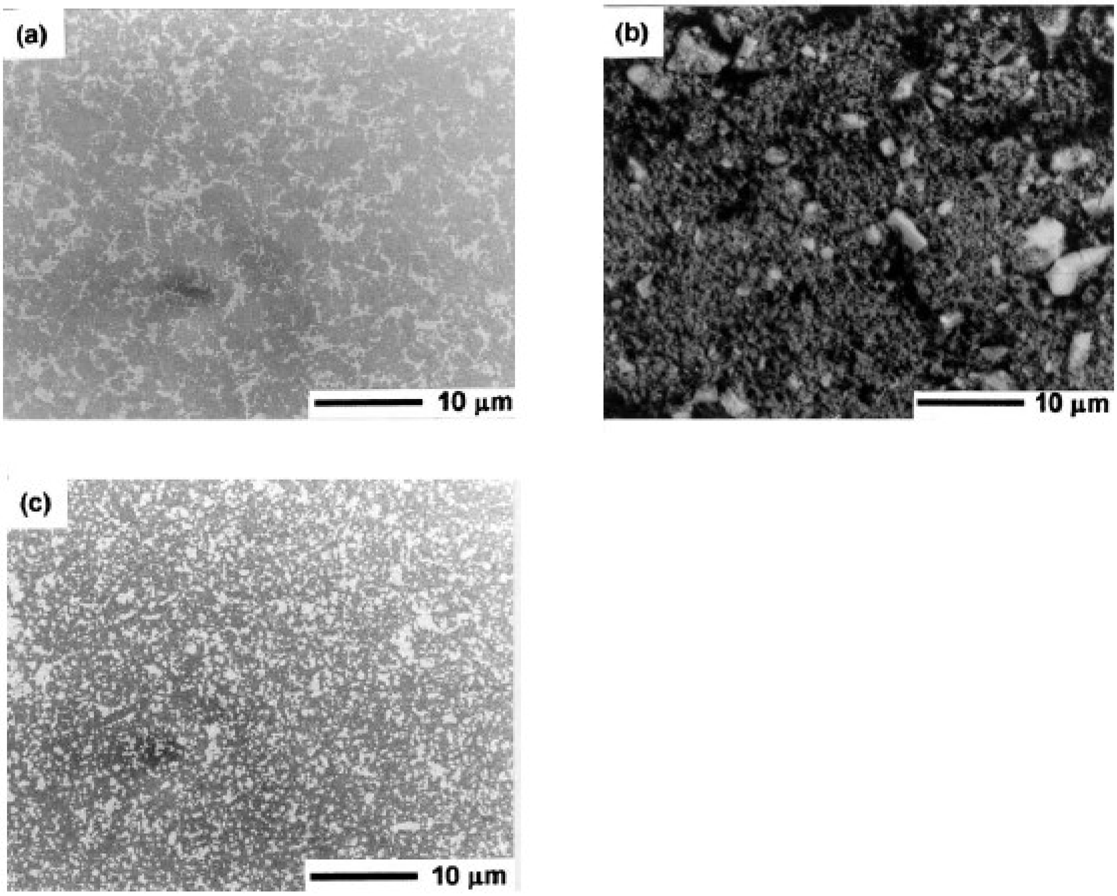

Figure 7: Backscattered SEM images of polished Si_3N_4/TiN ceramics containing 25 vol. % of TiN prepared from (a) TiN-coated Si_3N_4 particles, (b) a mechanical mixture of commercial TiN and Si_3N_4 and (c) a mechanical mixture of nano-sized TiN and Si_3N_4.[78]

The above authors showed that these ceramics did not sinter. In contrast to the TiN-coated Si_3N_4-derived materials, the surface of the mechanical mixture of the nano-sized TiN and Si_3N_4 (Figure 7 c) shows isolated TiN particles of around 1–2 µm in size and Si_3N_4 particles. On the basis of these results, they concluded that the mechanical mixtures of TiN and Si_3N_4 do not form continuous TiN networks, which are necessary to make the composite electrically conductive. In Figure 8 a[78] it can be seen that the relative densities of the Si_3N_4/TiN composites prepared from TiN-coated Si_3N_4 powders measured as a function of the TiN content increase sharply from 64 % (17.5 vol. % TiN) to 91 % (25 vol. %), respectively, followed by a gradual increase to 97 % for single-phase TiN. On the other hand, composites containing 25 vol. % of TiN derived from the a mechanical mixture of commercial TiN and Si_3N_4 and the mechanical mixture of nano-sized TiN and Si_3N_4 in which the TiN particle sizes from the starting powder mixture were 1.43 µm and 20 nm exhibited relative densities of 50 and 98 %, respectively.

Kawano et al. also measured the change in the electrical resistivity of the composites prepared from the TiN-coated Si_3N_4 powders which is shown as a function of the TiN content in Figure 8 b.[78] These authors showed that resistivity rapidly decreases from 2 x 10^6 Ωcm in the 10 vol. % TiN sample to 10^{-4} Ωcm in the 25 and 32.5 vol. % of the TiN samples. This rapid decrease was explained by the formation of a TiN network around the Si_3N_4 grains, as shown in Figure 7 a. They demonstrated that the content of the TiN required to fabricate the Si_3N_4/TiN composites by EDM was a maximum of 23 vol. %, which is lower than the previously reported value (33 vol. %).[12]

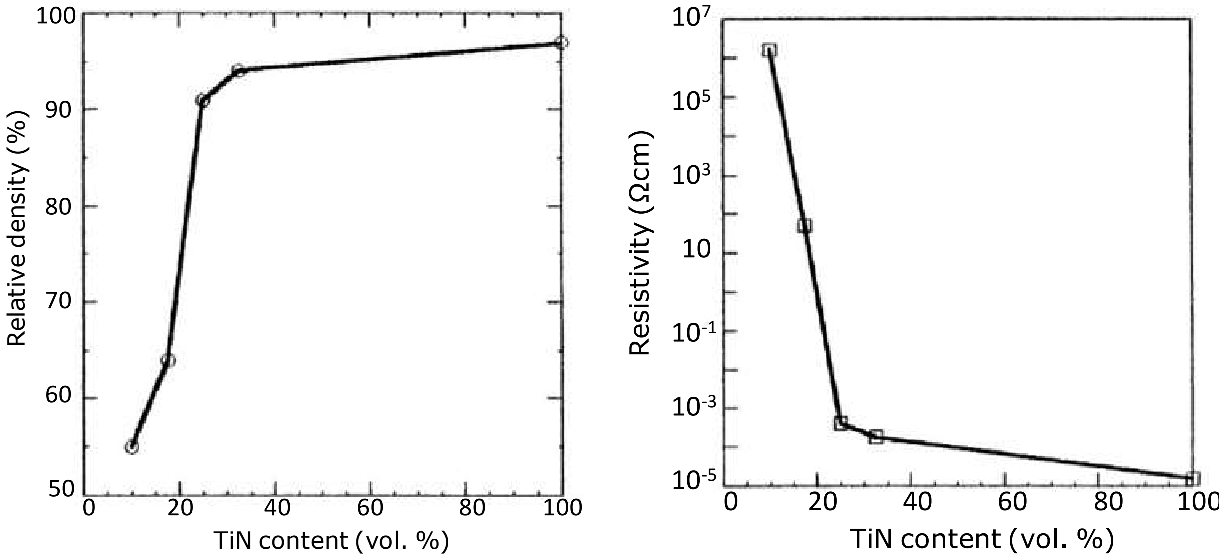

a) b)

Figure 8: Relationship dependence of a) relative density and b) electrical resistivity with TiN content of Si_3N_4/TiN composites prepared from TiN-coated Si_3N_4 particles.[78]

The electrical resistivity of the composite prepared from a mechanical mixture of nano-sized TiN and Si_3N_4 containing 25 vol. % of TiN was 1 Ωcm, higher, by a factor of 10^4, than the composites prepared from TiN-coated Si_3N_4 particles. The reason for the different electrical-resistivity values was found to be the fact that the continuous TiN networks do not exist in a mechanical mixture of nano-sized TiN and Si_3N_4 composite (Figure 7 c). Kawano's study showed that with the TiN coating on the Si_3N_4 particles it is possible to reduce the content of TiN needed to provide a low enough electrical resistivity for the EDM processing of the Si_3N_4 composites compared to the conventional composite method.

Recently, an effective approach to preparing electrically conductive SiAlON/TiN composites has been developed by Ayas et al.[33] These authors prepared granules of a designed composition of α-β SiAlON by spray-drying under suitable conditions in order to obtain spherical granules of around 100 μm in diameter and coated with varying amounts of the TiO_2 powder using electrostatic attraction. For the coating process, both SiAlON granules and TiO_2 powder (0-10 vol. %) were homogenized by mechanical mixing without using any liquid and grinding media. As-prepared powders were sintered by the SPS under a pressure of 50 MPa at 1650 °C for 5 min.

They demonstrated that during sintering, several possible chemical reactions could occur between TiO_2-AlN and TiO_2-Si_3N_4 leading to the formation of TiN. In order to avoid the grain growth of the matrix and the in-situ formed TiN grains they selected 1650 °C as the maximum sintering temperature of the TiO_2-incorporated composites. The microstructures of the SiAlON/TiN composites are given in Figure 9.[33] In both cases a segregated network of the TiN particles was formed successfully. Ayas et al. showed that with an increasing amount of TiO_2 (above 5 vol. %) large clusters of TiN phases formed along the grain boundary, indicating that the agglomeration of the TiO_2 particles starts during the mixing process above this value.

The electrical resistivity of the sintered SiAlON/TiN composites, as a function of the amount of TiO_2, is shown in Figure 10.[33] With electrical-resistivity measurements the above authors confirmed that even 2.5 vol. % of the TiO_2 addition causes a substantial decrease in the resistivity, by nearly ten orders of magnitude, to a value of 9 x 10^1 Ωm.

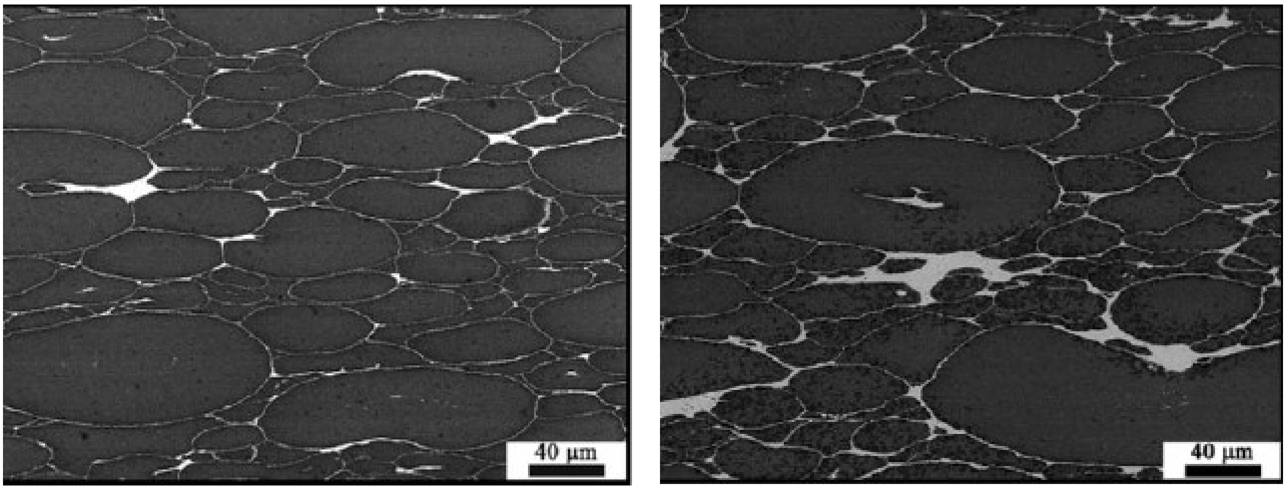

a) b)

Figure 9: Back-scattered images of the investigated composites containing: a) 7.5 vol. % of TiO_2 and b) 10 vol. % of TiO_2 after sintering at 1650 °C.[33]

Further increasing the amount of TiO_2 to 5 vol. % results in lower values of the electrical resistivity, down to 2.1 x 10^{-4} Ωm. However, these authors concluded that increasing the TiO_2 amount over 5 vol. % does not bring any further decrease. The reason is that with over 5 vol. % of TiO_2, the conductivity is established due to the physical contact of the in-situ formed TiN particles.

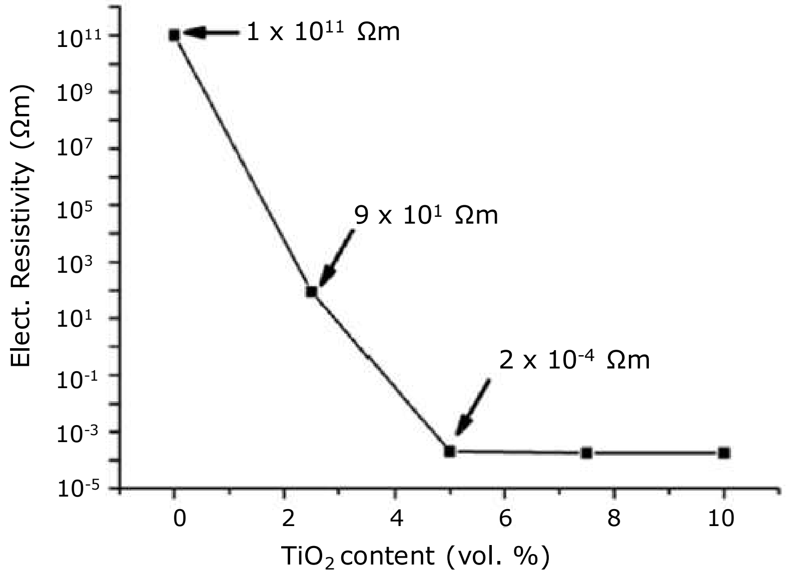

Figure 10: Electrical resistivity of the composites as a function of TiO_2 content.[33]

Another interesting study was made by Ahmad et al.[91], where the electrically conductive Si_3N_4/TiN composites were fabricated via the high-energy planetary ball milling of 70 wt. % of Si_3N_4 (with Y_2O_3 and Al_2O_3 additives) and 30 wt. % of Ti powders, followed by the SPS at 1250-1350 °C. The mean particle sizes of the Si_3N_4 and Ti powders were 60 nm and 45 μm. The SPS process was carried out in vacuum (10 Pa) by heating to the sintering temperature with a holding time of 10 min and an applied pressure of 40 MPa. They showed that the in-situ synthesis process, which used the Si_3N_4 and Ti powders, enables the production of composites with the following benefits: low cost, reduced process step, a desirable microstructure, fine-scale reinforcement and enhanced sinterability.

Ahmad et al.[91] proposed that during the sintering several reactions can occur. The first reaction is the oxidation of Ti, where TiO_2 is formed. The oxidation is promoted by the SPS due to the presence of residual oxygen in the compact. TiO_2 formed on the surface of the Ti powder reacts with Si_3N_4 to form TiN according to reaction 9 (presented on page 20).[33] On the other hand, residual Ti reacts with Si_3N_4 to form TiN by this reaction[91]:

$$1/4Si_3N_4 + Ti \rightarrow TiN + 3/4Si \qquad (\Delta G = -140\ kJ/mol;\ 1250\ °C) \qquad (7)$$

Following reaction 7, the reaction of Si_3N_4 becomes dominant, leading to the formation of Si_2N_2O at higher temperatures, according to reaction 8.

$$Si_3N_4 + SiO_2 + Ti + 1/2N_2 \rightarrow TiN + Si_2N_2O \quad (\Delta G = -220\ kJ/mol;\ 1250\ °C) \qquad (8)$$

Reaction 8 involves the dissolution of Si_3N_4 into the SiO_2 melt, which provides an easy transport medium for the reaction. According to the thermodynamic calculations for all the mentioned reactions Ahmad et al. showed that these reactions are exothermic, indicating that they take place at 1250 °C in N_2.

Figure 11 a[91] shows a back-scattered electron (BSE) image of a sintered Si_3N_4/TiN composite prepared by SPS at 1250 °C. The sintered sample exhibited a microstructure with long shaps of TiN (white area) in a Si_3N_4 (black area) matrix. The electrical resistivity of the sintered compacts prepared by SPS at different temperatures is shown in Figure 11 b.[91] The electrical resistivity significantly decreased from 1.24 to 6.3 x 10^{-3} Ωcm as the sintering temperature increased from 1200 to 1250 °C. When the sintering temperature exceeded 1250 °C, it increased with the increasing sintering temperature.

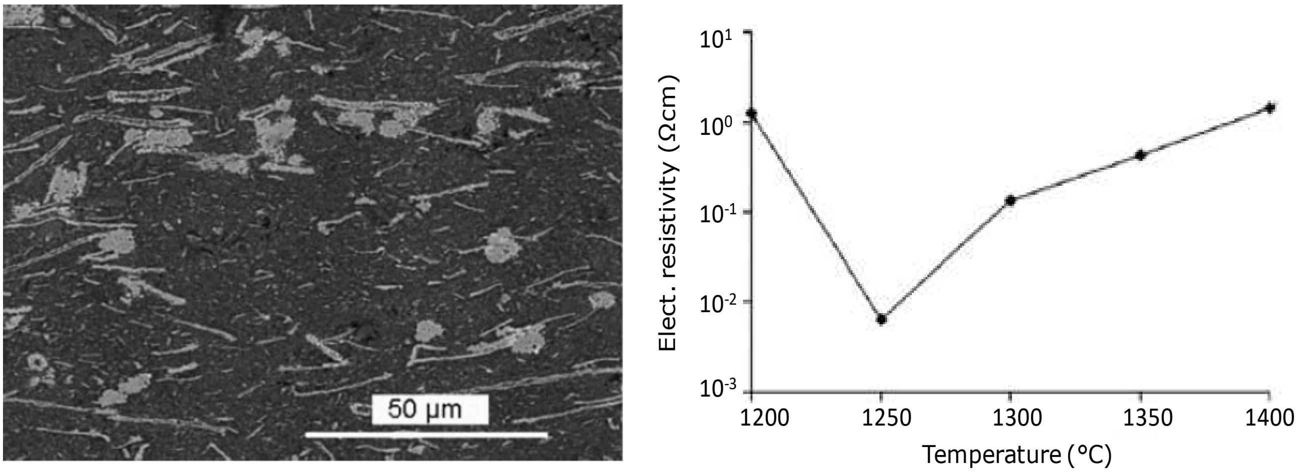

a) b)

Figure 11: a) BSE image of a sintered sample prepared by the SPS at 1250 °C and b) electrical resistivity of a sintered composite as a function of sintering temperature.[91]

These authors demonstrated that a sintered composite prepared by SPS at 1250 °C has a small quantity of pores and a large amount of TiN, resulting in a low electrical resistivity. The increases in the electrical resistivity in the temperature range of 1250-1400 °C are explained by the increases in the amount of Si_2N_2O.

They concluded that such composites sintered at 1250-1350 °C could be easily machined by EDM, exhibiting a high hardness (17.8 GPa) and a good machinability.

1.2.1 Si_3N_4-TiO_2 reaction system

Si_3N_4 is a chemical compatible with TiO_2 when it is sintered or heat-treated in an inert atmosphere (Ar, N_2).[84,85,86] Possible reactions with calculated Gibbs free energy at 1100 °C between the Si_3N_4-TiO_2 system leading to the formation of TiN are given in reactions 9[33,87], 10[33,88] and 11[89].

$$6TiO_2 + 2Si_3N_4 \leftrightarrow 6TiN + 6SiO_2 + N_2\uparrow \qquad (\Delta G = -\ 240\ \text{kJ/mol, } 1100\ ^\circ\text{C}) \qquad (9)$$

$$6TiO_2 + 4Si_3N_4 \leftrightarrow 6TiN + 12SiO\uparrow + 5N_2\uparrow \qquad (\Delta G = +\ 50\ \text{kJ/mol, } 1100\ ^\circ\text{C}) \qquad (10)$$

$$3TiO_2 + 4Si_3N_4 \leftrightarrow 3TiN + 6Si_2N_2O + 1/2N_2\uparrow \qquad (\Delta G = -\ 120\ \text{kJ/mol, } 1100\ ^\circ\text{C}) \qquad (11)$$

All the above reactions could occur during sintering and/or heat treatment at elevated temperatures, where TiO_2 reacts with Si_3N_4 to form TiN and secondary-based products, such as SiO, SiO_2, Si_2N_2O and N_2. The SiO_2 and Si_2N_2O products might have an effect on both the densification and the phase formation in terms of sintering temperature. Reactions 9 and 11 occurred at temperatures as low as 1100 °C, where the Gibbs free energy is negative. Thus, reaction 9 is thermodynamically the most favourable at elevated temperatures, while the reaction 10 only becomes feasible above 1680 °C. In addition, reaction 10 is sensitive to the partial pressure of SiO. Therefore, it would proceed until the partial pressure of SiO will reach that of the equilibrium.

The reaction between TiO_2 and Si_3N_4 leading to the formation of TiN became especially interesting since the Si_3N_4-TiN composite with a very fine distribution of TiN in the Si_3N_4 matrix can be fabricated by sintering the TiO_2 and Si_3N_4 powder mixtures. Thus, in the past two decades sintering by using a chemical reaction has introduced a novel route for the preparation of Si_3N_4-TiN composites. A higher starting amount of TiO_2 results in Si_2N_2O formation according to reaction 11.[90] The reason is that TiO_2, added as a sinter additive to Si_3N_4, is completely converted to TiN. This reaction consumes α-Si_3N_4 and results in the formation of SiO_2. In the presence of Y_2O_3, the formed SiO_2 reacts with the residual Si_3N_4 to form Si_2N_2O. Ahmad[91] has recently confirmed that the decrease in the density and hardness in a Si_3N_4/TiN composite at a higher sintering temperature can be attributed to the formation of Si_2N_2O, since it has a lower density and hardness compared to Si_3N_4. Furthermore, SiO_2 present on the Si_3N_4 powder surface may additionaly react with the Si_3N_4 particles to form Si_2N_2O, as displayed in reaction 12[89], but in that case the reaction is less energetically feasible than reaction 11.

$$SiO_2 + Si_3N_4 \leftrightarrow 2Si_2N_2O \qquad (\Delta G = -80\ \mathrm{kJ/mol},\ 1100\ °C) \qquad (12)$$

The densification of the TiN-containing composites begins at temperatures lower than those of the densification of the pure Si_3N_4 matrix. The reason is that the solution of TiO_2, which adheres to the surface of the TiN powder particles, reduces the viscosity of the liquid phase. At temperatures above 1350 °C TiN precipitates from the liquid phase in relation to reaction 9.[87,92]

However, according to the published data[93], up to 7 wt. % of Si_3N_4 can be dissolved in TiN at 1650 °C and up to 30 at. % Ti can be dissolved in Si_3N_4 at 1725 °C. The formation of the solid solution of Si_3N_4 in TiN under equilibrium conditions in real systems seems to be hindered by the presence of intergranular silicate phases.

In the literature, only a few reports[94,95] on the formation of TiN followed by the reaction between TiO_2, Si_3N_4 and the addition of AlN can be found (reaction 13). According to these papers, TiO_2 reacts with AlN and Si_3N_4 during sintering to form SiAlON, TiN and O_2, which goes into the atmosphere. The reaction is energetically feasible above 1100 °C, where the Gibbs free energy is - 270 kJ/mol.[95]

$$2TiO_2 + 3AlN + 5Si_3N_4 \leftrightarrow 3Si_5AlON_7 + 2TiN + 1/2O_2\uparrow$$
$$(\Delta G = -270\ \mathrm{kJ/mol},\ 1100\ °C) \qquad (13)$$

$$2TiO_2 + 2AlN \leftrightarrow 2TiN + Al_2O_3 + 1/2O_2\uparrow \qquad (\Delta G = -140\ \mathrm{kJ/mol},\ 1100\ °C) \qquad (14)$$

Studies by Ueno[96] and Zheng[97] showed that TiO_2 could also react with AlN to form TiN and Al_2O_3 according to reaction 14. They confirmed that the reaction occurred in the temperature range from 1100 to 1450 °C, prior to the sintering of the Si_3N_4 matrix. AlN was intended to act as a nitrogen supplier and an oxygen acceptor. Al_2O_3 was one of the reaction products, and became one of the sintering agents. Furthermore, as demonstrated by Yano et al.,[98] the reaction can proceed if the oxygen partial pressure is lower than the equilibrium. They showed that the presence of small amounts of TiO_2 improves the transformation from α to β-Si_3N_4. Al_2O_3 and

Y_2O_3, which are generally added as a sintering additive, usually lower the viscosity of the liquid phase and thereby lower the reaction temperature and enhance the transformation kinetics.

1.3 Preparation and properties of composites based on the Si-Zr-O-N system

According to the available scientific reports, much less work has been done on the Si-Zr-O-N system than on the Si-Ti-O-N system. In the past two decades much attention has been devoted to the engineering of particulate ceramic composites based on Si_3N_4 with incorporated ZrO_2 particles, especially because of their improved fracture toughness and strength as well as their oxidation and corrosion resistance. It has been demonstrated that ZrO_2 has the potential to be a toughening and strengthening agent in the Si_3N_4-based ceramic materials.[125,99,100,101] An addition of small amounts (≤ 3 wt. %) of the Zr-compounds (ZrO_2, ZrN, ZrC or $ZrSiO_4$) can promote the densification of Si_3N_4 during hot pressing, leading to the formation of more refractory grain-boundary phases in the nitride.[37,102,103,104,105] Further investigations in the Si-Zr-O-N system were carried out by Terao et al.[99], who found that a dispersion of up to 30 vol. % of 2.5 mol. % yttria-stabilized-zirconia in Si_3N_4 was advantageous for increasing the room-temperature toughness without any degradation of the hardness, due to the stress-induced transformation of the ZrO_2 from the tetragonal to the monoclinic phase.

Figure 12[99] illustrates the room-temperature fracture toughness (K_{IC}) as a function of the composition for Si_3N_4-ZrO_2 composites fabricated by HIP. Fine Si_3N_4 powder and three types of ZrO_2 powders – pure monoclinic ZrO_2 ($mZrO_2$), tetragonal ZrO_2 containing 2.5 mol. % of Y_2O_3 ($2.5YZrO_2$) and cubic, 12 mol. % of Y_2O_3 ($12YZrO_2$) – were used as the starting materials. Sintering was conducted as a densification of Si_3N_4 without additives at 1900 °C for 1 h using 10 bar of Ar. The results[99] showed that the increases in K_{IC} were small, both in the Si_3N_4-$mZrO_2$ and Si_3N_4-$12YZrO_2$ series, but in the Si_3N_4-$2.5YZrO_2$ series, the K_{IC} value reached a maximum of 7.5 $MPam^{1/2}$ for an addition of 20 wt. % of $2.5YZrO_2$. This value is 2.5 times higher than that for Si_3N_4 without additives (3.1 $MPam^{1/2}$). The enhanced values of K_{IC} were thus attributed to the martensitic tetragonal-monoclinic (t-m) transformation of ZrO_2 in the vicinity of the stress field of a propagating crack. The contribution to the K_{IC} arising from this phenomenon is expected to decay as this temperature is increased to a value of T_{ms}, the t-m martensitic start temperature (800 °C). At this temperature the driving force for the transformation no longer exists and the tetragonal ZrO_2 becomes the thermodynamically stable polymorph. The K_{IC}

measured at 800 °C was consistently lower for each composition, indicating that stress-induced transformation toughening was the dominant toughening mechanism operating in these composites.

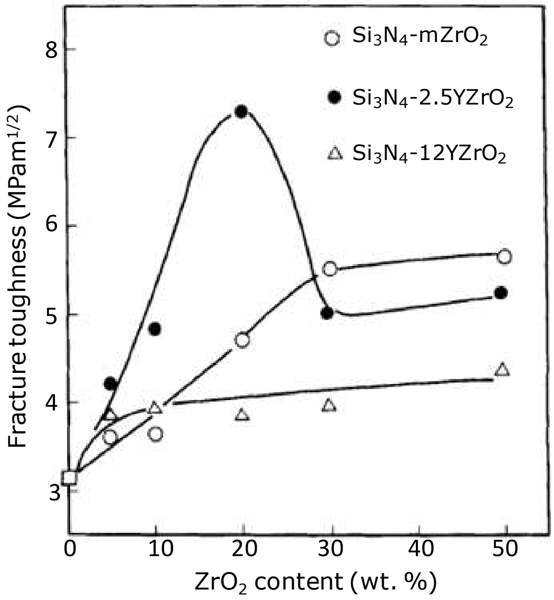

Figure 12: Room-temperature fracture toughness of Si_3N_4-ZrO_2 composites.[99]

Furthermore, stabilizing the ZrO_2 powder with suitable oxides, such as Y_2O_3, CaO or MgO, will further promote an increase in the strength and fracture toughness in a Si_3N_4/ZrO_2 composite.[129,106]

The chemical compatibility of the ZrO_2 and β-Si_3N_4 compound has been investigated in more detail[107,108,109] and the reaction between ZrO_2 and Si_3N_4 has been demonstrated to take place at temperatures above 1600 °C under reducing conditions, where ZrN or ZrON could be formed.[124]

Studies by Lange[107] of the Si_3N_4/ZrO_2 system, with and without Al_2O_3 additions, showed that the ZrO_2-containing phase, which appeared cubic in an x-ray diffraction analysis, is actually the Zr-oxynitride solid solution that is distinguished from the cubic ZrO_2 by detecting additional, very weak, reflections. Lange also indicated that the Zr-oxynitride phase in a composite readily oxidizes at low temperatures (500 °C) to produce a monoclinic ZrO_2. When the ZrO_2 in the starting powder exceeds 10 vol. %, the surface compressive stresses produced by the oxidation of ZrON cause a structural modification of the composite, observed either as a surface spalling or as a complete disintegration. This phenomenon was not observed above 1000 °C because the surface stresses are relieved through a deformation in a manner similar to that observed for the other Si_3N_4 ceramics containing secondary phases that readily oxidize and produce a large molar volume increase.[110] However, many studies were performed in which the formation of ZrN or ZrON was undesirable. The reason is that ZrO_2 in the composite was aimed at improving the fracture toughness. The formation of ZrN or ZrON can be suppressed if the following conditions are considered: the processing temperature should be kept below the outset of the reaction between ZrO_2 and Si_3N_4[88], a rapid densification of the composite is required[111], the atmosphere must be carefully controlled[112] and/or the ZrO_2 should be stabilized with an oxide additive such as Y_2O_3[113]. Falk et al.[114] showed that the use of Y_2O_3, as a stabilizing agent, reduces the nitrogen uptake of the ZrO_2 during the densification. It was proposed that if ZrO_2 is stabilized with larger Y_2O_3 concentrations (above 4.1 mol. %), it would be possible to avoid the formation of ZrON and/or ZrN in the microstructure of the final composite material. In addition, at higher sintering temperatures a significant amount of ZrO_2 might dissolve inside the liquid phase. This was shown by Cheng and Thompson, who studied the Y_2O_3-Al_2O_3-SiO_2 liquids containing additions of ZrO_2.[115] These authors observed that the solubility of ZrO_2 is around 10 wt. % at 1700 °C, but that dissolved ZrO_2 precipitates, during the cooling, from the liquid. This is in agreement with the work carried out on composite ceramics formed in the Si_3N_4-ZrO_2(+Y_2O_3) system with additions of Al_2O_3, which indicated that the ZrO_2 underwent a solution-precipitation process during the densification. Even when Al_2O_3 is absent, ZrO_2 probably has a high solubility at high temperatures, as shown by Falk et al.[113] These authors noted that ZrO_2 grains often had irregular shapes, which strongly implies that the ZrO_2 grains grew from the liquid during the cooling. The microstructures of the hot-pressed SiAlON-30 vol. % ZrO_2 composites with the ZrO_2 partially stabilized with either Y_2O_3 or CeO_2 are shown in Figure 13.[125] It can be seen that the SiAlON grains surrounding the ZrO_2 grains often appear prismatic and faceted, whereas the white ZrO_2 grains often have a rounded, irregular morphology. This suggests that some ZrO_2 precipitated during the formation of the liquid phase and thus partially acted as a sintering aid.

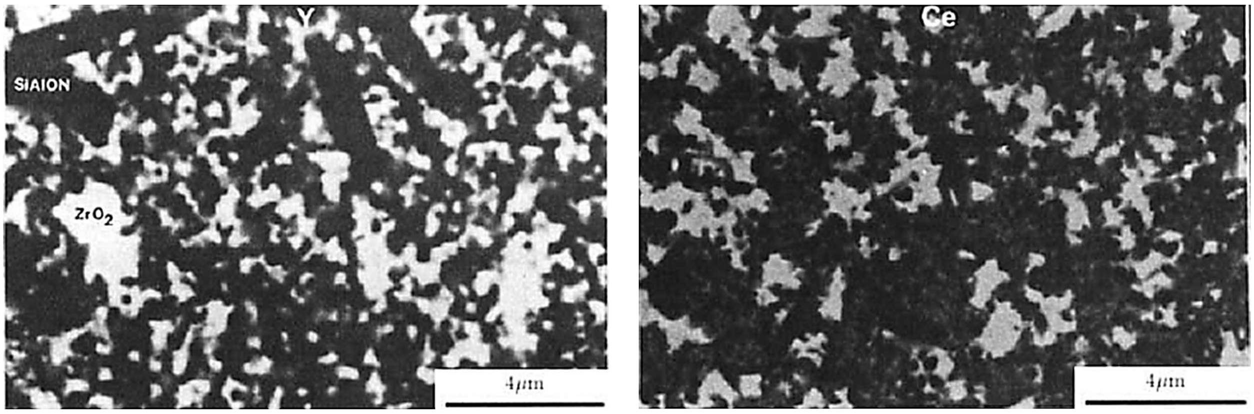

a) b)

Figure 13: SEM micrograph of SiAlON-30 vol. % ZrO_2 composite hot pressed at 1700 °C starting from: a) 3Y-ZrO_2 (stabilized with 3 mol. % of Y_2O_3) and b) 13Ce-ZrO_2 (stabilized with 12 mol. % of CeO_2).[125]

For the preparation of the Si_3N_4-ZrN composites a few reports can be found in the literature. These composites were fabricated by using a conventional composite method from mechanically mixed powders. Moreover, until now there exists no literature report about the preparation of Si_3N_4-ZrN composites from Si_3N_4 powder coated with ZrN nanoparticles.

The Si_3N_4-ZrN composites could be fabricated from a Si_3N_4 and ZrO_2 powder mixture containing oxide sintering additives, where the reaction between ZrO_2 and Si_3N_4 leading to the formation of ZrN has to occur. The formation of ZrN is also made possible by the reduction-nitridation of ZrO_2.[116] Fu et al. showed that the nanocrystalline ZrN powder can be synthesized by the reduction-nitridation of the nanosized ZrO_2 powder in NH_3 gas with magnesium (Mg) as a reducing agent. Indeed, in the preparation of ZrN, it has been reported that at very high temperature (>2000 °C) the oxidation stage of the zirconium is reduced from IV to III under the NH_3 flow (reaction 15):[117]

$$ZrO_2 + 4/3NH_3 \rightarrow ZrN + 2H_2O\uparrow + 1/6N_2\uparrow \qquad (\Delta G < 0, > 2000\ °C) \qquad (15)$$

Fu et al.[116] confirmed that reaction 15 could be possible even at temperatures above 900 °C if elemental Mg is used as a reductant. An instantaneous reaction between ZrO_2 and Mg will release a mass reaction heat, which allows the nitridation process to be finished at a lower heating temperature and in a shorter time. In this way, the high-purity ZrN powder with a 30-100 nm particle size can be obtained at 1000 °C for 6 h, under a $Mg:ZrO_2$ mole ratio of 10:1. Figure 14[116] shows a TEM micrograph of the powder that was synthesized at 1000 °C for 6 h. These authors concluded that the absolute majority of the ZrN particles in the sample are 30-50 nm in size, and only very few particles show a large size of 100 nm, indicating that the increase in the synthesizing temperature has led to a significant growth of the ZrN particles.

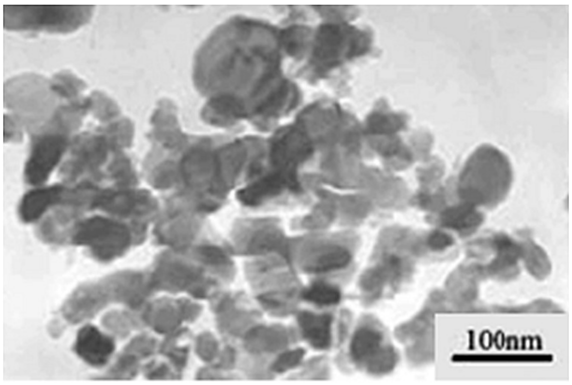

Figure 14: TEM micrograph of the ZrN nanopowder nitrided at 1000 °C for 6 h.[116]

One of the crucial studies about the preparation of Si_3N_4/ZrN composites was made by Ade et al.[59] These authors produced a dense, low-to-zero shrinkage electroconductive Si_3N_4/ZrN composite with the reaction of a transition-metal silicide ($ZrSi_2$), containing Y_2O_3 and Al_2O_3 as sintering aids, with N_2 gas in the temperature range 700-1500 °C. The chemical reaction which occurs during the sintering between $ZrSi_2$ and N_2 is described below.[59]

$$6ZrSi_2 + 11N_2 \rightarrow 6ZrN + 4Si_3N_4 \qquad (\Delta G < 0, > 700\ °C) \qquad (16)$$

After the transformation to ZrN (reaction 16), the densification of the reaction-bonded composite was achieved (95 % TD) in a subsequent sintering step at 1750 °C for 2 h in flowing N_2. Ade et al.[59] showed that since the chemical reaction (reaction 16) is accompanied by volume expansions, the linear shrinkage of the sintered body, in relation to the die-pressed powder compact, is very low. The electrical conductivity of the obtained Si_3N_4/ZrN composite differs a great deal due to the volume amounts of the conductive phase and microstructure. The microstructure of the reaction-bonded Si_3N_4/ZrN composite, post sintered at 1750 °C for 2 h in N_2, is shown in Figure 15.[59] ZrN is presented as light grey, whereas the Si_3N_4 grains appear as dark grey. The electrical resistivity of the composite made from pure $ZrSi_2$ was 10^2 Ωcm. Ade's study[59] indicated that the reaction-bonding process should allow the low-to-zero shrinkage manufacturing of electroconductive ceramic microcomponents in the near future.

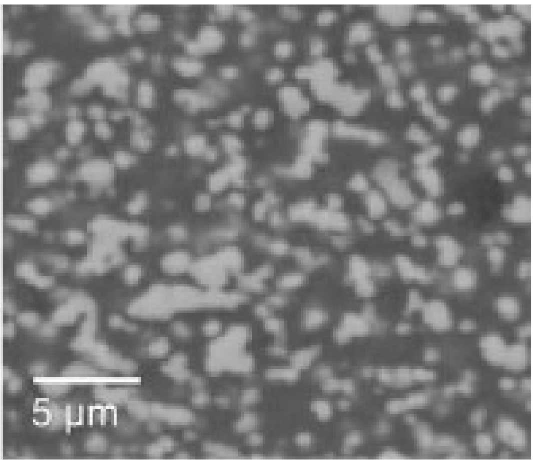

Figure 15: BSE image of the microstructure of the reaction-bonded Si_3N_4/ZrN composite, post sintered at 1750 °C for 2 h in N_2.[59]

Ekström et al.[118] fabricated Nd_2O_3-doped SiAlONs with ZrN additions (2-20 wt. %) formed by sintering at 1775 °C for 2 h in 1 atm of N_2. These authors found that the addition of ZrN strongly inhibited the formation of the α-SiAlON phase, and this effect was especially pronounced when small amounts of Nd_2O_3 were added. The addition of ZrN up to 20 wt. % in the SiAlON matrix caused a drastic decrease in the hardness and an increase in the toughness. Thus, at 10 wt. % of added ZrN the hardness was only 1000-1100 MN/m^2, partly due to the high porosity (around 5 vol. %) of the composites, but, at the same time, K_{IC} increased to around 5.5 $MPam^{1/2}$. Moreover, studies by Chockalingam et al.[119] indicated that the β-SiAlON/ZrN composites could be prepared from a mixture of SiAlON and various contents of the 3 mol. % Y_2O_3-stabilized ZrO_2 powders by using microwave sintering. In this case the microwave sintering was performed at 1700 °C for 15 min under flowing N_2 by using 2.45-GHz microwaves. Neither the α-Si_3N_4 nor ZrO_2 powder absorbed 2.45-GHz microwaves at room temperature due to their low dielectric losses; however, the Y_2O_3-stabilized ZrO_2 starts to couple with microwaves in the temperature range from 250 to 400 °C.[120] These authors showed that when the temperature increases the dielectric loss of ZrO_2 increases rapidly and it starts to absorb microwave energy and generate heat within the material more efficiently. Chockalingam et al. confirmed that during sintering above 1600 °C in N_2 the reactions between ZrO_2 and Si_3N_4 or AlN take place, leading to the formation of ZrN. An XRD analysis revealed that the complete conversion of ZrO_2 to ZrN in the case of the microwave-sintered samples, starting from 5 to 25 wt. % of ZrO_2 from the starting composition could be due to the continuous dissolution of N_2 through the open pores available at the surface of the sample. There is also the possibility of the development of high temperatures within the ZrO_2 grains due to the high dielectric loss of ZrO_2 compared to Si_3N_4 above 800 °C where N_2 diffusion is high enough for the complete conversion of ZrO_2 to ZrN.[119] These authors also showed that the microwave-sintered composites exhibited a higher density compared to conventionally sintered samples at 1800 °C for 1 h in N_2. The improved densification behaviour is attributed to volumetric fast heating. The aspect ratios of the β-SiAlON grains were found to be higher in the microwave-sintered samples. The presence of the tetragonal ZrO_2 was indentified in the case of conventionally sintered composites, whereas ZrO_2 completely transformed to ZrN in the microwave-sintered samples. The hardness of the microwave-sintered samples was found to be lower than that of the conventionally sintered samples due to a reverse porosity gradient.

Recently, a novel approach to preparing the Si_3N_4/ZrN powder from zircon, a form of zirconium silicate, has been reported by Bei-yue et al.[121] In this work the phase compositions and the overall reaction for synthesizing of the Si_3N_4/ZrN composite were investigated. The Si_3N_4/ZrN composite was fabricated from zircon by the carbothermal-nitridation (CTRN) process. The samples were prepared by mixing carbon black with an average particle size of less than 30 μm and zircon of 40 μm with a C/$ZrSiO_4$ mass ratios of 0.2, 0.3, 0.4 and 0.5. The prepared samples were subjected to the CTRN process in the temperature range from 1400 to 1500 °C for 6, 9 and 12 h. The CTRN process was conducted in an atmosphere-controlled tubular furnace in a N_2 gas flow of 1.0 L/min. The overall reaction using the CTRN process was expressed as follows:[122]

$$6ZrSiO_4 + 24C + 7N_2 \rightarrow 6ZrN + 2Si_3N_4 + 24CO\uparrow \quad (\Delta G < 0, > 1500\ °C) \quad (17)$$

It was shown that the mass ratio of the carbon black and zircon (C/$ZrSiO_4$) according to reaction 17 was 0.26. Bei-yue et al.[123] found that the proper technological parameters to synthesize a Si_3N_4/ZrN composite were a C/$ZrSiO_4$ mass ratio of 0.4, a synthesis temperature of 1500 °C and a holding time of 12 h. These authors also indicated that by increasing the C/$ZrSiO_4$ mass ratio, the synthesis temperature and the holding time could promote the densification of $ZrSiO_4$ as well as the formation of ZrN and Si_3N_4, and a synthesis temperature above 1450 °C was necessary for the completion of the decomposition of $ZrSiO_4$. The microstructure of this material sintered at 1500 °C for 6 h in a N_2-gas flow is presented in Figure 16. The figure shows large, white ZrN particles (denoted as 1) in between the Si_3N_4 matrix phase (denoted as 2). Unfortunately, these authors did not present any data about the mechanical and electrical properties of this composite. They believed that by combining ZrN, ZrO_2 and Si_3N_4 into a composite, the materials might yield excellent high-temperature properties and that this work can provide a new, low-cost route for the synthesis of Si_3N_4/ZrN from a large amount of available, natural raw materials, and is favourable for decreasing the manufacturing costs of a high-performance Si_3N_4/ZrN ceramic composite.

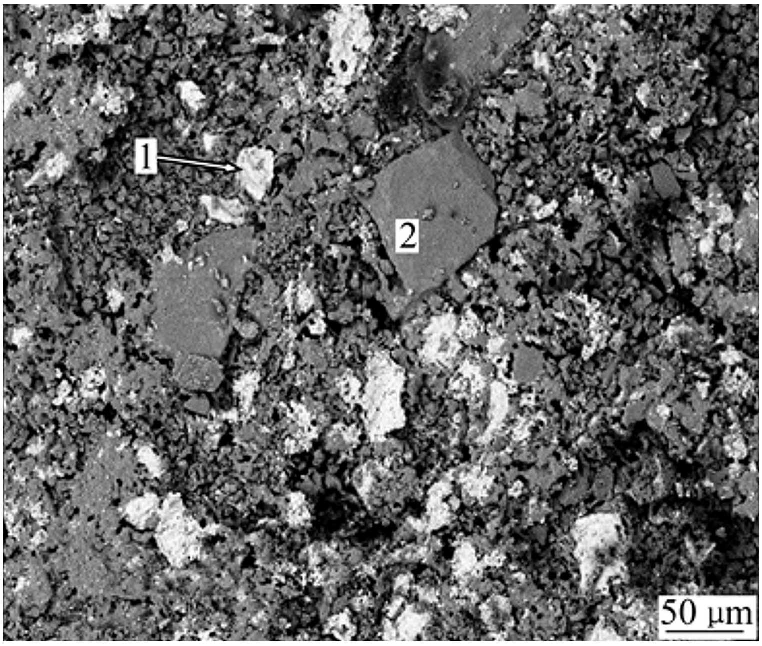

Figure 16: SEM image of sintered sample at 1500 °C for 6 h under N_2-gas flow.[123]

1.3.1 Si_3N_4-ZrO_2 reaction system

In the Si-Zr-O-N system no reaction, even at 1400 °C, was reported by Trigg and McCartney.[88] Weiss et al.[124] demonstrated that Si_3N_4 is stable with ZrO_2 up to 1600 °C. During the thermal treatment or sintering above 1600 °C in N_2 the ZrO_2 reacts with Si_3N_4 following these reactions (18[125,126],19[126,127], 20[128,129]):

$$6ZrO_2 + 4Si_3N_4 \leftrightarrow 6ZrN + 12SiO\uparrow + 5N_2\uparrow \quad (\Delta G = -120\ \text{kJ/mol}, 1600\ °C) \quad (18)$$

$$6ZrO_2 + 2Si_3N_4 \leftrightarrow 6ZrN + 6SiO_2 + N_2\uparrow \quad (\Delta G = +50\ \text{kJ/mol}, 1600\ °C) \quad (19)$$

$$3ZrO_2 + 4Si_3N_4 \leftrightarrow 3ZrN + 6Si_2N_2O + 1/2N_2\uparrow \quad (\Delta G = -50\ \text{kJ/mol}, 1600\ °C) \quad (20)$$

All these reactions indicate that in reducing conditions, at temperatures above 1600 °C, ZrN, Si_2N_2O and gaseous species can be formed. Reaction 18 is thermodynamically more favourable above 1600 °C than reactions 19 and 20, due to a more negative Gibbs free energy.[129] The formation of ZrN cannot occur by reaction 19 below 2230 °C. Reaction 20 suggests that a solid solution of Si_2N_2O is formed instead of SiO or SiO_2, which can improve the mechanical properties of the sintered samples, due to the development of elongated grains. These grains can be used to toughen the Si_3N_4 when they are properly dispersed.[89] By the reaction 18 the gaseous SiO and N_2 are formed that can influence the density of the final material due to the formation of open porosity. Besides, the formation of SiO can influence the reaction of ZrO_2 with Si_3N_4 to form ZrN because of the silicon monoxide partial pressure, since the equilibrium partial pressure of the gas phase is related to the free-energy change.[88] Therefore, reaction 18 should proceed until the equilibrium partial pressure is reached. For instance, in the system Si-Zr-O-N, the equilibrium partial pressure of SiO at 1400 K would be 4×10^{-7} MPa, whereas at 2000 K it would rise to 1×10^{-1} MPa. The reaction rate would be dependent on the rate of removing SiO from the system.[88]

The chemical reaction between the ZrO_2 and Si_3N_4 powder mixture was studied by Weiss.[127] A mixture of 50 mol. % of Si_3N_4 and 50 mol. % of ZrO_2 was heat treated at 1600 °C and 1700 °C for different lengths of time in N_2. The phases present after heat treatments at 1600 °C and 1700 °C are shown in Figure 17. Weight loss was considered as the gas species in the Figure 17. These results indicated that Si_3N_4 and ZrO_2 reacted, giving ZrN and gaseous species, whereas Si_2N_2O was the intermediate phase. The comparison of the heat treated powders, at 1600 °C for 20 h and 1700 °C for 4 h in N_2, showed that the major phases were ZrN and gaseous species, while the minor phases were β-Si_3N_4 and ZrO_2. This investigation indicated that the reaction between ZrO_2 and Si_3N_4 is more favorable at 1700 °C, since reaction 18 occurred.

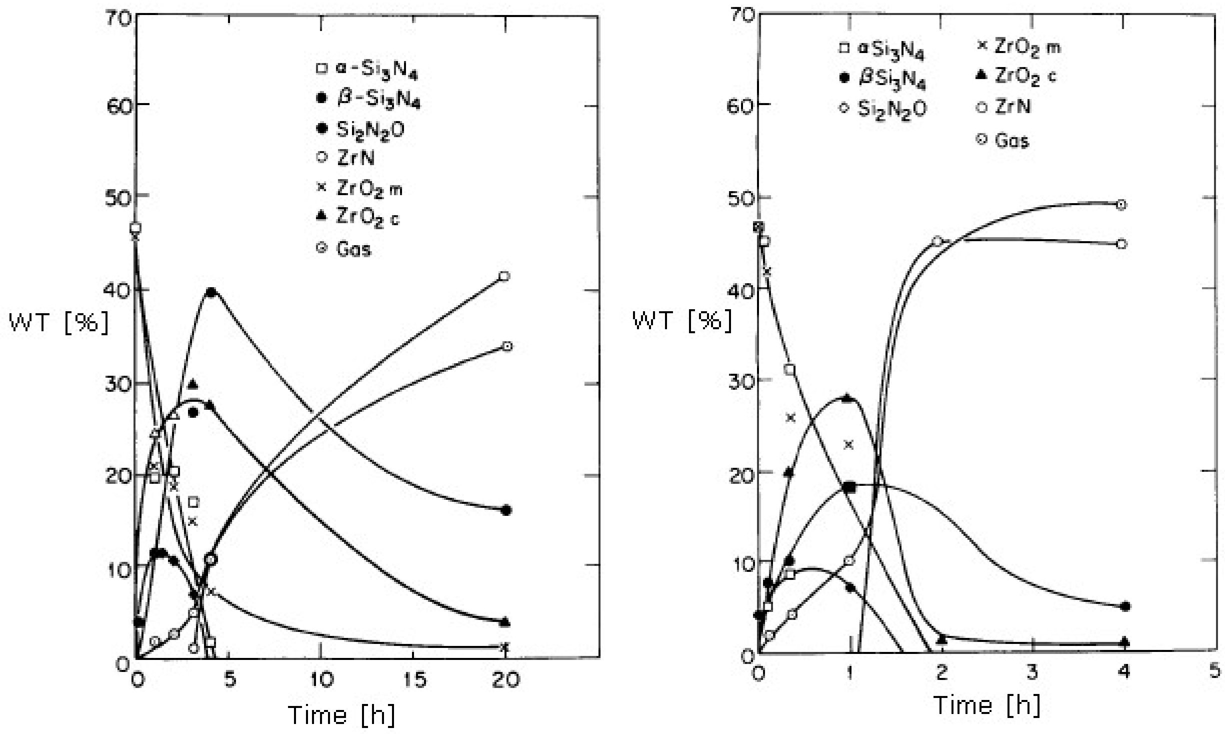

a) b)

Figure 17: Time dependence of the phases present after heat treatment of Si_3N_4-ZrO_2 mixtures at a) 1600 °C and b) 1700 °C.[127]

In the Si-Zr-O-N system the least-stable nitride-oxide composition exists between SiO_2 and ZrN. At 1400 °C the following reaction is possible:

$$2SiO_2 + ZrN \leftrightarrow ZrO_2 + 2SiO\uparrow + 1/2N_2\uparrow \qquad (21)$$

The Si_3N_4-ZrN-SiO_2-ZrO_2 nitride oxide compositions in this system do not react to form a liquid phase because of their immediate thermal decomposition according to reactions 18 & 21 and therefore show poor sintering behaviour. The only stable liquid phase in the Si_3N_4-ZrN-SiO_2-ZrO_2 system forms between ZrO_2 and SiO_2 on the oxide quasibinary ZrO_2-SiO_2.

Weiss et al.[124] also showed that at 1700 °C the reaction between AlN and ZrO_2 is possible following this reaction:

$$8AlN + 6ZrO_2 \leftrightarrow 6ZrN + 4Al_2O_3 + N_2\uparrow \qquad (22)$$

where ZrN is formed together with Al_2O_3 and N_2. Al_2O_3 can act as a sintering additive, thereby forming a transient liquid resulting in rapid densification.

1.4 Percolation theory

Percolation theory is a general mathematical theory of connectivity and transport in geometrically complex systems. The remarkable fact is that many results can often be encapsulated in a small number of simple algebraic relationships.[130] Thus, for example, percolation theory gives a phenomenological equation for the conductivity of the system (or composite medium) near to the metal-insulator (conductor-perfect insulator) transition. Although the theory has largely been developed in the context of regular lattices, it is also used to describe the conductivity of continuum systems, such as metal-metal oxide (cermet) and graphite-polymer mixtures. Wide-ranging reviews on percolation and related phenomena were given in recent review book.[131]

In theoretical model percolation studies, a lattice can be considered to be built up of sites (intersections between bonds) and bonds (pairwise connections between sites). The simplest types of percolation systems are those where there is only a pure-bond or a pure-site percolation. In both cases one starts with a large regular periodic lattice. There are two alternatives for a site: being occupied or not (or being filled with either conducting or insulating material). Similarly, there are two alternatives for bonds: being connected or disconnected. These two alternatives occur irregularly and randomly from site to site (or bond to bond), and the probability p for one of the two alternatives is given in advance. This can be explained, for example with a square grid where individual sites are small squares with a probability p. In the case of small values of this probability, mostly isolated occupied sites can be noticed, with occasional pairs of neighbouring sites that are both occupied. If two or more neighbouring (touching) sites are occupied, this is called a cluster. As the occupancy probability increases we get, at first, more isolated clusters, but some clusters start to grow and some even merge. So the clusters, on the whole, get larger, as shown in Figure 18.

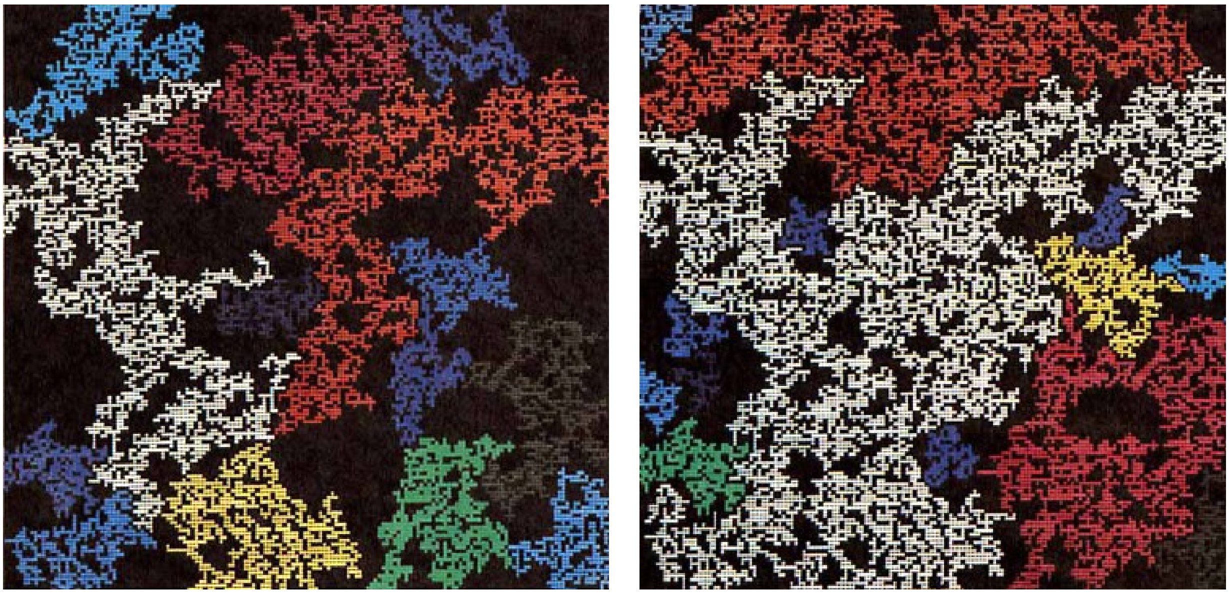

a) $p = 0.58$

b) $p = 0.6$

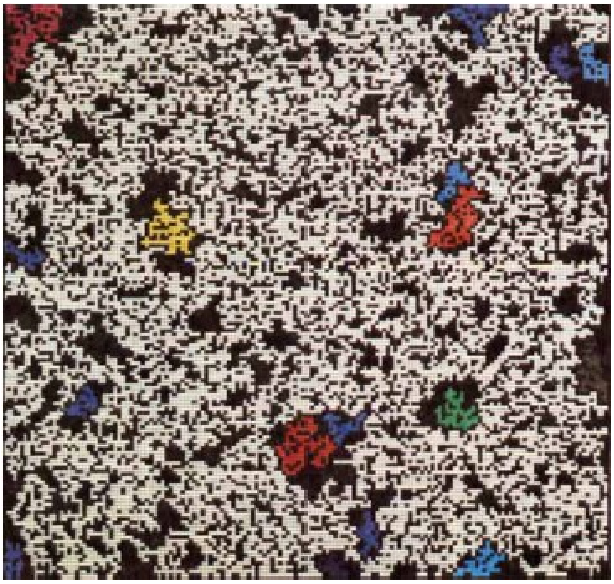

c) $p = 0.62$

Figure 18: Effect of increasing the occupation probability *p* on a 160 x 160 quadratic lattice. In each of the three figures the largest cluster is white. The other clusters are colored, according to their size decrease, with the colors of cyan, red, orange, yellow, light green, green, turquoise, and blue in different light-to-dark shades. The smallest clusters and isolated single occupied sites are not visible in this coloring scheme.[132]

When *p* is increased further, one of the clusters starts to dominate until it becomes (theoretically, for an infinite lattice) infinitely large at a particular-threshold value of the occupancy probability *p*. This percolating cluster spans over the whole lattice (or available space). For even higher values of occupancy probability more and more remaining clusters are absorbed (merged) into the percolating cluster until at $p = 1$ every site is occupied. In these figures different colors simply label different clusters and have no other significance. The threshold value of the occupancy probability with a sudden span of the leading (percolation) cluster over the lattice is known as the percolation threshold (p_C) and is the fundamental characteristic of percolation theory. The theoretically predicted exact value of the percolation threshold depends on the shape of the grid and its spatial dimensionality and it holds in the limit of an infinitely large grid. On the other hand, for small finite grids the percolation threshold is not exactly defined because of the probabilistic nature of the percolation theory.[133]

1.4.1 Percolation threshold

The percolation threshold is a mathematical term related to the percolation theory, which is the formation of a long-range connectivity in random systems. The percolation threshold is the critical value of the occupation probability p, or more generally, a critical surface for a group of parameters p_1, p_2, …, allowing an infinite connectivity (percolation) to occur for the first time. When electrically conducting particles are randomly distributed within an insulating matrix, like in metal-ceramic matrix composites, the whole material may be insulating or conducting, depending on the volume of the conducting phase. Just near the percolation threshold, where the critical amount of the conductive particles for the onset of electrical conduction is reached, the electrical properties of the material exhibit a non-linear critical behaviour.[134,135,136] Conducting particles of different shapes in two and three dimensions (2D and 3D) are considered in the reported calculations of the percolation threshold: mostly spherical,[137,138] thin and thick elongated particles,[139,140,141] and even 2D random polygons with random plane-orientations in 3D space.[142] For instance, if the hard-core conductive spheres, all of an equal size, are considered in 3D space, the percolation volume ratio is 35 % ± 2 %.[141] The term hard-core indicates that the spheres cannot overlap (intersect) or be deformed due to mutual pressure; they can only touch to make electric (or other kind of) contacts. In the case of completely "soft", conductive, equal, spherical particles (i.e., they can overlap without limit) the percolation volume ratio is only 28.9 %.[143] This latter value may hold well for a system of "Swiss cheese" or the percolation of water through a porous medium with open porosity and ideally spherical pores of the same sizes, but it does not seem to be realistic for conducting particles which cannot just overlap or be deformed easily. The threshold volume fraction of the conductive filler particles $x = x^*$, at which the transition from the non-conducting to the conducting state is observed, is the most essential characteristic of the percolation behaviour. Here, x is the ratio of the volume of conducting particles to the total volume of the system. For example, the concentration dependence of the electrical conductivity $\sigma(x)$ near the percolation point obeys the following scaling laws above and below the percolation threshold (both not in its direct vicinity), respectively:

$$\sigma(x) = a(x - x^*)^t, \qquad x > x^*, \tag{23}$$

$$\sigma(x) = b(x^* - x)^{-s}, \qquad x < x^*, \tag{24}$$

where a and b are the scaling coefficients and s and t are the positive electrical conductivity exponents. The concentration dependence of the electrical conductivity is represented in Figure 19.

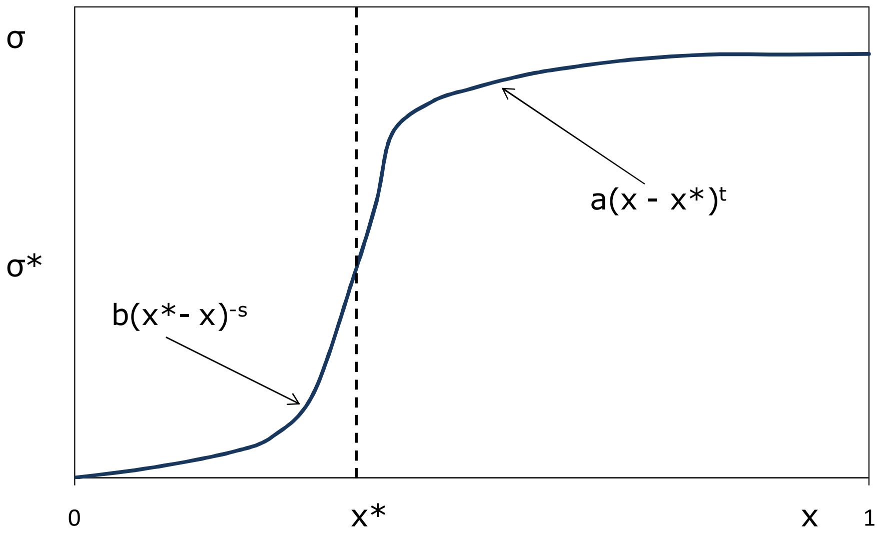

Figure 19: Electrical conductivity as a function of the volume fraction of the conductive particles.[144]

It is believed that s and t only depend on the dimensionality and universality of the class of the problem. For the random percolation, $s = t \approx 4/3$ for 2D systems and $s \approx 0.75$, $t \approx 2.0$ for 3D systems.[144] The value of x^* is a complex function of the space dimensionality, the shape and the size of the particles, local variations in their concentration, their spatial arrangement and many other factors.[145] The percolation values of x^* may be significantly lower for filler particles of an elongated geometry (rods or discs) and multiple percolation thresholds can occur in this case.

The percolation threshold for the electrical conductivity of the ceramic composites predominantly depends on the particle shape and size, and the volume fraction and the spatial arrangement of the conductive particles. Time-consuming Monte Carlo simulations demonstrated that ceramic composites with equal, spherical, distributed, conductive particles within an insulating matrix have about 30 vol. % of the percolation-threshold volume.[146]

1.4.2 Dependence of percolation threshold on conductive-particles' shape and size

The percolation threshold is a particle-size (more exactly, a size distribution of unequal particles) and geometry-dependent parameter. The non-homogeneity in the distribution of the particles' centres in space can have a considerable influence on the percolation-threshold volume and also on the anisotropy of the electrical properties of the material. The spatial non-homogeneity can be described by the probability-distribution function for the particle-center coordinates, which varies in space. Using Maxwell's theory,[147] the equation for the electrical conductivity of the composite was derived by Xue et al.[148] The shape and size dependence of the percolation threshold are presented in Figure 20. It can be seen that the percolation-threshold value decreases significantly with the increasing metal-particle aspect ratio, M, and the thickness, t, of the interfacial shell for the rod-like particles. Many more metal particles with a smaller aspect ratio are needed to form a conductive network through the entire matrix. Figure 20 b indicates that larger particle sizes result in a higher percolation threshold if the system is not very (infinitely) large in comparison with the particle size (i.e., when the particle sizes are comparable with at least one dimension of the system under consideration).[148] Ambrožič et al.[149] also showed that a greater diversity of the particles' dimensions results in a larger percolation-threshold volume. The large spheres could represent agglomerates of conductive particles in a real composite system.

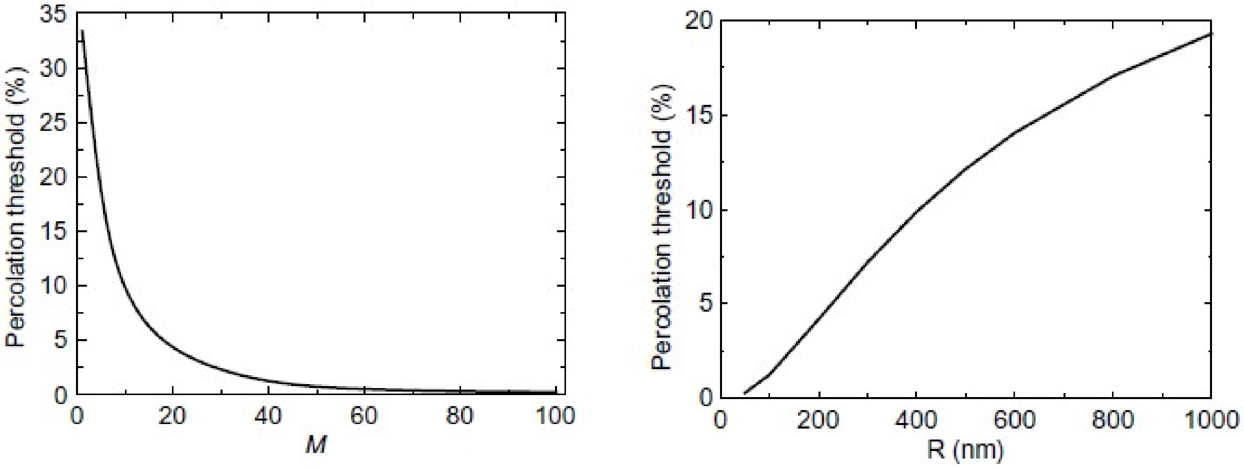

a) b)

Figure 20: Relation between the percolation threshold (vol. %) and a conductive particle a) aspect ratio and b) size.[148]

The dependence of the conductivity percolation threshold on the conductive-particle size distribution and the aspect ratio is the principal factor that should be carefully examined when making conductive ceramic composites. Using conductive particles with a larger aspect ratio and a smaller size helps to reduce the minimum of the conductive-phase content required to reach a certain conductivity value.[150]

1.4.3 Method for decreasing the percolation threshold

In order to impart electrical conductivity to insulating ceramics, dispersions of conducting second-phase particles have been considered.[15,32,151,152,153] In such composites the conducting-particle contents of above 25-35 vol. % are necessary to produce an electrically conductive ceramic, as shown in Figure 21 a. However, such relatively large amounts of the second phase are usually undesirable due to the poor sinterability and the reduced mechanical properties.

It has been reported recently that carbon nanotubes (CNTs), in proportions as low as several vol. %, can serve effectively as a conducting second phase in insulating materials such as polymers and ceramics.[154,155] However, since CNTs are highly reactive with oxide and nitride ceramics at high temperature, it is difficult to maintain the nanotube structure during sintering. Furthermore, the fabrication of the electoconductive CNT-dispersed nitride ceramics by pressureless sintering has not been possible because carbon inhibits the densification of most nitride ceramics.

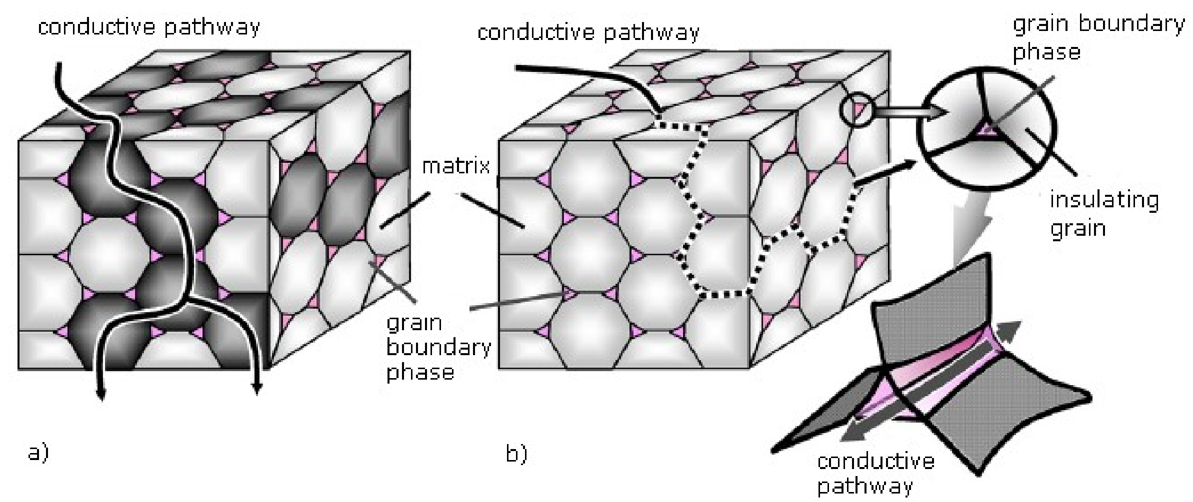

Figure 21: Models of conferring electrical conductivity on insulating ceramics: a) dispersion of the second-phase particles with electrical conductivity b) propagation of an electrically conductive grain-boundary phase.[156]

According to the basic electrical conduction theories such as the effective media and the percolation, it is possible to obtain low resistivity values by forming a continuous network of conductive particles around the insulating matrix particles with very low volume fractions (1-10 vol. %) of the conductive particles. Considering these theories, a grain boundary, as described in Figure 21 b, propagating three-dimensionally in a sintered body could be produced. If the grain-boundary phase can be used as a conductive pathway where electricity flows through the grain-boundary phase, then a grain-boundary phase content of a few vol. % may be sufficient to impart electrical conductivity to insulating ceramics.

The amount of shell (conductive) particles needed to continuously cover the surface of the core (matrix) particles could be calculated with the following equation (see appendix):

$$\frac{m_C}{m_S} = \frac{\rho_C \cdot R}{\rho_S \cdot k \cdot 2r} \tag{25}$$

where m_C, m_S, R, r, ρ_C, ρ_S are the masses, the radii, and the densities of the core and shell particles, respectively. The coefficient of the surface filling *k* is determined according to the percolation theory.[133] The equation is correct for the supposition that the shell and core particles are spherical and that the shell particles are much smaller than the core particles (so that very many shell particles can reside on the surface of one core particle).

Kusunose et al.[156] have already produced a grain-boundary phase as a conductive pathway in insulating AlN ceramics. They showed that electrically conductive AlN ceramics with a high thermal conductivity were obtained by precipitating yttrium oxycarbide as a conductive pathway at the grain boundaries. The yttrium oxycarbide was formed when the AlN was sintered with a Y_2O_3 additive in nitrogen and was subsequently reduced in a carbon gas atmosphere. The electrical conductivities can be controlled by varying the sintering conditions and the additive compositions. The scanning transmission electron microscopy (STEM) dark-field image of a sintered AlN ceramic with and without additives is shown in Figure 22. The grain-boundary phase containing rare-earth elements appears bright, while the AlN grains appear dark. The grain-boundary phase yttrium oxycarbide forms a three-dimensional network in the electrically-conductive AlN sintered body, whereas no obvious grain-boundary phase was observed in the hot-pressed insulating AlN sample without any additive. Furthermore, the electrically conductive AlN can be shaped by EDM and reverted to insulating AlN by anodic oxidation of yttrium oxycarbide.

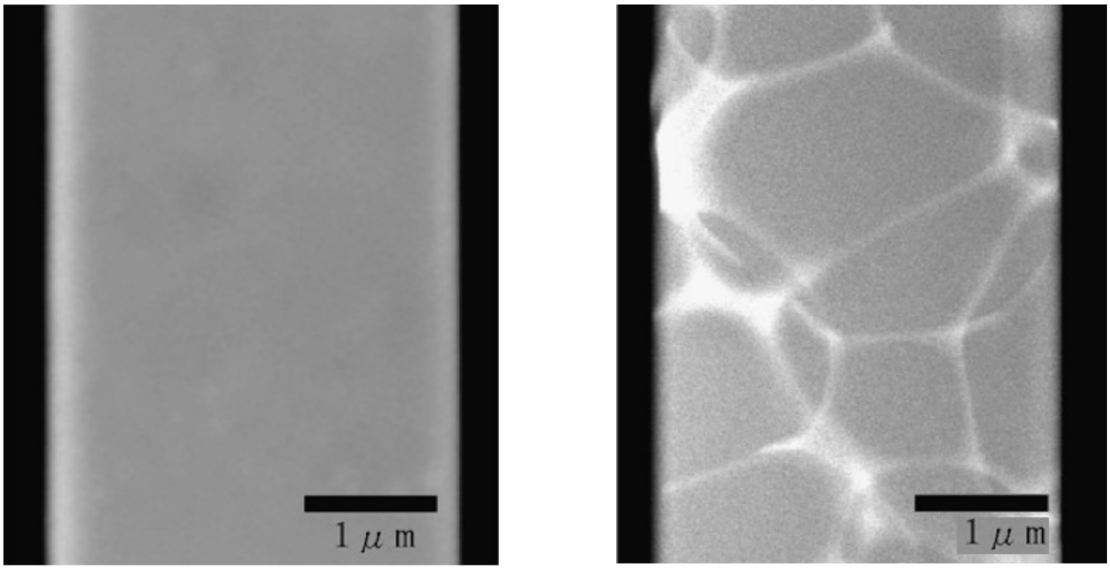

a) b)

Figure 22: STEM dark-field image of (a) the insulating AlN produced by hot pressing without any additive at 1850 °C for 1 h under an applied pressure of 30 MPa in N_2, and (b) the electrically conductive AlN produced by sintering AlN containing 1 wt. % Y_2O_3 and 4 wt. % CeO_2 at 1600 °C for 12 h in N_2.[156]

2 Aims and Hypothesis

Electrically conductive ceramic composites fabricated by mixing the powders of different phases often exhibit an inferior flexural strength compared to the base ceramic materials (for example, Si_3N_4 ceramic). This is due to the negative effect of the large amount (> 30 vol. %) of dispersed electroconductive particles needed to reach the percolation threshold on the sintering behaviour and the resulting mechanical properties. Different approaches are being applied, including attempts to decrease the percolation threshold for the electrical conductivity by decreasing the size of the electroconductive particles to promote the sintering of the matrix phase. An alternative method, developed recently, is the in-situ composite method, where nano-sized TiN conductive particles are formed on the Si_3N_4 powder surface from inorganic precursors with a consequent chemical reaction between the metallic oxides and Si_3N_4 and a subsequent densification by modern sintering techniques (HP or SPS). However, these techniques of densification under pressure are relatively expensive and are limited to simple shapes of the sintered specimens.

In this thesis we tried to prepare dense and electrically conductive Si_3N_4/TiN and Si_3N_4/ZrN composites with a reduced amount and size of the conductive particles by the pressureless sintering of pressed TiN- and ZrN-coated Si_3N_4 powders with oxide additives. Moreover, Si_3N_4/ZrN composites prepared with an in-situ composite method represent a novel system for the preparation of the electrically conductive composites.

The aim of the work was to form nano-sized TiN or ZrN particles on the surface of the Si_3N_4 powder using the gel-precipitation of titanium and zirconium hydroxides in aqueous Si_3N_4 suspensions and a subsequent thermal treatment. After calcinations at 600 °C in air titania and zirconia were formed. The TiN particles on the Si_3N_4 powder surface were synthesized by the nitridation reaction of the TiO_2 and the NH_3 gas. Meanwhile, ZrN particles on the surface of the Si_3N_4 were formed by the reaction between ZrO_2 and Si_3N_4 at temperatures above 1600 °C in N_2.

The goal of this research was to produce electrically conductive Si_3N_4/TiN and Si_3N_4/ZrN composites by pressureless sintering the pressed powder mixtures of the TiN-coated or ZrN-coated Si_3N_4 powders with oxide additives, e.g., Y_2O_3 and Al_2O_3 which will have good mechanical properties. The results of the dissertation include an explanation of the chemical reactions and mechanisms that may lead to the formation of a matrix and a conductive phase fabricated from different precursors. The work focuses on preserving the size of the TiN or ZrN particles, so that they will form an electrically conductive network around the larger Si_3N_4 particles and a much lower amount of the conductive phase will be needed. The thermodynamics of several overall reaction mechanisms was evaluated, including the effects of the gas-phase composition to determine the most energetically favourable course for each reaction. In addition, the amount of conductive phase (TiN, ZrN) in the coated powders and final composites was calculated by using the proposed chemical reaction and was quantitatively determined from the x-ray diffraction patterns of coated powders and sintered composites. The influence of the amount of conductive phase in the Si_3N_4/TiN and Si_3N_4/ZrN composites on the relative density, flexural strength and electrical conductivity was investigated. Moreover, the percolation threshold for electrical conductivity of sintered composites was determined experimentally and compared to the proposed simple theoretical percolation-threshold model. At the end of this research work the functional properties and their applicability for ceramic heaters and ceramic glow plugs are examined.

The hypotheses of this dissertation are that with the gel-precipitation of titanium and zirconium hydroxides and a subsequent thermal treatment it is possible to attain homogeneously distributed TiN and ZrN nanoparticles on the surface of the Si_3N_4 particles. By sintering pressed powder mixtures of the TiN-coated or ZrN-coated Si_3N_4 powders with oxide additives it is possible to prepare electrically conductive composites with a decreased amount of the conductive phase in the Si_3N_4 matrix and by this means, preserve the mechanical properties of Si_3N_4, which differs from the results of the conventional composite method including mechanically mixed powders.

3 Materials and Methods

3.1 Starting materials

In the experimental work a commercially available, α-rich Si_3N_4 powder (SN-E10, UBE Industries, Ltd., Tokyo, JPN), was used as the basic raw material for the matrix phase. The characteristic data of this Si_3N_4 powder is presented in Table 3.

Table 3: Characteristics of the Si_3N_4 powder according to the producer's specification

Grade	UBE SN-E10
Average particle size (d_{50})	0.50 μm
Phase	α-phase crystal > 95 %
N (wt. %)	> 38.0
O (wt. %)	1.05
Cl (ppm)	< 100
Fe (ppm)	< 100
Ca (ppm)	< 50
Al (ppm)	< 50
β/(α + β) (wt. %)	< 5
Crystallinity (wt. %)	< 99.5
SSA (BET) (m^2/g)	9.1

With the aim to enhance the densification of the Si_3N_4 matrix, the following oxide additives were added:

- yttria powder (Y_2O_3), grade fine, H.C. Starck, Berlin, DE
- alumina powder (Al_2O_3), A-16, Alcoa, USA

The characteristic data of these oxide powders are shown in Tables 4 and 5.

Table 4: Characterstics of the Y_2O_3 powder acoording to the producer's specification

Grade	Fine
d_{50}	0.90 μm
Y_2O_3 (wt. %)	99.95
Al (wt. %)	0.005
Ca (wt. %)	0.003
Fe (wt. %)	0.005
SSA (BET) (m^2/g)	10-16

Table 5: Characteristics of the Al_2O_3 powder according to the producer's specification

Grade	A-16
d_{50}	0.50 μm
α-Al_2O_3 (wt. %)	99.7
Na_2O (wt. %)	0.08
SiO_2 (wt. %)	0.02
Fe_2O_3 (wt. %)	0.01
CaO (wt. %)	0.01
B_2O_3 (wt. %)	0.001
SSA (BET) (m^2/g)	3-7

For the conductive secondary phase TiN and ZrN were used. The TiN and ZrN were formed from the TiO_2 and ZrO_2 nano-particles that were synthesized by an in-situ gel-precipitation method using various inorganic precursors. The TiO_2 particles were formed from a titanil sulphate solution – $TiOSO_4$ (Cinkarna Celje, SL). The ZrO_2 particles were formed by using a zirconium acetate solution – $Zr(CH_3COO)_2$ (Sigma-Aldrich Chemie, Steinheim, DE).

3.2 Preparation of the coated powders

Our investigative work was based on the Si-Ti-O-N and Si-Zr-O-N systems, where the α-rich Si_3N_4 powder was coated with various amounts of metal oxides (TiO_2 and ZrO_2), thereby establishing a uniform coating on the surface of the Si_3N_4. Afterwards the TiO_2- and ZrO_2-coatings were thermally treated at elevated temperatures in order to form TiN and ZrN nanoparticles on the surface of the Si_3N_4 powders.

3.2.1 Si-Ti-O-N system

Preparation of the TiO_2-coated Si_3N_4 powders

The TiO_2-coated Si_3N_4 powders containing 10, 20, 25, 30 and 35 vol. % of TiO_2 in the starting compositions were prepared by the in–situ gel-precipitation of titanium hydroxides in the Si_3N_4 aqueous suspension. For the preparation of the TiO_2 nano-coatings the following procedure was performed: the Si_3N_4 powder and deionised water were mixed in the calculated proportion and homogenized by ball milling for 2

h. After the homogenisation, $TiOSO_4$ was dripped into the stirred Si_3N_4 aqueous suspension, shown in Figure 23. The concentration of $TiOSO_4$ was 0.25 mol/L of the liquid phase. The precipitation of $Ti(OH)_4$ was adjusted to pH 3.0 by using a tetramethylammonium hydroxide – TMAH (Alfa Aesar, Karlsruhe, DE). The as-prepared precipitates were separated from the mother solution, and then washed several times with deionised water and anhydrous ethanol. After the final filtration the cakes were dried at 80 °C for 18 h and subsequently calcined at 600 °C for 2 h.

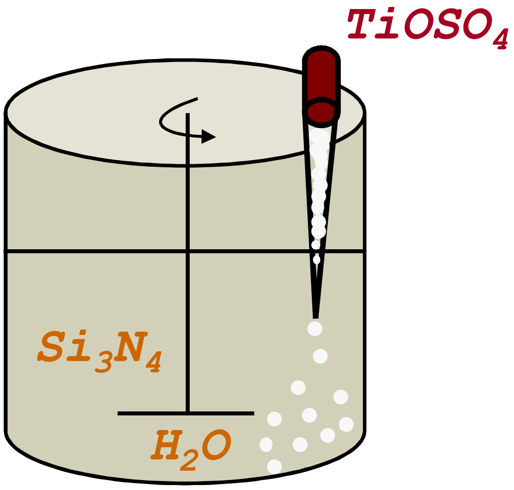

Figure 23: Scheme of coating the Si_3N_4 powder with $Ti(OH)_4$.

Preparation of the TiN-coated Si_3N_4 powders

The as-prepared TiO_2-coated Si_3N_4 powders were nitrided at 900 °C for 6 h in a tube furnace to obtain the TiN-coated Si_3N_4 powders. The ammonia gas – NH_3 (Messer, Zaprešić, CRO) − was employed as the nitriding medium with a flow rate of 225 ml/min. The nitrided powders were taken out from the furnace after cooling to room temperature in the flow of NH_3 gas.

3.2.2 Si-Zr-O-N system

Preparation of the ZrO_2-coated Si_3N_4 powders

The ZrO_2-coated Si_3N_4 powders containing 10, 20, 25, 30 and 35 vol. % of ZrO_2 in the starting composition were prepared by a heterogeneous precipitation of zirconium hydroxides in a Si_3N_4 aqueous suspension. The Si_3N_4 powder and zirconium acetate were mixed in an appropriate ratio and homogenized for 2 h by ball milling using deionised water as the liquid medium. The concentration of the zirconium acetate in the suspension was 0.2 mol/L of the liquid phase. The precipitation of the zirconium hydroxides was initiated by increasing the pH, which involved blowing gaseous ammonia through the suspension, as schematically presented in Figure 24. The precipitation started at pH 3.8 and was finished at pH 7.0. The coated Si_3N_4 powders were filtered, washed several times with deionised water and anhydrous ethanol and dried at 80 °C for 18 h. The dried powders were then calcined at 600 °C for 2 h to obtain crystalline ZrO_2 on the surface of the Si_3N_4 powders.

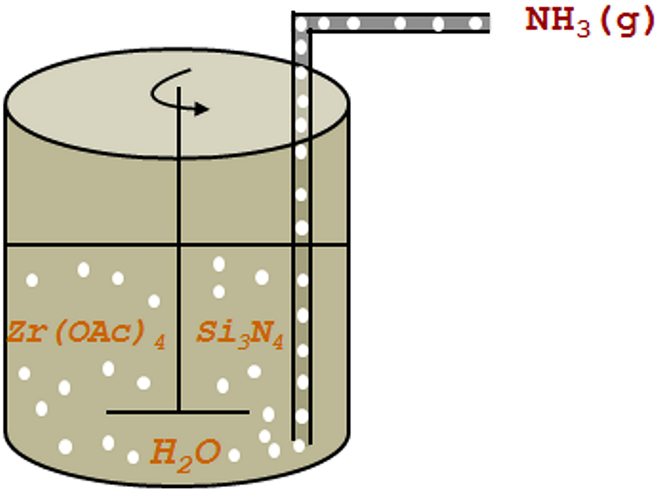

Figure 24: Schematic view of coating the Si_3N_4 particles with $Zr(OH)_4$ using gaseous ammonia.

Preparation of the ZrN-coated Si_3N_4 powders

After completing the calcinations, the ZrO_2-coated Si_3N_4 powders were thermally treated at 1600 °C for 2 h using nitrogen atmosphere in order to obtain ZrN on the surface of the Si_3N_4. Furthermore, the ZrO_2 coatings were also thermally treated at 1600 °C for 3 h in flowing nitrogen at low-pressure (P_{N_2} = 0.4 atm).

3.3 Preparation of the composites

3.3.1 Preparation of the sintered Si_3N_4/TiN composites

The TiN-coated Si_3N_4 powders (containing 10, 20, 25, 30 and 35 vol. % of TiO_2 in the starting composition) were mixed together with 5 wt. % yttria and 3 wt. % alumina additives (with respect to the Si_3N_4 powder) for 4 h in isopropanol using a planetary mill equipped with Si_3N_4 balls (Figure 25). The compositions of the Si_3N_4-TiN powder mixtures (denoted as sample A) containing various amounts of TiO_2 in the starting composition are shown in Table 6.

Table 6: Chemical composition of the Si_3N_4-TiN powder mixtures

Mixture	Composition (vol. %)			
	Si_3N_4	Y_2O_3	Al_2O_3	TiN
A10	88.6	3.1	2.3	6.0
A20	82.9	2.9	2.2	12.0
A25	79.1	2.8	2.1	16.0
A30	74.5	2.6	1.9	21.0
A35	72.2	2.5	1.9	24.0

After the evaporation of the isopropanol at 80 °C, the mixed powders (A10-A35) were ground, sieved and uniaxially pressed at a pressure of 50 MPa into 5 mm × 42 mm × 3 mm rectangular bars and subsequently cold isostatically pressed at 380 MPa. The green compacts, placed in a graphite crucible and embedded in the Si_3N_4 and BN powder bed, were sintered at 1850 °C for 2 h in flowing N_2 (referred to as the pre-reacted powder as shown in Figure 25).

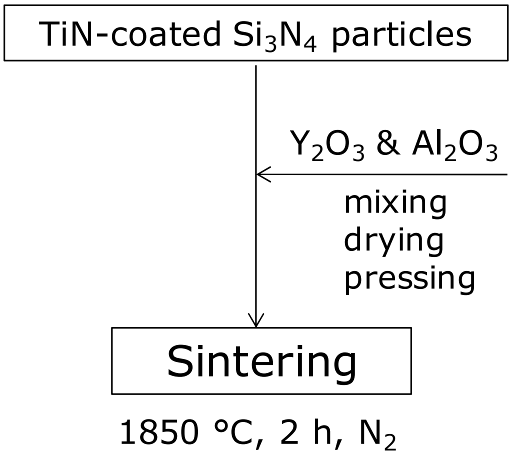

Figure 25: Flow chart of the preparation of the Si_3N_4-TiN composites from the pre-reacted powder.

3.3.2 Preparation of the sintered Si_3N_4/ZrN composites

To fabricate the Si_3N_4/ZrN composites, the ZrN-coated Si_3N_4 powders containing 10, 20, 25, 30 and 35 vol. % of ZrO_2 in the starting composition, were first mixed with 5 wt. % yttria and 3 wt. % alumina additives with respect to the Si_3N_4 powder (denoted as the samples B) for 4 h in isopropanol using a planetary mill equipped with the Si_3N_4 balls. The compositions of the Si_3N_4-ZrN powder mixtures that initially contained various amounts of ZrO_2 in the starting composition are shown in Table 7.

Table 7: Chemical composition of the Si_3N_4-ZrN powder mixtures

Mixture	Composition (vol. %)			
	Si_3N_4	Y_2O_3	Al_2O_3	ZrN
B10	87.7	3.0	2.3	7.0
B20	79.1	2.8	2.1	16.0
B25	73.6	2.5	1.9	22.0
B30	60.4	2.0	1.6	36.0
B35	50.0	1.7	1.3	47.0

In addition, the ZrO_2-coated Si_3N_4 powders containing 10 and 20 vol. % of ZrO_2 in the starting composition were also mixed with 5 wt. % yttria and 3 wt. % alumina additives with respect to the Si_3N_4 powder (denoted as the samples C). The compositions of the Si_3N_4-ZrO_2 powder mixtures containing various amounts of ZrO_2 in the starting composition are presented in Table 8.

Table 8: Chemical composition of the Si_3N_4-ZrO_2 powder mixtures

Mixture	Composition (vol. %)			
	Si_3N_4	Y_2O_3	Al_2O_3	ZrO_2
C10	85.3	3.0	2.2	9.5
C20	76.3	2.7	2.0	19.0

After evaporation of the isopropanol at 80 °C by means of a rotating evaporator, the dry powder mixtures were cold uniaxially pressed at a pressure of 50 MPa into 5 mm × 42 mm × 3 mm rectangular bars and subsequently cold isostatically pressed at 380 MPa. The green compacts, placed in a graphite crucible and embedded in the Si_3N_4 and BN powder bed, were sintered using two regimes (Figure 26). In the first regime the green compacts (B10-B35) were sintered at 1850 °C under a N_2 atmosphere at a pressure of 0.1 MPa, with a holding time of 2 h (referred to as the pre-reacted powder). In the second regime the compacts (C10 & C20) were directly sintered under the same conditions (referred to as the in-situ reacted powder). Both regimes are shown in Figure 26.

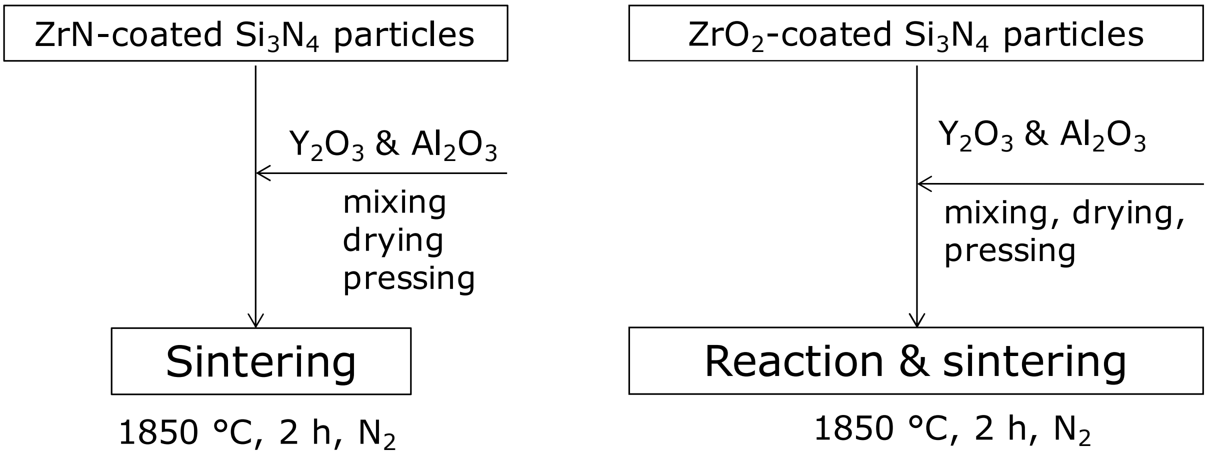

a) b)

Figure 26: Flow chart of the preparation of the Si_3N_4-ZrN composites from: a) pre-reacted powder and b) in-situ reacted powder.

3.4 Characterization

3.4.1 Particle size analysis

The particle size distributions of starting materials (Si_3N_4, Y_2O_3 and Al_2O_3) were measured with the particle size distribution analyzer (HORIBA LA-920, Kyoto, JPN), which operates on the basis of a static light scattering. The static laser light scattering can be used for the analysis of emulsions, suspensions and/or dry samples.

In addition the average particle size of nanosized oxide (TiO_2, ZrO_2) and nitride (TiN and ZrN) coatings was determined by using an XRD of coated powders and a Scherrer equation:

$$\tau = \frac{K \cdot \lambda}{\beta \cdot \cos\theta} \qquad (26)$$

where K is the shape factor, λ is the x-ray wavelength, β is the line broadening at half the maximum intensity in radians, and θ is the Bragg angle. τ is the mean size of the ordered (crystalline) domains, which may be smaller or equal to the grain size. The dimensionless shape factor has a typical value of about 0.9, but varies with the actual shape of the crystallite. The Scherrer equation is limited to nano-scale particles.

3.4.2 X-ray powder diffraction

The nanosized oxide (TiO_2, ZrO_2) and nitride (TiN and ZrN) coatings and the sintered Si_3N_4/TiN and Si_3N_4/ZrN composites were analyzed with the X-ray powder diffraction (D4 Endeavor, Bruker-AXS, Germany) using CuKα radiation with a wavelength of 1.542 nm. The XRD measurements were performed in the 2 θ range from 10 to 70 ° with a scan step of 0.02° 2 θ and an integration time of 3 s per a step.

3.4.3 Rietveld method

The Rietveld method was originally developed to refine the structure of crystalline materials by means of neutron and X-ray powder diffraction, allowing a determination of the mass fraction for different phases.[157]

A model of the phase(s) is used to generate a calculated diffraction pattern. This is then compared with the observed data, and the difference between the observed and calculated is minimised by varying the parameters in the model through a least-squares process.

In the Rietveld method the least-squares refinements are carried out until the best fit is obtained between the entire observed powder-diffraction pattern, taken as a whole, and the entire calculated pattern, based on the simultaneously refined models for the crystal structure(s), diffraction optics effects, instrumental factors, and other specimen characteristics (e.g., lattice parameters) that may be required and can be modelled. A key feature is the feedback, during the refinement, between improving the knowledge of the structure and improving the allocation of the observed intensity to the partially overlapping individual Bragg reflection.[158] This requires extended measurement times of around 60 to 80 minutes. In addition, the method is made complicated by long calculation times, and is more or less controlled manually.

The oxide (TiO_2 and ZrO_2) and nitride (TiN and ZrN) coated Si_3N_4 powders and the sintered Si_3N_4/TiN and Si_3N_4/ZrN composites were analyzed with the Rietveld method using Topas software in order to determine the mass fraction of each component.

3.4.4 Density measurements and the microstructure of the sintered composites

The densities of the sintered samples were determined using Archimedes' method of immersing the bulk into deionised water. The composites were weighted in the air and afterwards in the water while suspended by a thread.

The microstructures of the sintered Si_3N_4/TiN and Si_3N_4/ZrN composites were observed with a scanning electron microscopy (SEM, JSM 5800 and JSM-7600F, Jeol, Japan).

3.4.5 TEM analysis

All the oxide (TiO_2 and ZrO_2) or nitride (TiN and ZrN) coated Si_3N_4 powders and the Si_3N_4/TiN composite prepared from the pre-reacted powder containing 30 vol. % of the TiO_2 and Si_3N_4/ZrN composite prepared from the pre-reacted powder containing 25 vol. % of ZrO_2 (in the starting composition) were analysed with transmission electron microscopy (TEM, JEM 2100, Jeol, Japan), HRTEM (high-resolution transmission electron microscopy), SAED (selected-area electron diffraction) and EDXS (energy-dispersive x-ray spectroscopy).

3.4.6 Flexural-strength measurements of the sintered samples

The flexural strength was measured with an Instron–1362 testing machine (Instron, USA), using the four-point bending method with an outer-span length of 20 mm and an inner-span length of 10 mm, and a crosshead speed of 1 mm/min. The instrument records the force when the fracture occurred.

For the flexural-strength measurements five samples of each composition were tested. In this case, Weibull statistics was not used due to the small number of tested samples.

3.4.7 Electrical-resistivity measurements of the sintered samples

The electrical resistivity of the sintered materials was measured with a DC Multimeter-3457A-testing machine (HP, USA) using four-point technique at the room temperature (25°C) with a direct current. Prior to the electrical-resistivity measurements a thin layer of In-Ga paste was put onto the surface of the samples. For the electrical-resistivity measurements two samples of each composition were examined.

4 Results and discussion

4.1 Particle size of the starting materials

Before preparing the powder mixtures, the particle-size distributions of the starting materials were characterized. The results (shown in Figure 27) indicate that all the powders have a monomodal particle-size distribution and can be used for the preparation of the powder mixtures without using a precedent milling.

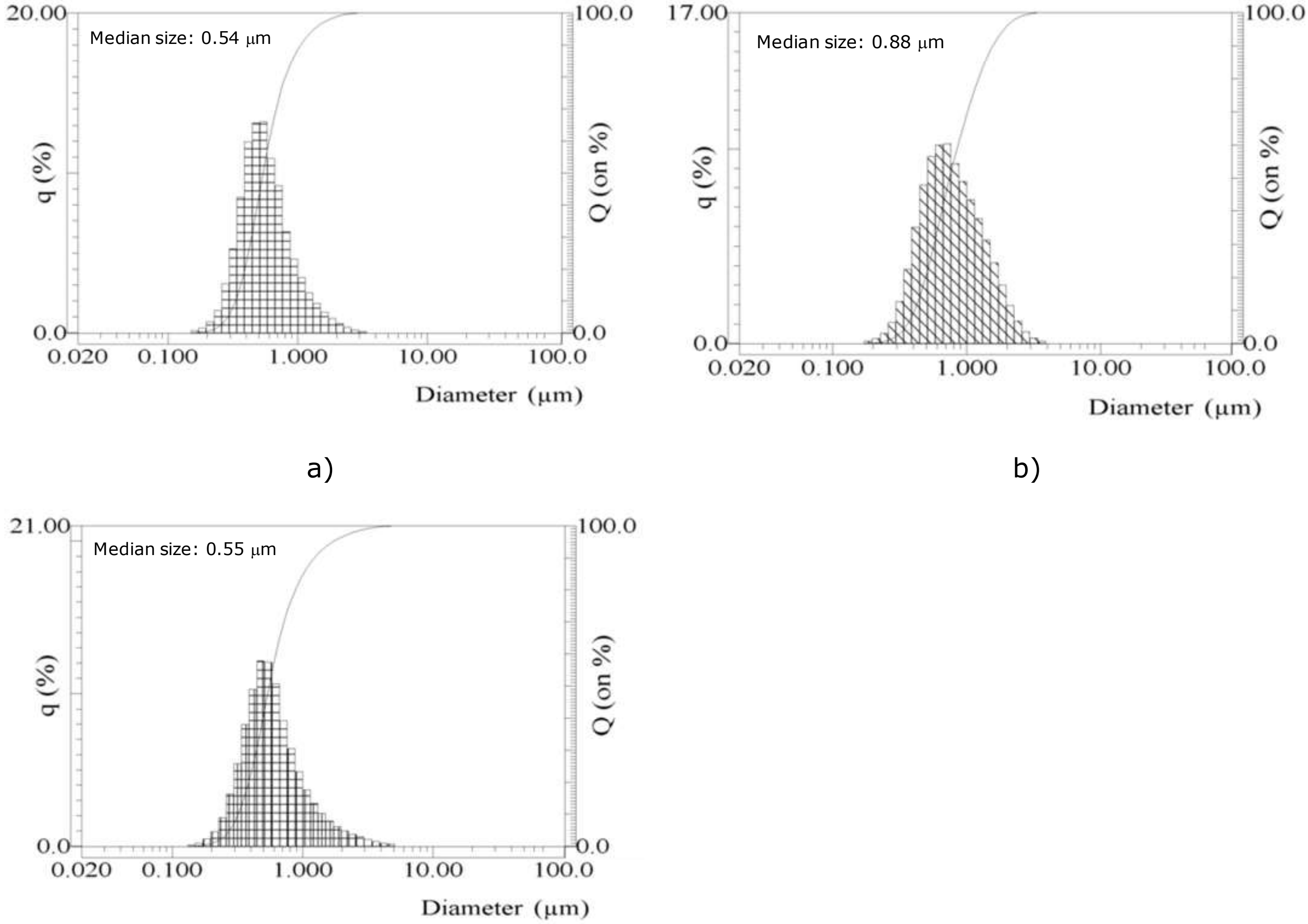

a)

b)

c)

Figure 27: Particle-size distribution of the starting powders: a) Si_3N_4 (UBE SN-E10), b) Y_2O_3 (grade fine) and c) Al_2O_3 (A16).

The measured median sizes of the Si_3N_4 (0.54 µm), Y_2O_3 (0.88 µm) and Al_2O_3 (0.55 µm) powders are comparable to the values included in the producer's specification, as shown in Tables 3, 4 & 5. The morfology of the starting Si_3N_4 powder is presented in Figure 28, showing uniform particle size distribution which is in agreement with the measured particle size distribution. The SEM analysis of this powder (Figure 28) indicates that some elongated β-Si_3N_4 particles are also present between equiaxial α-Si_3N_4 particles.

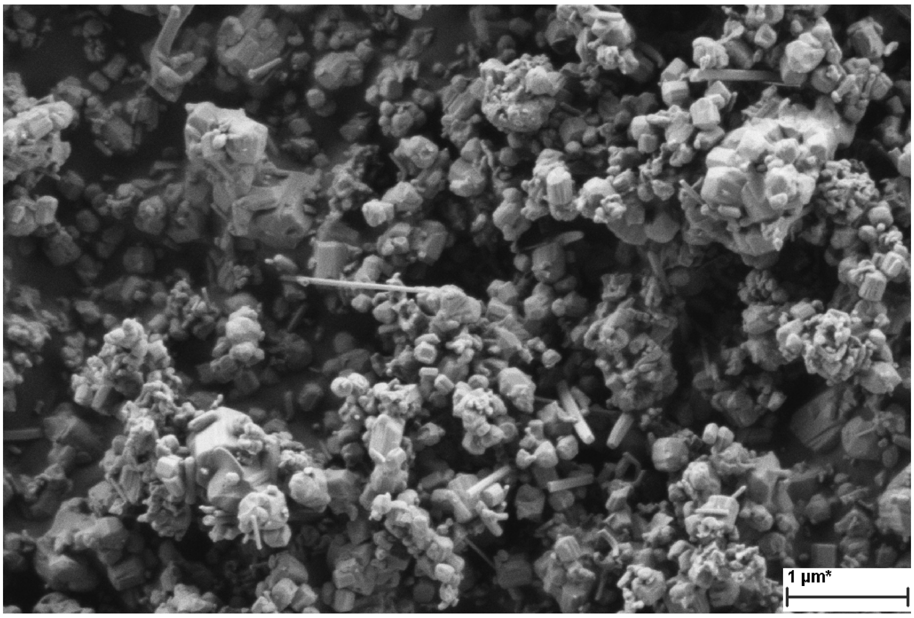

Figure 28: SEM image of the Si_3N_4 powder.

4.2 Si_3N_4/TiN composites

4.2.1 Coating of the Si_3N_4 powder

Preparation of the TiO_2-coated Si_3N_4 powders

The TiO_2-coated Si_3N_4 powders containing 10, 20, 25, 30 and 35 vol. % of nanosized TiO_2 particles in the starting composition were prepared by an in-situ gel precipitation. In this process, titanium hydroxide ($Ti(OH)_4$) was precipitated on the surface of the Si_3N_4 powder using $TiOSO_4$ and TMAH. After the precipitation, the coated powder was dried at 80 °C and calcined at 600 °C to transform the $Ti(OH)_4$ into the crystalline TiO_2.

The formation of the crystalline TiO_2 was verified by an XRD analysis. Figure 29 shows the XRD spectra of the TiO_2-coated Si_3N_4 powder containing 25 vol. % of TiO_2

in the starting composition after being dried at 80 °C (I) and calcined at 600 °C (II). After drying there are no visible peaks of the crystalline TiO_2 in the coated Si_3N_4 powder. XRD pattern indicates that the precipitates were either amorphous $Ti(OH)_4$ or TiO_2. After the calcinations carried out at 600 °C and for 2 h the crystal structure of anatas – TiO_2 – was detected.

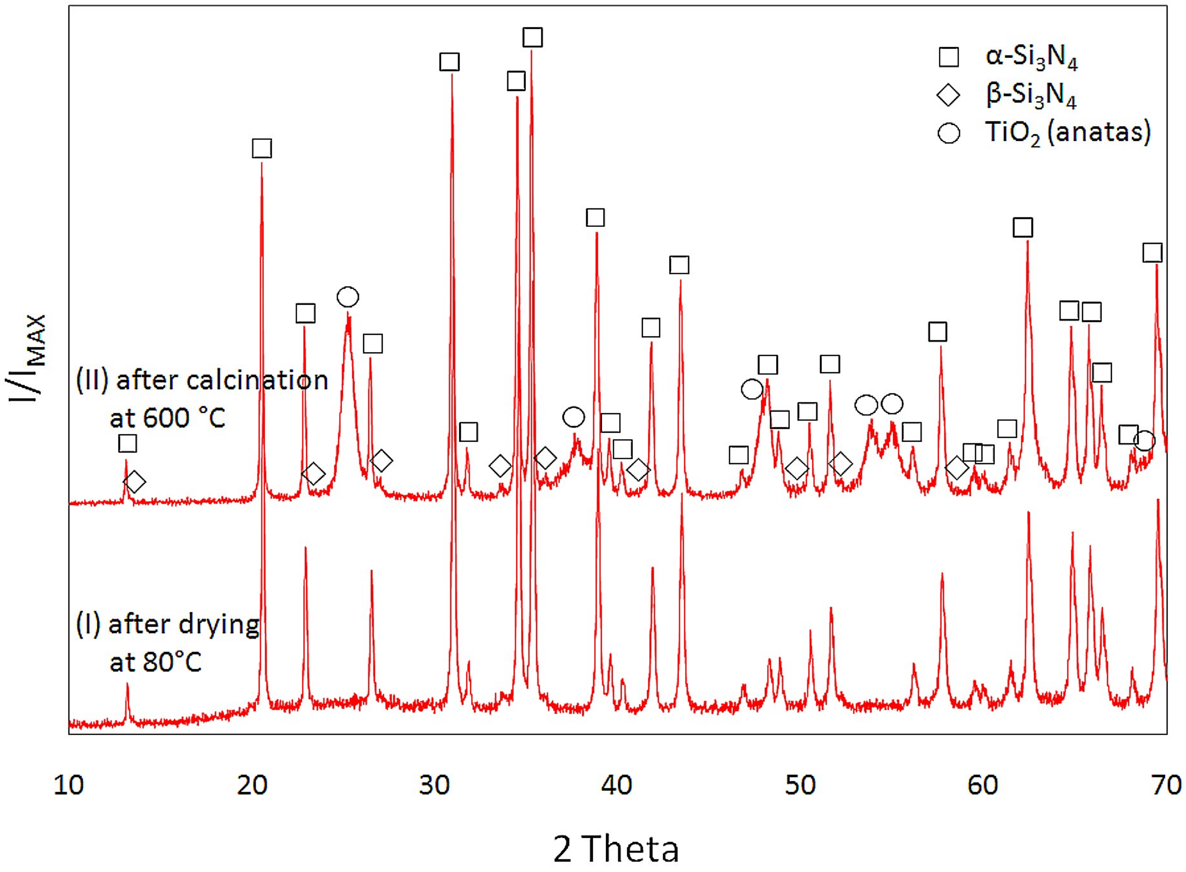

Figure 29: X-ray diffraction pattern of the TiO_2-coated Si_3N_4 powder containg 25 vol. % of TiO_2 in the starting composition: I) after drying at 80 °C and II) after calcination at 600 °C.

The XRD patterns of the TiO_2-coated Si_3N_4 powders containing various amounts of TiO_2 in the starting composition after the calcinations at 600 °C are displayed in Figure 30 showing the presence of Si_3N_4 and TiO_2. Whereby, the intensity of the latter increases with an increasing amount of TiO_2 in the starting powder mixture.

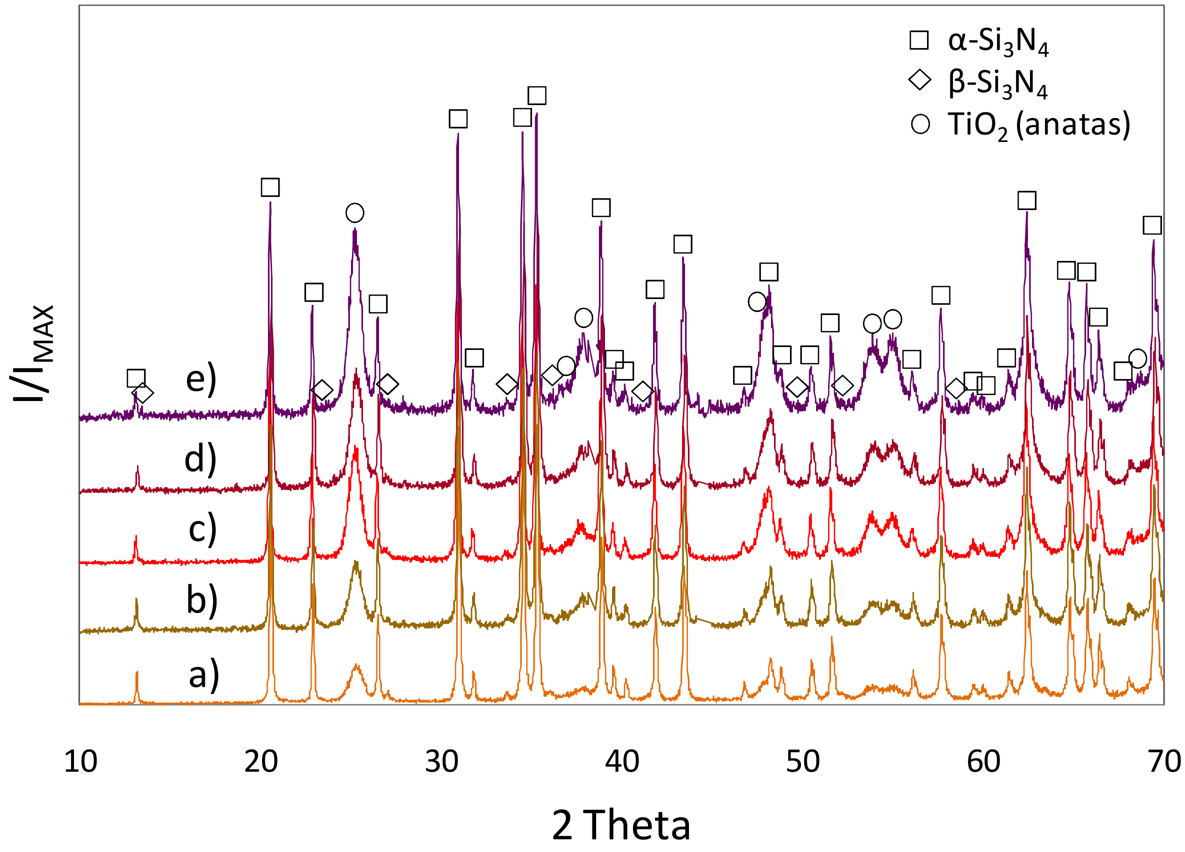

Figure 30: X-ray diffraction pattern of the coated powders after the calcinations at 600 °C for 2 h in air containing: a) 10, b) 20, c) 25, d) 30 and e) 35 vol. % of TiO_2.

The amount of TiO_2 was quantitatively determined from the x-ray diffraction patterns of the coated powders using Rietveld analyses (Table 9). The quantitative analyses showed that the amount of TiO_2 in the Si_3N_4 powders corresponds resonably well to the amount of TiO_2 in the starting composition.

Table 9: Quantitative-phase composition of the TiO_2-coated Si_3N_4 powders after the calcinations, obtained by the Rietveld analyses

Starting composition *Coated Si_3N_4 powder* TiO_2 (vol. %)	Composition after calcination *Rietveld refinement* (vol. %) Si_3N_4	 TiO_2
10	91	9
20	80	20
25	75	25
30	69	31
35	66	34

The morphology of the TiO_2-coated Si_3N_4 powders containing various amounts of TiO_2 in the starting composition was observed with the TEM and the micrographs are presented in Figure 31. It can be seen that the large Si_3N_4 particles are coated with TiO_2 nanometric particles exhibiting relatively uniform size distribution ranging from 4 to 10 nm. The average particle size of TiO_2 particles was determined from the XRD spectra of coated powders using a Scherrer equation. The results showed that the TiO_2 particles have an average particle size of 11 nm, which is in good agreement with the geometrically determined size from TEM micrographs.

The TEM images of the coated powders (Figure 31) indicate that with larger amount of TiO_2 in the starting compositions, the surface of the Si_3N_4 particles becomes completely coated with TiO_2 nanoparticles. In fact, even a larger amount of TiO_2 in the starting composition leads to a thicker TiO_2 coating on the Si_3N_4 powder surface, as displayed in Figure 31. The structure of TiO_2 was confirmed with the SAED. In Figure 31 c the SAED analysis of the coated powder containing 25 vol. % of TiO_2 (in the starting composition) revealed the anatas crystal structure of TiO_2. The simulation of the polycrystalline TiO_2 electron-diffraction pattern presented on the left-hand side of the SAED image (Figure 31 c) corresponds to the experimental electron diffraction.

This coating procedure for the preparation of the TiO_2-coated Si_3N_4 powder is comparable with the other accessible reports[32,77,78,81,83], where the main difference is that in our investigation $TiOSO_4$ was used as a new precursor for the preparation of the TiO_2 nanoparticles on the Si_3N_4 powder surface. Thus, tetra-butyltitanate (TBT)[32,80,83] and $TiCl_4$[79,81] have been the most frequently used as a raw materials for the fabrication of nano-sized TiO_2 particles. Gao et al.[32] and Kawano et al.[77] showed that by using a sol-gel or a thermal hydrolysis of these precursors the TiO_2 with a particle size of 20 nm can be easily achieved. Our coating procedure demonstrates that by using $TiOSO_4$ as a raw material, the uniform coating of TiO_2 on the surface of the Si_3N_4 powder can be successfully fabricated. Furthermore, it is believed that, in our case, the size distribution of the nano-sized TiO_2 particles is much smaller than those prepared by Gao and Kawano.

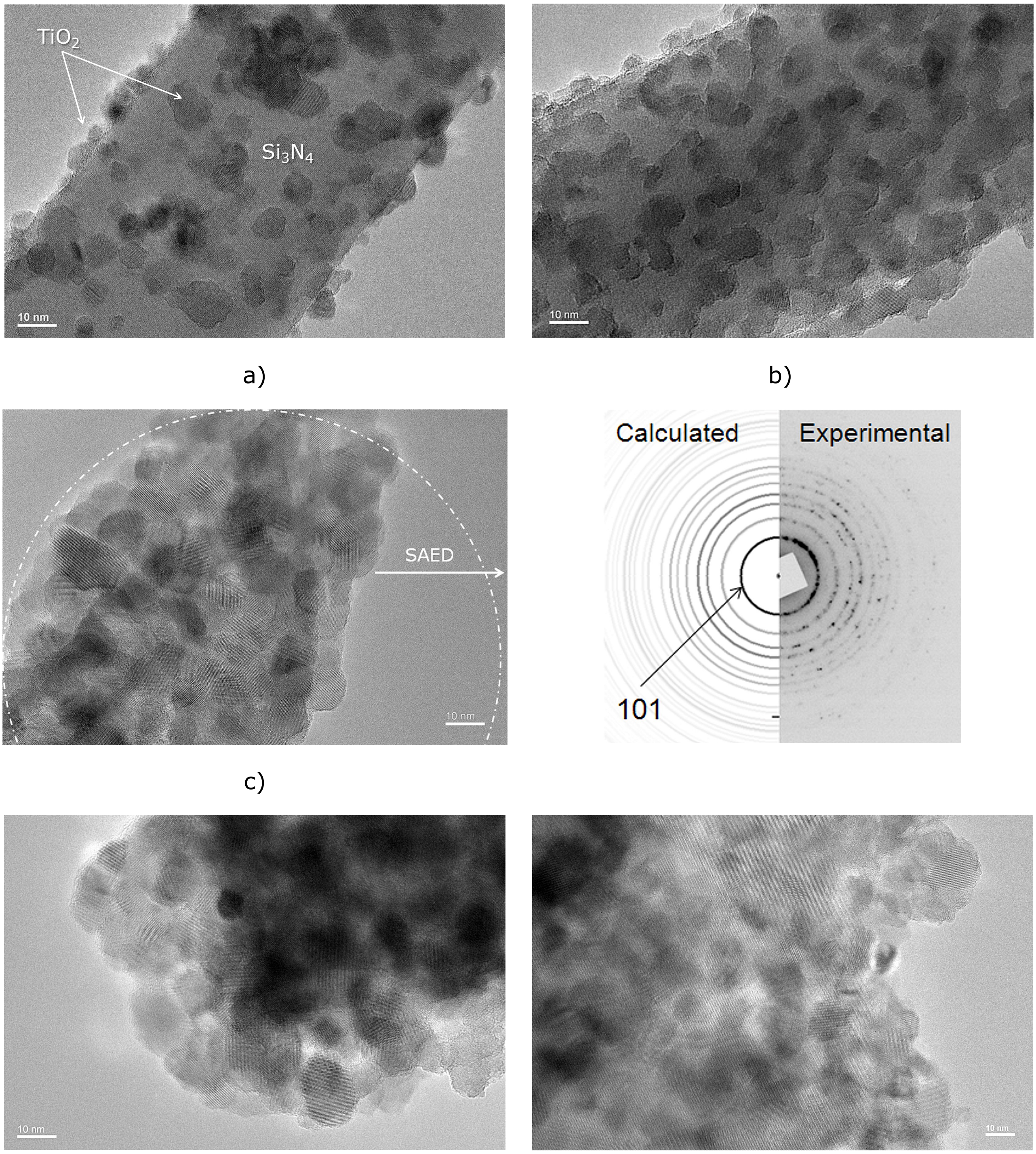

a) b)

c)

d) e)

Figure 31: TEM analyses of the TiO$_2$-coated Si$_3$N$_4$ powders after the calcinations at 600 °C for 2 h in air containing: a) 10, b) 20, c) 25, d) 30 and e) 35 vol. % of TiO$_2$. In Figure 31 c the polycrystalline electron diffraction pattern of crystals visible on bright field image is compared with the calculated electron diffraction of anatas TiO$_2$ (I4$_1$/amd) and the experimental SAED.

Nitridation of the TiO_2-coated Si_3N_4 powders

Preliminary experiments showed that the TiO_2 precipitated on Si_3N_4 powders produced from a $TiOSO_4$ was completely converted to the TiN particles after a nitridation at above 900 °C in the NH_3 gas flow. Therefore, the TiO_2-coated Si_3N_4 powder containing 10 vol. % of TiO_2 in the starting composition was nitrided under various nitridation conditions (Figure 32) in order to examine whether the nitridation of TiO_2 to TiN was complete. From Figure 32 it is clear that at a temperature of above 900 °C in the flowing NH_3, the TiN is formed from TiO_2 and NH_3 according to reaction 6 (presented on page 13). The x-ray diffraction pattern of the nitride coated Si_3N_4 powder at 900 °C for 3 h showed that the peak of TiO_2 (rutil) coexists with those of TiN (cubic) and Si_3N_4. This indicates that the TiO_2 (anatas) particles were converted to TiN, but that the nitridation reaction was not complete. When the nitridation time was prolonged by 6 h and the nitridation temperature was raised to 1000 °C (Figure 32), the conversion of TiO_2 to TiN was complete. Since the nitridation reaction is a gas solid-phase reaction with a relatively low reaction rate, it is important to ensure a long enough holding time and the required temperature to completely convert TiO_2 into TiN.

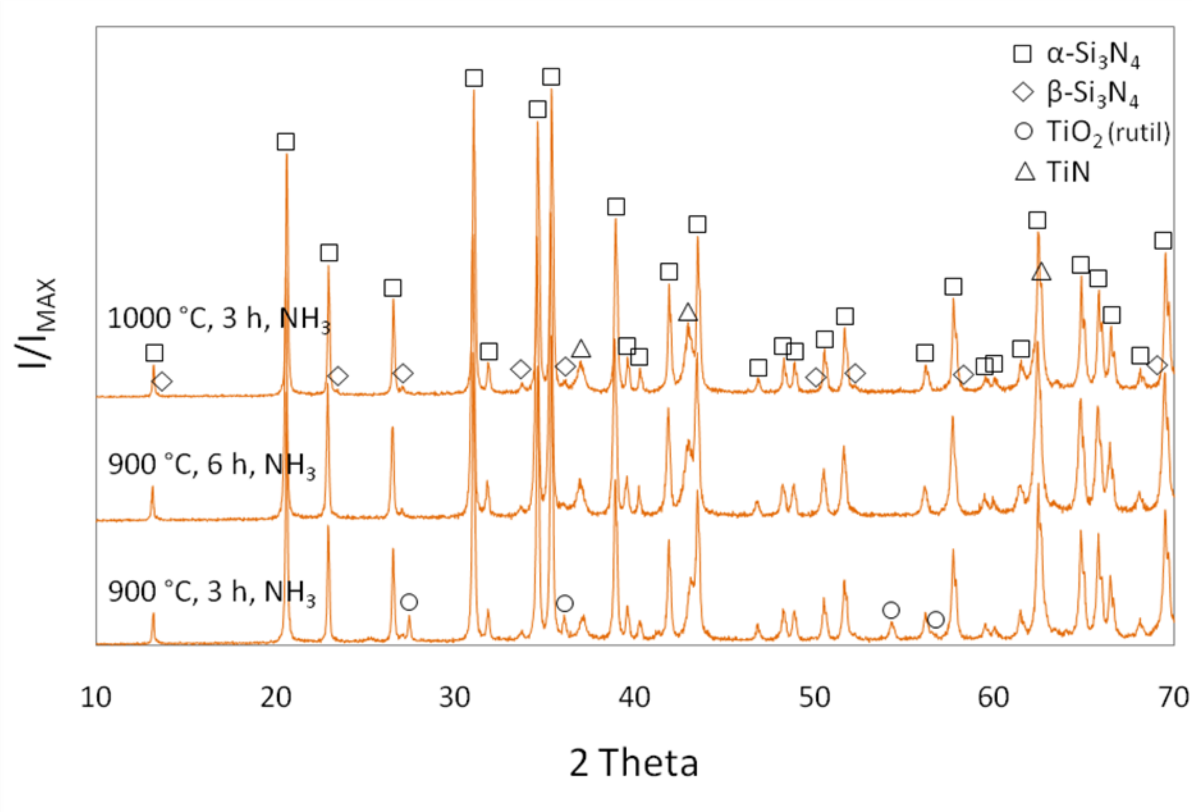

Figure 32: XRD analysis of the TiO_2-coated Si_3N_4 powder containing 10 vol. % of TiO_2 nitrided under different conditions.

In order to verify the formation and the grain growth of TiN the morphology of the nitrided coated powders was investigated. Figure 33 shows TEM images of the TiO_2-coated Si_3N_4 powders containing 10 vol. % of TiO_2 (in the starting composition) after nitridation at 900 °C for 6 h and at 1000 °C for 3 h. From TEM images it can be seen that at higher nitridation temperature the TiN nanoparticles have grown in size. The reason is that conducting the reaction at higher temperature delivers more energy into the system and increases the reaction rate leading to the larger particle size.

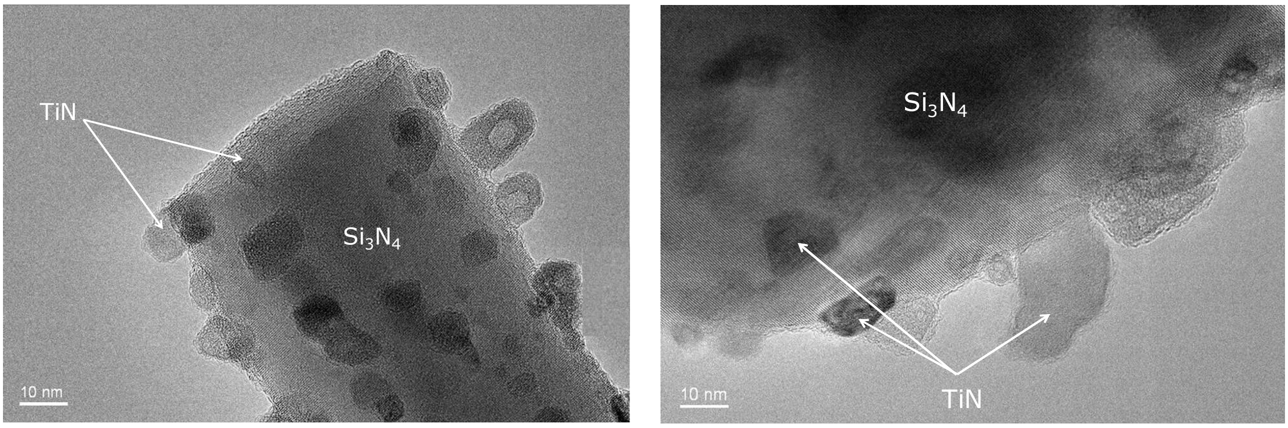

a) b)

Figure 33: TEM micrographs of the TiO_2-coated Si_3N_4 powder containing 10 vol. % of TiO_2 in the starting powder-mixture after the nitridation at: a) 900 °C for 6 h and b) 1000 °C for 3 h in the flowing NH_3.

The average size distribution of the TiN nanoparticles was geometrically defined from 5 TEM micrographs of each coated powder shown in Figure 33 and in both cases at least 20 TiN particles were measured from each image. The results revealed that the average particle size of the TiN increased from 5.9 nm at 900 °C to 12.6 nm at 1000 °C. The similar relationship between the particle size and the nitridation temperature of the nitrided TiO_2 particles prepared from TBT was shown by Li et al.[83] These authors demonstrated that the average particle sizes of the TiN powders ranging from 20 to 72 nm were obtained at different nitridation temperatures from 800 to 1100 °C for 5 h. At the nitridation temperature of 800 °C for 5 h the conversion of TiO_2 to TiN was completed, whereas the critical temperature was observed at 1000 °C, where the particle size of the TiN increased rapidly.[83] Furthermore, Gao et al.[32] confirmed that the nitridation of TiO_2 to TiN synthesized from TBT is completed at 900 °C for 5 h. When the TiO_2-coated Si_3N_4 powder was nitrided at a lower nitridation temperature or for a shorter nitridation time, the peak of TiO_2 coexisted with those of TiN and Si_3N_4.[32] However, Kawano et al.[78] showed that the nitrided

TiO_2-coated Si_3N_4 powder, prepared from $TiCl_4$, at 1000 °C for 3 h converted to the TiN particles, but the x-ray diffraction pattern revealed that the peaks of TiN were slightly shifted, meaning that the TiN contained a small amount of oxygen. In our study, we did not notice any such feature of the nitrided powders. This is probably due to the flow rate of NH_3, which was, in our case and in Gao's work[32], higher than in Kawano's study[78].

Considering the above mentioned reports, it can be concluded that in our investigation much smaller TiN nanoparticles were obtained on the Si_3N_4 powder surface for both nitridation conditions (Figure 33). The reason is that the use of $TiOSO_4$ as a precursor results in a smaller particle size of TiO_2 compared to the other applied precursors for the formation of TiO_2. Actually, we can say that starting with a smaller size distribution of TiO_2 nanoparticles leads to a smaller size of TiN particles after the nitridation reaction. It was shown that both prolonging the nitridation time and raising the nitridation temperature (Figure 32) are successful methods for producing nanocrystalline TiN particles, while the first way is appropriate for obtaining small nanoparticles.

Our investigation of the nitrided coated powders showed that the complete conversion of TiO_2 to TiN was obtained already at 900 °C for 6 h. Thus, these two nitridation parameters were used in the following for the preparation of the TiN-coated Si_3N_4 powders from the calcined TiO_2-coated Si_3N_4 powders containing various amounts of TiO_2 in the starting composition. As shown in Figure 34 the x-ray diffraction patterns of these coated powders after nitridation is presented. The results show that there is no TiO_2 present and that the nitridation reaction was completed in all samples, including the coated powder containing 35 vol. % of TiO_2 in the starting composition. It can also be seen that the peak intensity of the TiN in the Si_3N_4 powders increases with the increasing of amount of TiO_2 in the starting powder mixture (Figure 34).

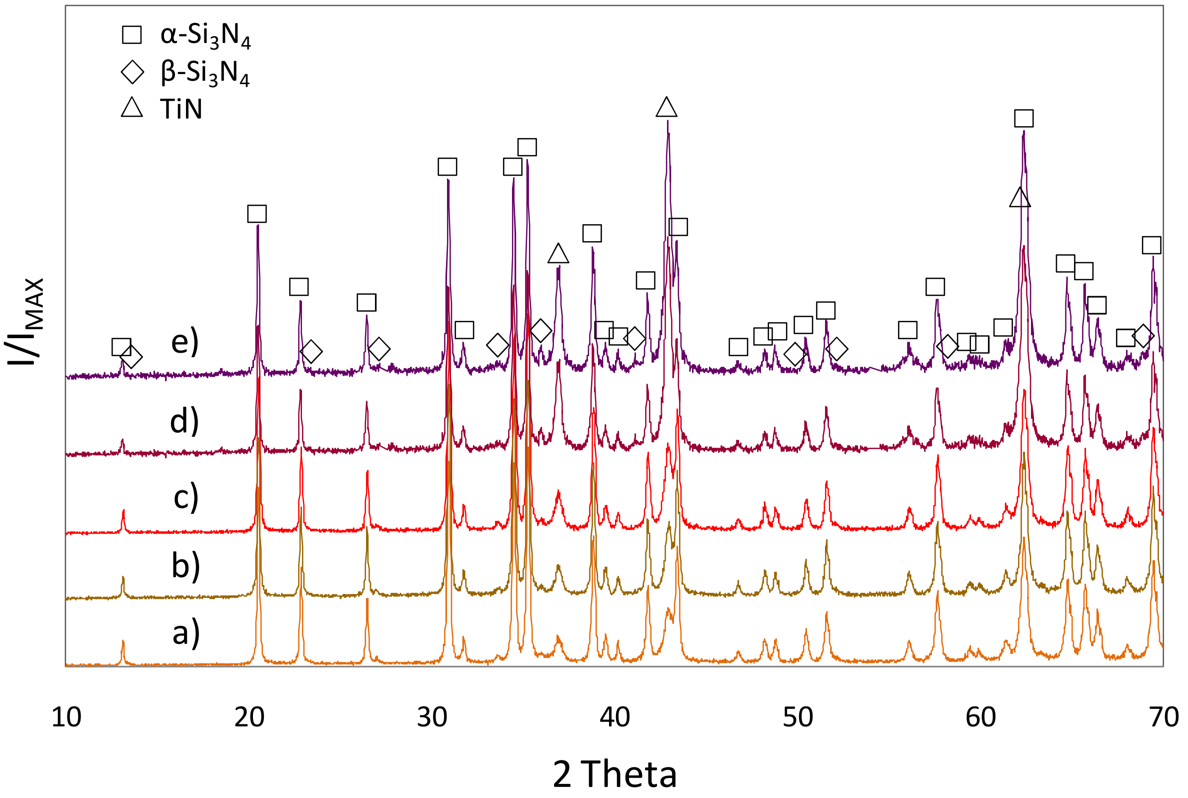

Figure 34: X-ray diffraction pattern of the coated powders after nitridation at 900 °C for 6 h in flowing NH_3 containing: a) 10, b) 20, c) 25, d) 30 and e) 35 vol. % of TiO_2 in the starting composition.

The amount of TiN in the TiN-coated Si_3N_4 powders was quantitatively determined from the x-ray diffraction patterns of the nitrided coated powders using Rietveld analysis and calculated with the proposed chemical reaction between TiO_2 and NH_3, as shown in Figure 35. For the calculated amount of TiN in the nitrided coated powders, the mass balance of the starting materials was considered in relation to reaction 6 (presented on page 13). From Figure 35 it is clear that the determined amount of TiN in the Si_3N_4 powders from the x-ray diffraction patterns of the nitrided powders corresponds well to the calculated amount of TiN from the proposed chemical reaction. This demonstrates that the calculated amount of TiN from the chemical reaction between TiO_2 and NH_3 based on the various amounts of TiO_2 in the starting composition is sufficiently correct.

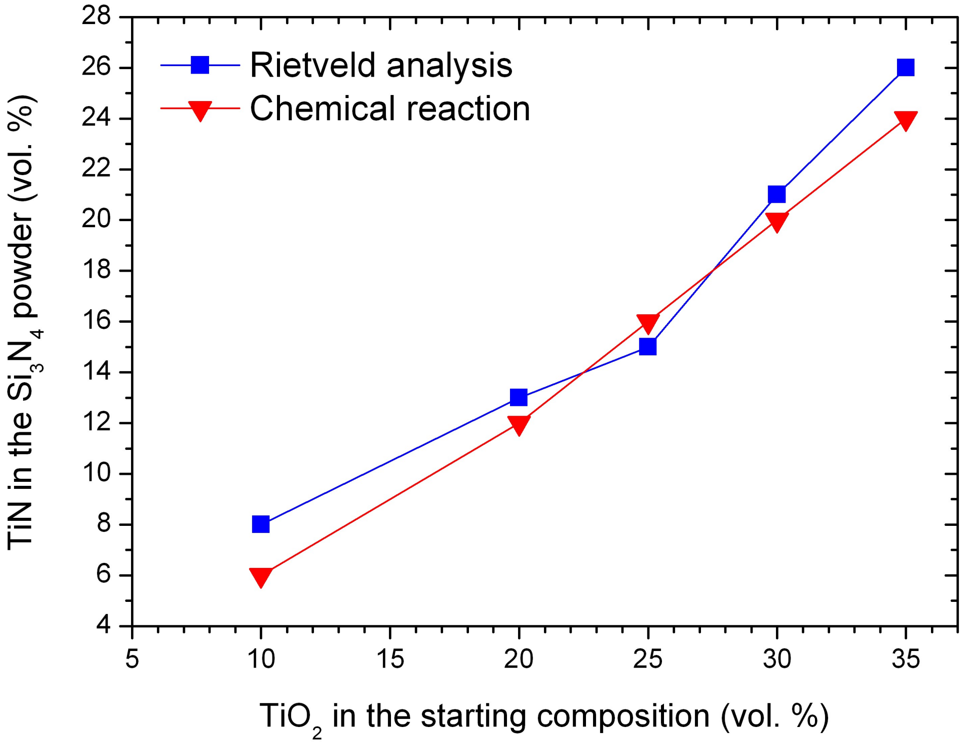

Figure 35: Amount of TiN in the TiN-coated Si_3N_4 powders versus the amount of TiO_2 in the starting powder mixture (using Rietveld analysis and chemical reaction).

The morphology of the nitride coated powders containing various amounts of TiO_2 in the starting composition after nitridation was observed by TEM (Figure 36). It can be seen that after the nitridation at 900 °C for 6 h the size of TiN nanoparticles was retained. Their morphology is relatively uniform, with the size distribution ranging from 2.5 nm to 10 nm. The average particle size of TiN particles was also determined from the XRD spectra of the nitrided powders using a Scherrer equation. The results revealed that the TiN particles have an average particle size of 16 nm, which is somewhat larger than the geometrically determined size from TEM micrographs. The reason for this difference is that when determining the size from TEM micrographs some of the largest particles can be overlooked. This average particle size of the TiN nanoparticles is 2 times smaller than the particle size of the TiN particles prepared by Gao et al.[32] and Kawano et al.[77] This can be attributed to the smaller starting size of the TiO_2 nanoparticles in the Si_3N_4 powders before the nitridation reaction. It was calculated that during the nitridation of TiO_2 to TiN, the accompanying volume shrinkage of the particles was 39.2 % due to a higher theoretical density of TiN compared to TiO_2. The nitrided coated powders containing 30 and 35 vol. % of TiO_2 (in the starting powder mixture) indicate that the surface of the Si_3N_4 powder is completely covered with nano-sized TiN particles.

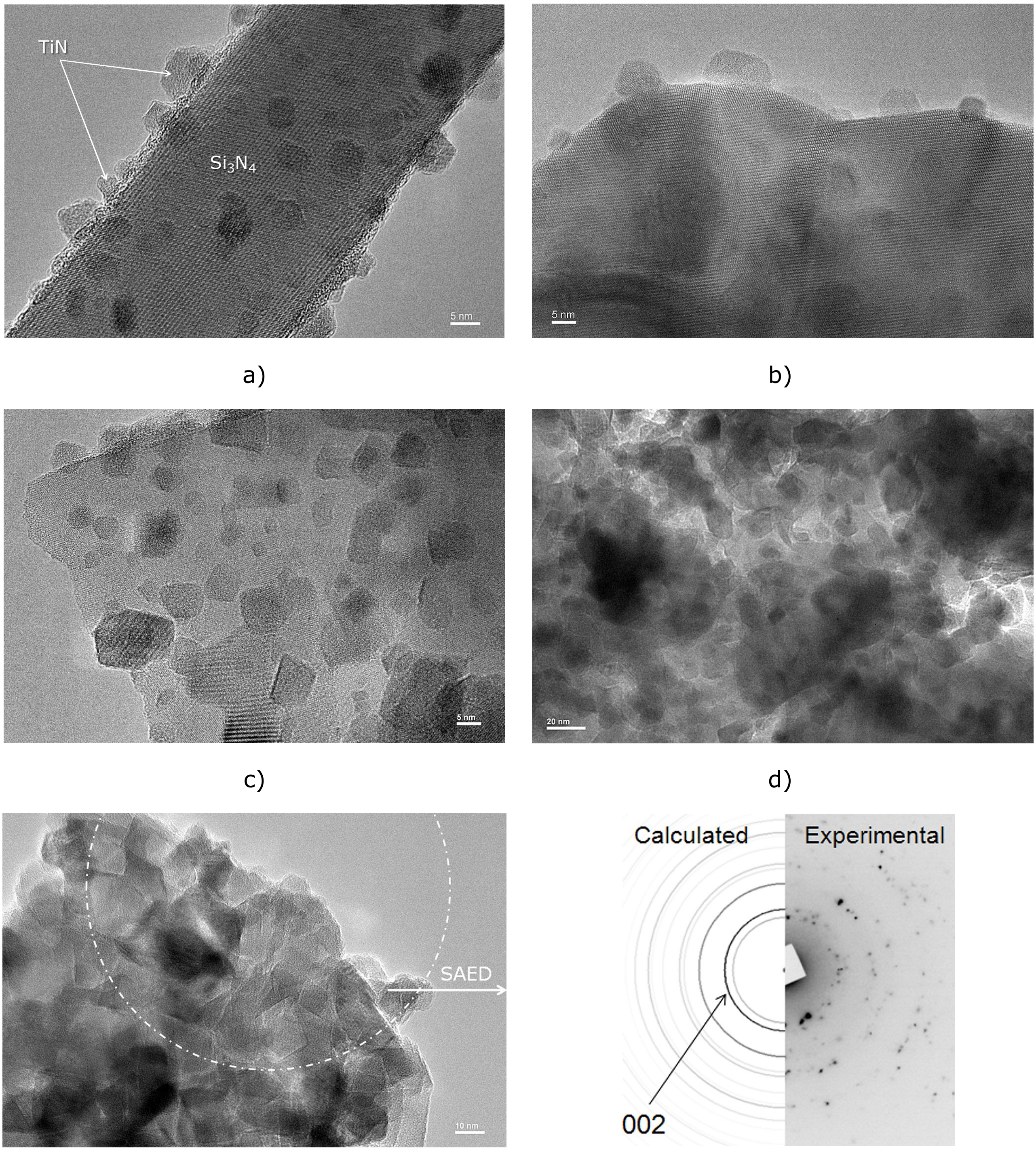

a) b)

c) d)

e)

Figure 36: TEM micrographs of TiO_2-coated Si_3N_4 powders after the nitridation at 900 °C for 6 h in flowing NH_3 containing: a) 10, b) 20, c) 25, d) 30 and e) 35 vol. % of TiO_2 in the starting composition. In Figure 36 e the polycrystalline electron diffraction pattern is inserted, where the calculated electron diffraction of cubic TiN (Fm3m) is compared with the experimental SAED.

TiN-coated Si_3N_4 powders that initially contained larger amount of TiO_2 show that some TiN particles appear to be agglomerated. Their structure was examined with

SAED (Figure 36 e), confirming the cubic TiN. The simulation of the polycrystalline TiN electron diffraction pattern presented on the left-hand side of the SAED image (Figure 36 e) corresponds well to the experimental electron diffraction. In addition, from the experimental electron diffraction besides TiN some of the Si_3N_4 reflections can be also visible.

4.2.2 Thermodynamic calculations of the chemical reaction for the formation of TiN

The Gibbs free-energy change (ΔG) for the nitridation reaction between TiO_2 and NH_3 to form TiN (reaction 6, shown on page 13) calculated on the basis of the available thermodynamic data[159] is plotted as a function of temperature in Figure 37. The calculation reveals that this reaction is energetically favourable at elevated temperatures. The TiN will be formed if the ΔG is negative, i.e., when a temperature above 1100 K is reached. From these results it can be concluded that the present results of obtained TiN-coated Si_3N_4 powders after the nitridation in NH_3 reasonably correspond well to thermodynamic calculation of the nitridation reaction.

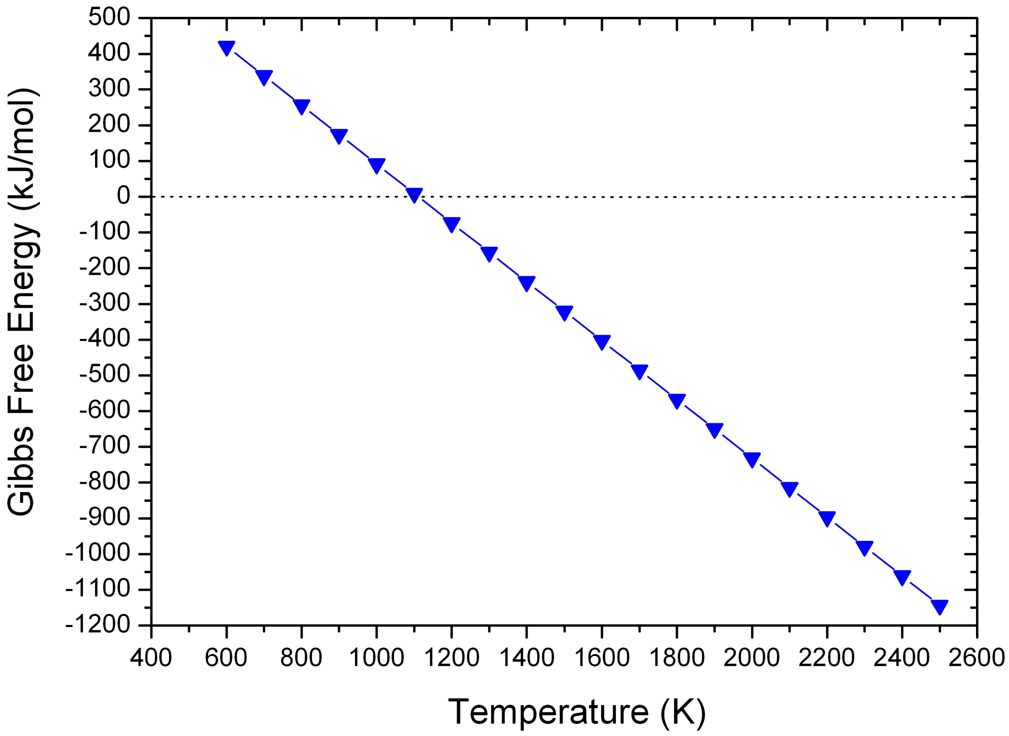

Figure 37: Calculated Gibbs free energy of reaction 6 as a function of temperature.

4.2.3 Microstructure and phase analysis of the sintered composites

To fabricate the Si_3N_4/TiN composites, the TiN-coated Si_3N_4 powders containing various amounts of TiO_2 in the starting composition were mixed with yttria and alumina additives, pressed and sintered at 1850 °C for 2 h in flowing N_2 (Figure 25, displayed on page 47). The cross-section microstructures of the sintered composites containing various amounts of TiO_2 in the starting composition shown on the left-hand side of Figure 38, indicating that all samples are homogeneous and fairly dense with uniformly distributed pores. SEM images of polished surfaces of the sintered composites that initially contain various amounts of TiO_2 in the starting composition are displayed on the right-hand side of Figure 38. Shape and size distribution of bright TiN particles are relatively homogeneously dispersed in between grey β-Si_3N_4 grains. During sintering in the presence of a liquid phase, the TiN grains coarsened and consequently the particle size grew to approximately 0.5 μm. Actually, the TiN particles have a relatively broad size distribution ranging from 0.1 to 0.8 μm. This can be attributed to the aggregation of TiN particles during sintering, especially when the samples contained larger amount of TiO_2 in the starting powder mixture, as visible in Figures 38 d & e. In an instance, when the Si_3N_4/TiN composites with and without oxide additives were prepared by HP and SPS, as shown by Gao et al.[32] and Kawano et al.[77], their situation regarding the grain growth of the TiN particles during the sintering process was similar to our situation. From that it can be concluded that even if the composites are sintered by using modern sintering techniques allowing sintering at lower temperatures (below 1700 °C) and applying high pressures (above 100 bar) it is impossible to keep all the TiN particles on a nanometric scale. The reason for the grain growth of TiN is the fact that these particles can be easily sintered to a relatively high density in the presence of yttria and alumina additives. For this reason also the particles in our system grew during sintering in the presence of the liquid phase.

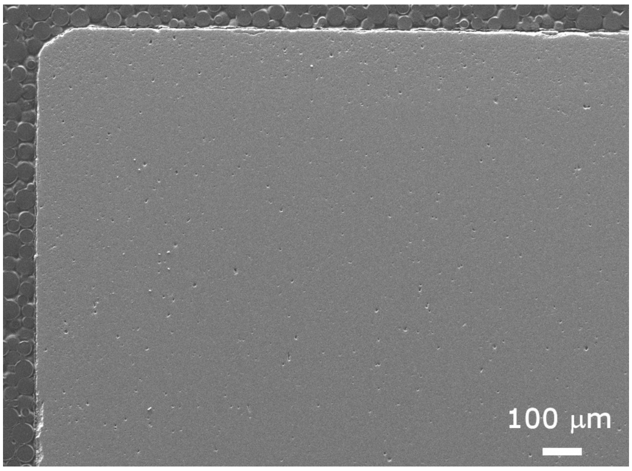

a) CS

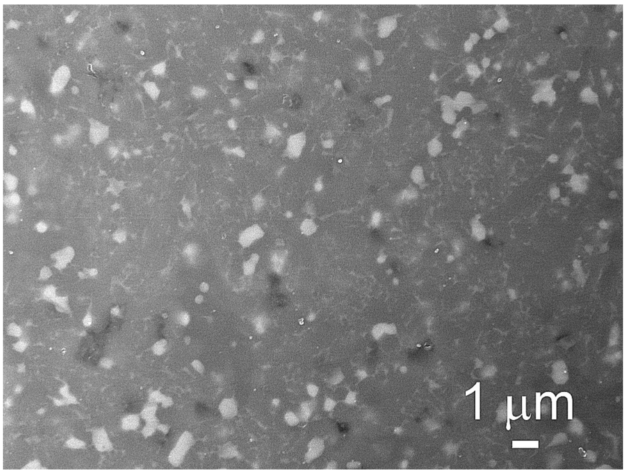

a) IP

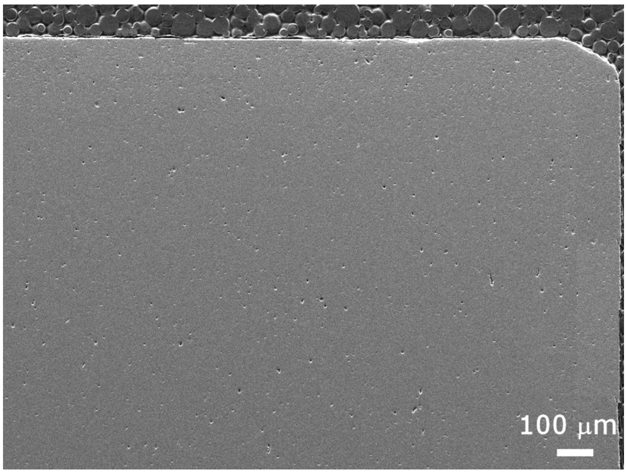

b) CS

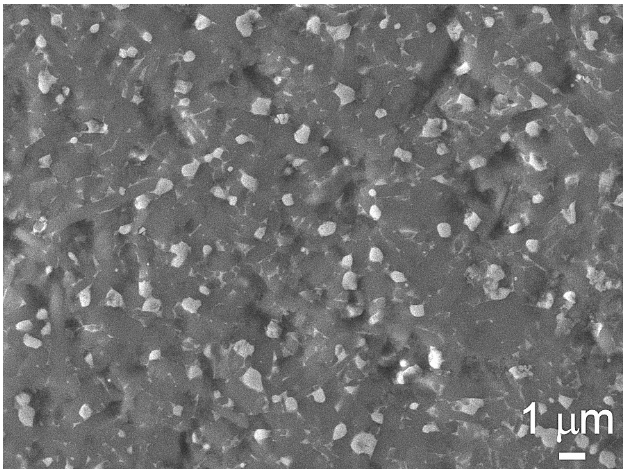

b) IP

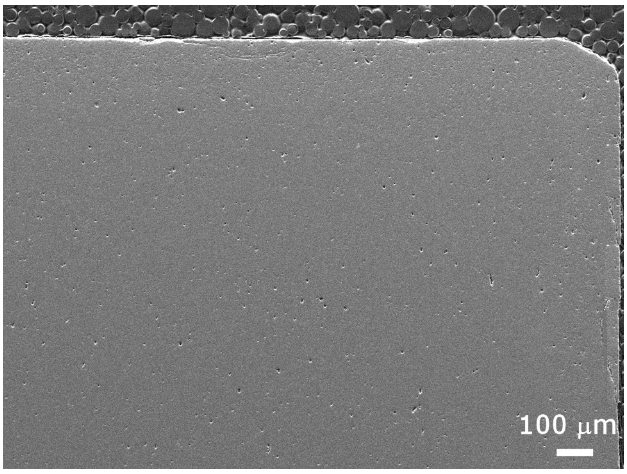

c) CS

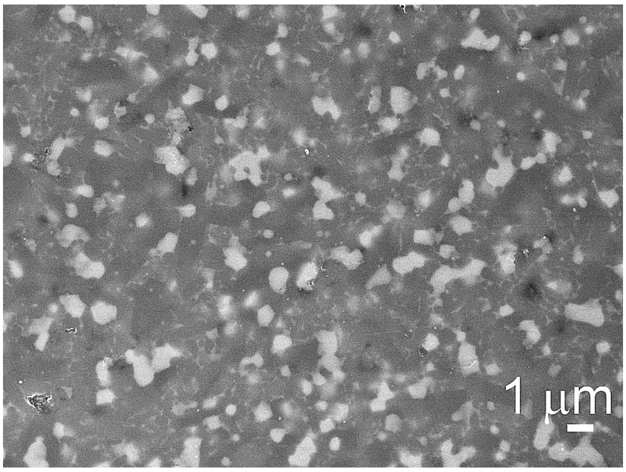

c) IP

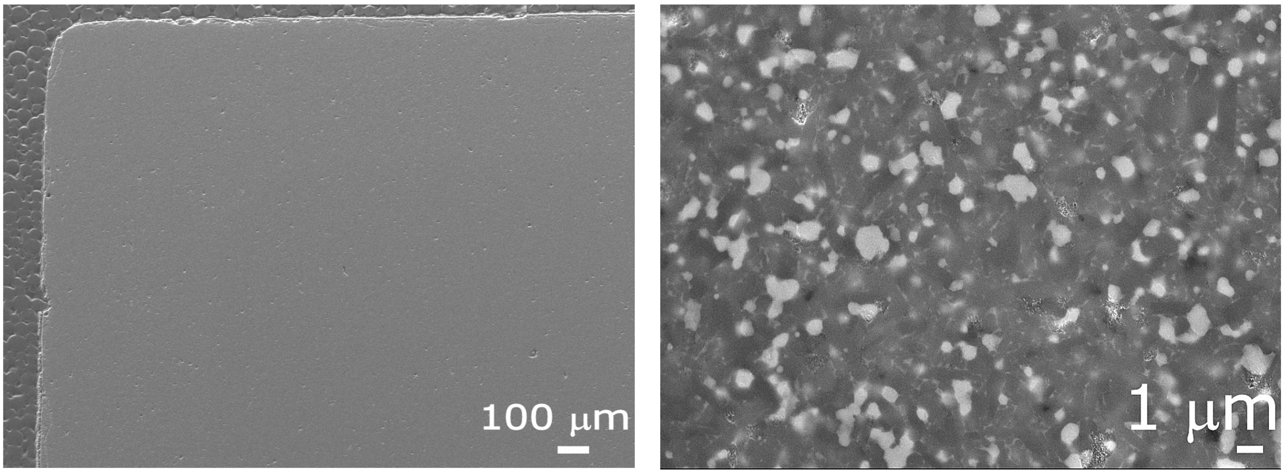

d) CS d) IP

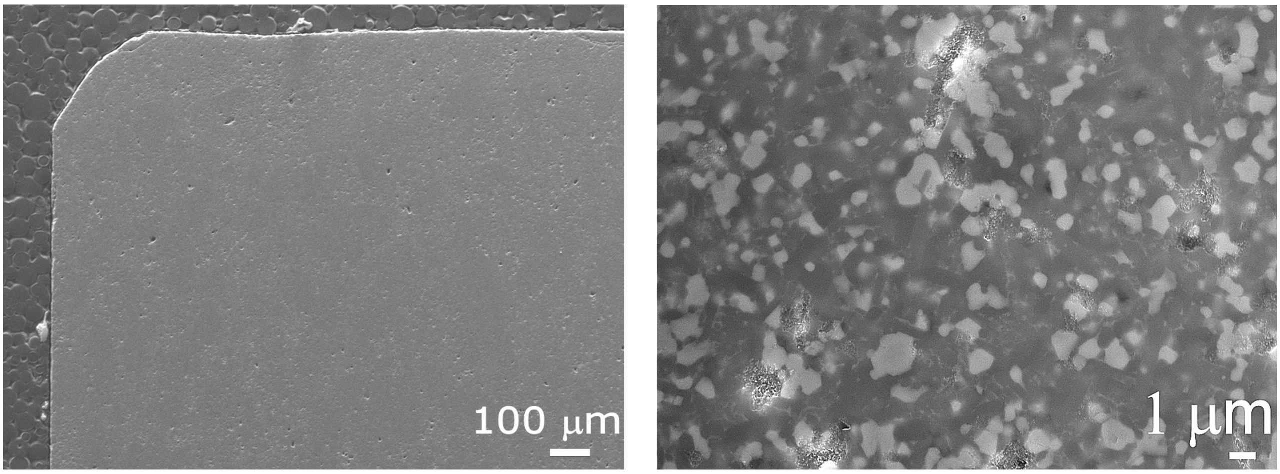

e) CS e) IP

Figure 38: Microstructures of sintered Si_3N_4/TiN composites produced from a pre-reacted powder containing: a) 10, b) 20, c) 25, d) 30 and e) 35 vol. % of TiO_2 in the starting powder mixture (cross-section images of samples are referred to as CS and internal-part images as IP).

The microstructures of the polished surfaces of the sintered samples containing 25 and 35 vol. % of TiO_2 in the starting composition are presented in Figure 39. At this magnification besides the elongated β-Si_3N_4 grains also a brighter, transient liquid phase in between the β-Si_3N_4 grains and white TiN particles can be clearly seen. We noted that the TiN particles often had irregular shapes, which strongly implies that at least some of the TiN particles grew from the liquid during cooling. The same interpretation was found in Hermann's study,[92] who reported that the TiN precipitates from the liquid phase above 1350 °C. Furthermore, the SEM analysis (Figure 39) of the samples with 25 and 35 vol. % of TiO_2 (in the starting powder mixture) revealed that some porosity is present in the composites. The composite with a 35 vol. % of TiO_2 has poor sinterability, as a consequence of a large amount of TiO_2 in the starting composition and a lower amount of the oxide additives (Table 6, presented on page 47).

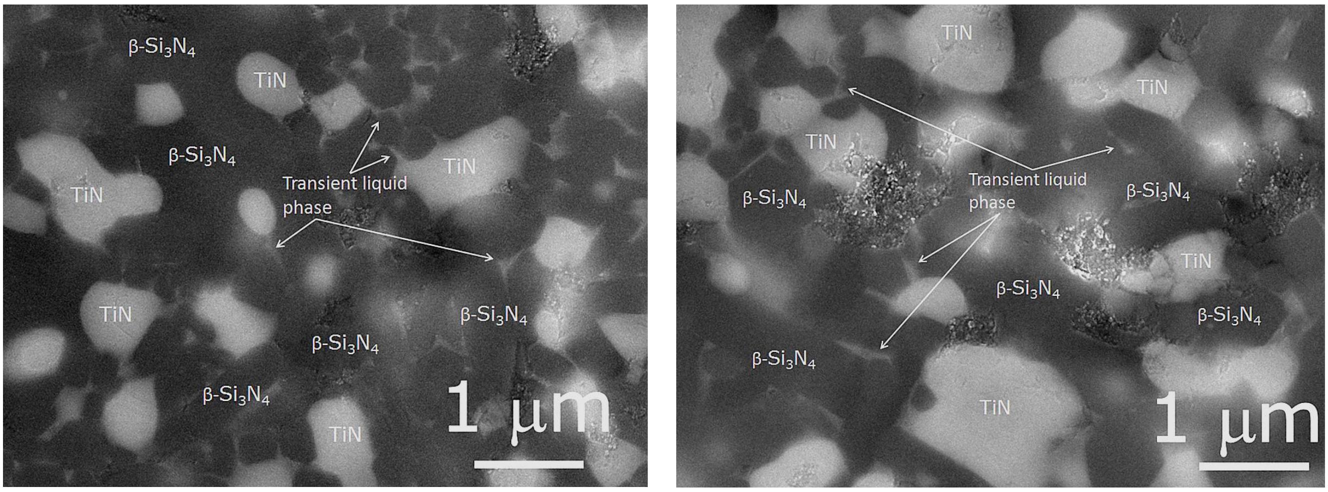

a) b)

Figure 39: SEM images at higher magnification of the sintered Si_3N_4/TiN composites at 1850 °C for 2 h in N_2, which initially contained: a) 25 and b) 35 vol. % of TiO_2 in the starting composition.

Anyway, the existence of TiN was confirmed by XRD analysis (shown in Figure 40), which revealed that the peaks of TiN coexisted with β-Si_3N_4. It is clear that with increasing the amount of TiO_2 in the starting composition the intensity of TiN increases with a simultaneous decrease of Si_3N_4.

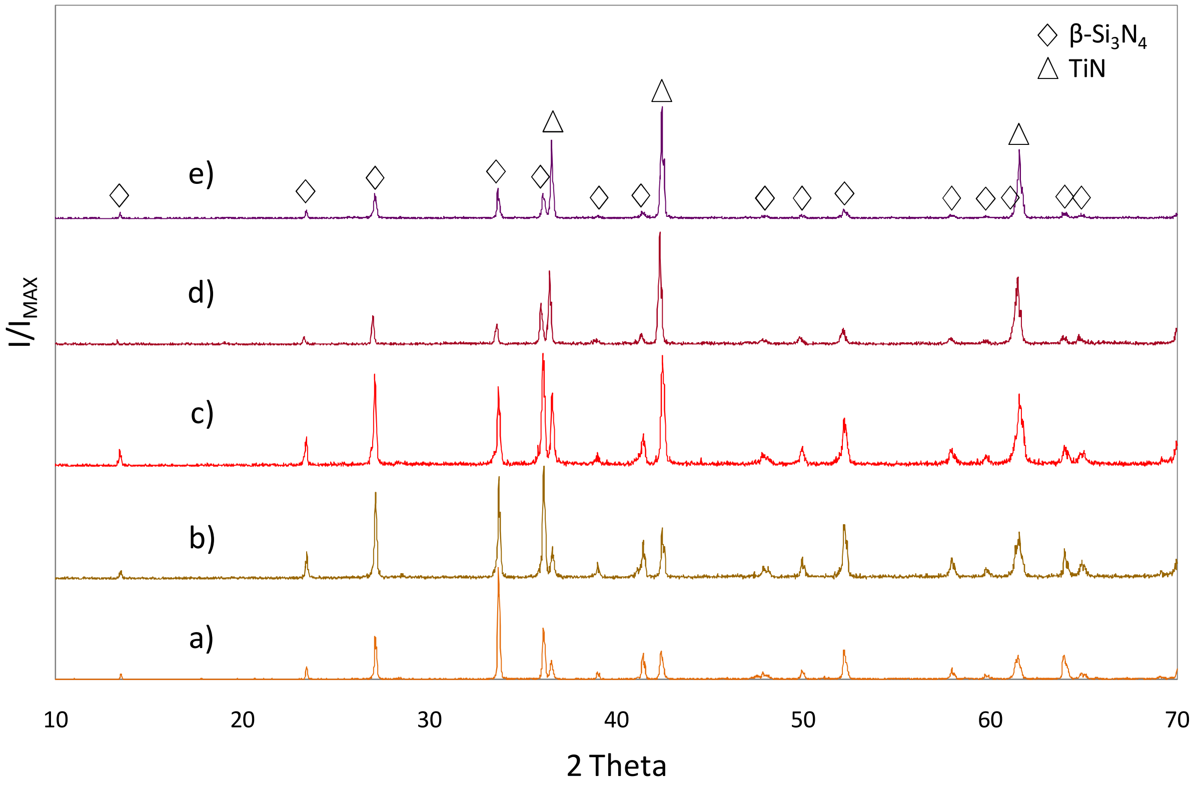

Figure 40: XRD analyses of Si_3N_4/TiN composites sintered from a pre-reacted powder containing: a) 10, b) 20, c) 25, d) 30 and e) 35 vol. % of TiO_2 in the starting powder mixture.

In order to confirm that the Si_3N_4/TiN composites are homogenous, the x-ray diffraction pattern of sintered composites containing various amounts of TiO_2 (in the starting powder mixture) was examined after a 300 μm thick surface layer was removed. The results, displayed in Figure 41, indicate that the phase analysis of the composites is entirely the same as the XRD analysis presented in Figure 40.

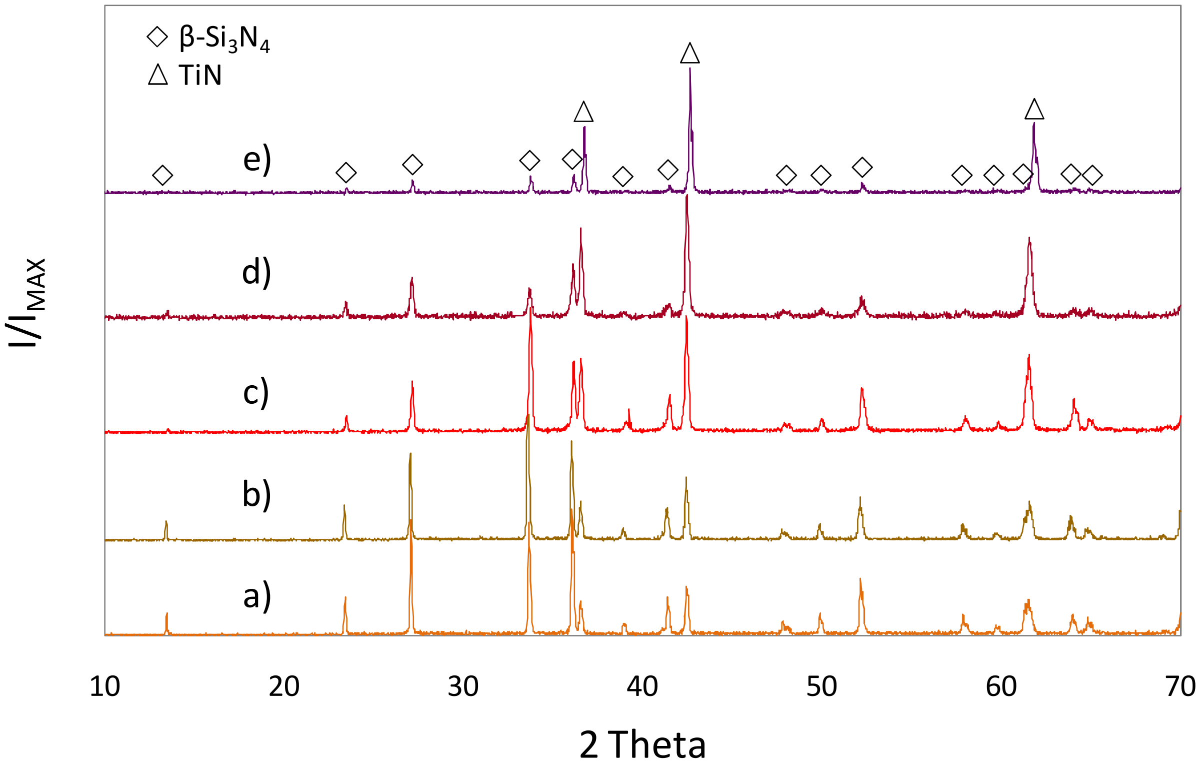

Figure 41: X-ray diffraction pattern of sintered Si_3N_4/TiN composites containing: a) 10, b) 20, c) 25, d) 30 and e) 35 vol. % of TiO_2 in the starting powder mixture after a 300 μm thick surface layer was removed.

4.2.4 Quantitative-phase analysis of TiN in the final composites

The amount of TiN in the final Si_3N_4/TiN composites containing various amounts of TiO_2 (in the starting composition) was quantitatively determined from the x-ray diffraction patterns of sintered composites using the Rietveld analysis, as shown in Table 10. The results of the Rietveld analysis of the XRD spectra of the sintered composites demonstrate that the amount of TiN corresponds well to the amount of TiN observed in the TiN-coated Si_3N_4 powder containing various amounts of TiO_2 in the starting composition displayed in Figure 35 (shown on page 63). Moreover, the estimated values of the TiN, presented in Table 10, are in a very good agreement (± 2 vol. %) with the calculated amount of TiN in the TiN-coated Si_3N_4 powders containing various amounts of TiO_2 in the starting composition, shown in Figure 35, in relation to the chemical reaction (reaction 6, presented on page 13).

Table 10: Quantitative phase composition of Si_3N_4/TiN composites containing various amounts of TiO_2 in the starting composition verified by the Rietveld analysis

Starting composition	Composition after sintering in Si_3N_4/TiN composite		
Coated Si_3N_4 powder	*Rietveld refinement* (vol. %)		
TiO_2 (vol. %)	Si_3N_4	TiN	YAG (Y_2O_3 + Al_2O_3)
10	87	8	5
20	82	13	5
25	79	16	5
30	73	23	4
35	69	27	4

For all further results the calculated amount of TiN (Figure 35) according to reaction 6 was used in the next plotted graphs. The reason is that the calculated values of TiN obtained by the nitridation reaction of TiO_2 to TiN are more accurate than the determined values of TiN verified by the Rietveld analysis of the x-ray diffraction patterns.

4.2.5 Influence of the amount of conductive phase of the Si_3N_4/TiN composites on density, flexural strength and electrical conductivity

The change in the relative density and flexural strength of the Si_3N_4/TiN composites is shown as a function of the TiN content in Figure 42. The relative density and flexural strength decrease with increasing TiN content in the composite. The composite with 6 vol. % of TiN exhibits the highest relative density of 98.3 % with a relatively high flexural strength of 615 MPa. A further increase in the TiN content resulted in decreasing relative density and flexural strength. At 24 vol. % of TiN the relative density was only 91.1 % and the corresponding flexural strength dropped to 360 MPa. In the literature, only a few reports[32,77,78,160] on the preparation of the Si_3N_4/TiN composites fabricated from TiN-coated Si_3N_4 powder by using modern sintering techniques (HP or SPS) were found, indicating the change in relative density of these composites as a function of the TiN content. Kawano et al.[77,78] showed that the relative density of Si_3N_4/TiN composites prepared by SPS without using sintering additives sharply increases with increasing TiN content from the relative density of 55 % at 10 vol. % of TiN to 93 % at 30 vol. % of TiN. In addition, these authors also indicated that when the composites were prepared by SPS from TiN-coated SiAlON powder than the sinterability of SiAlON/TiN composites is similar to our results, shown in Figure 42. This strongly implies that if the oxide additives such as Y_2O_3 and Al_2O_3 are present already in the SiAlON structure[78] or are added to the starting powder mixture as in our work than the material can attain high theoretical density already at 10 vol. % of TiN irrespective to applied sintering technique. However, in our study the relative density and flexural strength of the Si_3N_4/TiN composites (Figure 42) decrease with increasing TiO_2 content in the starting composition. The reason is that at larger amounts of TiO_2 in the starting powder mixture a lower amount of oxide additives is present in the powder mixture (Table 10), which consequently after sintering results in a lower relative density and flexural strength.

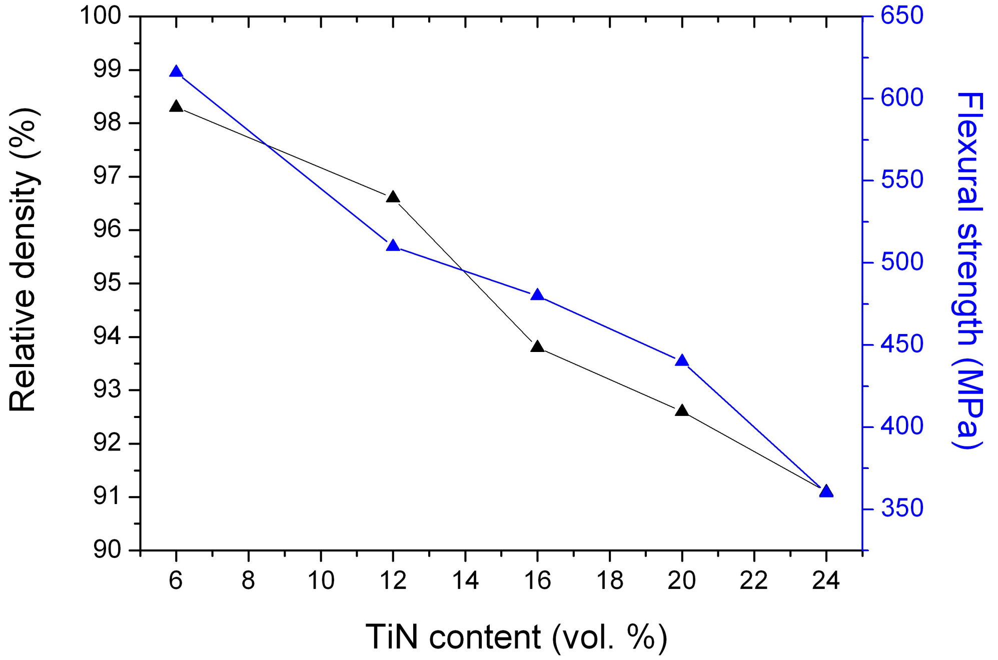

Figure 42: Change in the relative density and flexural strength of Si_3N_4/TiN composites with various TiN contents sintered at 1850 °C for 2 h in N_2.

Furthermore, Gao et al.[32] was the only one group who indicates that the flexural strength of Si_3N_4/TiN composites was measured. In this case the composites were hot pressed in the presence of yttria and alumina additives at 1650 °C with a pressure of 300 bar for 1 h in N_2. The prepared Si_3N_4/TiN composite with 20 vol. % of TiN exhibited the flexural strength of 1154 MPa which is much higher than the flexural strength of our composite (440 MPa) with the same TiN content. Sintering at high-pressure obviously results in higher relative density and flexural strength.

The electrical conductivity of the Si_3N_4/TiN composites as a function of the TiN content is presented in Figure 43. The electrical conductivity of the composites increases sharply from 7 x 10^{-9} $\Omega^{-1}m^{-1}$ at 6 vol. % of TiN to 3.6 x 10^{3} $\Omega^{-1}m^{-1}$ at 24 vol. % of TiN. These experimental results showed that the Si_3N_4/TiN composites prepared from the pre-reacted powders had a good electrical conductivity. The percolation threshold for the electrical conductivity of these composites was obtained at 12 vol. % of TiN content (Figure 43), which is two times lower than in the case of composites prepared using a conventional composite method from mechanically mixed powders[15].

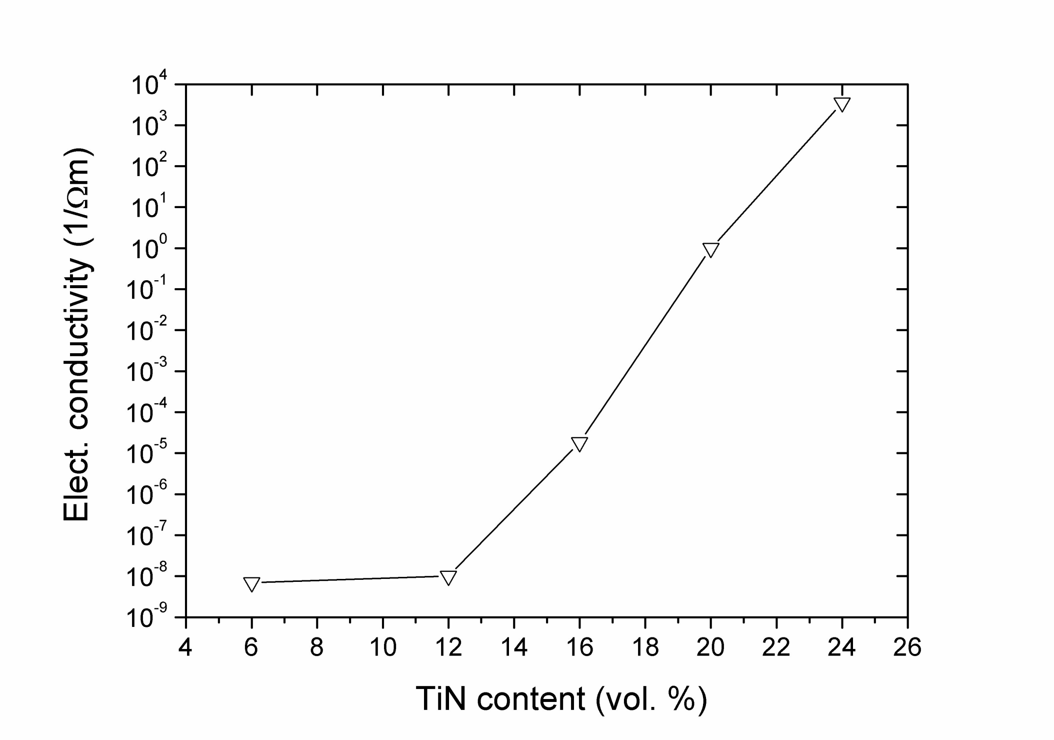

Figure 43: Change in electrical conductivity of Si_3N_4/TiN composites with the TiN content.

The electrical conductivity of the composite containing 24 vol. % of TiN (Figure 43) was 3.6 x 10^{3} $\Omega^{-1}m^{-1}$, higher by a factor of 4 than in the case of the composites prepared by Gao et al.[32] and sintered by HP, and lower, by a one order of magnitude, than in the case of the ones fabricated by Kawano et al.[77] that were sintered by SPS and contained the same amount of TiN. This can be explained by the formation of an electrically conductive network of the TiN phase within the Si_3N_4 matrix and the distribution of TiN. This composite prepared from the pre-reacted powder (Figure 25, presented on page 47) have a high electroconductivity, making it suitable for the production of heating elements.

4.2.6 A simple theoretical percolation-threshold model

A simple model of the percolation threshold in the case of small conducting grains, as compared to anisotropic insulating grains, was performed in order to explain the experimental facts of the sintered Si_3N_4/TiN composites including the proper TiN content for percolation threshold of electrical conductivity and the size of TiN particles. The simple theoretical percolation-threshold model is thoroughly described in an appendix (page 142). The volume fraction of the conducting phase (percolation threshold) as a function of the particle size (diameter) of the conductive particles, shown in Figure 44, was calculated using our proposed simple theoretical percolation-threshold model. The volume fraction of the conducting phase as a function of the particle size of the conductive phase varies with the aspect ratios of the insulating ellipsoids. In our model the aspect ratio of the insulating ellipsoids varies regarding 2a axis from 0.6 μm to 1.4 μm and regarding 2c axis from 4 μm to 10 μm, as presented in Figure 44.

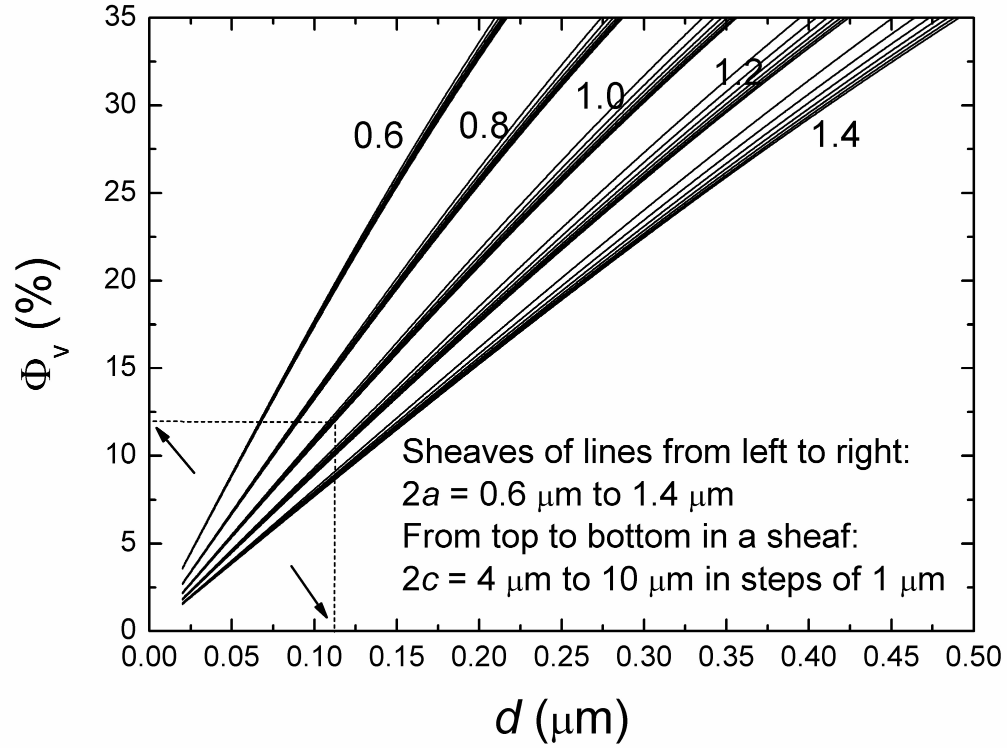

Figure 44: Calculated percolation threshold for the proposed model in the Si_3N_4/TiN system considering various aspect ratios of the insulating ellipsoids as a function of the diameter of the conductive particles.

It can be seen that the percolation threshold for electrical conductivity is much dependent on the size distribution of conductive particles between insulating, nonconductive grains. Figure 44 indicates that with an increase of the particle size of the conductive particles, the percolation threshold increases as well. Furthermore, the percolation threshold decreases with the lowering of the aspect ratio of the insulating ellipsoids at the defined particle size of the conductive phase. In order to do so, the following parameters were used: the aspect ratio of the elongated β-Si_3N_4 grains in the Si_3N_4/TiN composites was estimated from the SEM micrographs and was 5, and the experimental percolation threshold of this system was 12 vol. % of the TiN content. These experimental values were plotted in the graph presented in Figure 44 (see the arrow points). The result of our model indicates that by considering this percolation threshold value and aspect ratio of the insulating grains, the particle size of the TiN is 110 nm, as denoted with the arrow points in the Figure 44. The size of the TiN particles in our sample was confirmed by the geometrically evaluated size distribution of the TiN particles from the 2D SEM micrograph (Figure 45) and TEM images (Figures 46 & 47) of the Si_3N_4/TiN composite, which initially contained 30 vol. % of TiO_2 in the starting composition. Figure 45 shows that this composite exhibits a wide size distribution of the TiN particles, where most of these particles have an average particle size from 83 nm to 187 nm.

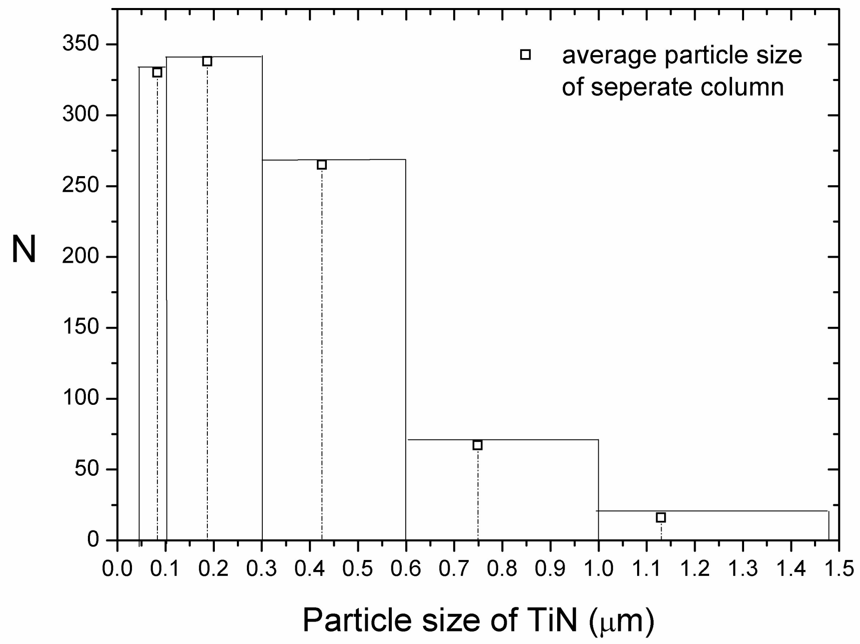

Figure 45: Evaluated number of TiN particles in the Si_3N_4/TiN composite containing 30 vol. % of TiO_2 in the starting composition versus their size distribution.

The nanosized TiN particles are also visible from the TEM analysis of this composite shown in Figures 46 & 47. Figure 46 shows that the TiN particles can be present in between Si_3N_4 particles or are incorporated within the Si_3N_4 particles. It is completely reasonable that if the TiN particles are incorporated within the Si_3N_4 particles their nanometric size will be preserved. This indicates that the nanosized TiN particles remain spherical, whereas the larger ones obtain an irregular form due to the grain growth and the aggregation of the TiN during sintering. All the denoted phases in Figure 46 were confirmed by EDXS.

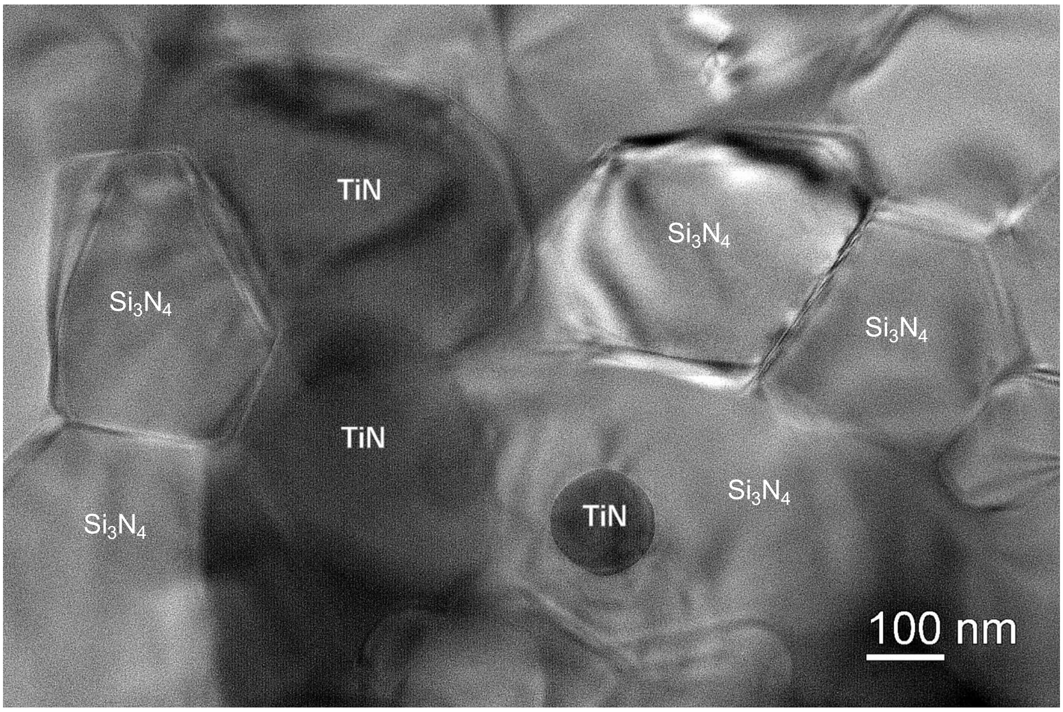

Figure 46: TEM micrograph of the Si_3N_4/TiN composite containing 30 vol. % of TiO_2 in the starting composition after sintering at 1850 °C for 2 h in N_2.

The nanosized TiN particles were found in the contact where the grain boundary between the Si_3N_4 grains is present, as displayed in Figure 47. Their particle size is very small – around 100 nm. This means that the particle size of the TiN with regard to the 2D SEM micrograph and the TEM image of the composite, which initially contained 30 vol. % of TiO_2 in the starting composition, is in good agreement with the results of the simple theoretical percolation-threshold model. Their existence of the nanosized TiN particles was confirmed by the EDXS analysis presented in Figure 48 a. The EDXS spectrum of the analyzed nanometric particle, displayed in Figure 48 a, (see the arrow denoted as EDXS A in Figure 47) shows the signals of Ti and N containing a trace of Si, which comes from the vicinity since the TiN is surrounded by Si_3N_4. Moreover, the transient liquid phase, shown in Figure 47 (see the arrow denoted as EDXS B) was analyzed at a triple point. The EDXS spectrum, displayed in Figure 48 b, shows strong signals of O, Si and Y, and weak signals of Al, Ti and N. The formation of a transient liquid phase during cooling from the sintering temperature should be described with Equation 1:

$$\alpha\text{-}Si_3N_4 + SiO_2 + M_XO_Y \rightarrow \beta\text{-}Si_3N_4 + \text{M-Si-O-N phase}$$

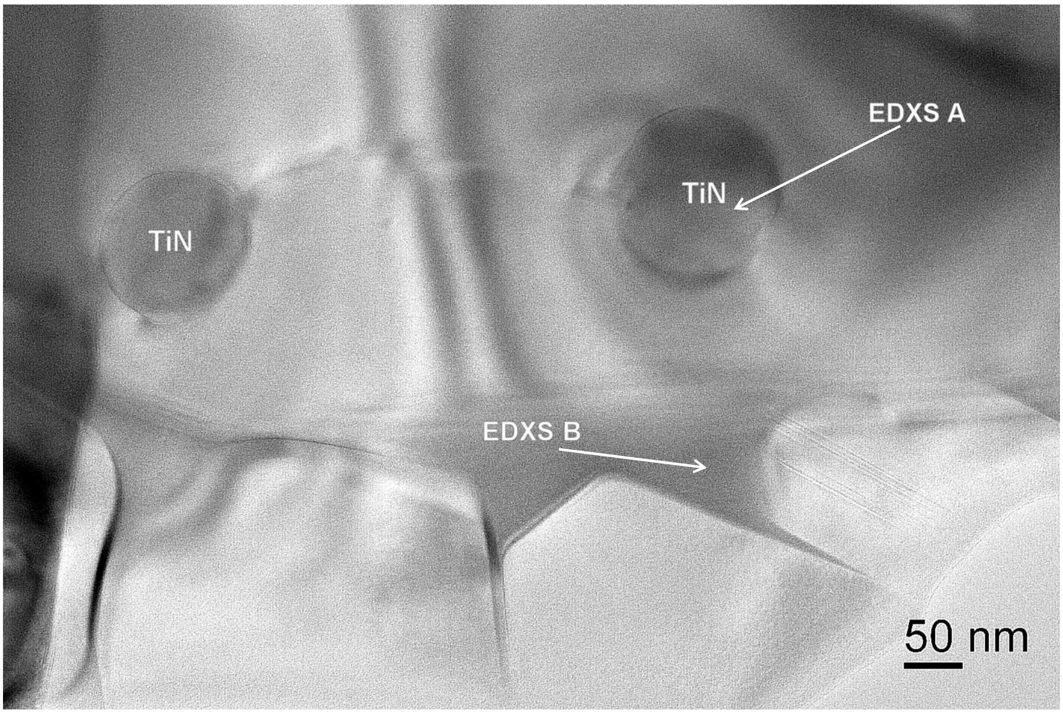

Figure 47: TEM image of the sintered Si_3N_4/TiN composite containing 30 vol. % of TiO_2 in the starting composition.

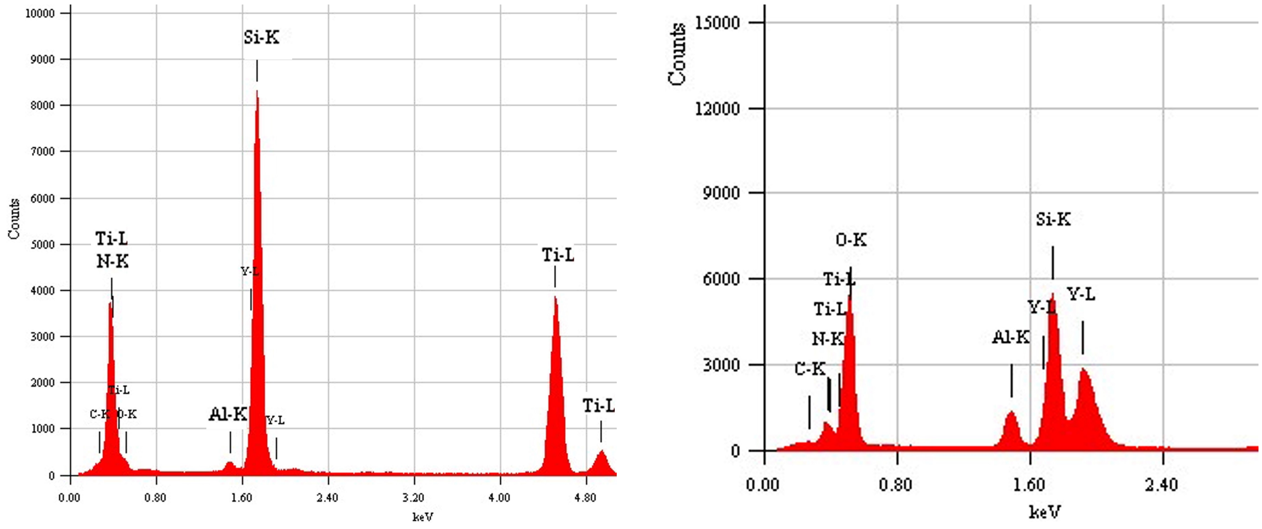

a) b)

Figure 48: EDXS analysis of the sintered Si_3N_4/TiN composite with 30 vol. % of TiO_2 detected as shown in the previous figure: a) EDXS A and b) EDXS B.

4.3 Si_3N_4/ZrN composites

4.3.1 Coating of the Si_3N_4 powder

Preparation of the ZrO_2-coated Si_3N_4 powders

The ZrO_2-coated Si_3N_4 powders containing 10, 20, 25, 30 and 35 vol. % of ZrO_2 nanoparticles in the starting powder mixture were prepared by an in-situ gel precipitation. The zirconia hydroxides ($Zr(OH)_4$) were precipitated on the surface of the Si_3N_4 powder using a zirconium acetate suspension and ammonia. After the precipitation, the powders were dried at 80 °C and subsequently calcined at 600 °C to transform the $Zr(OH)_4$ to crystalline ZrO_2.

In order to determine the appropriate experimental conditions, for effective precipitation of ZrO_2 the precipitation at various pH values was performed and the structure after calcinations was verified by XRD. Figure 49 shows the XRD spectrum of the calcined ZrO_2-coated Si_3N_4 powder containing 10 vol. % of ZrO_2 precipitated at various pH values. From this XRD analysis it is impossible to distinguish between a cubic and tetragonal crystal structure of ZrO_2. Since it was later confirmed by the SAED analysis that the crystal structure of these particles is cubic ZrO_2, the intensity of the ZrO_2 (111) cubic peak at $2\ \theta = 30.126°$ was compared for samples precipitated at various pH values. The results demonstrated that the precipitation of the ZrO_2 starts already at pH 4.5. This was also shown by Marinšek et al.[161] and Wang el al.[162], who synthesized ZrO_2 nanoparticles from sol-gel by using $ZrCl_4$ and NH_3. Further increasing of the pH leads to an increase in the intensity of the ZrO_2 peak and reaches a maximum at pH 7.0 (Figure 49). After this pH the intensity of the ZrO_2 does not change any more (slightly decreases), which indicates that at pH 7.0 the precipitation of ZrO_2 is finished.

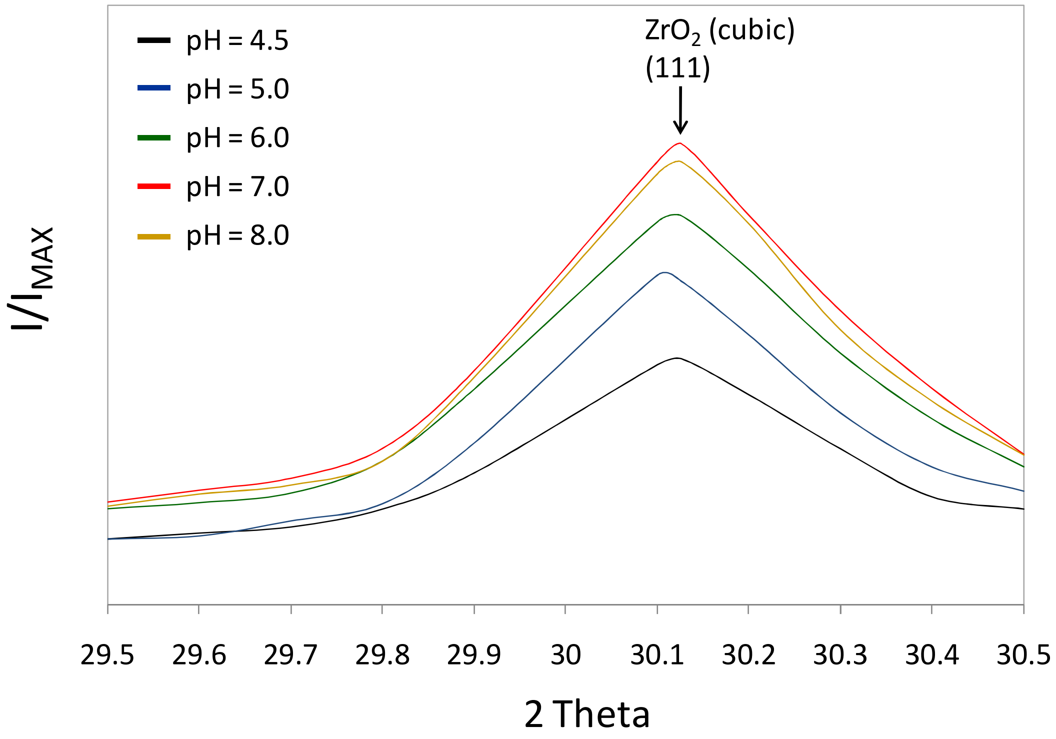

Figure 49: XRD spectrum of the calcined ZrO_2-coated Si_3N_4 powder containing 10 vol. % of ZrO_2 analysed in the 2 θ range from 29.5 to 30.5 ° precipitated at different pH values.

Therefore, we used this pH for the coating procedure. Figure 50 indicates the x-ray diffraction pattern of the ZrO_2-coated Si_3N_4 powders containing various amounts of ZrO_2 in the starting composition after the calcinations at 600 °C. It is clear that with an increasing ZrO_2 content in Si_3N_4 powder mixture the intensity of the ZrO_2 peaks increases as well.

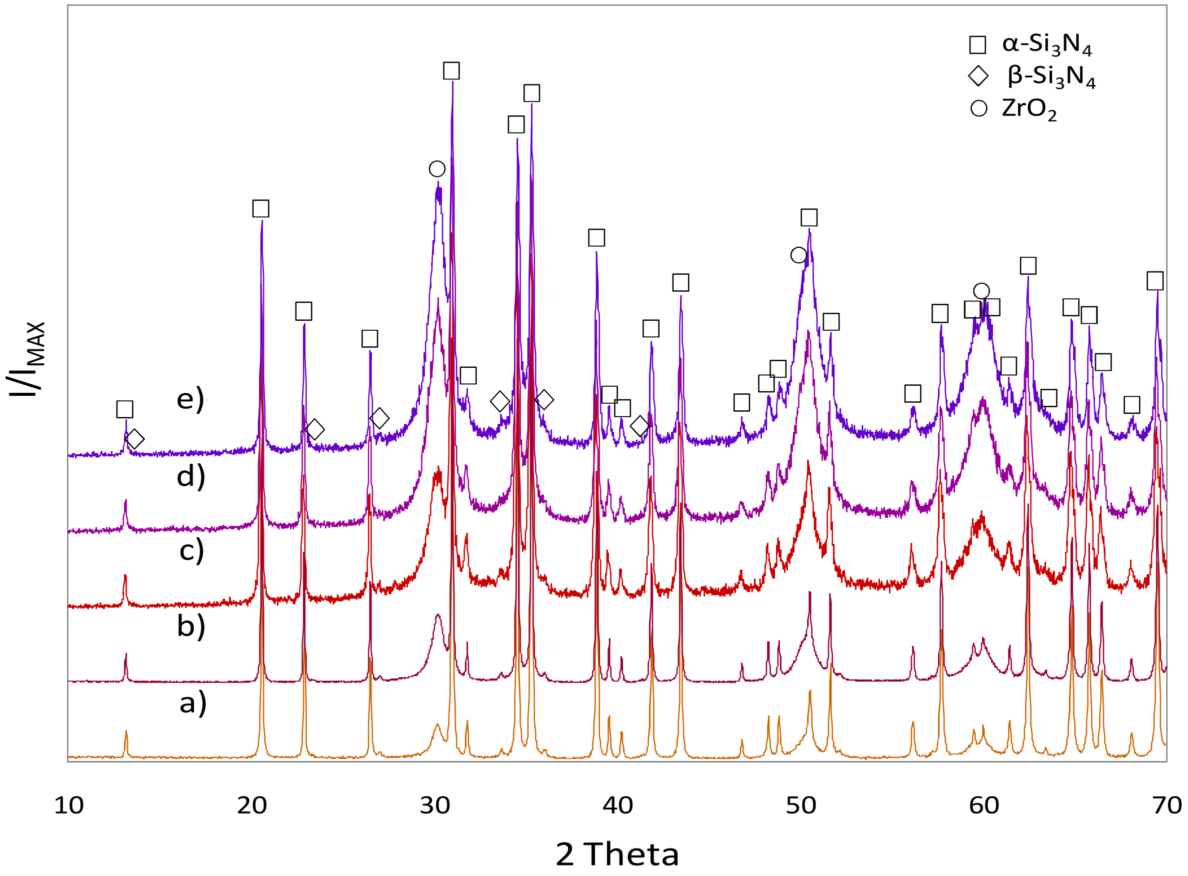

Figure 50: X-ray diffraction pattern of coated powders after the calcinations at 600 °C for 2 h in air containing: a) 10, b) 20, c) 25, d) 30 and e) 35 vol. % of ZrO_2.

The amount of ZrO_2 was quantitatively determined from the x-ray diffraction patterns of coated powders using Rietveld analysis (Table 11). The quantitative analysis showed that the determined amount of ZrO_2 in the Si_3N_4 powders is somewhat lower compared to the amount of ZrO_2 in the starting composition. The samples that initially contain larger amounts of ZrO_2 (in the starting powder mixtures) exhibit a higher deviation of the ZrO_2 content determined from the Rietveld analysis of the XRD spectrum of the coated powders. This indicates that some of the zirconium acetate in the Si_3N_4 aqueous suspension probably remained unreacted and was subsequently removed during filtration from the mother solution.

Table 11: Quantitative-phase composition of ZrO_2-coated Si_3N_4 powders after calcinations using a Rietveld analysis

Starting composition	Composition after calcination	
Coated Si_3N_4 powder	*Rietveld refinement* (vol. %)	
ZrO_2 (vol. %)	Si_3N_4	ZrO_2
10	92	8
20	84	16
25	80	20
30	73	27
35	69	31

The morphology of the ZrO_2-coated Si_3N_4 powders containing various amounts of ZrO_2 in the starting composition, as observed with the TEM, is shown in Figure **51**. From the figures it can be seen that the surface of the Si_3N_4 is completely covered with ZrO_2 nanoparticles. Their size distribution is relatively uniform with the average size of 6 nm. The average particle size of ZrO_2 particles was also determined from the XRD spectra of coated powders using a Scherrer equation. The results revealed that the ZrO_2 particles have an average particle size of 10 nm, which is comparable to the geometrically determined size from TEM micrographs.

It can be seen that with an increasing amount of ZrO_2 in the starting powder mixture the coating on the surface of the Si_3N_4 is thicker. Furthermore, some of the nanosized ZrO_2 particles in the coated powders containing larger amounts of ZrO_2 (Figures 51 c, d & e) seem to be a little bit larger than the samples that initially contain 10 and 20 vol. % of ZrO_2 in the starting composition. As a matter of fact, a larger amount of ZrO_2 nanoparticles can cause an agglomeration of these small particles to form larger clusters onto the Si_3N_4 particles. The structure of ZrO_2 was confirmed with the SAED. The simulation of a cubic and tetragonal-polycrystalline ZrO_2 electron-diffraction pattern shown on the left-hand side of the SAED images (Figure **51** e) was compared to the experimental SAED of the coated powder containing 35 vol. % of ZrO_2 in the starting composition. The results revealed that the simulation of a cubic-polycrystalline ZrO_2 electron-diffraction pattern corresponds well to the experimental electron diffraction. From these results it can be concluded that an in-situ gel precipitation of $Zr(OH)_4$ followed by a thermal treatment resulted in the formation of the cubic ZrO_2 nanoparticles with a size of 10 nm on the surface of the Si_3N_4 particles.

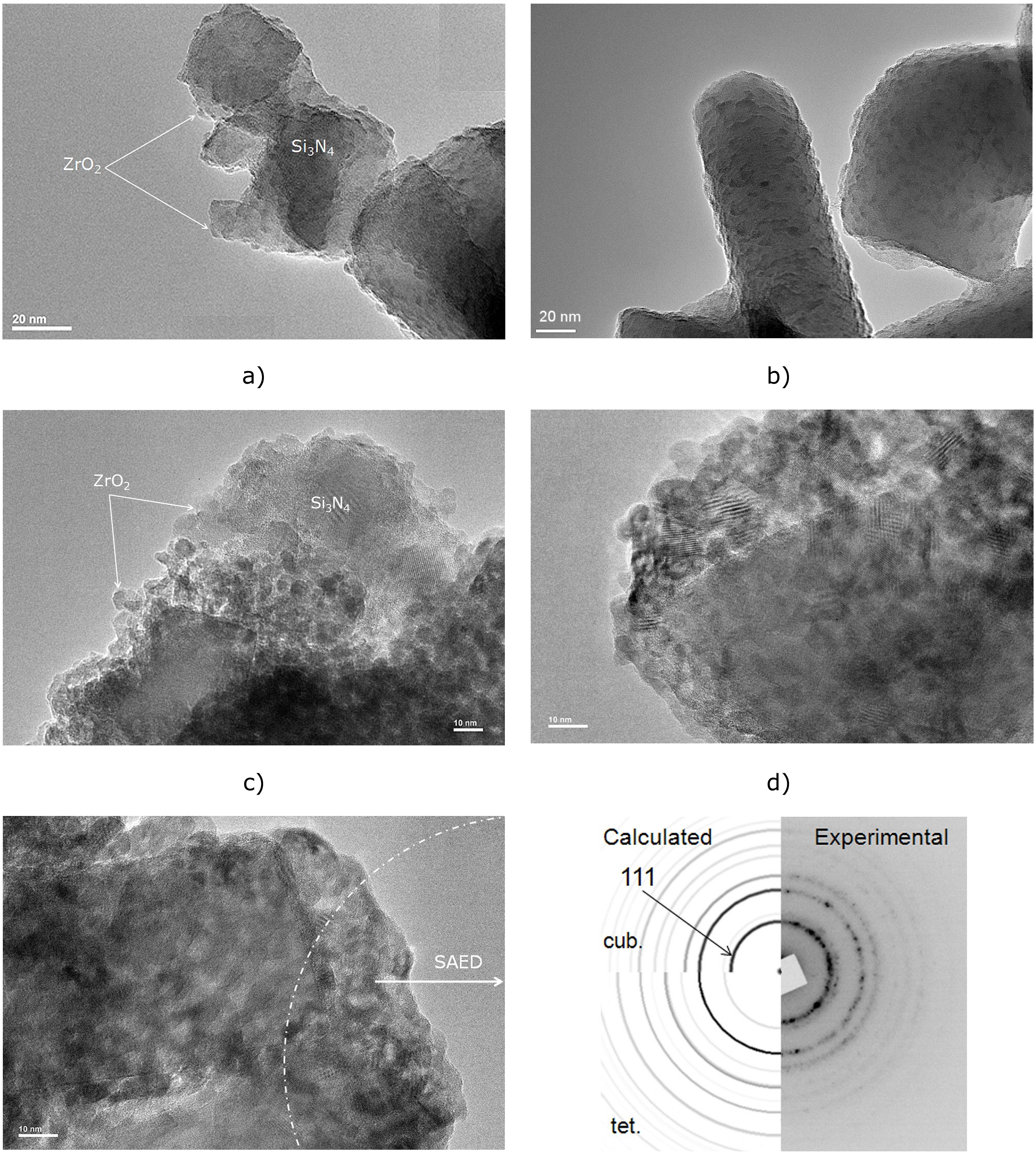

a) b)

c) d)

e)

Figure 51: TEM analyses of ZrO_2-coated Si_3N_4 powders after the calcinations at 600 °C for 2 h in air containing: a) 10, b) 20, c) 25, d) 30 and e) 35 vol. % of ZrO_2. In Figure 51 e the polycrystalline electron-diffraction pattern is inserted, where the calculated electron diffraction of the cubic (Fm3m) and tetragonal ($P4_2/nmc$) ZrO_2 is compared to the experimental SAED.

This finding is in agreement with some literature data found about the synthesis of ZrO_2 nanoparticles prepared from different inorganic precursors in which cubic or tetragonal crystal structure of ZrO_2 is reported after the calcinations at 500 °C.[163,164] In our investigation the cubic ZrO_2 was confirmed with the SAED analyses of the calcined ZrO_2-coated Si_3N_4 powders. It was reported that the structure of the ZrO_2 nanoparticles depends on the synthesis conditions and the crystal size of the polymorphs. The high temperature form can exist at room temperature if the zirconia is prepared either by precipitation from alkaline aqueous solution or by calcining a salt such as the chloride or nitride at low temperatures.[165] One report suggests that the ultrafine, undoped ZrO_2 particles are cubic for sizes of above 4 nm and tetragonal for sizes between 20 and 60 nm.[166] Thus, the cubic structure of ZrO_2 is the most stable in the case when a particle size from 4 to 10 nm is attained, as in our case.

Preparation of the ZrN-coated Si_3N_4 powders

To confirm the reaction of ZrO_2 particles with the Si_3N_4 powder leading to the formation of ZrN, the ZrO_2-coated Si_3N_4 powders containing 10 and 20 vol. % of ZrO_2 (in the starting composition) were heat treated at 1600 °C for 2 h in nitrogen. Subsequent XRD analysis showed that the reaction between ZrO_2 and Si_3N_4, according to reaction 18 (presented on page 29) was not completed if the ZrO_2-coated Si_3N_4 powder contained 20 vol. % of ZrO_2 particles. This is demonstrated in Figure 52, where the conversion of ZrO_2 to ZrN is complete as the coated powder contains 10 vol. % of ZrO_2. For the larger amount (20 vol. %) of ZrO_2 in the starting composition both ZrO_2 and ZrN (cubic) particles were detected in the Si_3N_4 powder. Also in this case the structure of the cubic and tetragonal ZrO_2 cannot be distinguished, as shown in Figure 52. Even when the heat treatment of this coated powder was prolonged to 6 h, keeping the same temperature, the reaction between ZrO_2 and Si_3N_4 leading to the formation of ZrN was incomplete. It can be seen that by prolonging the heat treatment at 1600 °C in N_2 the intensity of the ZrO_2 was significantly reduced (Figure 52). This is in accordance with Weiss et al.[127], who demonstrated that the prolonged time and raising the temperature of the heat treatment lead to the complete conversion of ZrO_2 to ZrN.

The TEM analysis of the ZrO_2-coated Si_3N_4 powders after the heat treatment at 1600 °C for 2 h in N_2 is presented in Figure 53. The SAED analysis of the coated Si_3N_4 powder that initially contained 10 vol. % of ZrO_2, as shown in Figure 53 a, revealed the presence of ZrN particles with the cubic-crystal structure, implying that during the heat treatment the nanosized ZrO_2 particles reacted with Si_3N_4 to form larger ZrN particles.

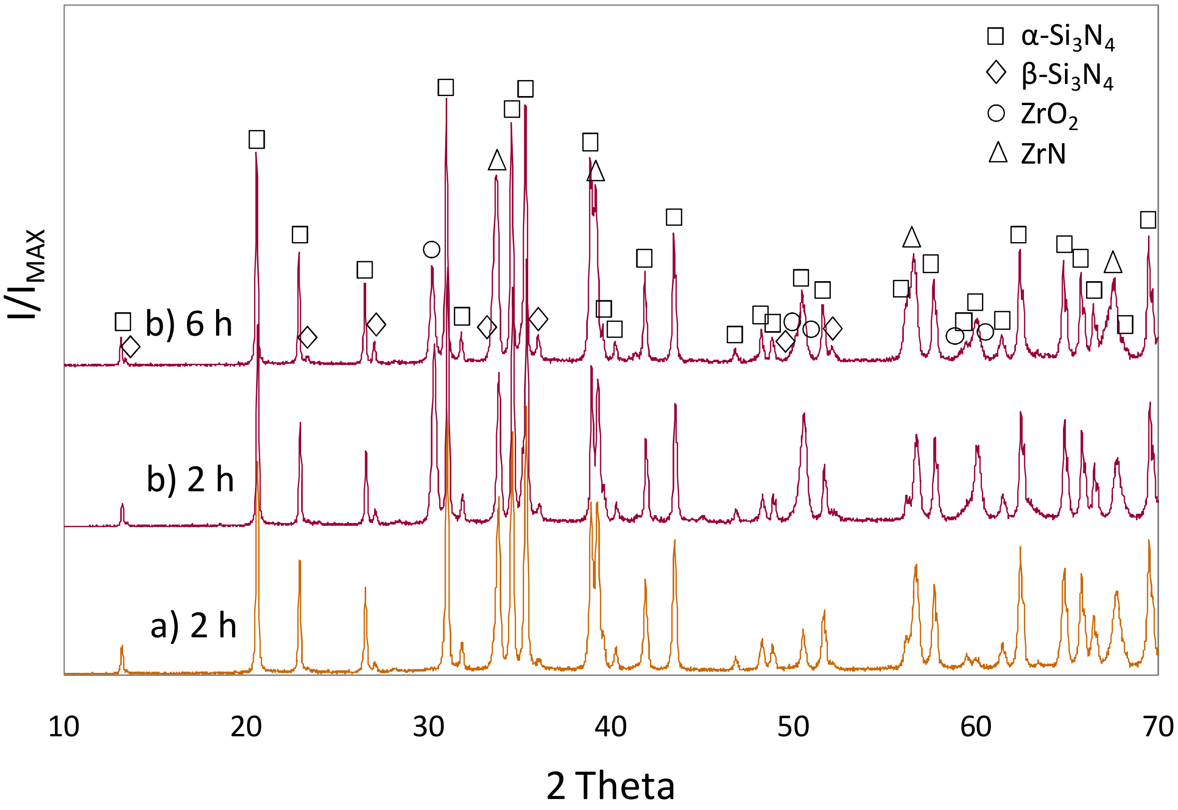

Figure 52: X-ray diffraction pattern of coated powders containing: a) 10 and b) 20 vol. % of ZrO_2 in the starting-powder mixture after the thermal treatment at 1600 °C for 2 h and 6 h in flowing N_2.

For the larger amount (20 vol. %) of ZrO_2 in the starting composition, however, both ZrO_2 and ZrN particles were observed on the surface of the Si_3N_4 (Figure 53 b). An attempt to distinguish whether the crystal structure of ZrO_2 remains as cubic or transforms into a tetragonal using SAED failed because the difference in the distance between the crystal planes of the two phases is too small. Furthermore, it is important to consider that in the case of the polycrystalline electron-diffraction pattern of ZrO_2 (
Figure 51 e) it is possible to distinguish both phases due to the presence of the reflections of all planes in the same pattern and due to the different intensity of those reflections. However, in the case of the electron-diffraction of a ZrO_2 single crystal the difference in the intensity is difficult to compare, since only a few of the defined planes have a visible reflection on the individual diffraction pattern.

The average size distribution of ZrN (Figure 53) and ZrO_2 (Figure 53 b) nanoparticles was geometrically determined from 5 TEM micrographs of both coated powders. From each image at least 10 ZrN and 10 ZrO_2 particles were measured. The result revealed that the average particle size of ZrN and ZrO_2 is 40 nm and 50 nm, respectively.

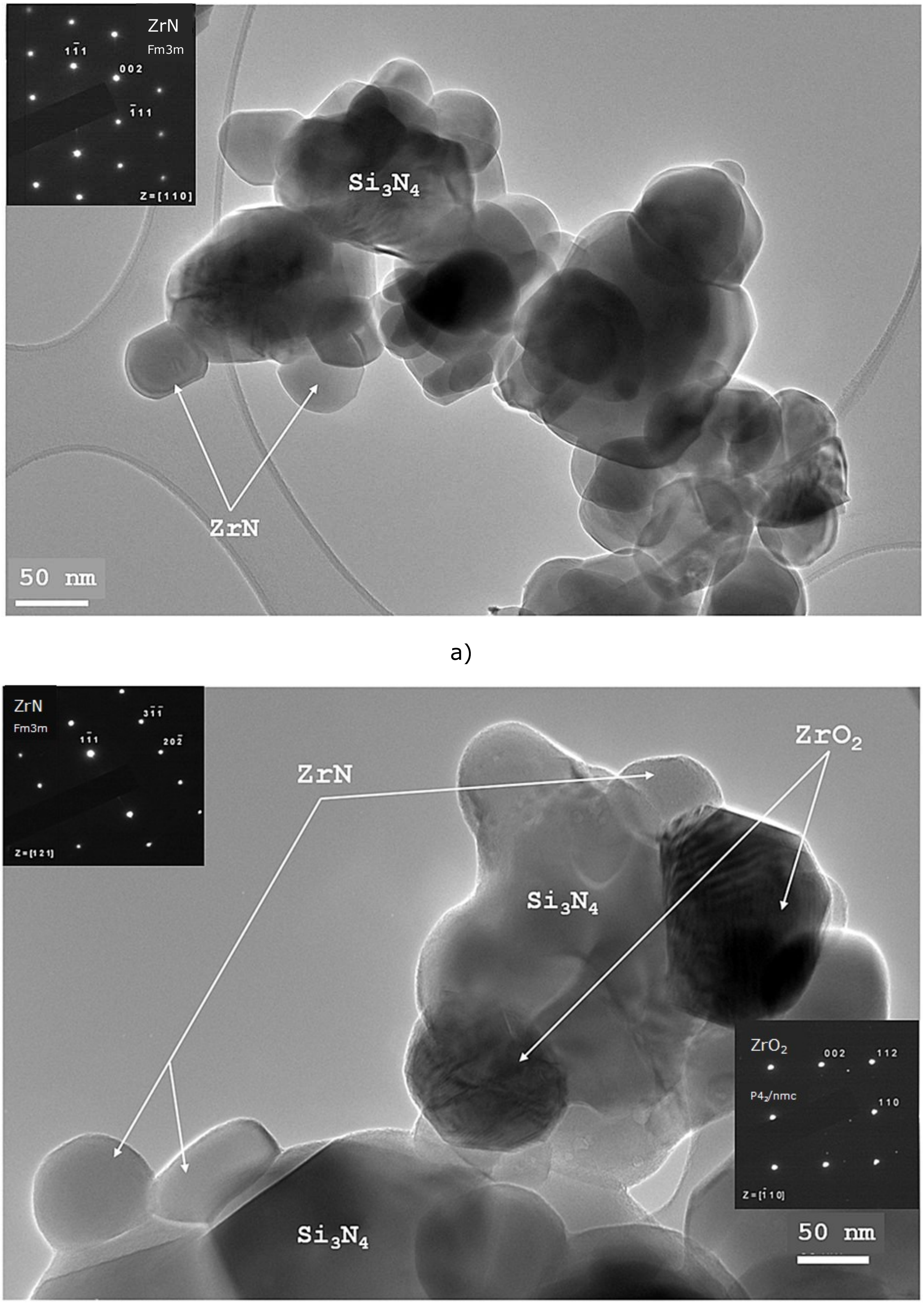

a)

b)

Figure 53: TEM images of ZrO_2-coated Si_3N_4 powders after a thermal treatment at 1600 °C for 2 h in flowing N_2 containing: a) 10 and b) 20 vol. % of ZrO_2 in the starting powder mixture.

In addition, the average particle size of these particles was also determined from the x-ray diffraction pattern of both coated powders using a Scherrer equation. The particle size analysis showed that an average particle size of ZrN is 37 nm and for ZrO_2 is 31 nm. From that it can be concluded that the geometrically determined particle size from TEM micrographs can result in a larger deviation. The examination of coated powder with 20 vol. % of ZrO_2 in the starting composition show that during the thermal treatment cubic ZrO_2 particles that had not reacted with the Si_3N_4 grew in size. An exaggerated grain growth of ZrO_2 particles on the Al_2O_3 powder surface has been reported by Schneider et al.[167] Based on the fact, that neither ZrO_2 nor Al_2O_3 particles are not perfectly spherical, the change in diffusion coefficients in ZrO_2 drops occurred due to the various curvatures of particles. Tendency to a decrease of the overall system's energy presents a driving force, whereas the difference of the diffusion coefficients can be demonstrated by a migration mechanism[167] of the ZrO_2 particles on Al_2O_3 powder surface until they reach a stabile position. According to this explanation, the nano-sized ZrO_2 particles in our system most probably grew because of particle coalescence during thermal treatment to form larger clusters.[168]

The reason for the incomplete reaction of ZrO_2 to ZrN was found to be in the silicon-monoxide partial pressure[88], which forms during the reaction between ZrO_2 and Si_3N_4 (reaction 18, shown on page 29). The formation of SiO can influence the reaction of ZrO_2 with Si_3N_4 because of the silicon-monoxide partial pressure that builds up in the powder mixture or in the powder compact. The equilibrium partial pressure of the gas phase is related to the free-energy change by Equation 27[88] under the assumption that $p(N_2)$ is a unity.

$$-\Delta G^\circ = RT\ln(p_{SiO}\,p_{N_2}^{5/12}) \tag{27}$$

Thus, reaction 18 (shown on page 29) will only proceed until the equilibrium partial pressure of SiO is reached. This reaction was studied by Trigg et al.[88] in order to explain an influence of the silicon-monoxide partial pressure in the Si-Zr-O-N system on the formation of ZrN at various temperatures, as shown in Figure 54. It can be seen that the equilibrium partial pressure of silicon-monoxide strongly depends on the temperature at which the reaction between ZrO_2 and Si_3N_4 takes place. Therefore, the equilibrium partial pressure of silicon-monoxide at 1400 K would be 4×10^{-7} MPa, whereas at 2000 K it would rise to 1×10^{-1} MPa. This indicates that at higher temperatures the reaction 18 is heavily controlled by the presence of the SiO in the system. The reaction rate would therefore be dependent on the rate of SiO removal from the system. Because of that fact, the ZrO_2-coated Si_3N_4 powders containing 20, 25, 30 and 35 vol. % of ZrO_2 in the starting composition were heat treated at 1600 °C for 3 h in flowing nitrogen at low-pressure (P_{N_2} = 0.4 atm). This atmosphere was used in order to remove the forming gaseous SiO from the system, so that the conversion of ZrO_2 to ZrN could be completed.

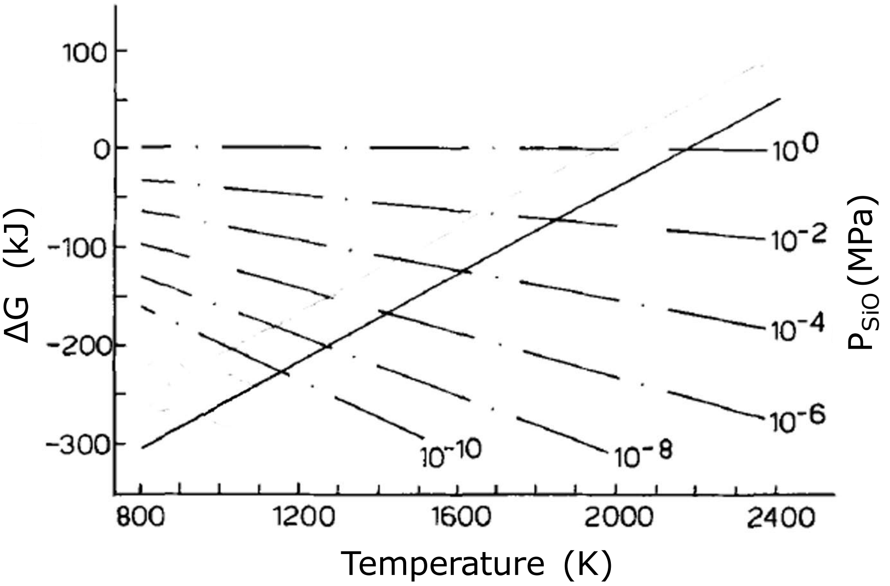

Figure 54: Free-energy change vs. temperature for reaction 18. SiO partial pressures are shown to enable the feasability above the reaction to be expressed in dependence of p_{SiO}.[88]

The results of the XRD analysis for these coated powders, as shown in Figure 55, clearly show that no ZrO_2 peaks could be detected, indicating that the reaction between ZrO_2 and Si_3N_4 was indeed completed. Furthermore, it can be seen that by increasing the amount of ZrO_2 in the starting powder mixture, the intensities of the ZrN peaks increase, while the intensities of the Si_3N_4 peaks decrease.

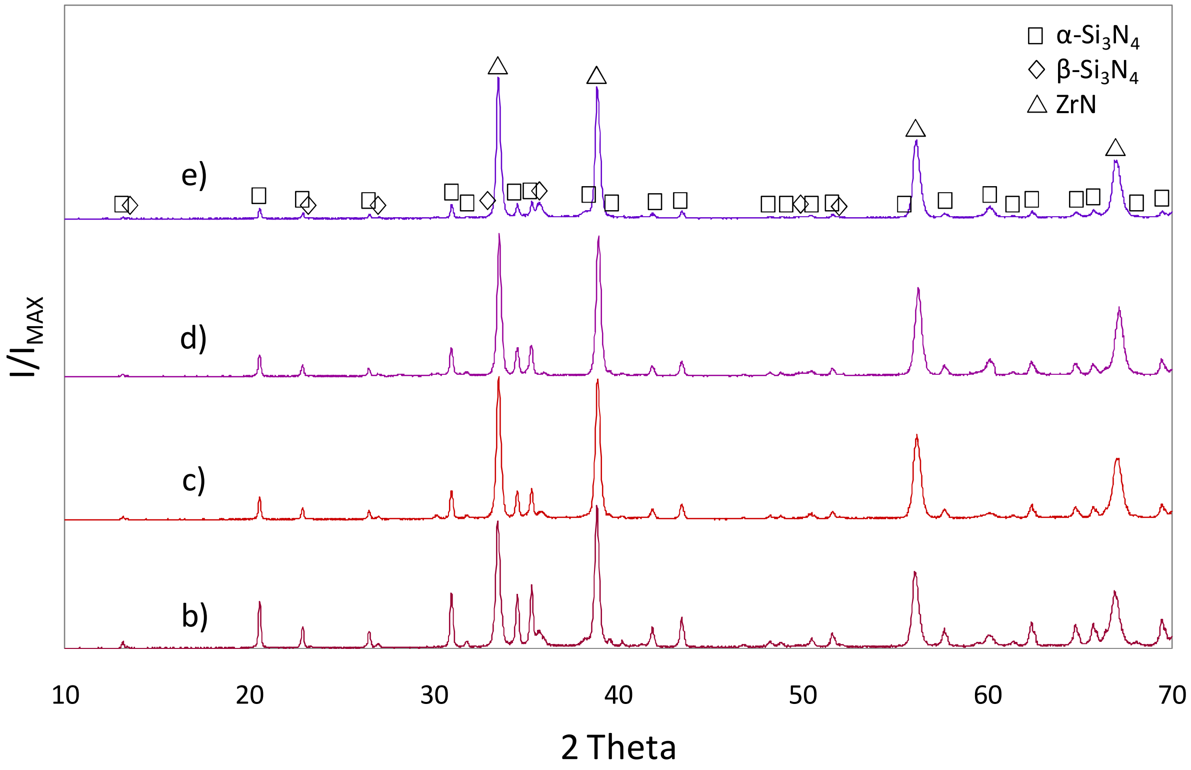

Figure 55: XRD analysis of ZrO_2-coated Si_3N_4 powders after thermal treatment at 1600 °C for 3 h in flowing nitrogen at low-pressure containing: b) 20, c) 25, d) 30 and e) 35 vol. % of ZrO_2 in the starting composition.

The amount of ZrN in the ZrN-coated Si_3N_4 powders was quantitatively determined from the x-ray diffraction patterns of the heat treated ZrO_2-coated Si_3N_4 powders at 1600 °C for 3 h in flowing nitrogen at low-pressure and was calculated by the proposed chemical reaction between ZrO_2 and Si_3N_4 (reaction 18, shown on page 29), as presented in Figure 56. On the x axis the determined amount of ZrO_2 (Table 11) from the x-ray diffraction patterns of the calcined coated powders containing various amounts of ZrO_2 in the starting composition are presented. For the calculation of the ZrN content in the heat-treated coated powders, the mass balance of the starting materials was considered in relation to reaction 18. Figure 56 shows that the determined ZrN content in the Si_3N_4 powders from the XRD spectra of the heat-treated coated powders are in good agreement with the calculated ZrN content using the proposed chemical reaction. Furthermore, it can be seen that with increasing ZrO_2 in the starting composition leads to a larger ZrN content in the ZrN-coated Si_3N_4 powders (Figure 56).

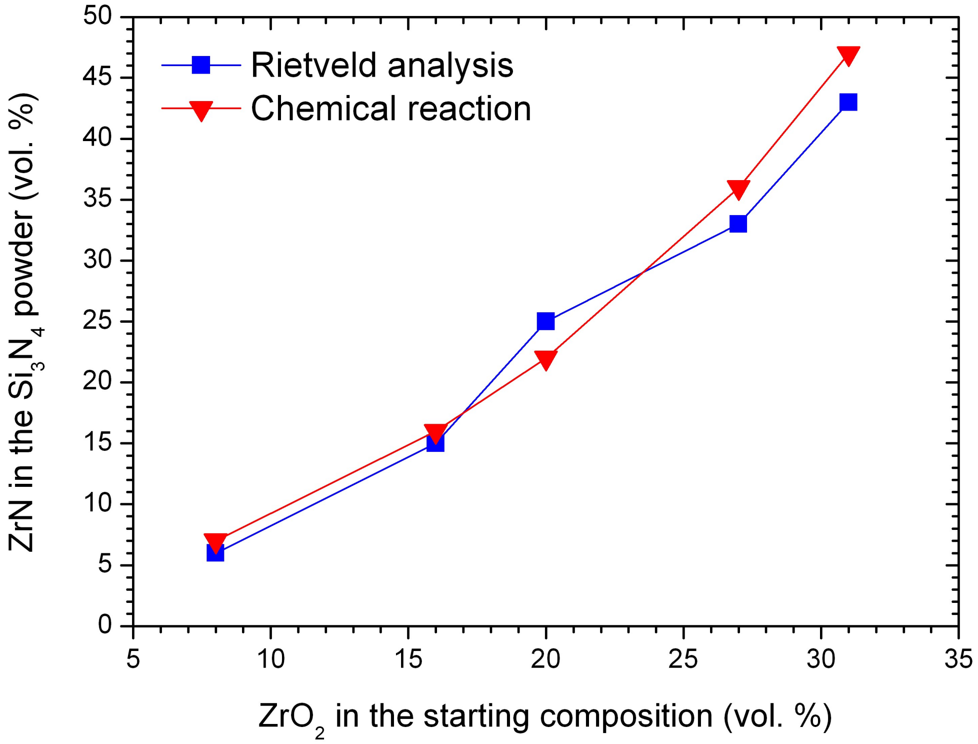

Figure 56: Amount of ZrN in ZrN-coated Si_3N_4 powder versus the amount of ZrO_2 in the starting powder mixture (using Rietveld analysis and chemical reaction).

The TEM analysis of heat-treated ZrO_2-coated Si_3N_4 powders at 1600 °C for 3 h in flowing nitrogen at low-pressure containing various amounts of ZrO_2 (in the starting powder mixture), as displayed in Figure 57, shows that on the surface of Si_3N_4 small ZrN particles can be observed. TEM observations confirmed the results of XRD analysis (Figure 55) that due to an increase in the ZrO_2 content in the starting powder mixture, a larger amount of the ZrN nanoparticles is present on the Si_3N_4 powder. During the heat treatment and a chemical reaction between the ZrO_2 particles and the Si_3N_4 powder surface, the ZrN grew into larger particles with a average size distribution ranging from 40 nm to 60 nm. This average size of ZrN was geometrically defined from 5 TEM micrographs of each coated powder shown in Figure 57 and in each sample at least 10 ZrN particles were measured. The similar average particle size of ZrN particles was also confirmed from the XRD spectra of coated powders using a Scherrer equation. The results revealed that the ZrN particles with the size of 30 nm are present on the Si_3N_4 powder. Their nanometric size is more specifically visible in Figure 58.

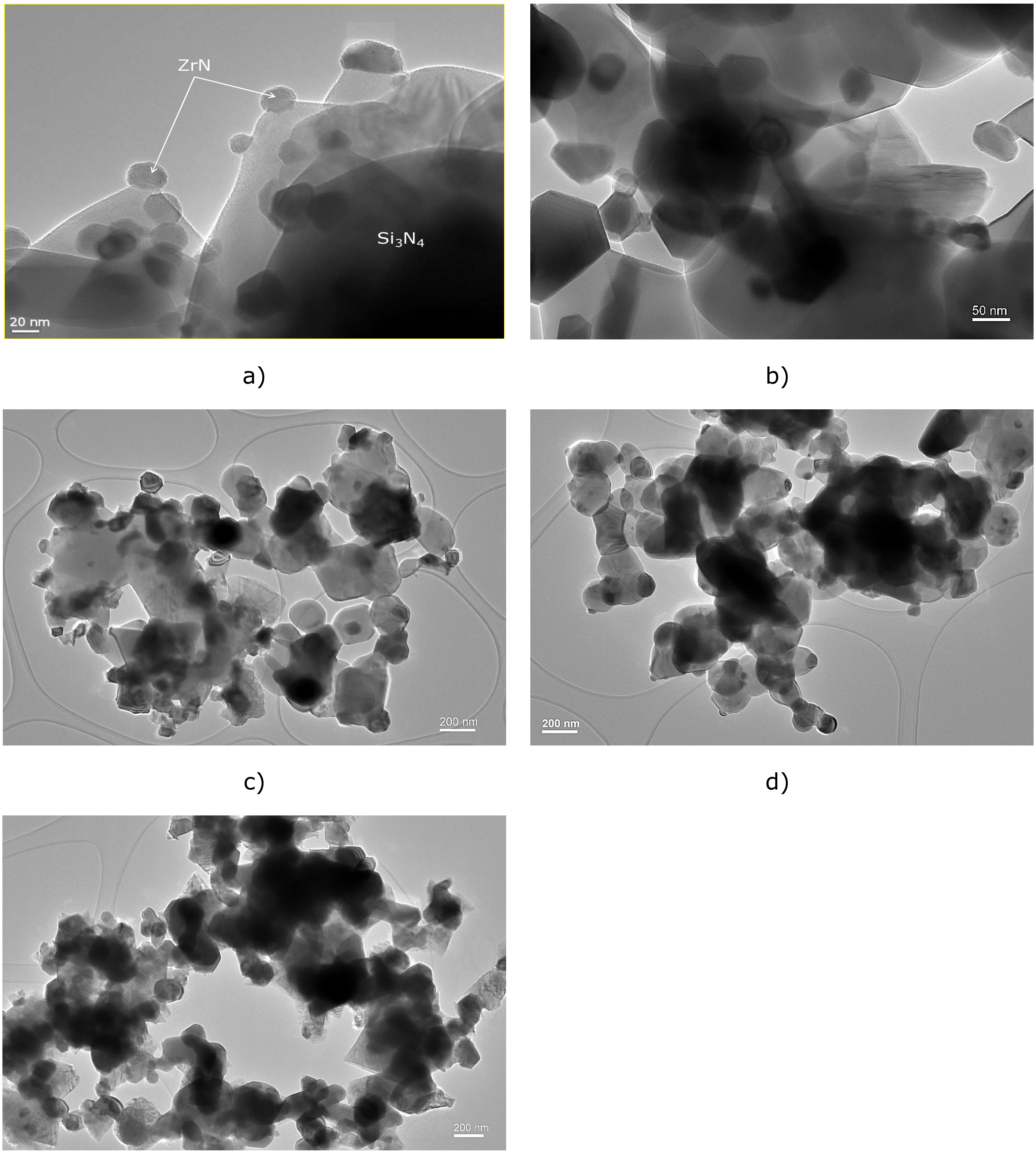

a) b)

c) d)

e)

Figure 57: TEM micrographs of ZrO_2-coated Si_3N_4 powders after thermal treatment at 1600 °C for 3 h in flowing nitrogen at low-pressure containing: a) 10, b) 20, c) 25, d) 30 and e) 35 vol. % ZrO_2 in the starting composition.

After the heat treatment at 1600 °C, the surface coverage of Si_3N_4 particles with the nanosized ZrN particles (Figure 57) is not so perfect as in the case of the nitrided TiN-coated Si_3N_4 powders, shown in Figure 36 (presented on page 64). The reason for this is different reaction mechanism and the much higher temperature, i.e., 1600 °C, for the formation of ZrN compared to the nitridation temperature (900 °C) for the formation of TiN. From Figure 57 it is seen that after the heat treatment the ZrN particles have grown larger and thus prevent a connection between the nanoparticles. Moreover, it was calculated that during the heat treatment the accompanying volume shrinkage of the conversion of ZrO_2 to ZrN was 27 % due to a higher theoretical density of ZrN compared to ZrO_2. It should be mentioned, that there is no literature on the preparation of Si_3N_4 powder coated by ZrN nanoparticles, prepared by an in-situ reaction of ZrO_2 nanoparticles with Si_3N_4 except for only our preliminary research[169], for the coating the surface of the Si_3N_4 powder with ZrN nanoparticles produced by using a zirconium acetate with urea as the precipitating agent, followed by a reaction between ZrO_2 and Si_3N_4 above 1600 °C in N_2. However, Fu et al.[116] showed that the ZrN nanoparticles can be synthesized by a reduction-nitridation of the nanosized ZrO_2 powder at 1000 °C in the NH_3 gas with Mg as a reducing agent. Even in this case the particles have grown to a larger size of 50 nm, which is comparable to our particle size of the ZrN particles, displayed in Figure 58, prepared by an in-situ reaction of the ZrO_2 nanoparticles with Si_3N_4.

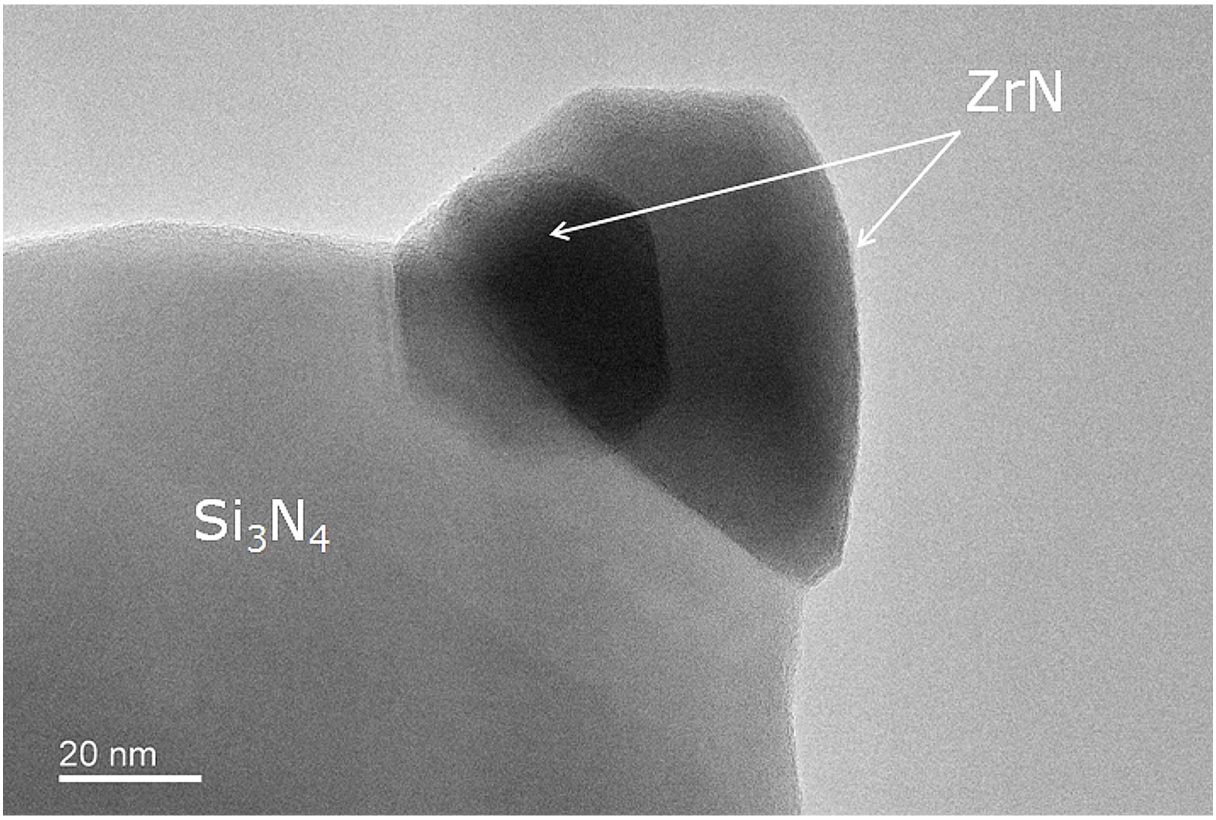

Figure 58: TEM micrograph of the ZrO_2-coated Si_3N_4 powder, initially containing 30 vol. % of ZrO_2 in the starting composition, after thermal treatment at 1600 °C for 3 h in flowing nitrogen at low-pressure.

4.3.2 Thermodynamic calculations of the chemical reactions for the formation of ZrN

The Gibbs free-energy change for the chemical reactions between ZrO_2 and Si_3N_4 to form ZrN (reactions 18 & 19, presented on page 29), calculated by using the available thermodynamic data[170], are plotted as a function of temperature in Figure 59. Due to the fact that Si_2N_2O phase was never detected by an XRD or TEM analyses, reaction 20 (shown on page 29) was not considered as possible. A comparison of reactions 18 & 19 reveals that the formation of ZrN from the reaction between ZrO_2 and Si_3N_4 is associated with a larger ΔG of reaction 18, due to the formation of SiO and N_2 gaseous species. Thus, above 1200 K reaction 18 is thermodynamically more favourable than reaction 19. Figure 59 demonstrates that the formation of ZrN by reaction 18 can occur at 1873 K where the ΔG is negative, whereas reaction 19 becomes energetically favourable at above 2460 K. The calculated ΔGs of reaction 18 at 1873 K and of reaction 19 at 2500 K are in agreement with the ΔGs of these reactions calculated at the same temperatures, as presented in Weiss's[124] work.

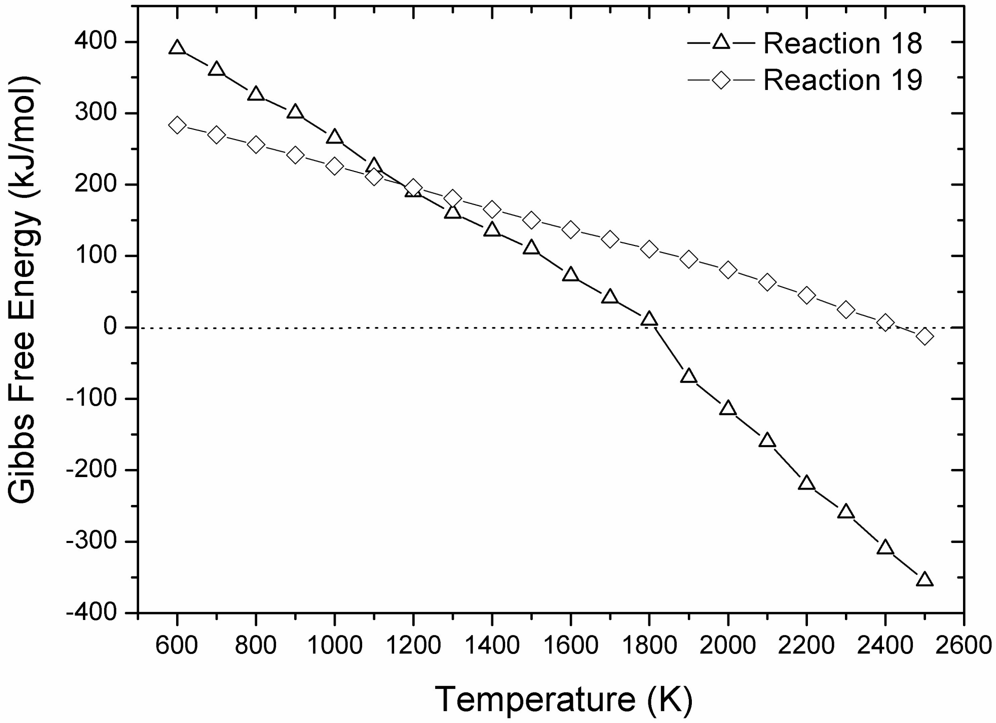

Figure 59: Calculated Gibbs free energy of reactions 18 and 19 as a function of temperature.

4.3.3 Sintering by using pre-reacted powder

4.3.3.1 Microstructure and phase analysis of the sintered composites

To fabricate the Si_3N_4/ZrN composites, the ZrN-coated Si_3N_4 powders containing various amounts of ZrO_2 in the starting composition were mixed together with yttria and alumina additives, pressed and sintered at 1850 °C for 2 h in flowing N_2 (Figure 26 a, shown on page 49). The cross-section microstructures of the sintered composites containing various amounts of ZrO_2 in the starting composition shown on the left-hand side of Figure 60, indicating that all samples are homogeneous and fairly dense with uniformly distributed pores. The microstructures of the polished surfaces of the sintered composites that initially contained various amounts of ZrO_2 in the starting composition are displayed on the right-hand side of Figure 60. Shape and size distribution of bright ZrN particles are relatively homogeneously dispersed in between grey β-Si_3N_4 grains. During sintering in the presence of a liquid phase, the ZrN grains coarsened and because of that the particle size grew to approximately 0.54 μm. SEM images indicate that these composites have a relatively broad size distribution of ZrN particles ranging from 0.15 μm to 1.0 μm. This can be attributed to the aggregation of ZrN particles during sintering, especially when the samples contained larger amounts of ZrO_2 in the starting powder mixture, as visible in the Figures 60 d & e.

Apart from our preliminary report[169] there is no literature reporting on the preparation of Si_3N_4-ZrN composites from Si_3N_4 powder coated with ZrN nanoparticles, prepared by an in-situ reaction of ZrO_2 nanoparticles with Si_3N_4. In contrast, there are several literature reports dealing with these composites fabricated with the conventional composite method starting from mechanically mixed Si_3N_4 and ZrN powders[118], by mixing carbon black and zircon powders followed by a carbothermal-nitridation process[123] or by a reaction[59] between $ZrSi_2$ and N_2 during reaction sintering. In these reports the Si_3N_4-ZrN composites exhibited an even larger ZrN particle size, i.e., > 5 μm, which is much larger than the size of our composites prepared by an in-situ reaction of ZrO_2 nanoparticles with Si_3N_4.

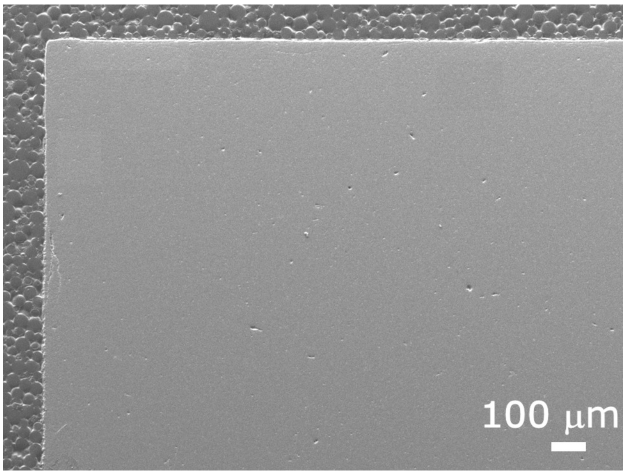

a) CS

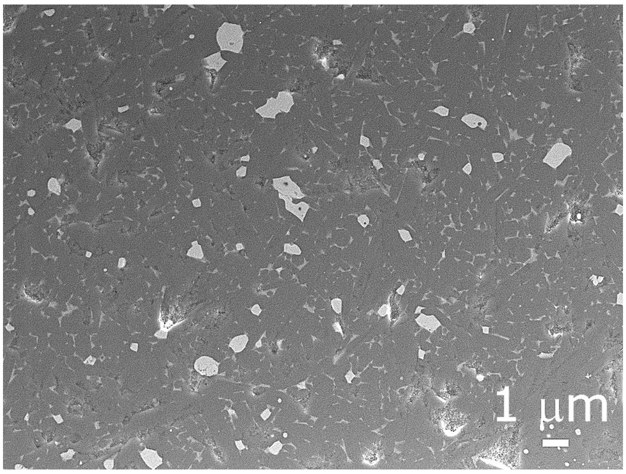

a) IP

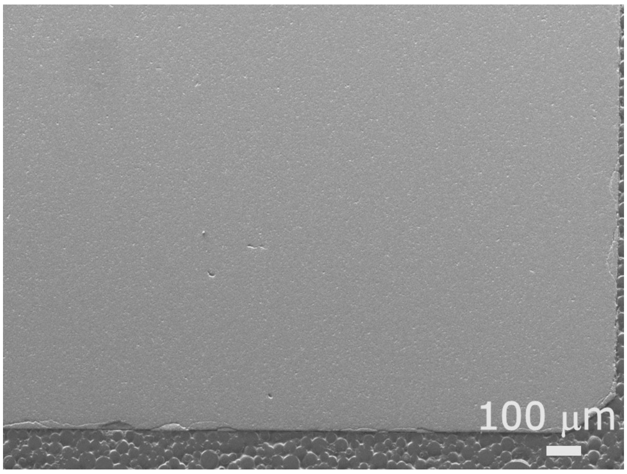

b) CS

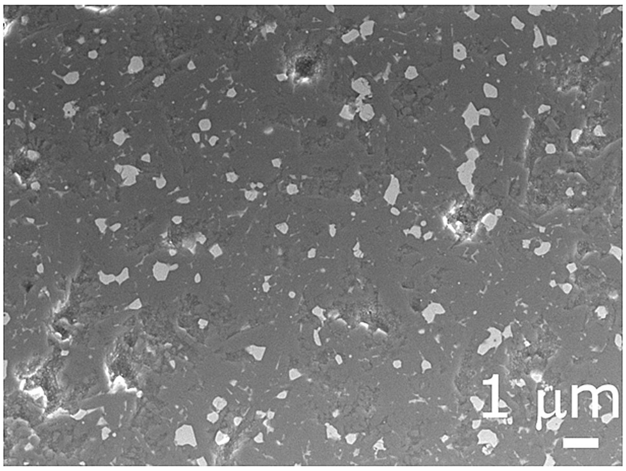

b) IP

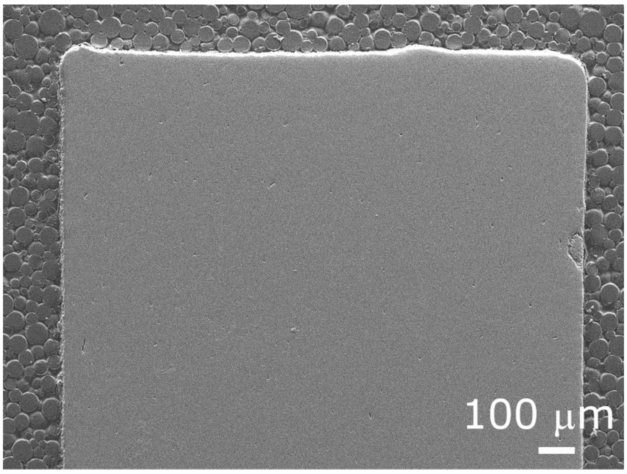

c) CS

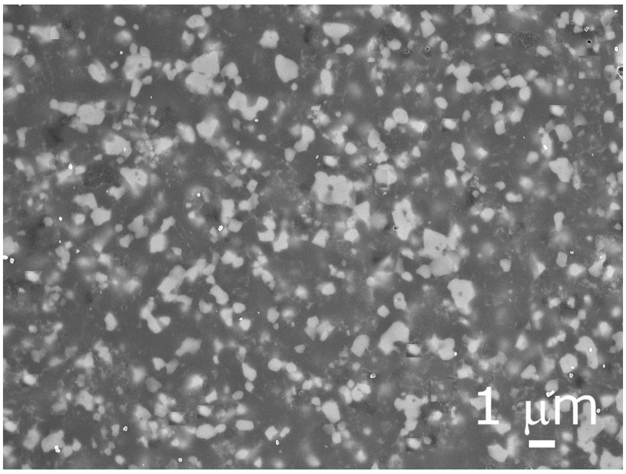

c) IP

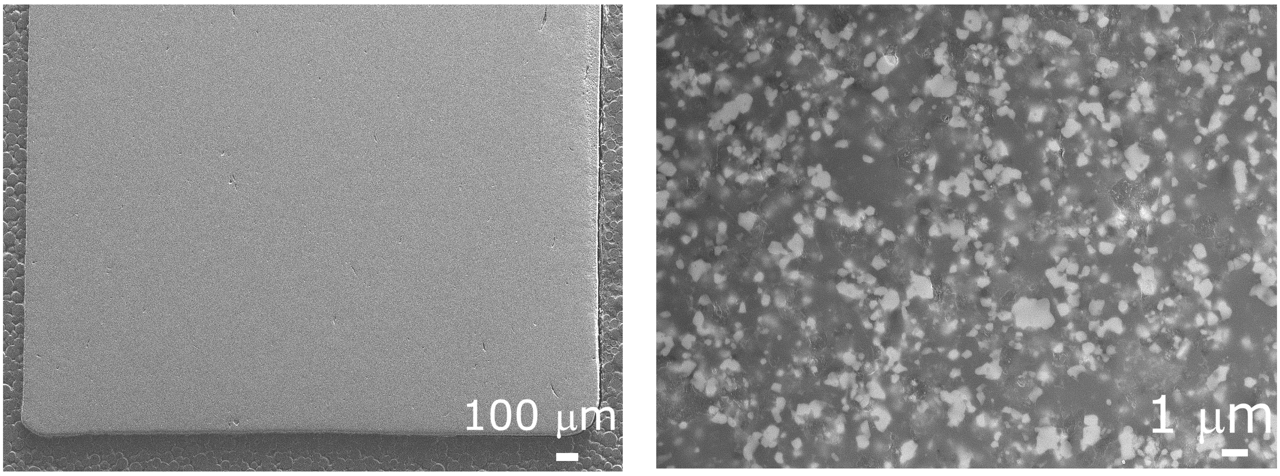

d) CS d) IP

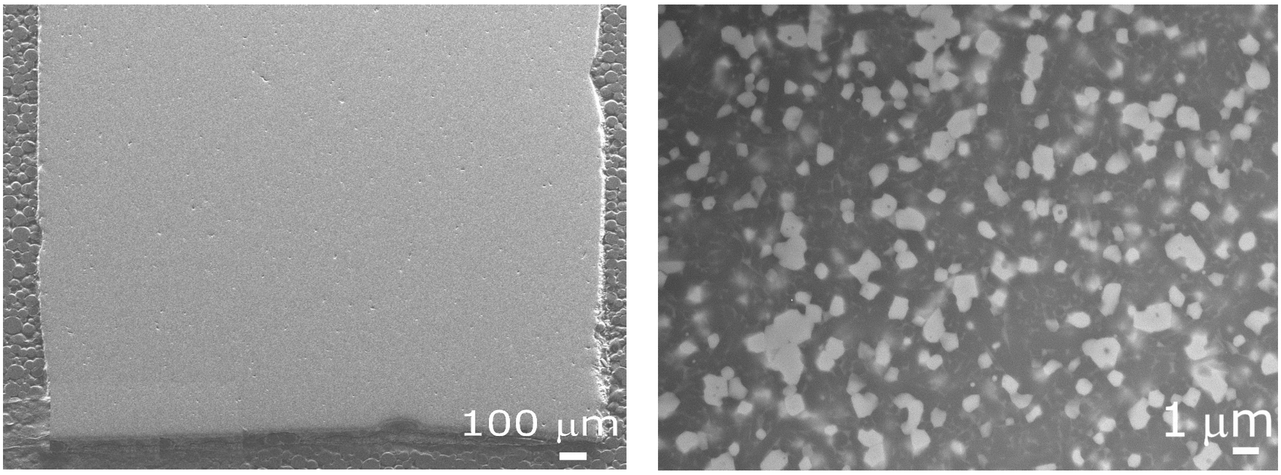

e) CS e) IP

Figure 60: Microstructures of Si_3N_4/ZrN composites sintered at 1850 °C for 2 h in N_2 from pre-reacted powder containing: a) 10, b) 20, c) 25, d) 30 and e) 35 vol. % of ZrO_2 in the starting compositions (cross-section images of samples are referred to as CS and the internal-part images as IP).

SEM images of the sintered samples, initially containing 25 and 35 vol. % of ZrO_2 in the starting powder-mixture, shown in Figure 61, demonstrate that the ZrN grains have irregular shapes, which implies that at least some of the ZrN grains grew from the liquid during cooling. Furthermore, from the SEM micrographs it can be seen that at larger amounts (35 vol. %) of ZrO_2 (in the starting composition), the ZrN particles are much larger than the particles in the sample that contains 25 vol. % of ZrO_2. This indicates that when a sample is prepared from a mixture containing larger amount of ZrO_2 in the starting composition the ZrN particles tend to aggregate forming larger ones, as shown in Figure 61 a. At this magnification, a brighter, transient liquid phase in between the grey β-Si_3N_4 grains and the white, irregular ZrN particles can be seen.

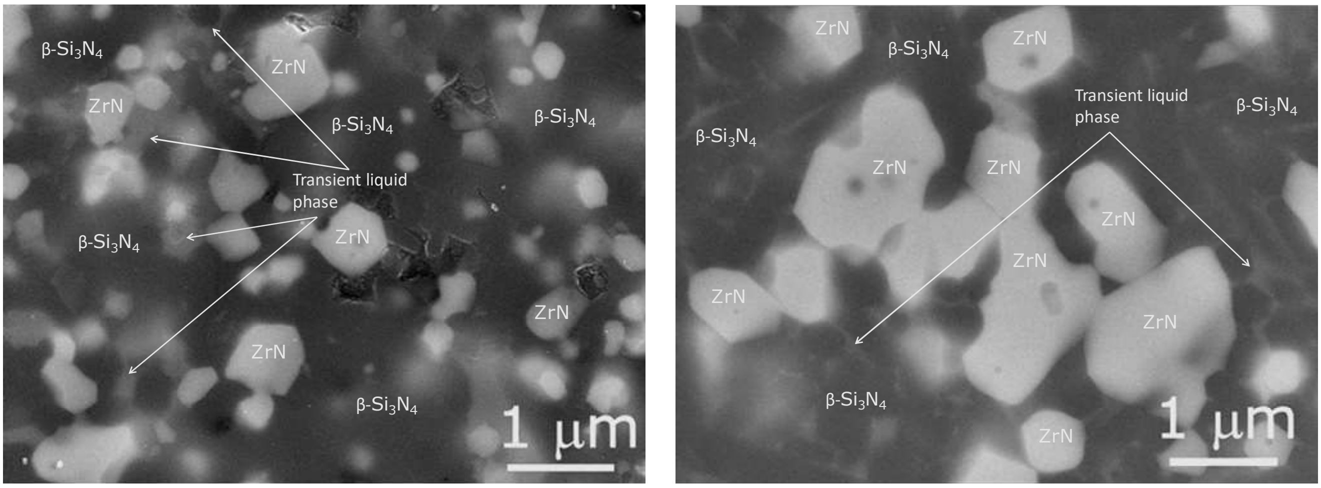

a) b)

Figure 61: SEM images, at a higher magnification, of sintered Si_3N_4/ZrN composites at 1850 °C for 2 h in N_2 produced from pre-reacted powders which initially contained: a) 25 and b) 35 vol. % of ZrO_2 in the starting powder mixtures.

XRD analysis of the sintered Si_3N_4-ZrN composites containing various amounts of ZrO_2 in the starting powder mixture (Figure 62) confirmed the presence of the cubic ZrN coexisting with β-Si_3N_4. Besides, with increasing amount of ZrO_2 in the starting composition the intensity of the ZrN peaks increases and at the same time the intensity of Si_3N_4 decreases. This is due to the reaction between ZrO_2 and Si_3N_4 (reaction 18, presented on page 29), by which ZrN is formed. A larger amount of ZrO_2 in the starting composition causes a larger amount of Si_3N_4 to be reacted due to the reaction 18, resulting in an increase of ZrN and a decrease of the Si_3N_4 intensity.

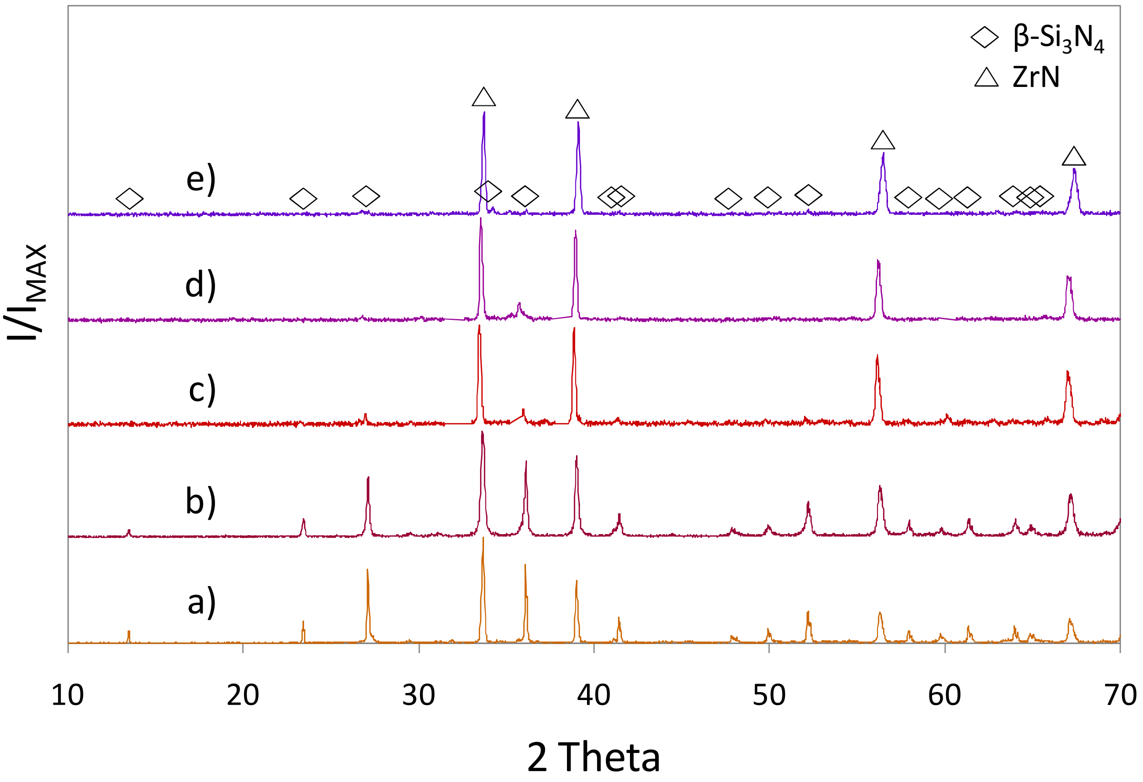

Figure 62: X-ray difraction patterns of Si_3N_4/ZrN composites sintered at 1850 °C for 2 h in N_2 from pre-reacted powders containing: a) 10, b) 20, c) 25, d) 30 and e) 35 vol. % of ZrO_2 in the starting composition.

The XRD analysis of the sintered samples containing various amounts of ZrO_2 was repeated after a 300 μm thick surface layer was removed. Results in Figure 63 revealed similar patterns as that obtained from as-sintered samples shown in Figure 62, confirming that these composites are homogeneous.

However, a further investigation revealed that the structure of ZrN in the XRD profile is slightly shifted in all the sintered composites containing various amounts of ZrO_2 in the starting composition. In order to demonstrate this detection, the enlarged XRD profile of ZrN (001) peak at 2 θ range from 32 to 34.5 ° is shown for the sample containing 35 vol. % of ZrO_2 in the starting powder mixture (Figure 64). Results revealed that at 2 θ = 33.49° the ZrN (001) peak is slightly shifted to the right. This indicates that the lattice constant of ZrN (a_o) was reduced, which strongly implies that during sintering some oxygen was incorporated into the crystal structure of the ZrN, resulting in a reduced lattice constant. However, since this phenomenon was not observed in the ZrO_2-coated Si_3N_4 powders containing various amounts of ZrO_2 in the starting composition after the calcinations at 1600 °C in flowing nitrogen at low-pressure (Figure 55, shown on page 89), it is believed that the oxygen was incorporated from a transient liquid phase.

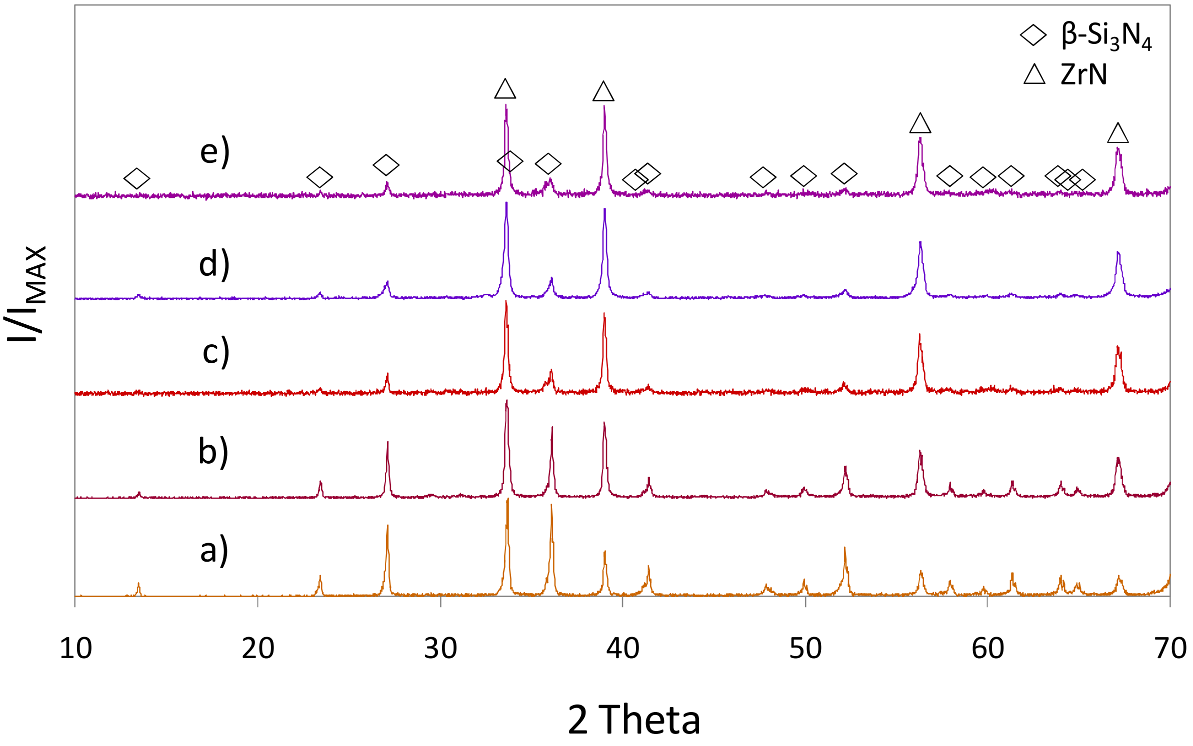

Figure 63: XRD analysis of sintered Si_3N_4/ZrN composites from pre-reacted powders which initially contained: a) 10, b) 20, c) 25, d) 30 and e) 35 vol. % of ZrO_2 in the starting composition after the surface (300 µm) was removed.

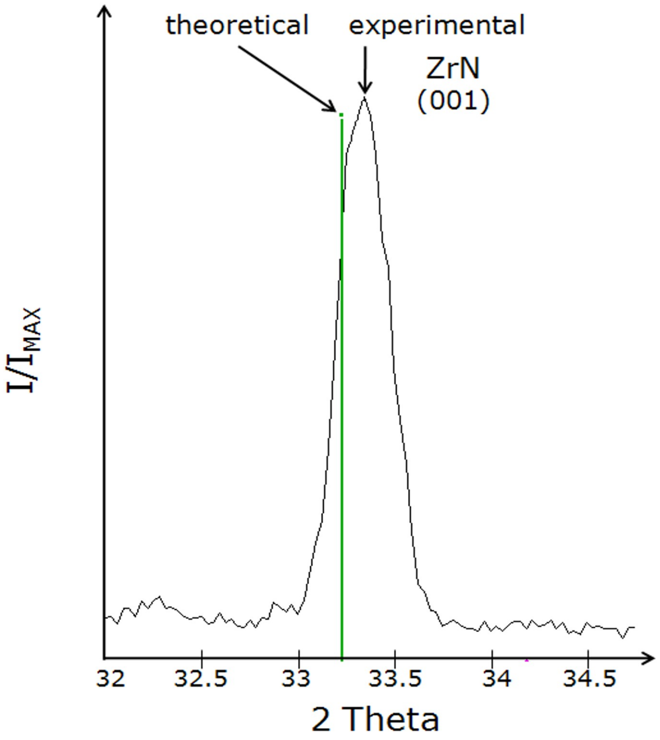

Figure 64: XRD spectrum of a sintered Si_3N_4/ZrN composite containing 35 vol. % of ZrO_2 (in the starting composition) analysed in the 2 θ range from 32 to 34.5 °.

4.3.3.2 Quantitative-phase analysis of ZrN in the final composites

The amounts of ZrN in the sintered Si_3N_4/ZrN composites that initially contain various amounts of ZrO_2 in the starting composition were quantitatively determined from the XRD spectra of the sintered composites using a Rietveld analysis, shown in Table 12. The results of this analysis indicate that the determined amounts of ZrN from the x-ray diffraction paterns of sintered composites, shown in Table 12, are in good agreement with the determined ZrN contents from the XRD spectra of ZrN-coated Si_3N_4 powders containing various amounts of ZrO_2 in the starting composition (Figure 56, presented on page 90). Furthermore, the determined ZrN amounts, presented in Table 12, correspond (± 2 vol. %) to the calculated ZrN contents (Figure 56) that were obtained according to the reaction 18 (presented on page 29).

Table 12: Quantitative-phase composition of Si_3N_4/ZrN composites containing various amounts of ZrO_2 in the starting composition verified by a Rietveld analysis

Starting composition *Coated Si_3N_4 powder*	Composition after sintering in Si_3N_4/ZrN composite *Rietveld refinement* (vol. %)		
ZrO_2 (vol. %)	Si_3N_4	ZrN	YAG (Y_2O_3 + Al_2O_3)
10	89	6	5
20	80	15	5
25	71	25	4
30	61	35	4
35	54	43	3

For all further investigations the calculated amounts of ZrN (Figure 56) according to reaction 18 was used in the next plotted graphs.

4.3.3.3 Influence of the amount of conductive phase of the Si_3N_4/ZrN composites on the density, flexural strength and electrical conductivity

Figure 65 shows the influence of the amount of ZrN present in the sintered Si_3N_4/ZrN composites on the relative density and flexural strength. It can be seen that both the relative density and flexural strength decrease with increasing ZrN content in the final composites. The Si_3N_4/ZrN composite, that initially contained 7 vol. % of ZrN, exhibited the highest relative density of 97 % with the flexural strength of 600 MPa.

Larger amount of ZrN leads to a decrease in the relative density and consequently, in a decrease in the flexural strength. With a 47 vol. % of ZrN in the composite a relative density of 90 % and a flexural strength of only 350 MPa were obtained. From this it can be concluded that an increase in the ZrN content leads to poor sinterability of the system and thereby exhibiting relatively low density and flexural strength. Furthermore, we have to consider that with increasing ZrN content in the sample the amount of Si_3N_4 becomes lower, which eventually results in the poor sinterability of the system.

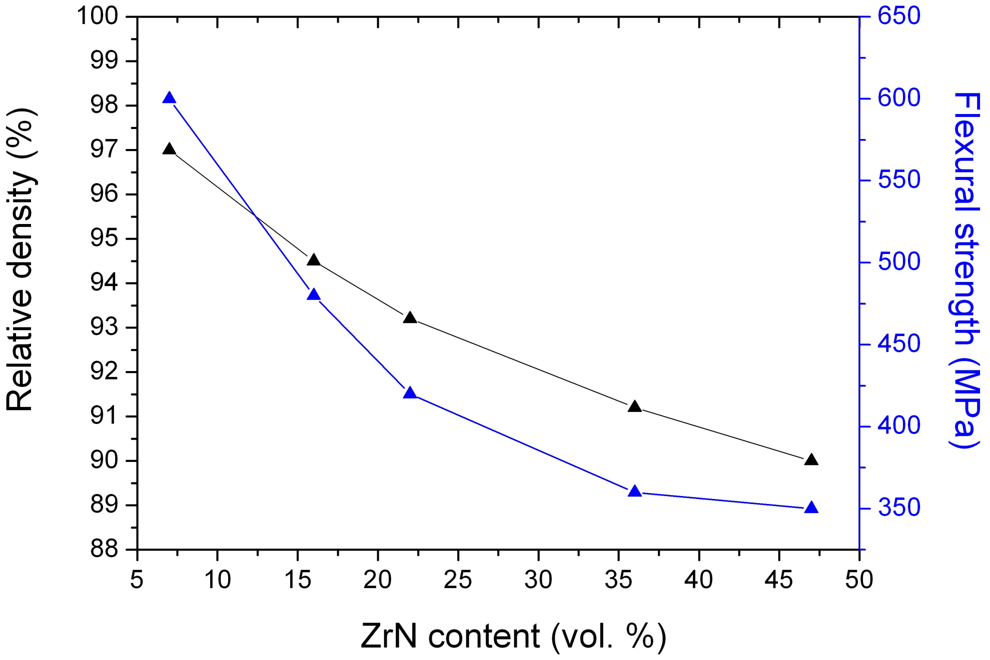

Figure 65: Change in the relative density and flexural strength of Si_3N_4/ZrN composites with various ZrN contents sintered at 1850 °C for 2 h in N_2.

The electrical conductivity of the Si_3N_4/ZrN composites is displayed in Figure 66 as a function of the ZrN content. We can see that electrical conductivity of the sintered composites increases sharply from $1.4 \times 10^{-6}\ \Omega^{-1}m^{-1}$ at 7 vol. % of ZrN to $0.6\ \Omega^{-1}m^{-1}$ at 22 vol. % of ZrN and then slowly reaches a maximum at $85\ \Omega^{-1}m^{-1}$ for 47 vol. % of ZrN.

By comparing these values with the results of the electrical conductivity of Si_3N_4/TiN composites, shown in Figure 43 (shown on page 74), it can be seen that the curve of the electrical conductivity of the Si_3N_4/ZrN composites with a ZrN content above 22 vol. % is not as sharp as in the case of the Si_3N_4/TiN composites. This was explained by the XRD analysis of the sintered samples (Figure 64), where it was shown that the ZrN peaks are slightly shifted, suggesting that the ZrN particles contain a small amount of oxygen. From this it can be assumed that during sintering in a liquid phase the oxygen incorporates into the ZrN results in a lower electrical conductivity.[171]

Moreover, Figure 66 indicates that the percolation threshold for the electrical conductivity of the Si_3N_4/ZrN composites prepared from pre-reacted powders was obtained at 16 vol. % of the ZrN content, which is almost two times lower than in the case of the composites prepared with the conventional composite method using mechanically mixed powders[15].

The main difference between our Si_3N_4/ZrN composites prepared from pre-reacted powders and those fabricated with the one of the conventional methods starting from the mechanically mixed Si_3N_4 and ZrN powders[118], by mixing carbon black and zircon powders followed by the carbothermal-nitridation process[123] or by a reaction[59] between $ZrSi_2$ and N_2 during sintering is that a much lower percolation threshold for the electrical conductivity can be obtained in our composites, because the ZrN particles with a relatively small size distribution are well dispersed within the matrix phase. Furthermore, the Si_3N_4/ZrN composites prepared from the ZrN-coated Si_3N_4 powders can be explored in a novel approach for preparing electrically conductive ceramic composites, provided that oxygen will not be traped into the lattice.

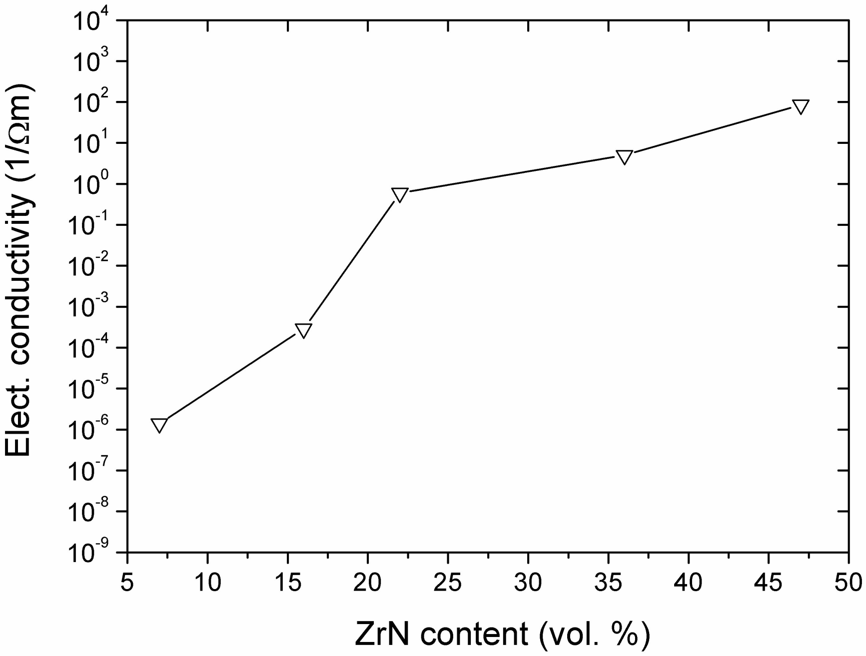

Figure 66: Change in the electrical conductivity of Si_3N_4/ZrN composites with the ZrN contents.

4.3.3.4 A simple theoretical percolation-threshold model

Here again, a simple model of the percolation threshold in the case of small conducting grains compared to anisotropic insulating grains was used to interpret the results of electrical conductivity of the Si_3N_4/ZrN composites. According to the proposed simple theoretical percolation-threshold model, shown in Figure 80 (see page 143), the volume fraction of the conductive phase (percolation threshold) as a function of the particle size (diameter) of the conductive phase, presented in Figure 67, was calculated using Equation 29 (presented on page 144). It can be seen that the percolation threshold as a function of the diameter of the conductive particles varies with the aspect ratio of the insulating ellipsoids. In this system the aspect ratio of the insulating ellipsoids varied with regard to the 2a axis from 0.6 μm to 1.4 μm and with regard to the 2c axis from 4 μm to 10 μm, as shown in Figure 67. The percolation threshold for the electrical conductivity of the ceramic composites predominantly depends on the particle shape and size, the volume fraction and the spatial arrangement of the conductive particles. Our proposed model demonstrates that by increasing the particle size of the conductive particles, the percolation threshold increases as well. In addition, the percolation threshold decreases with a lower aspect ratio of insulating ellipsoids at the defined particle size of the conductive phase (Figure 67). In order to do so, the following parameters were considered: the aspect ratio of elongated β-Si_3N_4 grains (insulating ellipsoids) from the SEM images of the Si_3N_4/ZrN composites was found to be 5; and the experimental percolation threshold of 16 vol. % of the ZrN content was used for this system. These two experimental values were plotted on the graph presented in Figure 67 (see the arrow points). According to this model, the particle size of the conductive particles at the experimental percolation threshold (see the arrow points) was found to be 155 nm.

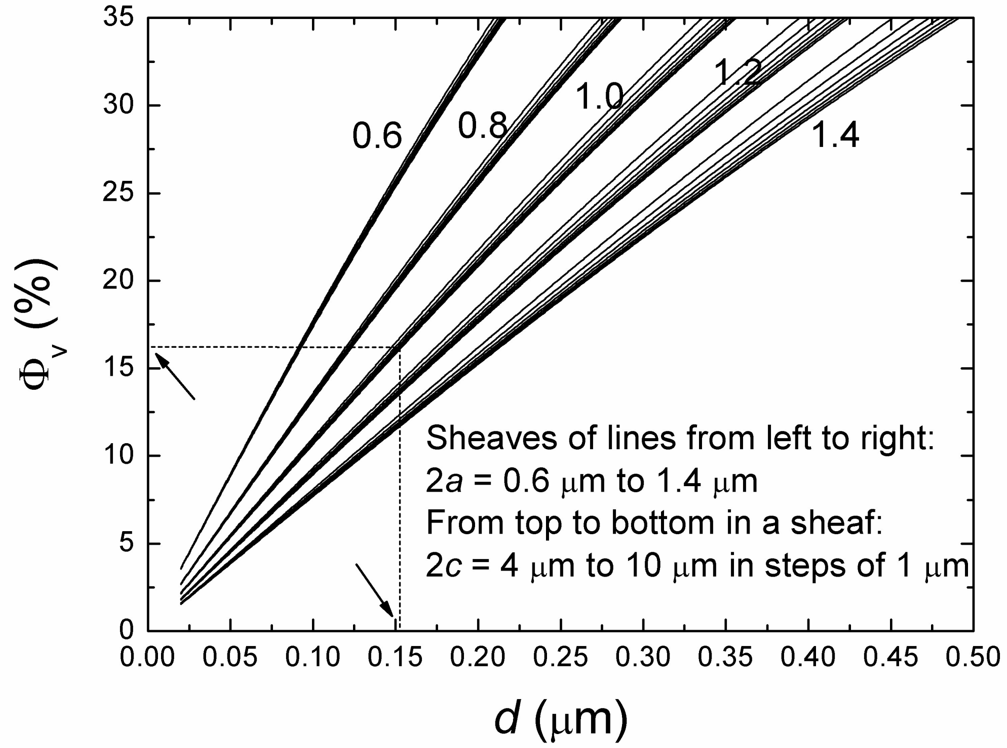

Figure 67: Calculated percolation threshold for the proposed model of the Si_3N_4/ZrN system considering various aspect ratios of insulating ellipsoids as a function of the diameter of the conductive particles.

In order to confirm the presence of ZrN particles with this particle size, the size distribution of the ZrN particles was evaluated from the 2D SEM micrograph (Figure 68) and the TEM image (Figures 69 & 70) of the Si_3N_4/ZrN composite, which initially contained 25 vol. % of ZrO_2 in the starting composition. The evaluated size distribution of the ZrN particles from the 2D SEM micrograph of this sample, shown in Figure 68, indicates that the composite exhibits a relatively wide size distribution of these particles. In addition, it can be seen that most of the ZrN particles in the composite have an average particle size from 157 nm to 185 nm. Besides these small particles, a few larger ZrN particles were found having a particle size ranging from 0.3 μm to 1.2 μm, which implies that these particles had grown and agglomerated during the sintering.

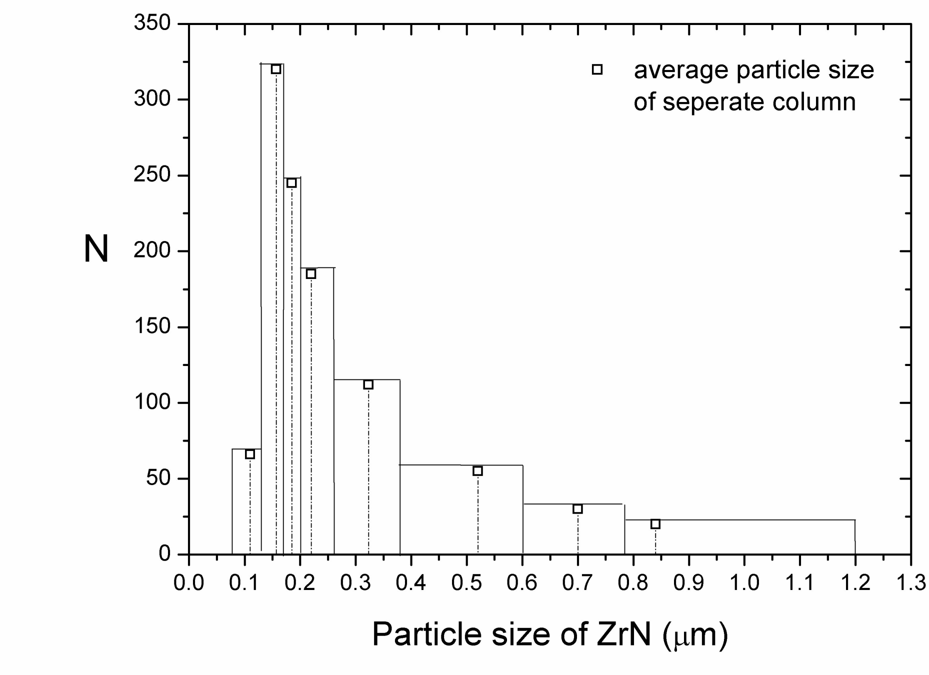

Figure 68: Evaluated numbers of ZrN particles in the Si_3N_4/ZrN composite containing 25 vol. % of ZrO_2 in the starting composition versus their size distribution.

The same size distribution of ZrN particles in this sample was confirmed by a TEM analysis. From Figures 69 & 70 it can be seen that the ZrN particles are present in between Si_3N_4 grains or are incorporated into the Si_3N_4 grains. The latter have a particle size of 158 nm, which is in good agreement with the estimated particle size (155 nm) of the ZrN particles from the simple, theoretical percolation-threshold model. This strongly implies that the nanosized ZrN particles can be preserved only when the conductive particles are incorporated within the Si_3N_4 grains. Therefore, the nanosized ZrN particles remained spherical, whereas the larger ones, which were present in between Si_3N_4 grains, became irregular due to the grain growth and aggregation of the ZrN during the sintering in a liquid phase. All the denoted phases from Figure 69 were confirmed by EDXS.

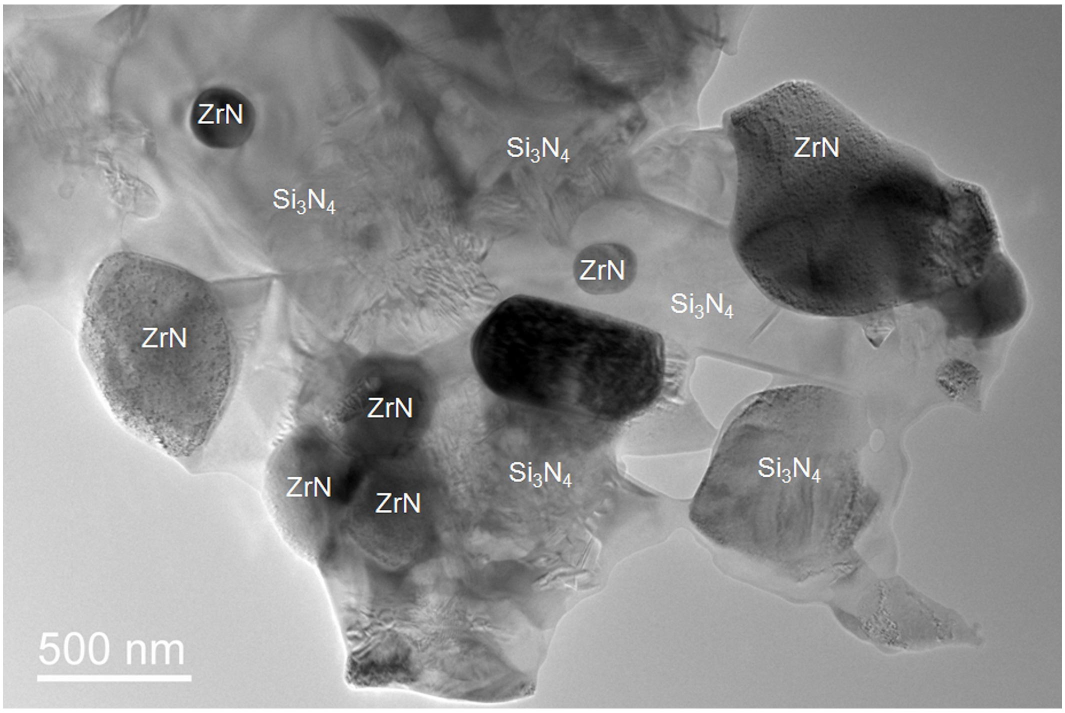

Figure 69: TEM micrograph of the sintered Si_3N_4/ZrN composite containing 25 vol. % of ZrO_2 in the starting composition.

A TEM image of this composite observed at a higher magnification is shown in Figure 70. The denoted spots (a nanosized particle and a triple point near a large particle) were examined by an EDXS analysis. Figure 71 a shows the EDXS spectrum of the analyzed nanometric particle (see the arrow denoted as EDXS A in Figure 70), where the signals of Zr and N containing a trace of Si were detected. The signal of Si comes from the vicinity because ZrN is surrounded by Si_3N_4 particles. Moreover, the transient liquid phase at the triple point (see the arrow denoted as EDXS B in Figure 70) was examined.

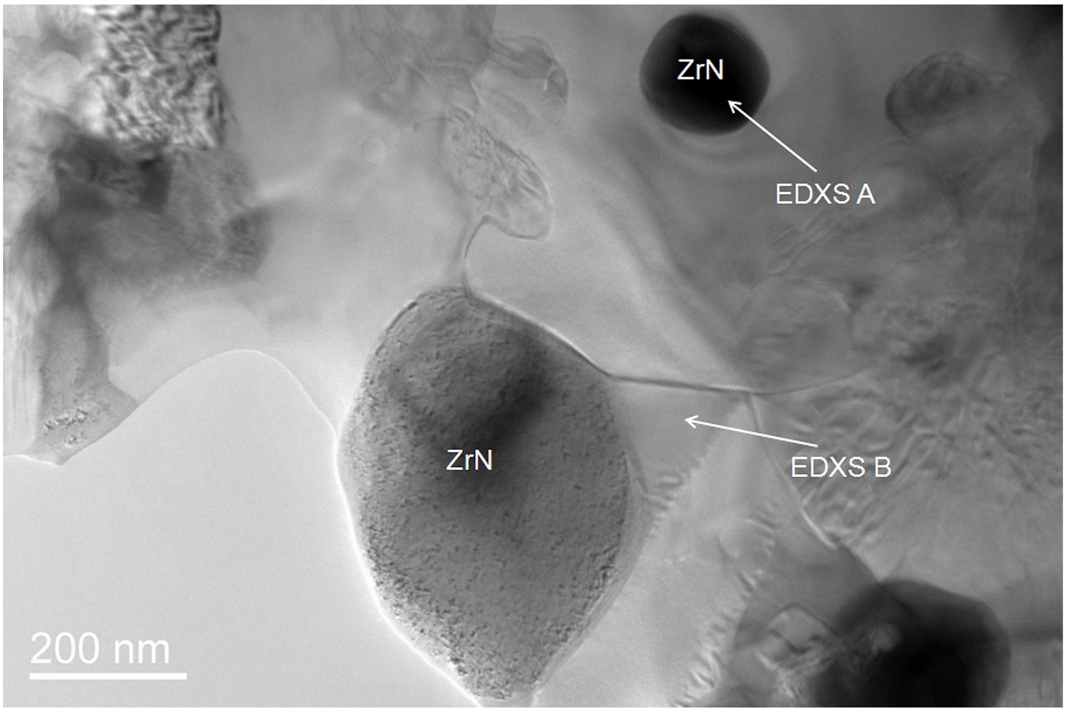

Figure 70: TEM image of the sintered Si_3N_4/ZrN composite containing 25 vol. % of ZrO_2 in the starting composition.

The EDXS spectrum, displayed in Figure 71 b shows strong signals of Y, O and Si, and weak signals of Al and Zr. The trace of Zr in the transient liquid phase indicates that some ZrN probably dissolves in the liquid phase and afterwards precipitates from the liquid during cooling. The formation of the transient liquid phase during cooling from the sintering temperature should be described by Equation 1 (presented on page 7).

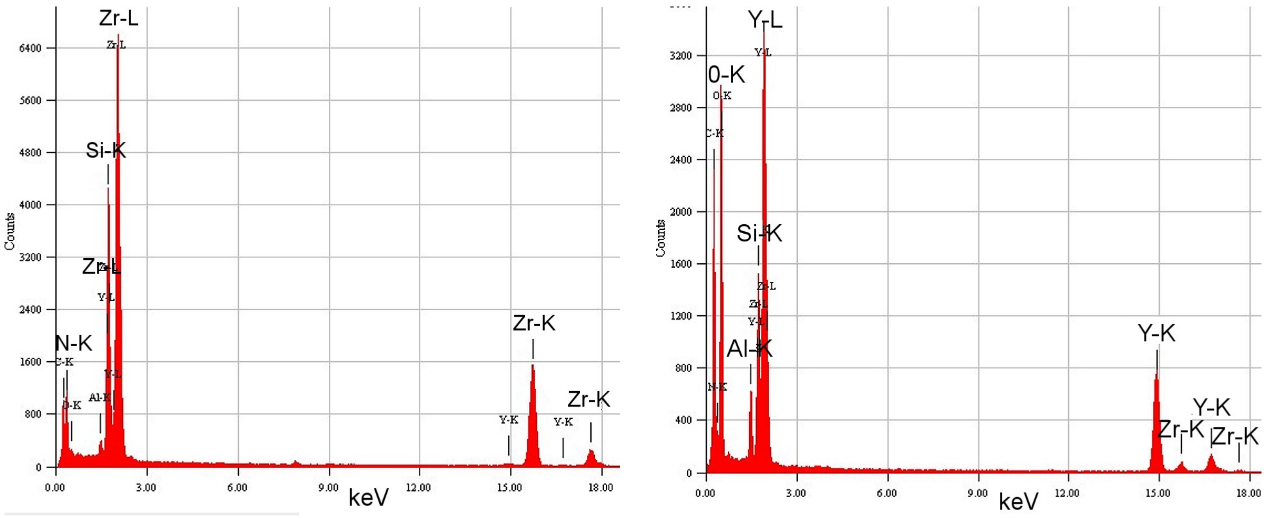

a) b)

Figure 71: EDXS analysis of the sintered Si_3N_4/ZrN composite with 25 vol. % of ZrO_2 detected as shown in the previous figure: a) EDXS A and b) EDXS B.

4.3.4 Sintering using an in-situ reacted powder

As mentioned in the previous section, sintering of the pre-reacted powder may result in the presence of a small amount of oxygen into the ZrN. In order to suppress the incorporation of oxygen into the ZrN lattice, the powder preparation was changed, such that the ZrO_2-coated Si_3N_4 powders were mixed together with yttria and alumina additives, pressed and directly sintered at 1850 °C for 2 h in N_2. Si_3N_4 powders containing 10 and 20 vol. % of ZrO_2 in the starting composition were referred to as the in-situ reacted powder (Figure 26 b, shown on page 49). It was expected that during the sintering process ZrO_2 would also react with Si_3N_4 to form ZrN in the final Si_3N_4/ZrN composites.

4.3.4.1 Analyses of the sintered composites

A cross-section microstructure at lower magnification of the sintered composite that initially contained 10 vol. % of ZrO_2 in the starting composition shown in the Figure 72, indicating that sample is fairly dense with uniformly distributed pores. The microstructure of this sample, displayed in Figure 72 b, showed a uniform distribution of white, irregular ZrN particles around the β-Si_3N_4 grains. Even when the composites were prepared from in-situ reacted powders, the ZrN particles coarsened during sintering in the presence of a liquid phase. The average particle size was approximately 0.8 μm, which is a little bit higher than in the case of the composite prepared from a pre-reacted powder, which initially contained the same amount of ZrO_2 in the starting composition.

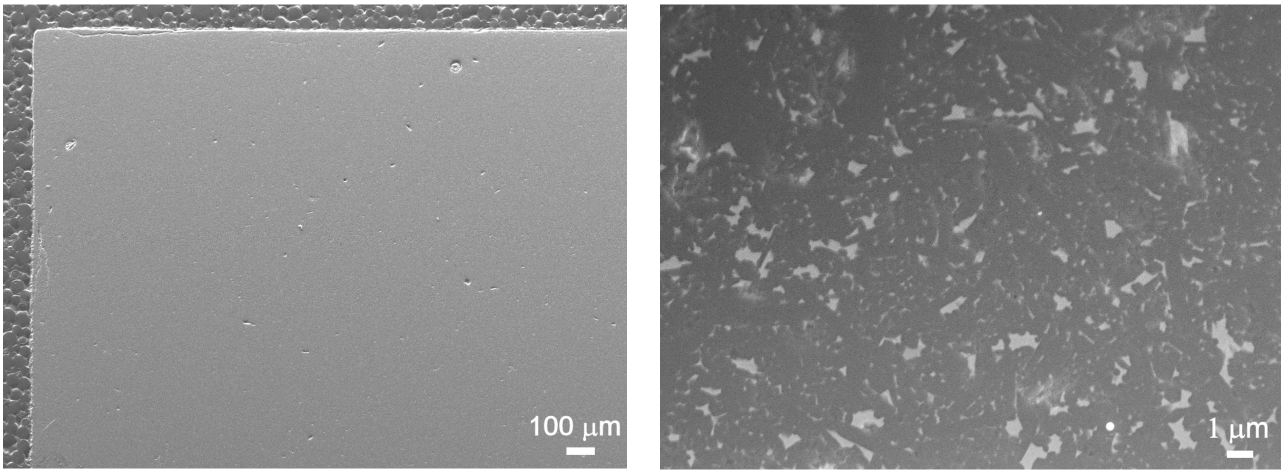

a) b)

Figure 72: SEM micrographs of the Si_3N_4/ZrN composite containing 10 vol. % of ZrO_2 produced by sintering the ZrO_2-coated Si_3N_4 powder and the Y_2O_3 and Al_2O_3 powder mixture at 1850 °C for 2 h in N_2: a) cross-section and b) internal part of material.

The XRD analysis of this sample, presented in Figure 73, confirmed the presence of ZrN in the sample and, besides that no ZrO_2 signals were detected, indicating that the conversion of ZrO_2 to ZrN was complete. Furthermore, it was observed that ZrN peaks are not shifted as in the case of the sintered samples prepared from pre-reacted powders. This means that ZrN, which forms with the reaction between the ZrO_2 particles and the Si_3N_4 powder surface during sintering in a liquid phase, does not contain incorporated oxygen. This can be explained with the reaction between ZrO_2 and Si_3N_4 leading to the formation of ZrN, which takes place above the formation of a liquid phase in the Y_2O_3-Al_2O_3-SiO_2 system.[172]

This composite exhibited a relatively high density of 3.38 g/cm^3 and a high flexural strength of 950 MPa, whereas the density of the sample after the removal of the 100 μm surface layer was even higher, 3.54 g/cm^3. The higher porosity of the surface layer of the sample could be explained by the evaporation of the SiO and N_2 gaseous species formed during the chemical reaction between the ZrO_2 and Si_3N_4 (reaction 18, presented on page 29). A similar observation was reported by Chockalingam et al.[119] in the case of the microwave-sintered β-SiAlON/ZrO_2 composites.

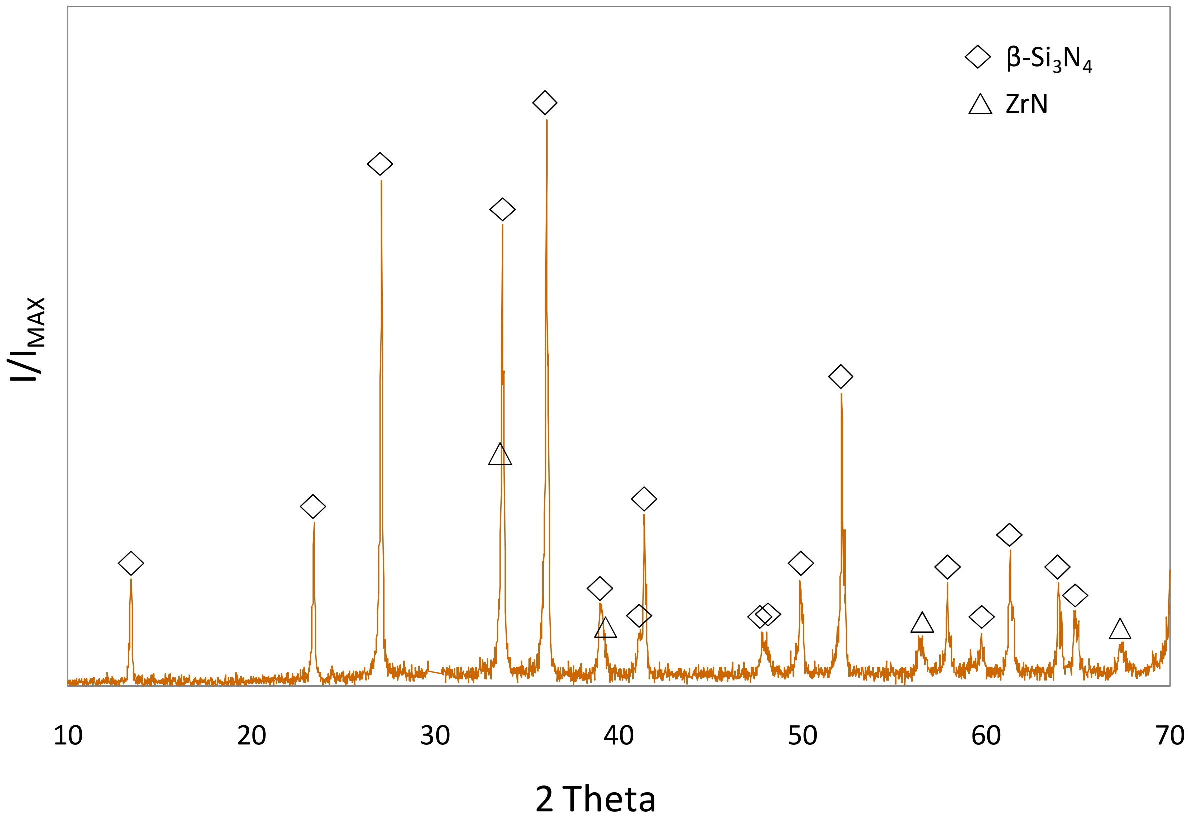

Figure 73: XRD analysis of the Si_3N_4/ZrN composite sintered from an in-situ reacted powder containing 10 vol. % of ZrO_2 in the starting composition.

In the case, when a composite contained a larger amount (20 vol. %) of ZrO_2 in the starting powder mixture, the situation was somewhat different. The SEM analysis of this sample, presented in Figure 74, indicated that the material was not homogeneous. On the surface of the composite two different partially porous surface layers were observed with a thickness of around 200 μm, whereas the internal part of the sample was fully dense. The EDXS analysis of the partially porous outer surface layers of the composite revealed that ZrN is the major phase. Individual layers of the composite (Figure 74 a) were examined by an XRD analysis which is shown in Figure 75. This was done by grinding the sample to various thicknesses and analysing the grinded surfaces. The results show that the external surface layer (referred to as I) mostly contained ZrN, in addition to β-Si_3N_4, while in the internal surface layer (referred to as II) the only important difference is that the amount of ZrN is slightly decreased due to the increased amount of Si_3N_4. Also, in this case, the ZrN peaks from the XRD analysis regarding the removed surface layers were not shifted, which implies that the ZrN particles do not contain any oxygen.

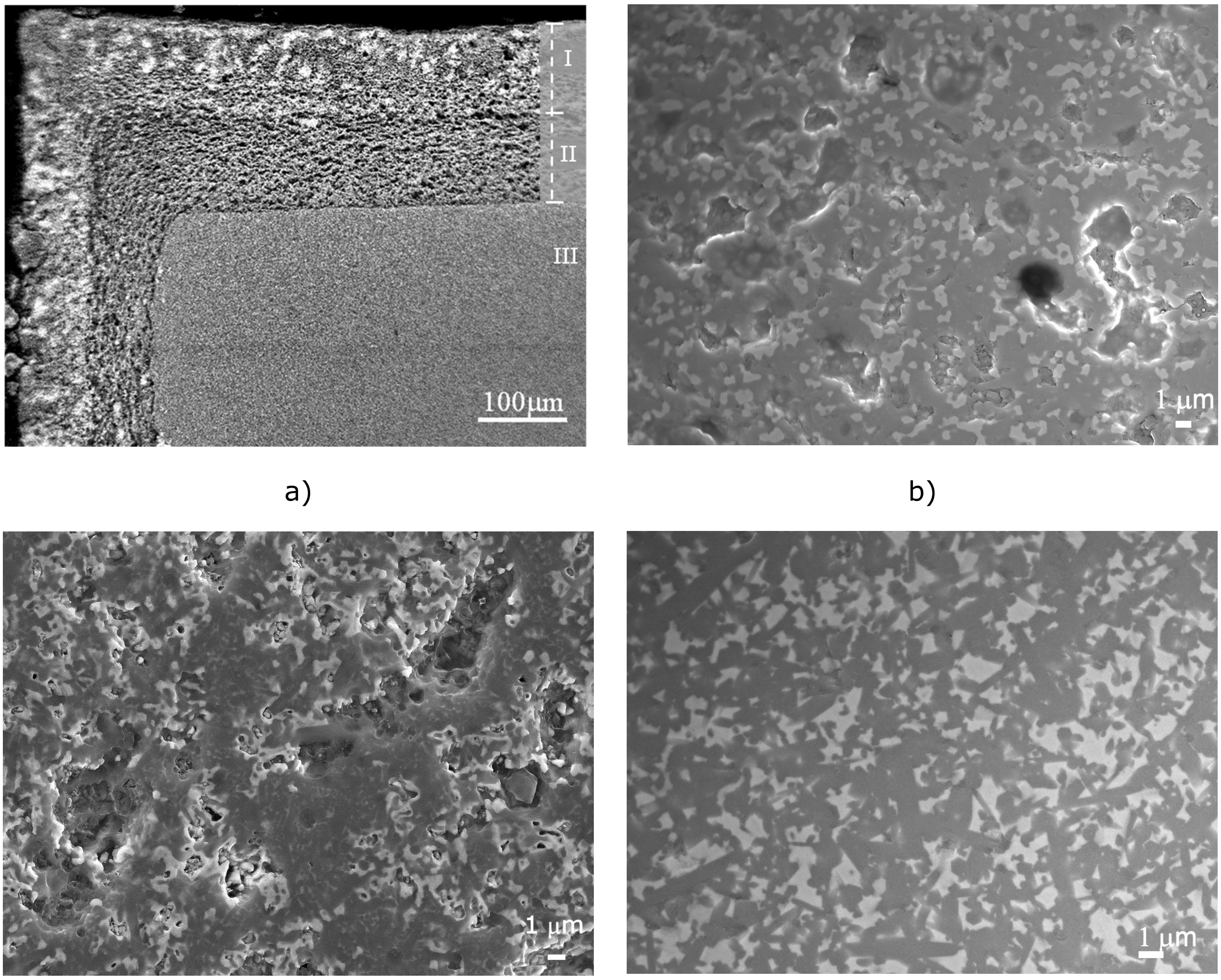

a) b)

c) d)

Figure 74: SEM images of the Si_3N_4/ZrN composite sintered at 1850 °C for 2 h in N_2 from an in-situ reacted powder containing 20 vol. % of ZrO_2 in the starting powder mixture: a) cross-section b) external surface layer (I) c) internal surface layer (II) and d) internal part of the sample (III).

The analysis of the internal part of the sample (referred to as III) showed that, in this region, ZrO_2 is still present in addition to ZrN and Si_3N_4. The presence of this phase can be attributed to the built-up of the SiO partial pressure in the powder compact sintered in flowing nitrogen at 1 atm. This is in agreement with the results obtained on the thermally treated ZrO_2-coated Si_3N_4 powder at 1600 °C for 2 h in flowing N_2 that contained the same amount of ZrO_2 in the starting composition (Figure 52, presented on page 85). In comparison to the external layers (I & II) we also found that here the ZrN peaks are slightly shifted, indicating that also in this case some oxygen was incorporated in to the ZrN lattice during sintering.

The amount of ZrO_2 that transformed to ZrN was calculated from the XRD diffraction patterns using Rietveld analysis and was around 50 %.

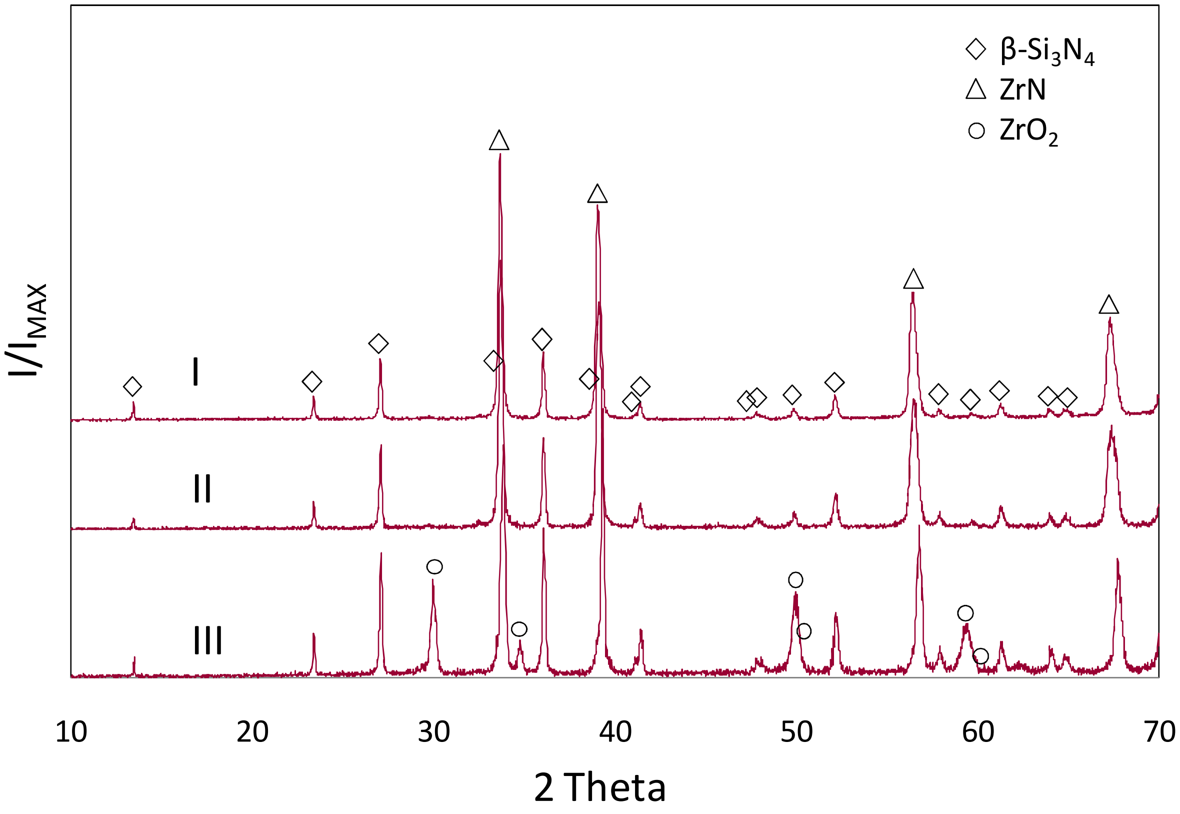

Figure 75: X-ray diffraction pattern of the sintered Si_3N_4/ZrN composite prepared from an in-situ reacted powder containing 20 vol. % of ZrO_2 in the starting composition: I) external surface layer, II) internal surface layer and III) internal part of the composite.

In order to distinguish whether the structure of the ZrO_2 is cubic or tetragonal the XRD analysis, shown in Figure 76, was performed on the internal part of the composite (III), after a subsequent grinding of the surface, in the 2 θ range from 25 to 40 ° with a longer integration time of 5 s per step. On the supposition that the ZrO_2 is in a tetragonal form, after the grinding of the surface a monoclinic phase should have formed due to the mechanical stress. The results of the XRD analysis however showed that after grinding there are no peaks of the monoclinic ZrO_2 visible, indicating that the ZrO_2 has a cubic crystal structure.

The microstructures of the external surface layers (shown in Figures 74 b & c) are partially porous. The distribution of ZrN particles between the β-Si_3N_4 grains was irregular, with a particle size of 1.0 μm. The density of the whole sample, including the layers, was 3.6 g/cm^3, whereas the density of the internal part (i.e., after removal of the porous surface layers) was 3.9 g/cm^3. In this case, the absolute density of this composite is given due to the presence of various phases in the individual layers of the material and a calculation of the theoretical density is not possible. The flexural strength of the as-sintered sample was 860 MPa, which is relatively high, especially considering the surface of the composite is partially porous.

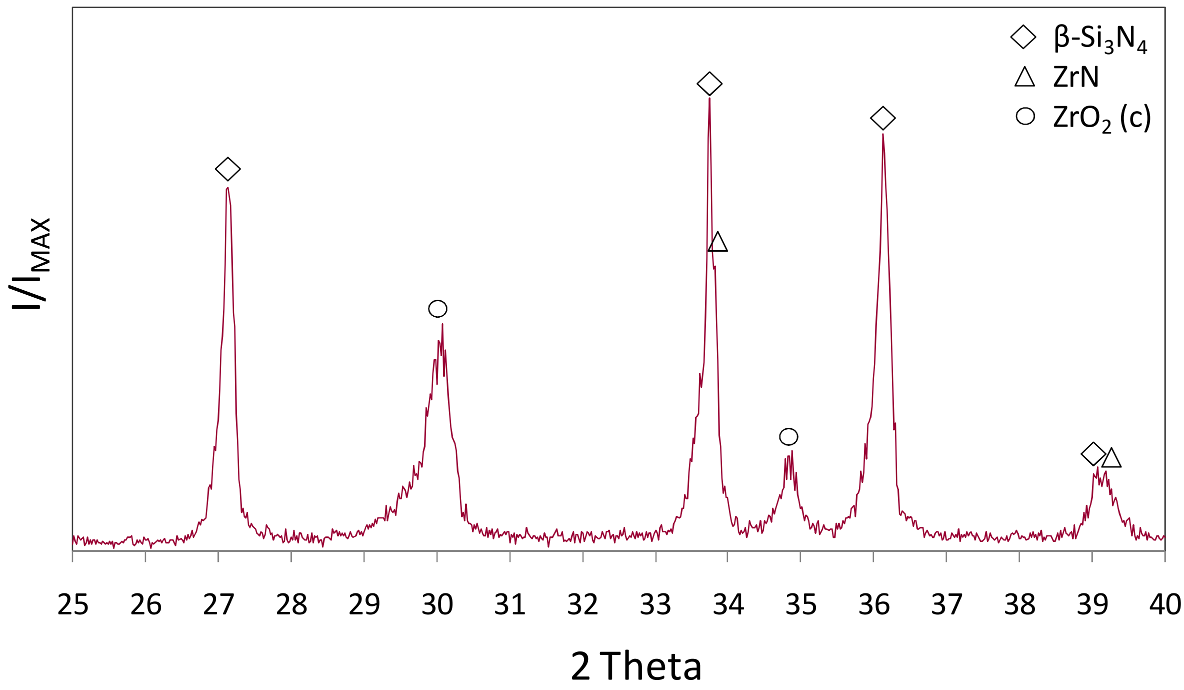

Figure 76: XRD spectrum of a internal part (III) of the sintered Si_3N_4/ZrN composite prepared from an in-situ reacted powder containing 20 vol. % of ZrO_2 analysed in the 2 θ range from 25 to 40 °.

It is believed that the porosity in these layers is a consequence of gaseous species formed during the reaction between ZrO_2 and Si_3N_4. In the internal part of the sample, as shown in Figure 74 d, the microstructure was completely homogeneous and fully dense with about 50 % of ZrN and about 50 % of ZrO_2 as the secondary phase. The size of ZrO_2 particles was 1.2–1.5 μm due to the grain growth of ZrO_2 during sintering. It was observed that ZrO_2 and ZrN grains often had irregular shapes, which implies that at least some of the ZrO_2 and ZrN grains grew from the liquid during cooling. Cheng and Thompson[115] who studied Y_2O_3-Al_2O_3-SiO_2 liquids containing 20 wt. % of ZrO_2 showed that about 10 wt. % of ZrO_2 can be dissolved at 1700 °C in the liquid phase and the rest remains as crystalline zirconia. The dissolved ZrO_2 will precipitate from the liquid phase on existing zirconia grains during cooling, resulting in a larger grain size.

The incomplete conversion of ZrO_2 to ZrN can be explained by the simultaneous sintering and the chemical reaction between ZrO_2 and Si_3N_4 above 1600 °C in N_2. It was demonstrated by Weiss at al.[127] that a larger amount of ZrO_2 in the starting-composition mixture prolongs the conversion reaction of ZrO_2 to ZrN above 1600 °C in N_2. In addition, it has to be considered that during sintering the densification already starts at 1600 °C, due to the formation of the liquid phase, namely in the Y_2O_3-Al_2O_3-SiO_2 system the ternary eutectic forms at 1375 °C.[172] The reaction between ZrO_2 and Si_3N_4 also takes place at this temperature and, because of the densification, the diffusion of the gaseous species out of the sample is aggravated. This leads to an increase in the SiO partial pressure, which then hinders the formation of ZrN.

Since such electroconductive engineering ceramic materials could be used for the production of heating elements, the electrical conductivity of the samples was also measured. Because samples were not homogenous, the electrical conductivity was measured at various thicknesses from the surface such that surface layers were ground off. From the results presented in Figure 77, it can be seen that the sample containing 10 vol. % of ZrO_2 (denoted as C10) in the starting powder mixture is not electrically conductive, neither on the surface of the sample nor in its core. Since we started from very fine ZrO_2 nanoparticles, it was speculated that they would not grow too much during reacting and sintering and that their size would remain small enough to lower the percolation threshold of the electrical conductivity below 10 vol. %. However, as it can be observed from the microstructural analysis (Figures 72 & 74), ZrN particles are relatively coarse and consequently we ended well below the percolation threshold. On the other hand, the surface of the sample that contained 20 vol. % of ZrO_2 (denoted as C20) in the starting powder was conductive (Figure 77). The conductivity slightly dropped when the two-porous surface layers (layer I & II) were removed, but the rest of the sample remained an electrical conductor, until 550 μm of the material was removed. As already mentioned, the transformation of ZrO_2 to ZrN in the core was estimated to be around 50 %. Based on this, the concentration of ZrN in the core material is approximately the same as in the sample C10 and so is the electrical conductivity, since ZrN grains also grew in this case.

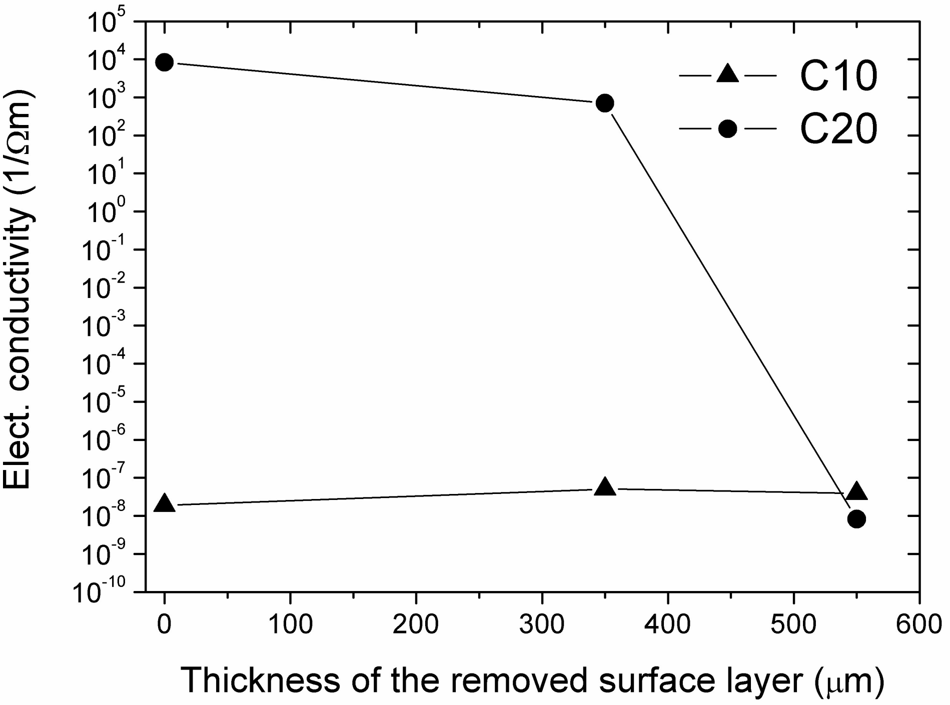

Figure 77: Change in the electrical conductivity of Si_3N_4/ZrN composites prepared from an in-situ reacted powder containing 10 vol. % of ZrO_2 (denoted as C10) and 20 vol. % of ZrO_2 (denoted as C20) in the starting powder mixture as a function of the thickness of the removed surface layer.

From these results it can be concluded that sintering of Si_3N_4/ZrN composites prepared from in-situ reacted powders enables the formation of ZrN by the reaction between ZrO_2 and Si_3N_4 without incorporation of oxygen, when starting powder contained 10 vol. % of ZrO_2. Furthermore, it was demonstrated that in samples C20, the conversion of ZrO_2 to ZrN was not completed. Most probable due to the SiO partial pressure, which forms during the reaction between ZrO_2 and Si_3N_4. During sintering, the diffusion of the gaseous species out of the sample is aggravated, which leads to an increase in the SiO partial pressure and, consequently, hinders the formation of ZrN. Irrespective of the density gradient from the core to the outer surface of the sample, the composite exhibited a high flexural strength and its surface is electrically conductive.

4.3.4.2 Application of the Si_3N_4/ZrN composites prepared from an in-situ reacted powder

The preparation of Si_3N_4/ZrN composites from an in-situ reacted powder containing 20 vol. % of ZrO_2 in the starting powder mixture showed that after sintering at 1850 °C for 2 h in flowing N_2 the reaction between ZrO_2 and Si_3N_4 is not complete. SEM and XRD analyses revealed that the sample is not homogenous and that the ZrN is mostly formed on its surface. Since the electrical resistivity showed that the surface of the sample was electrically conductive, whereas the internal part remained an insulator, we found that such a composite is already prepared for ceramic heaters or glow plugs. In this way, we designed the sample geometry, shown in Figure 78, where the lateral sides of the prototype were cut in order to remove the conductive layer, so that the current would flow on the internal side of the conductive layer.

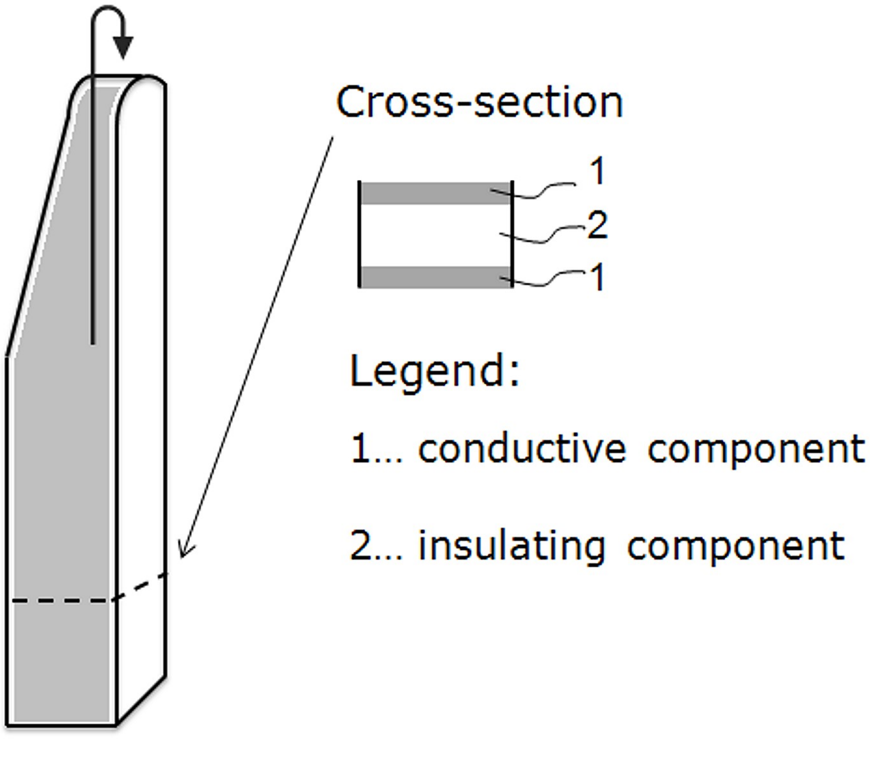

Figure 78: Geometry of a prototype ceramic heater.

The functioning of this tested sample was confirmed by applying 12 volts and it started to glow at 1300 °C and 8 amperes of current at the nib of the sample, as shown in Figure 79. The tested sample has an extremely short preheat time, i.e., 2.0 seconds, before achieving the operating temperature of 1300 °C. The calculated resistivity of the prototype was 1.56 Ω, which corresponds to the operating characteristics of a conventional ceramic heater.[173] We have found that these results are promising for the production of heating elements. Therefore, the one-step manufacturing process of composite ceramic heater was patented (P2-201100015). Irrespective of the concept of the glow plugs and the geometry of the ceramic heater, the common characteristic of the patents for the production of ceramic heaters is a two– or multi-step production by injection moulding or slip casting.

Figure 79: Glowing of the designed prototype at 1300 °C.

The modelling of the ceramic heaters by a multi-step process is technologically challenging. In addition, during sintering or during the operation of a heater problems can occur due to the incomplete contact between the conductive and insulating components, which leads to a poor operation or even to the failure of the material. Our innovation demonstrates that a ceramic heater can be developed using only a one-step process, which significantly reduces the extent of the technology and the costs of the production.

5 Conclusions

Coating of the Si_3N_4 powder

1. The surface of submicron-sized commercially available Si_3N_4 powder can be successfully coated with various amounts (10-35 vol. %) of TiO_2 and ZrO_2 by using an in-situ gel precipitation of titanium and zirconium hydroxides and a subsequent thermal treatment. Nanosized TiO_2 (tetragonal) and ZrO_2 (cubic) particles were uniformly distributed on the Si_3N_4 powder surface with a narrow particle size distribution ranging from 4 nm to 10 nm.
2. The formation of TiN particles on the Si_3N_4 powder surface was achieved by a thermal treatment of the coated powders at 900 °C for 6 h in a NH_3 gas flow. The conversion of TiO_2 to TiN can be completed by a thermal treatment in all the coated powders containing 10-35 vol. % of TiO_2 in the starting composition. In addition, after the nitridation the TiN particles preserved almost the same size as that of TiO_2 nanoparticles. The formation of ZrN particles on the Si_3N_4 powder surface is more challenging, due to a higher reaction temperature (1600 °C) between the ZrO_2 and Si_3N_4 and due to the change in the SiO partial pressure. The complete conversion of ZrO_2 to ZrN in all the coated powders (containing various amounts of ZrO_2 in the starting composition) can be attained at 1600 °C for 3 h in flowing nitrogen at low-pressure (P_{N_2} = 0.4 atm). Furthermore, in this case after the thermal treatment the ZrN particles can be preserved in the nanometric scale with a particle size of 40 nm.

Preparation of the Si_3N_4/TiN composites

1. Dense and homogeneous Si_3N_4/TiN composites can be fabricated from pre-reacted powders containing various amount of TiO_2 in the starting powder mixture by pressureless sintering at 1850 °C for 2 h in the flowing N_2.
2. The results of the flexural-strength measurements of the Si_3N_4/TiN composites revealed that with an increase in the amount of TiN in composites, the flexural strength decreases from 615 MPa (98.3 % of the relative density) to a value of 360 MPa (91.1 % of the relative density) at 24 vol. % of TiN.
3. The electrical conductivity of the sintered composites increases sharply from 7 x 10^{-9} $\Omega^{-1}m^{-1}$ at 6 vol. % of TiN to 3.6 x 10^{3} $\Omega^{-1}m^{-1}$ at 24 vol. % of TiN, making

this ceramic suitable for the production of heating elements. The percolation threshold for the electrical conductivity of the Si_3N_4/TiN composites prepared from pre-reacted powders was obtained at 12 vol. % of the TiN content, which is two times lower than in the case of the composites prepared with the conventional composite method using mechanically mixed powders but still higher by a factor of two, than in the case of the composites fabricated by Ayas et al. that were sintered by SPS from TiO_2-coated SiAlON granules.

4. The simple theoretical percolation-threshold model was developed by considering various aspect ratios of insulating ellipsoids as well as different diameters of conductive particles. The results revealed that the simple model of percolation threshold is a good interpretation for the obtained experimental results for electrical conductivity of the Si_3N_4/TiN composites.

Preparation of the Si_3N_4/ZrN composites

1. Relatively dense and homogeneous Si_3N_4/ZrN composites can be prepared starting from pre-reacted powders initially containing 10-35 vol. % of precipitated ZrO_2 by pressureless sintering at 1850 °C for 2 h in N_2. In contrast, composites prepared from an in-situ reacted powder which initially contained 10 and 20 vol. % of precipitated ZrO_2 that were in-situ reacted under the same conditions revealed that in the composite with 20 vol. % of ZrO_2 the reaction between ZrO_2 and Si_3N_4 was not completed.

2. The XRD analysis of the Si_3N_4/ZrN composites prepared from pre-reacted powders containing various amounts of ZrO_2 demonstrated that the ZrN peaks are slightly shifted in all samples suggesting that some oxygen was incorporated into the ZrN lattice. In the case, when the composites were prepared from an in-situ reacted powder containing 10 vol. % of ZrO_2 this was not observed but with the addition of 20 vol. % of ZrO_2 in the starting composition the surface of the as-sintered sample mostly contained ZrN, in addition to β-Si_3N_4, while with grinding the sample to the core of the material, the amount of ZrN decreased due to the increased amount of β-Si_3N_4 and the presence of unreacted ZrO_2.

3. Flexural strength of the Si_3N_4/ZrN composites prepared from pre-reacted powders containing various amount of ZrO_2 in the starting composition decreases with increasing the ZrN content from 600 MPa (97 % of the relative density) at 7 vol. % of ZrN to 350 MPa (90 % of the relative density) at 47

vol. % of ZrN. The Si_3N_4/ZrN composites prepared from in-situ reacted powder containing 10 vol. % and 20 vol. % of ZrO_2 (in the starting composition) exhibited a high flexural strength of 950 MPa and 860 MPa, respectively. However, irrespective of the density gradient from the core to the outer surface of these samples, the materials had a high flexural strength.

4. The results of the electrical conductivity measurements of the Si_3N_4/ZrN composites prepared from pre-reacted powders containing various amounts of ZrO_2 (in the starting composition) showed that the electrical conductivity increased steeply to the value of 85 $\Omega^{-1}m^{-1}$ at 47 vol. % of ZrN with increasing the ZrN content. The low electrical conductivity of these composites which initially contained large amounts of ZrN was explained by an incorporation of a small amount of oxygen into the ZrN. When Si_3N_4/ZrN composites were prepared from an in-situ reacted powder, a sample which initially contained 20 vol. % of ZrO_2 (in the starting composition) was electrically conductive only on the as-sintered surface. The conductivity dropped a little from 8.3 x 10^3 $\Omega^{-1}m^{-1}$ to 7.0 x 10^2 $\Omega^{-1}m^{-1}$ when the surface of 350 μm was removed. After the removal of 550 μm of the sample, this material became an insulator.

5. The simple theoretical percolation-threshold model was developed by considering various aspect ratios of insulating ellipsoids as well as different diameters of conductive particles. The results revealed that the simple model of percolation threshold is a good interpretation for the obtained experimental results for electrical conductivity of the Si_3N_4/ZrN composites prepared from pre-reacted powders.

6 Acknowledgements

I would like to gratefully and sincerely thank my Ph.D. supervisor, Prof. Dr. Tomaž Kosmač, for his guidance, understanding and patience during my graduate studies at the Jožef Stefan Institute. His mentorship was paramount in providing a well-rounded experience, consistent with my long-term career goals. He encouraged me to not only grow as an experimentalist and a chemist but also as an independent thinker.

I would like to thank my co-supervisor, Assist. Prof. Dr. Kristoffer Krnel, for his expert guidance, valuable discussions about my work as well as useful remarks and suggestions.

I would also like to thank Assist. Prof. Dr. Milan Ambrožič for his assistance, discussion and guidance in setting up a simple theoretical percolation-threshold model for the electrical conductivity of the ceramic composites.

I also thank Dr. Irena Pribošič for teaching me the basics of TEM and for discussions about SAED analysis.

Thanks to all my colleagues in the Engineering Ceramics Department, especially Dr. Aleš Dakskobler, Dr. Andraž Kocjan and Sebastjan Perko, for all the support and nice moments that we had spent together over the last four years.

Finally, and most importantly, I would like to thank my family and my girlfriend for their moral support, encouragement and quiet patience.

7 References

[1] Petzow, G.; Herrmann, M. Silicon nitride ceramics. *Structure and Bonding* **102**, 51 (2002).

[2] Hirosaki, N.; Okada, A.; Matoba, K. Sintering of Si_3N_4 with the Addition of Rare Earth Oxides. *Journal of American Ceramic Society* **71**, C144 (1988).

[3] Greil, P.; Petzow, G.; Tanaka, H. Sintering and hipping of siliconnitride–silicon carbide composite materials. *Ceramic International* **13**, 19 (1987).

[4] Medri, V.; Bracisiewicz, M.; Krnel, K.; Winterhalter, F.; Bellosi, A. Degradation of mechanical and electrical properties after long-term oxidation and corrosion of non-oxide structural ceramic composites. Journal of European Ceramic Society 25, 1723 (2005).

[5] Ayas, E.; Kara, A.; Mandal, H.; Turan, S.; Kara, F. Production of α-β SiAlON-TiN/TiCN composites by gas pressure sintering. *Silic. Ind.* **69**, 287 (2004).

[6] Han, C-J.; Chen, Q-G.; Du, Y-S.; Wood V. J. Synthesis of Si_3N_4-TiN-SiC composites by combustion reaction under high nitrogen pressures. *Journal of European Ceramic Society* **20**, 927 (2000).

[7] Jiang, D.; Vleugels, J.; Van der Biest, O.; Liu, W.; Verheyen, R.; Lauwers, B. Electrically Conductive and Wear Resistance Si_3N_4-based Composites with $TiC_{0.5}N_{0.5}$ Particles for Electrical Discharge Machining. *Materials Science Forum* **492**, 27 (2005).

[8] Bitterlich, B.; Bitsch, S.; Friederich, K. SiAlON based ceramic cutting tools. *Journal of European Ceramic Society* **28**, 989 (2008).

[9] Bracisiewicz, M.; Medri, V.; Bellosi, A. Factors including degradation of properties after long term oxidation of Si_3N_4-TiN electroconductive composites. *Applied Surface Science* **202**, 139 (2007).

[10] Guo, Z.; Blugan, G.; Graule, T.; Reece, M.; Kuebler, J. The effect of different sintering additives on the electrical and oxidation properties of Si_3N_4-$MoSi_2$ composites. *Journal of European Ceramic Society* **27**, 2153 (2007).

[11] Lee, T. B.; Yoon, J. Y.; Lee, H. K. Microstructural characterization of electroconductive Si_3N_4-TiN composites. *Materials Letters* **47**, 71 (2001).

[12] Martin, C.; Cales, B.; Vivier, P.; Mathieu, P. Electrical discharge machinable ceramic composites. *Material Science Engineering* **A109**, 351 (1989).

[13] Tamaoki, K.; Manabe, K.; Kataoka, S.; Aizawa, T. Electroconductive ceramic tooling for dry deep drawing. *Journal of Materials Processing Technology* **210**, 48 (2010).

[14] Jones, H. A.; Trueman, C.; Dobedoe, S. R.; Huddleston, J.; Lewis, H. M. Production and EDM of Si_3N_4-TiB_2 ceramic composites. *British Ceramic Transactions* **100**, 49 (2001).

[15] Zivkovic, Lj.; Nikolic, Z.; Boskovic, S.; Miljkovic, M. Microstructural characterization and computer simulation of conductivity in Si_3N_4-TiN composites. *Journal of Alloys and Compounds* **373**, 231 (2004).

[16] Sciti, D.; Balbo, A.; Melandri, C.; Pezzotti, G. Microstructure and properties of an electroconductive SiC-based composite. *Journal of Material Science* **42**, 5570 (2007).

[17] Petrovic, J. J.; Pena, I. M.; Reimanis, E. J.; Sandlin, S. M.; Conzone, D. S.; Kung, H. H.; Butt, P. D. Mechanical Behavior of $MoSi_2$ Reinforced-Si_3N_4 Matrix Composites. *Journal of American Ceramic Society* **80**, 3070 (1997).

[18] Kao, Y. M. Properties of Silicon Nitride-Molybdenum Disilicide Particulate Ceramic Composites. *Journal of American Ceramic Society* **76**, 2879 (1993).

[19] Gao, S.; Kagawa, Y. Thermal and Electric Properties in Hot-Pressed ZrB_2-$MoSi_2$-SiC Composites. *Journal of American Ceramic Society* **90**, 2255 (2007).

[20] Xikun, Li.; Jing, Liu.; Like, Qiu.; Tong, Cui.; Guanming, Qiu.; Yanbin, Sun. Composition, Characteristics and Development of Advanced Ceramic Cutting Tools. *Journal of Rare Earths* **25**, 287 (2007).

[21] Krnel, K.; Sciti, D.; Bellosi, A. Influence of long term oxidation on the microstructure, mechanical and electrical properties of pressureless sintered AlN-SiC-$MoSi_2$ ceramic composites. *Journal of European Ceramic Society* **23**, 3135 (2003).

[22] Landon, M.; Thevenot, F. The AlN–SiC system: influence of elaboration routes on the solid solution formation and its mechanical properties. *Ceramic International* **17**, 97 (1991).

[23] Huang, J. L.; Jih, J.M. Investigation of SiC–AlN system: part I. Microstructure and solid solution. *Journal of Material Research* **10**, 651 (1995).

[24] Lavrenko, V. A.; Desmaison-Brut, M.; Panasyuk, A. D.; Desmaison,J. Features of corrosion resistance of AlN–SiC ceramics in air up to 1600 °C. *Journal of European Ceramic Society* **18**, 2339 (1998).

[25] Grande, T.; Mokkelbost, T.; Tangen, L. I. Preparation and characterisation of aluminium nitride-silicon carbide composites. *Ceramics International* **30**, 931 (2004).

[26] Huang, R.; Gu, H.; Chen, Z. The sintering mechanism and microstructure evolution in SiC-AlN ceramics studied by EFTEM. *International Journal of Materials Research* **97**, 614 (2006).

[27] Bellosi, A.; Guricciardi, S.; Tampieri, A. Development and characterization of electroconductive Si_3N_4-TiN composites. *Journal of the European Ceramic Society* **9**, 83 (1992).

[28] QiLiang, H.; Juan, C.; Wei, P. In situ processing of TiN/Si_3N_4 composites by Ti-Si_3N_4 solid state reaction. *Materials Letters* **31**, 221 (1997).

[29] Duan, G. R.; Roebben, G.; Vleugels, J. Effect of TiX(X = C, N, O) additives on microstructure and properties of silicon nitride based ceramics. *Scripta Materiallia* **53**, 669 (2005).

[30] Gogotsi. G. Y.; Portz, F. The oxidation of particulate-reinforced Si_3N_4-TiN composites. *Corrosion Science* **33**, 627 (1992).

[31] Lences, Z.; Panek, Z. Electroconductive β-SiAlON/TiN composites prepared by reaction sintering. *Ceramics Silikaty* **43**, 81 (1999).

[32] Gao, L.; Li, J.; Kusunose, T.; Niihara, K. Preparation and properties of TiN-Si_3N_4 composites. *Journal of European Ceramic Society* **24**, 381 (2004).

[33] Ayas, E.; Kara, A.; Kara, F. A novel approach for preparing electrically conductive α/β SiAlON-TiN composites by spark plasma sintering. *Journal of the Ceramic Society of Japan* **116**, 812 (2008).

[34] Riley, L. F. Silicon Nitride and Related Materials. *Journal of American Ceramic Society* **83**, 245 (2000).

[35] Collins, F. L.; Gerby, W. R. New Refractory Uses for Silicon Nitride Reported. *Journals of Meteorology* **7**, 612 (1955).

[36] Parr, L. N.; Martin, F. G.; May, W. R. E. *Preparation, Microstructure, and Mechanical Properties of Silicon Nitride, in Special Ceramics 1*. (Popper, P., Heywood, London, 1960).

[37] Deeley, G. G.; Herbet, M. J.; Moore, C. N. Dense Silicon Nitride. *Powder Metallurgy* **8**, 145 (1961).

[38] Coe, F. R.; Lumby, J. R.; Pawson, F. M. *Some Properties and Applications of Hot-Pressed Silicon Nitride, in Special Ceramics 5*. (Popper, P., Stoke-on-Trent, U.K., 1972).

[39] Lange, F. F. The sophistication of ceramic science through silicon nitride studies. *Journal of Ceramic Society of Japan* **114**, 873 (2006).

[40] Weiss, L.; Engelhardt, T. On Nitrogen Compounds of Silicon. Journal of Inorganic Chemistry **65**, 38 (1910).

[41] Hardie, D.; Jack, H. K. Crystal Structures of Silicon Nitride. *Nature* **180**, 332 (1957).

[42] Turkdogan, T. E.; Bills, M. P.; Tippett, A. V. Silicon Nitrides: Some Physico-Chemical Properties. *Journal of Applied Chemistry* **8**, 296 (1958).

[43] Thompson, S. D.; Pratt, I. P. *The Structure of Silicon Nitride, in Science of Ceramics* (Stewart, H. G., Academic Press, New York, 1967).

[44] Priest, F. H.; Burns, C. F.; Priest, L. G.; Skaar, C. E. The Oxygen Content of Alpha Silicon Nitride. *Journal of American Ceramic Society* **56**, 395 (1973).

[45] Brook, J. R.; Messier, R. D.; Riley, L. F. The α/β Silicon Nitride Phase Transformation. *Journal of Material Science* **13**, 1199 (1978).

[46] Hampshire, S. Silicon nitride ceramics – review of structure, processing and properties. *Journal of Achievements in Materials and Manufacturing Engineering* **24**, 43 (2007).

[47] Bernal-Bocanegra, H. M.; Matovic, B. Dense and near-net-shape fabrication of Si_3N_4 ceramics. *Material Science and Engineering A* **500**, 130 (2009).

[48] Gazza, E. G. Effect of Yttria Additions on Hot-Pressed Si_3N_4. *American Ceramic Society Bulletin* **54**, 778 (1975).

[49] Santos, C.; Ribeiro, S.; Strecker, K.; Suzuki, A. P.; Kycia, S.; Silva, M. R. C. Crystallographic characterization of silicon nitride ceramics sintered with Y_2O_3-Al_2O_3 or E_2O_3-Al_2O_3 additions. *Ceramics International* **35**, 289 (2009).

[50] Tsuge, A.; Nishida, K. High-Strength Hot-Pressed Si_3N_4 with Concurrent Y_2O_3 and Al_2O_3 Additions. *American Ceramic Society Bulletin* **57**, 424 (1978).

[51] Gu, H.; Chen, H.; Guo, L. Effect of nano-Al_2O_3 and Y_2O_3 on the properties and microstructure of Si_3N_4. *Materials Science and Engineering A* **491**, 177 (2008).

[52] Loehman, E. R.; Rowcliffe, J. D. Sintering of Si_3N_4-Y_2O_3-Al_2O_3. *Journal Of American ceramic Society* **63**, 3 (1979).

[53] Hirosaki, N.; Okada, A.; Matoba, K. Sintering of Si_3N_4 with the Addition of Rare-Earth Oxides. *Journal of American Ceramic Society* **71**, C144 (1988).

[54] Sanders, A. W.; Miekowski, M. D. Strength and Microstructure of Si_3N_4 Sintered with Rare-Earth Oxide Additions. *American Ceramic Society Bulletin* **64**, 304 (1985).

[55] Hampshire, S.; Jack, H. K. The Kinetics of Densification and Phase Transformation in Nitrogen Ceramics. *Proceedings of British Ceramic Society* **31**, 37 (1981).

[56] Svoboda, J.; Riedel, H.; Gaebel, R. A model for liquid phase sintering. *Acta Materialica* **44**, 3215 (1996).

[57] Kingery, D. W. Sintering in the Presence of a Liquid Phase. *Journal of Applied Physics* **30**, 301 (1959).

[58] Bellosi, A.; Guicciardi, S.; Tampieri, A. Development and characterization of electroconductive Si_3N_4-TiN composites. *Journal of American Ceramic Society* **9**, 83 (1992).

[59] Ade, M.; Hauβelt, J. Electroconductive ceramic composites with low-to-zero shrinkage during sintering. *Journal of European Ceramic Society* **23**, 1979 (2003).

[60] Sawaguchi, A.; Toda, K.; Niihara, K. Mechanical and Electrical Properties of Silicon Nitride – Silicon Carbide Nanocomposite Material. *Journal of American Ceramic Society* **74**, 1142 (1991).

[61] Sciti, D.; Guicciardi, S.; Bellosi, A. Microstructure and Properties of Si_3N_4-$MoSi_2$ Composites. *Journal of Ceramic Processing Research* **3**, 87 (2002).

[62] Bae, K. S.; Shon, J. I.; Doh M. J.; Yoon, K. J.; Ko, Y. I. Properties and consolidation of nanocrystalline Nb_2-SiC-Si_3N_4 composite by pulsed current activated combustion. *Scripta Materialia* **58**, 425 (2008).

[63] Park, H-J.; Koh, H-Y.; Kim, E-H.; Hwang, S-C.; Kang, S-E. Densification and Mechanical Properties of Titanium Diboride with Silicon Nitride as a Sintering Aid. *Journal of American Ceramic Society* **82**, 3037 (1999).

[64] Gogotsi, G. Y. Review-Particulate silicon nitride-based composites. *Journal of Materials Science* **29**, 2541 (1994).

[65] Nagaoka, T.; Yasuoka, M.; Hirao, K.; Kanzaki, S. Effects of TiN Particle Size on Mechanical Properties of Si_3N_4/TiN Particulate Composites. *Journal of Ceramic Society of Japan* **100**, 617 (1992).

[66] Olagnon, C.; Bullock, E.; Fantozzi, G. Processing of high density sintered SiC whisker reinforced Si_3N_4 composites. *Ceramic International* **17**, 53 (1991).

[67] Sigulinski, F.; Boškovič, S. Phase composition and fracture toughness of Si_3N_4-ZrO_2 with CeO_2 additions. *Ceramic International* **25**, 41 (1999).

[68] Diserens, M.; Patscheider, J.; Levy, F. Mechanical properties and oxidation resistivity of nanocomposite TiN-SiN_x physical-vapor-deposited thin films. *Surface and Coatings Technology* **120**, 158 (1999).

[69] Samsonov, V. G.; Vinitskii, M. I. Handbook of Refractory Compounds (IFI/Plenum, New York, 1980).

[70] Shackelford, F. J.; Alexander, W. Materials Science and Engineering Handbook, Third Edition (CRS Press, New York, 2001).

[71] Cheng, D.; Wang, S.; Ye, H. First-principles calculations of the elestic properties of ZrC and ZrN. *Journal of Alloys and Compounds* **377**, 221 (2003).

[72] Voitovich, F. R. Oxidation of carbides and nitrides (Naukova Dumka, Kiev, 1981).

[73] Reddy, N. L. G.; Ramana, V. J.; Kumar, S.; Kumar, V.; Raju, S. V. Investigation on the oxidation of zirconium nitride films in air by nuclear reaction analysis and backscattering spectrometry. *Applied Surface Scence* **253**, 7230 (2007).

[74] Kamijo, E.; Honda, M.; Higuchi, M.; Takeuchi, H.; Tanimura, T. The preparation of Si_3N_4 nanocomposites with various amount of TiN. *Sumitomo Electr. Tech. Rev.* **24**, 183 (1985).

[75] Lin, W.; Yang, M-J.; Ting, J-S.; Ezis, A.; Shin, J. C. Processing and Microstructural Development of In Situ TiN-Reinforced Silicon Nitride/Silicon Oxynitride Composites. *Journal of American Ceramic Society* **75**, 945 (1992).

[76] Fricke, M.; Nonninger, R.; Schmidt, H. Production of Si_3N_4/TiN Nano Composites. *Advanced Engineering Materials* **10**, 647 (2000).

[77] Kawano, S.; Takahashi, J.; Shimada, S. The preparation and spark plasma sintering of silicon nitride-based materials coated with nano-sized TiN. *Journal of European Ceramic Society* **24**, 309 (2004).

[78] Kawano, S.; Takahashi, J.; Shimada, S. Highly electroconductive TiN/Si_3N_4 composite ceramics fabricated by spark plasma sintering of Si_3N_4 particles with a nano-sized TiN coating. *Journal of Material Chemistry* **12**, 361 (2002).

[79] Kawano, S.; Tsukurimichi, K.; Takahashi, J.; Shimada, S. Preparation of nano-sized TiN coated α-Si_3N_4 particles. *Journal of Materials Chemistry* **11**, 2625 (2001).

[80] Krnel, K.; Maglica, A.; Kosmač T. β-SiAlON/TiN nanocomposites prepared from TiO_2-coated Si_3N_4 powder. *Journal of European Ceramic Society* **28**, 953 (2008).

[81] Shimada, S.; Kato, K. Coating and spark plasma sintering of nano-sized TiN on Y-α-sialon. *Materials Science and Engineering A* **443**, 47 (2007).

[82] Kamiya, K.; Yoko, T.; Bessho, M. Nitridation of TiO_2 fibres prepared by the sol-gel method. *Journal of Materials Science* **22**, 937 (1987).

[83] Li, J.; Gao, L.; Sun, J.; Zhang, Q.; Guo, J.; Yan, D. Synthesis of Nanocrystalline Titanium Nitride Powders by Direct Nitridation of Titanium Oxide. *Journal of American Ceramic Society* **84**, 3045 (2001).

[84] Negita, K. Effective sintering aids for Si_3N_4 ceramics. *Journal of Material Science Letters* **4**, 755 (1985).

[85] Wusirika, R. R.; Chyung, K. C. Oxynitride Glasses and Glass-Ceramics. *Journal of Non-Crystall Solids* **38**, 39 (1980).

[86] Das, T. Oxynitride glasses-An overview. *Bulletin Material Science* **23**, 499 (2000).

[87] Herrmann, M.; Balzer, B.; Schubert, C.; Hermel, W. Densification, microstructure and properties of Si_3N_4–Ti(C,N) composites. *Journal of European Ceramic Society* **12**, 287 (1993).

[88] Trigg, B. M.; McCartney, R. E. Comparison of the Reaction Systems ZrO_2-Si_3N_4 and TiO_2-Si_3N_4. *Communications of the American Ceramic Society* **11**, C 151 (1981).

[89] Duan, R. G.; Roebben, G.; Vleugels, J. In situ formation of Si_2N_2O and TiN in Si_3N_4-based ceramic composites. *Acta Materialia* **53**, 1547 (2005).

[90] Wang, C. M. Microstructure development of Si_3N_4-TiN composite prepared by in situ compositing. *Journal of Materials Science* **30**, 3222 (1995).

[91] Ahmad, N.; Sueyoshi, H. Properties of Si_3N_4-TiN composites fabricated by spark plasma sintering by using a mixture of Si_3N_4 and Ti powders. *Ceramics International* **36**, 491 (2010).

[92] Hermann, M.; Schubert, C.; Hermel, W. The sintering behaviour, microstructure and properties of TiCN1-x/Si_3N_4 composites. *CFI-Ceramic Forum International* **73**, 434 (1996).

[93] Seifert, J. H.; Hoffmann, J. M.; Lukas, L. H.; Petzow, G. *in "Proceedings of the 2nd Conference of the European Ceramic Society"*. 131-135 (D. G. Köln, Augsburg, 1991).

[94] Lenčeš, Z.; Panek, Z. Electroconductive β-SiAlON/TiN composites prepared by reaction sintering. *Ceramics-Silikaty* **43**, 81 (1999).

[95] Duan, G. R.; Roebben, G.; Vleugels, J.; Van der Biest, O. Optimization of microstructure and properties of in situ formed β-O-sialon-TiN composite. *Material Science and Engineering A* **427**, 195 (2006).

[96] Ueno, K.; Inoue, T.; Sodeoka, S.; Suzuki, M.; Ishikawa, H.; Uchiyama, K.; Inui, T. Si_3N_4-matrix composite with TiN particles formed by in-situ reaction. *Journal of the Ceramic Society of Japan* **105**, 304 (1997).

[97] Zheng, S.; Gao, L.; Watanabe, H.; Tatami, J.; Wakihara, T.; Komeya, K.; Meguro, T. Improving the microstructure of Si_3N_4-TiN composites using various PEIs to disperse raw TiO_2 powder. *Ceramics International* **33**, 355 (2007).

[98] Yano, Toyohiko.; Tatami, Junichi.; Komeya, K.; Meguro, T. Microstructural Observation of Silicon Nitride Ceramics Sintered with Addition of Titania. *Journal of the Ceramic Society of Japan* **109**, 396 (2001).

[99] Terao, K.; Miyamoto, Y.; Koizumi, M. Characteristics of ZrO_2-Dispersed Si_3N_4 without Additives Fabricated by Hot Isostatic Pressing. *Journal of American Ceramic Society* **71**, C-167 (1988).

[100] Dutta, S.; Buzek, B. Microstructure, Strength, and Oxidation of a 10 wt% Zyttrite-Si_3N_4 Ceramic. *Journal of American Ceramic Society* **67**, 89 (1984).

[101] Claussen, N. Fracture Toughness of Al_2O_3 with an Unstabilized ZrO_2 Dispersed Phase. *Journal of American Ceramic Society* **59**, 49 (1976).

[102] Rice, W. R.; McDonough, J. W. Hot-Pressed Si3N4 with Zr-Based Additions. *Journal of American Ceramic Society* **58**, 264 (1975).

[103] Olsson, O. P., Ekström, T. Si_2N_2O-ZrO_2 composites prepared by hot isostatic pressing. *Journal of European Ceramic Society* **16**, 535 (1996).

[104] Ekström, T.; Falk, L. K. L. Si_3N_4-ZrO_2 composites with small Al_2O_3 and Y_2O_3 additions prepared by HIP. *Journal of Material Science* **26**, 4331 (1991).

[105] Garvie, C. R.; Hannink, H. R.; Pascoe, T. R. Ceramic Materials. *Nature* **258**, 703 (1975).

[106] Carpenter, W. H.; Campbell, Jr-J.; Russell, L. H.; Wright, D. E. Ceramic heat exchangers for closed-cycle gas. *Advances in Ceramics* **14**, 345 (1985).

[107] Lange, F. F. Compressive Surface Stresses Developed in Ceramics by an Oxidation-Induced Phase Change. *Journal of American Ceramic Society* **63**, 38 (1980).

[108] Sanders, A. W.; Mieskowski, M. D. Compatibility between Si_3N_4 and ZrO_2. *Advanced Ceramic Materials* **1**, 166 (1986).

[109] Tjernlund, K. A.; Pompe, R.; Holmström, M.; Carlsson, R. On the influence of atmosphere on the reactions involving the system Si_3N_4-ZrO_2. *British Ceramic Proceedings* **37**, 29(1986).

[110] Lange, F. F.; Davis, I. B. Development of Surface Stresses During the Oxidation of Several Si_3N_4/CeO_2 Materials. *Journal of American Ceramic Society*. **62**, 629 (1979).

[111] Gauckler, J. L.; Lukas, H. L.; Henig, E-Th.; Petzow, G. Representation of phase equilibria in systems with a double exchange reaction. *Calphad* **2**, 349 (1978).

[112] Lewis, H. M. Plasticity and Fracture Mechanisms in Ceramic Alloys Based on β-Si_3N_4. *Micro Plast Fract* 218, (1983).

[113] Falk, L. K. L.; Hermansson, T.; Rundgren, K. Microstructure of hot-pressed Si_3N_4-ZrO_2(+Y_2O_3) composites. *Journal of Materials Science Letters* **8**, 1032 (1989).

[114] Falk, L. K. L. Microstructure and Short-Term Oxidation of Hot-Pressed Si_3N_4-ZrO_2(Y_2O_3) Ceramics. *Journal of American Ceramic Society* **75**, 28 (1992).

[115] Cheng, Y.; Thompson, P. D. The behaviour of ZrO_2 in Y_2O_3-Al_2O_3-SiO_2 glasses. *British Ceramic Transaction* **87**, 107 (1988).

[116] Fu, B.; Gao, L. Synthesis of nanocrystaline Zirconium Nitride Powders by Reduction-Nitridation of Zirconium Oxide. *Journal of American Ceramic Society* **87**, 696 (2004).

[117] Fripiat, N.; Grange, P. Influence of the nitridation parameters on the stoichiometry, structure and specific surface area of zirconium phosphate oxynitride catalysts. *Journal of Materials Science* **34**, 2057 (1999).

[118] Ektröm, T.; Herbertsson, H.; James, M.; Fleck, I. Nd_2O_3-Doped Sialons with ZrO_2/ZrN Additions Formed by Sintering and Hot Isostatic Pressing. *Journal of American Ceramic Society* **77**, 3087 (1994).

[119] Chockalingam, S.; Kodi Traver, H. Microwave sintering of β-SiAlON-ZrO_2 composites. *Materials and Design* **31**, 3641 (2010).

[120] Nightingale, SA.; Worner, HK.; Dunne, DP. Microstructural development during the microwave sintering of yttria-zirconia ceramics. *Journal of American Ceramic Society* **80**, 394 (1997).

[121] Bei-yue, M.; Jing-kun, Y. Influence of processing parametrs on the phase composition of ZrN-Si_3N_4 synthesized from zircon. *Rare Metals* **28**, 367 (2009).

[122] Bei-yue, M.; Jin-kun, Y.; Tao, L.; Zheng-guo, Y. Preparation of β-SiAlON/ZrN bonded corundum composites from zircon by nitridation reaction sintering process. *Journal of Central South University of Technology* **16**, 725 (2009).

[123] Bei-yue, M.; Jin-kun, Y.; Hezheng, L.; Zhenming, W. Synthesis of ZrN-Si_3N_4 Composite by Carbothermal Reduction and Nitridation of Zircon. *China's Refractories* **1**, 19 (2010).

[124] Weiss, J.; Gauckler, J. L.; Lukas, L. H.; Petzow, G.; Tien, Y. T. Determination of phase equilibria in the system Si-Al-Zr/N-O by experiment and thermodynamic calculation. *Journal of Material Science* **16**, 2997 (1981).

[125] Cain, G. M.; Lewis, H. M. Microstructure and Fracture Toughness of Hot-Pressed Zirconia-Toughened Sialon. *Journal of American Ceramic Society* **76**, 1401 (1993).

[126] Li, X. H.; Yu, K. L.; Hiragushi, K.; Mizota, Y. Phase Composition of TiO_2-Coated ZrO_2/Si_3N_4 Composite. *Journal of European Ceramic Society* **19**, 299 (1999).

[127] Weiss, J.; Gauckler, J. L.; Tien, Y. T. The System Si_3N_4-SiO_2-ZrN-ZrO_2. *Journal of American Ceramic Society* **62**, 632 (1979).

[128] Lerch, M. Nitridation of Zirconia, *Journal of American Ceramic Society* **79**, 2641 (1996).

[129] Lange, F. F.; Falk, L. K. L.; Davis, I. B. Structural ceramics based on Si_3N_4-ZrO_2(+ Y_2O_3) compositions. *Journal of Material Research* **2**, 66 (1987).

[130] King, R. P.; Buldyrev, V. S.; Dokholyan, V. N.; Havlin, S.; Lopez, E.; Paul, G.; Stanley, E. H. Percolation Theory. http://www.lps.org.uk/dialogweb/current_articles/king_percolation_theory/precolation_th (access: November 2002).

[131] Deutscher, G.; Kapitulnik, A.; Rappapott, M. *Percolation Processes and Structures: Percolation in Metal-Insulator Systems* (Deutscher, G.; Zallen, Israel, 1983).

[132] McLachlan, S. D.; Blaszkiewicz, M.; Newnham, E. R. Electrical Resistivity of Composites. *Journal of American Ceramic Society* **73**, 2187 (1990).

[133] Stauffer, D. *Introduction to percolation theory* (Taylor & Francis, London, 1985).

[134] Efros, A. L.; Shklovskii, B. Critical behaviour of conductivity and dielectric constant near the metal–non-metal transition threshold. *Physica Status Solidi* **76**, 475 (1976).

[135] Pecharoman, C.; Moya, J. S. Experimental evidence of a giant capacitance in insulator-conductor composites at the percolation threshold. *Advanced Materials* **12**, 294 (2000).

[136] Lisjak, D.; Drofenik, M.; Kolar, D. Composite ceramics with a positive temperature coefficient of electrical resistivity effect. *Journal of Material Research* **15**, 417 (2000).

[137] Lux, F. Review: models proposed to explain the electrical conductivity of mixtures made of conductive and insulating materials. *Journal of Material Science* **28**, 285 (1993).

[138] Quintanilla, J.; Torquato, S.; Ziff, R. M. Efficient measurement of the percolation threshold for fully penetrable discs. *Journal of Physics A* **33**, L339 (2000).

[139] Robinson, P. C. Numerical calculations of critical densities for lines and planes. *Journal of Physics A* **17**, 2823 (1984).

[140] De Bondt, S.; Froyen, L.; Deruyttere, A. Electrical conductivity of composites: a percolation approach. *Journal of Material Science* **27**, 1983 (1992).

[141] Balberg, I.; Binenbaum, N.; Wagner, N. Percolation thresholds in the three-dimensional sticks system. *Physical Review Letters* **52**, 1465 (1984).

[142] Huseby, O.; Thovert, J. F.; Adler, P. M. Geometry and topology of fracture systems. *Journal of Physics A* **30**, 1415 (1997).

[143] Lorenz, C. D.; Ziff, R. M. Precise determination of the critical percolation threshold for the three-dimensional 'Swiss cheese' model using a growth algorithm. *Journal of Chemistry Physics* **114**, 3659 (2001).

[144] Lebovka, N.; Linsunova, M.; Mamunya, P. Ye.; Vygornitskii, N. Scaling in percolation behaviour in conducting-insulating composites with particles of different size. *Journal of Physics D: Applied Physics* **39**, 2264 (2006).

[145] Han, D. G.; Choi, G. M. Computer simulation of the electrical conductivity of composites: the effect of geometrical arrangement. *Solid State Ionics* **106,** 71 (1998).

[146] Drory, A.; Balberg, I.; Berkowitz, B. Application of the central-particle-potential approximation for percolation in interacting systems. *Physical Review* E **52**, 4482 (1995).

[147] Xue, Z. Q. Model for effective thermal conductivity of nanofluids. *Physical Letters A* **307**, 313 (2003).

[148] Xue, Q. The influence of particle shape and size on electric conductivity of metal-polymer composites. *European Polymer Journal* **40**, 323 (2004).

[149] Ambrožič, M.; Dakskobler, A. Some aspects of numerical analysis of conductivity percolation threshold. *Journal of European Ceramic Society* **27**, 541 (2007).

[150] Xie, P.; Gu, P.; Beaudoin J. J. Electrical percolation phenomena in cement composites containing conductive fibres. *Journal of Material Science* **31**, 4093 (1996).

[151] Vanmeensel, K.; Laptev, A., Van der Biest, O.; Vleugels, J. The influnece of percolation durinh pulsed electric current sintering of ZrO_2-TiN powder compacts with varying TiN content. *Acta Materialia* **55**, 1811 (2007).

[152] Jin, X.; Gao, L. Preparation of Highly Conductive Al_2O_3/TiN Interlayer Nanocomposite through Selective Matrix Grain Growth. *Journal of American Ceramic Society* **89**, 1129 (2006).

[153] Tatami, J.; Katashima, T.; Komeya, K.; Meguro, T.; Wakihara, T. Electrically Conductive CNT-Dispersed Silicon Nitride Ceramics. *Journal of American Ceramic Society* **88**, 2889 (2005).

[154] Balazsi, C.; Sedlačkova, K.; Czigany, Z. Structural characterization of Si_3N_4-carbon nanotube interfaces by transmission electron microscopy. *Composite Science and Technology* **68**, 1596 (2008).

[155] Rul, S.; Lefevre-schlick, F.; Capria, E.; Laurent, Ch.; Peigney, A. Percolation of single-walled carbon nanotubes in ceramic matrix nanocomposites. *Acta Materialia* **52**, 1061 (2004).

[156] Kusunose, T.; Sekino, T.; Niihara, K. Production of a grain boundary phase as conductive pathway in insulating AlN ceramics. *Acta Materialia* **55**, 6170 (2007).

[157] Albinati, A.; Willis, M. T. B. The Rietveld Method in Neutron and X-ray Powder Diffraction. *Journal of Applied Crystallography* **15**, 361 (1982).

[158] Young, A. R. *The Rietveld Method* (Oxford University Press, New York, 1993).

[159] Kubashewski, O; Ewans, L. E.; Alcock, B. C. *Metallurgical Thermochemistry* (Pergamon Press, London, 1967).

[160] Lee, Ching-Huan; Lu, Horng-Hwa; Wang, Chang-An; Nayak, K. P.; Huang, Jow-Lay. Microstructure and mechanical properties of TiN/Si_3N_4 nanocomposites by spark plasma sintering (SPS). *Journal of Alloys and Compounds*, Article in Press.

[161] Marinšek, M.; Maček, J.; Meden, T. Starved Water Hydrolysis of Different Precursors and its Influence on the Properties of Precipitated Zirconia. *Journal of Sol-Gel Science and Technology* **23**, 119 (2002).

[162] Wang, A. J.; Valenzuela, A. M.; Salamons, J; Bokhimi, X. Comparative study of nanocrystalline zirconia prepared by precipitation and sol-gel methods. *Catalysis Today* **68**, 21 (2001).

[163] Aarik, J.; Aidla, A.; Mändar, H.; Unstare, T.; Sammelselg, V. Growth kinetics and structure formation of ZrO_2 thin films in chlorid-based atoms layer deposition process. *Thin Solid Films* **408**, 97 (2002).

[164] Tahin, N. M.; Gorgishvili, L.; Li. J.; Gorelik, T.; Kolb, U.; Nasdala, L.; Tremel, W. Facile synthesis and characterization of monocrystalline cubic ZrO_2 nanoparticles. *Solid State Science* **9**, 1105 (2007).

[165] Garvie, C. R. The occurrence of metastable tetragonal zirconia as a crystallite size effect. *Journal of Physical Chemistry* **69**, 1238 (1965).

[166] Tsunekawa, S.; Ito, S.; Kawazoe, Y.; Wang, T. J. Crytical size of the phase transition from cubic to tetragonal in fine zirconia nanoparticles. *Nano Letters* **3**, 871 (2003).

[167] Schneider, H. G.; Ruth, V. Advances in Epitaxy and Endotaxy (VEB, Leipzig, 1971).

[168] Kibbel, B.; Heuer, H. A. Exaggerated Grain Growth in ZrO_2-Thoughened Al_2O_3. *Journal of American Ceramic Society* **69**, 231 (1986).

[169] Maglica, A.; Krnel, K.; Pribošič, I.; Kosmač, T. Preparation and properties of β-SiAlON/ZrN nano-composites from ZrO_2-coated Si_3N_4 powder. *Processing and Application of Ceramics* **1**, 49 (2007).

[170] Schick, L. H. Termodynamics of Certain Refractory Compounds, Volume II (Academic Press, New York, 1966).

[171] Egorov, F. F.; Lugovskaya, S. E. Effect of nitrogen on the sintering of ZrN-Al_2O_3 mixtures. *Powder Metallurgy and Metal Ceramics* **16**, 11 (1977).

[172] Kolitsch, U.; Seifert, H. J.; Ludwig, T.; Aldinger, F. Y_2O_3-Al_2O_3-SiO_2 system. *Journal of Material Science* **14,** 447 (1999).

[173] Maglica, A.; Ambrožič, M. Development of the ceramic glow plug. *Vakuumist* **28**, 4 (2008).

Index of Figures

Index of Tables

Appendix

A simple theoretical percolation-threshold model

A simple model of the percolation threshold in the case of small conducting grains as compared to anisotropic insulating grains, is performed by Milan Ambrožič in the following way. Insulating grains are approximated by elongated rotational ellipsoids with half-axes (*a*, *a*, *c*), where *a* < *c*. Much smaller conducting grains are approximated by spheres of radius *r* (*r* << *a* < *c*). It is supposed that the surface of an ellipsoid is covered by a layer of several smaller spheres. The volume of an ellipsoid is $V_{el} = \frac{4\pi}{3} a^2 c$ and the total volume of *N* spheres around the ellipsoid is $V_{Ns} = N \cdot \frac{4\pi}{3} r^3$. The volume ratio of the conducting and insulating phases is thus: $VR = \frac{V_s}{2V_{el}} = \frac{Nr^3}{2a^2c}$. Factor 1/2 is added because there is one conducting layer between two neighboring insulating ellipsoids (which thus share the sticking layer). The number *N* of the spheres on the surface of the ellipsoid is determined by the ratio of their areas: $N = \frac{kS_{el}}{S_{1s}}$. The area of the sphere is $S_{1s} = 4\pi r^2$, while the area of the elongated ellipsoid is $S_{el} = 2\pi a \cdot (a + \frac{c^2}{\sqrt{c^2 - a^2}} \arcsin(\frac{\sqrt{c^2 - a^2}}{c}))$. In fact, in the calculation, we take, instead of half-axes (*a*, *a*, *c*), the enlarged half-axes (*a*+*r*, *a*+*r*, *c*+*r*) made by a "concentric ellipsoid" going through the centers of the spheres on the ellipsoid (see the dashed ellipsoid in the sketch of the system in Figure 80). The filling factor *k* depends on the essentially 2D geometry of the circles on the concentric ellipsoid (these circles are approximate intersections of concentric ellipsoids with spheres for *r* << *a*). In the case of a close-packed structure of circles in an infinite plane the filling factor is *k* = 90.7 %. In reality the circles need not be closely packed to make an infinitely expanding sticking cluster in the plane. In the percolation theory, numerical calculations for the 2D problem of "hard" circles in the plane (the term hard circles means that they can only touch but not penetrate into each other) show, that the percolation threshold is reached when the area portion of the circles in the plane is about 68 %. This is a reasonable value for *k* as a starting point in our calculations. When the percolation threshold of spherical conducting grains in the layers around the insulating larger grains is reached, there is also a bulk percolation threshold for electrical conductivity. In a real situation *k* could be even smaller: there may be individual conducting paths of conducting grains between the boundaries of the insulating grains even if most insulating grains are not covered by a connected layer of the conducting smaller grains – this can be expected when the difference in size between the insulating and conducting grains is not so large and the conducting grains are, therefore, not evenly distributed around the insulating ones.

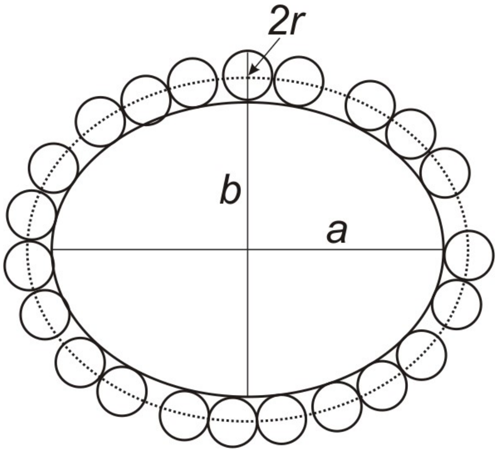

Figure 80: Sketch of an insulating ellipsoid with a layer of conducting spherical particles on its surface. Not all spheres need to be in contact in order to make an expanding percolation cluster on the surface of the ellipsoid.

Taking into account all the factors, we obtain a final expression for the volume ratio of the conducting and insulating phases:

$$VR = 2k\rho x \cdot \left(x + \frac{y^2}{\sqrt{y^2 - x^2}} \arcsin\left(\frac{\sqrt{y^2 - x^2}}{y}\right)\right), \qquad (28)$$

where $\rho = \frac{r}{\sqrt[3]{a^2 c}}$, $x = \sqrt[3]{\frac{a}{c}} + \rho$ and $y = \sqrt[3]{(\frac{c}{a})^2} + \rho$. The parameter ρ is viewed as the ratio between the radius of a spherical conducting grain and the effective radius $R = \sqrt[3]{a^2 c}$ of an ellipsoidal insulating grain.

For reference we add here simple formula for the case of spherical insulating particles of radius *R* instead of ellipsoids. The volume ratio of conducting and insulating phases is now: $VR = \frac{V_s}{2V_{el}} = \frac{Nr^3}{2R^3} = \frac{2kr}{R}$ The parameter *k* has the same meaning as above. Instead of the surface indicated by dotted line in Figure 80 we take the direct surface of the core particle (we suppose $r << R$). From this ratio we calculate the mass ratio of the amount of core and shell particles (Equation 25, page 38)

Instead of the volume ratio VR of both phases, the volume fraction of the conducting phase (relative to the whole composite) is used in the literature of percolation theory:

$$\phi_c = \frac{VR}{1+VR} \tag{29}$$

with VR from Equation 28. This is our simple model (rough estimation) for the percolation threshold.

Personal bibliography for the period of the doctoral study (2007-2011)

Articles and other component parts

Original scientific article

1. MAGLICA, Aljoša, KRNEL, Kristoffer, PRIBOŠIČ, Irena, KOSMAČ, Tomaž. Preparation and properties of β-SiAlON/ZrN nano-composites from ZrO_2-coated Si_3N_4 powder. *Processing and application of ceramics*, 2007, vol. 1, no. 1/2, p. 49-55. [COBISS.SI-ID 21575975]

2. KRNEL, Kristoffer, MAGLICA, Aljoša, KOSMAČ, Tomaž. β-SiAlON/TiN nanocomposites prepared from TiO_2-coated Si_3N_4 powder. V: ŠAJGALÍK, Pavol (ur.), HOFFMANN, Michael J. (ur.), RIEDEL, Ralf (ur.). *Engineering ceramics '07: from engineering to functionality : the Advanced Research Workshop, 06-10 May 2007, Smolenice, Slovakia*, (Journal of the European Ceramic Society, vol. 28, no. 5, 2008). Barking: Elsevier, 2008, vol. 28, iss. 5, p. 953-957. [COBISS.SI-ID 21574439]

3. MAGLICA, Aljoša, AMBROŽIČ, Milan. Razvoj keramične žarilne svečke = Development of a ceramic glow plug. *Vakuumist*, 2008, vol. 28, iss. 3, p. 4-8. [COBISS.SI-ID 22210343]

4. MAGLICA, Aljoša, KRNEL, Kristoffer, AMBROŽIČ, Milan. Keramični kompoziti na osnovi silicijevega nitrida = Ceramic composites based on silicon nitride. *Mater. tehnol.*, 2009, vol. 43, iss. 3, p. 165-169. [COBISS.SI-ID 22745639]

5. MAGLICA, Aljoša, KRNEL, Kristoffer, KOSMAČ, Tomaž. Preparation of Si_3N_4-TiN ceramic composites = Priprava keramičnih kompozitov na osnovi Si_3N_4-TiN. *Mater. tehnol.*, 2010, vol. 44, iss. 1, p. 31-35. [COBISS.SI-ID 23435303]

Published scientific conference contribution

6. KRNEL, Kristoffer, MAGLICA, Aljoša, KOSMAČ, Tomaž. Development of new electro-conductive ceramic composites for ceramic glow plugs. V: BELLOSI, Alida (ur.), BABINI, Gian Nicola (ur.). 2nd International Congress on Ceramics, [Verona, Italy, June 29 - July 4, 2008]. *Global roadmap for ceramics : ICC2 proceedings*. [S. l.]: Institute of Science and Technology for Ceramics, National Research Council, 2008, p. 6. [COBISS.SI-ID 22013223]

7. KRNEL, Kristoffer, MAGLICA, Aljoša, KOSMAČ, Tomaž. Reaction sintered Si_3N_4 based electroconductive ceramics composites. V: BELLOSI, Alida (ur.), BABINI, Gian Nicola (ur.). 2nd International Congress on Ceramics, [Verona, Italy, June 29 - July 4, 2008]. *Global roadmap for ceramics : ICC2 proceedings*. [S. l.]: Institute of Science and Technology for Ceramics, National Research Council, 2008, p. 6. [COBISS.SI-ID 22012967]

8. KRNEL, Kristoffer, MAGLICA, Aljoša, KOSMAČ, Tomaž. Development of new electro-conductive ceramic composites for ceramic glow plugs. V: ŽNIDARIČ, Aleš (ur.). TRA, Transport Research Arena Europe 2008, Ljubljana, Slovenia, 21-24 April 2008. *Greener, safer and smarter road transport for Europe, Proceedings*. Ljubljana: DDC svetovanje inženiring: ZAG, Zavod za gradbeništvo Slovenije: DRC, Družba v cestni in prometni stroki Slovenije, 2008, p. 6. [COBISS.SI-ID 22012455]

Published scientific conference contribution abstract

9. MAGLICA, Aljoša, KRNEL, Kristoffer, KOSMAČ, Tomaž. Preparation and properties of β-SiAlON/TiN nano-composites = Priprava in lastnosti nanokompozitov β-SiAlON/TiN. V: JENKO, Monika (ur.). 15. konferenca o materialih in tehnologijah = 15th Conference on Materials and Technology, 8-10 October, 2007 Portorož, Slovenia. *Program in knjiga povzetkov*. Ljubljana: Inštitut za kovinske materiale in tehnologije], 2007, p. 40. [COBISS.SI-ID 21403175]

10. MAGLICA, Aljoša, KRNEL, Kristoffer, KOSMAČ, Tomaž. Preparation and properties of β-SiAlON/ZrN nano-composites from ZrO_2-coated Si_3N_4 powder. V: SRDIĆ, Vladimir V. (ur.), RANOGAJEC, Jonjaua (ur.). The Seventh Students' Meeting SM-2007, Processing and Application of Ceramics, Novi Sad, December 6-8,2007. *Programme and book of abstracts*. Novi Sad: Faculty of Technology, p. 53-54. [COBISS.SI-ID 21416743]

11. MAGLICA, Aljoša, KRNEL, Kristoffer, KOSMAČ, Tomaž. Raziskave električno prevodnih keramičnih kompozitov za keramične grelce. V: PONIKVAR-SVET, Maja (ur.). Ljubljana, 15. 2. 2008. *Prispevki*. Ljubljana: Institut "Jožef Stefan", 2008. [COBISS.SI-ID 21580839]

12. MAGLICA, Aljoša, KRNEL, Kristoffer, KOSMAČ, Tomaž. The coating of Si_3N_4 powder with nanosized ZrN particles = Prekrivanje Si_3N_4 prahu z nanodelci ZrN. V: JENKO, Monika (ur.). 1. mednarodna konferenca o materialih in tehnologijah pod pokroviteljstvom FEMS in IUVSTA, 13.-15. oktober 2008, Portorož = 1st International Conference on Materials and Technology sponsored by FEMS and IUVSTA, 13-15 October 2008, Portorož, Slovenia. *Program in knjiga povzetkov*. Ljubljana: Inštitut za kovinske materiale in tehnologije, 2008, p. 33. [COBISS.SI-ID 22211111]

13. MAGLICA, Aljoša, KRNEL, Kristoffer, KOSMAČ, Tomaž. Preparation of electroconductive ceramic composites from Si_3N_4. V: 33rd International Conference and Exposition on Advanced Ceramics and Composites, January 18-23, 2009,

Daytona Beach, Florida, USA. *Abstracts book*. [S. l.]: The American Ceramic Society, 2009, p. 121. [COBISS.SI-ID 22790439]

14. MAGLICA, Aljoša, KRNEL, Kristoffer, KOSMAČ, Tomaž. Priprava električno-prevodnih keramičnih kompozitov na osnovi Si_3N_4. V: ISKRA, Jernej (ur.), MILOŠEV, Ingrid (ur.). *Dan mladih raziskovalcev 2009*. Ljubljana: Institut "Jožef Stefan", 2009, page. 1. [COBISS.SI-ID 22445607]

15. KRNEL, Kristoffer, MAGLICA, Aljoša, KOSMAČ, Tomaž. Reaction-sintered Si_3N_4/TiN electroconductive ceramic composites. V: 6th International Conference on Nitrides and Related Materials, March 15-18, 2008, Karlsruhe, Germany. *ISNT 2009*. [S. l.: s. n.], 2009, p. 88. [COBISS.SI-ID 22992167]

16. MAGLICA, Aljoša, KRNEL, Kristoffer, KOSMAČ, Tomaž. Electroconductive Si_3N_4/ZrN ceramic composites fabricated from Si_3N_4 powder coated by ZrO_2 nano-particles. V: 6th International Conference on Nitrides and Related Materials, March 15-18, 2008, Karlsruhe, Germany. *ISNT 2009*. [S. l.: s. n.], 2009, p. 180. [COBISS.SI-ID 22791207]

17. MAGLICA, Aljoša, KRNEL, Kristoffer, KOSMAČ, Tomaž. Preparation of electroconductive Si_3N_4/ZrN ceramic composite. V: JENKO, Monika (ur.). 17. konferenca o materialih in tehnologijah, 16.-18. november 2009, Portorož, Slovenija. *Program in knjiga povzetkov*. Ljubljana: Inštitut za kovinske materiale in tehnologije, 2009, p. 38. [COBISS.SI-ID 23127079]

18. MAGLICA, Aljoša, KRNEL, Kristoffer, KOSMAČ, Tomaž. Inovativni električno prevodni keramični kompoziti na osnovi silicijevega nitrida. V: ŠETINA, Barbara (ur.), JUNKAR, Ita (ur.), KALUŽA, Boštjan (ur.), ELERŠIČ, Kristina (ur.). 1st Jožef Stefan International Postgraduate School Student's Conference, 19th-20th May 2009, Ljubljana, Slovenia. *Zbornik prispevkov*. Ljubljana: Mednarodna podiplomska šola Jožefa Stefana, 2009, p. 30-31. [COBISS.SI-ID 22639399]

19. KRNEL, Kristoffer, MAGLICA, Aljoša, KOSMAČ, Tomaž. Preparation and properties of electro-conductive ceramic composites from Si_3N_4 powders coated by nano-sized ZrN and TiN. V: 3rd International Symposium on SiAlONs and Non-oxides, 1-4 June 2010, Cappadocia, Turkey. *Abstract book*. [S. l.: s. n.], 2010, p. 56. [COBISS.SI-ID 24409127]

20. MAGLICA, Aljoša, KRNEL, Kristoffer, KOSMAČ, Tomaž. Si_3N_4/ZrN ceramic composites produced from ZrO_2-coated Si_3N_4 powder. V: 34th International Conference and Exposition on Advanced Ceramics and Composites, January 24-29, 2010, Daytona Beach, Florida, USA. *Abstracts book*. [S. l.]: The American Ceramic Society, 2010, p. 28. [COBISS.SI-ID 23437863]

21. MAGLICA, Aljoša, KRNEL, Kristoffer, KOSMAČ, Tomaž. Inovativni električno prevodni keramični kompoziti na osnovi silicijevega nitrida. V: KUŠČER, Danjela (ur.), PERC, Branka (ur.). 4. Dan Mladih Raziskovalcev KMBO, Ljubljana, Slovenija, 11.2.2010. *[Program in povzetki]*. Ljubljana: Institut "Jožef Stefan", 2010, p. 38. [COBISS.SI-ID 23435559]

22. MAGLICA, Aljoša, KRNEL, Kristoffer, KOSMAČ, Tomaž. The preparation and sintering of silicon nitride powders coated with nano-sized ZrN. V: SRDIĆ, Vladimir V. (ur.), RANOGAJEC, Jonjaua (ur.). The Eighth Students' Meeting Processing and Application of Ceramics, SM 2009, December 2-5, 2009, Novi Sad, Serbia. *Programme and book of abstracts*. Novi Sad: Faculty of Technology, University of Novi Sad, 2009, p. 74. [COBISS.SI-ID 23952167]

23. MAGLICA, Aljoša, KRNEL, Kristoffer, KOSMAČ, Tomaž. Priprava in lastnosti Si_3N_4/TiN nanokompozitov. V: PRIBOŠIČ, Irena (ur.), KRNEL, Kristoffer (ur.). *5. Dan Mladih raziskovalcev,* Ljubljana, Slovenija, 17.2.2011. *[Program in povzetki]*. Ljubljana: Institut "Jožef Stefan", 2011, p. 51. [COBISS.SI-ID 24479527]

Monographs and other completed works

Treatise, preliminary study, study

24. KOSMAČ, Tomaž, KRNEL, Kristoffer, MAGLICA, Aljoša. *Razvoj keramičnega grelca za naročnika AET. 2. del*, (IJS delovno poročilo, 9607). 2007. [COBISS.SI-ID 21633575]

25. KOSMAČ, Tomaž, KRNEL, Kristoffer, MAGLICA, Aljoša, PRIBOŠIČ, Irena. *Razvoj keramičnega grelca za naročnika AET. 3. del*, (IJS delovno poročilo, 9653). 2007. [COBISS.SI-ID 21633831]

26. KOSMAČ, Tomaž, KRNEL, Kristoffer, MAGLICA, Aljoša. *Razvoj keramičnega grelca za naročnika Iskra ISD. 3. del*, (IJS delovno poročilo, 9643). 2010. [COBISS.SI-ID 23766823]

27. KOSMAČ, Tomaž, KRNEL, Kristoffer, MAGLICA, Aljoša. *Razvoj keramičnega grelca za naročnika Iskra ISD. 2. del*, (IJS delovno poročilo, 9608). 2007. [COBISS.SI-ID 21633063]

Patent application

28. MAGLICA, Aljoša, KRNEL, Kristoffer, KOSMAČ, Tomaž. *Enostopenjski postopek izdelave kompozitnega keramičnega grelca: patentna prijava P-201100015*. Ljubljana: Urad RS za intelektualno lastnino, 13. jan. 2011. [COBISS.SI-ID 24429607]

Performed works (events)

Unpublished conference contribution

29. MAGLICA, Aljoša. *β-SiAlON/TiN nano-composites prepared from TiO_2-coated Si_3N_4 powder: presented at 6th Workshop of Engineering Ceramics 2007, 6-10 May 2007, Smolenice, Slovakia*. 2007. [COBISS.SI-ID 21409063]

30. MAGLICA, Aljoša. *Reakcijsko sintranje keramičnih kompozitov na osnovi Si_3N_4-TiN : Dan MR kemije, materialov, biokemije in znanosti o okolju, Izobraževalni center Milana Čopiča, 17.01.2007, Ljubljana, Slovenija*. 2007. [COBISS.SI-ID 21404199]

31. MAGLICA, Aljoša, KRNEL, Kristoffer, KOSMAČ, Tomaž. *Preparation and properties of Si_3N_4/TiN nano-composites : lecture, presented at the European Conference Junior EUROMAT 2010, 26-30 July 2010, Lausanne, Switzerland*. 2010. [COBISS.SI-ID 23952679]